

2018

## Developing Electrically and Thermally Conductive Hydrogel Based on Graphene Suitable for Bio-Thermistor

Mohammad Haj Seyed Javadi  
*University of Wollongong*

Follow this and additional works at: <https://ro.uow.edu.au/theses1>

### University of Wollongong

#### Copyright Warning

You may print or download ONE copy of this document for the purpose of your own research or study. The University does not authorise you to copy, communicate or otherwise make available electronically to any other person any copyright material contained on this site.

You are reminded of the following: This work is copyright. Apart from any use permitted under the Copyright Act 1968, no part of this work may be reproduced by any process, nor may any other exclusive right be exercised, without the permission of the author. Copyright owners are entitled to take legal action against persons who infringe their copyright. A reproduction of material that is protected by copyright may be a copyright infringement. A court may impose penalties and award damages in relation to offences and infringements relating to copyright material.

Higher penalties may apply, and higher damages may be awarded, for offences and infringements involving the conversion of material into digital or electronic form.

Unless otherwise indicated, the views expressed in this thesis are those of the author and do not necessarily represent the views of the University of Wollongong.

### Recommended Citation

Haj Seyed Javadi, Mohammad, Developing Electrically and Thermally Conductive Hydrogel Based on Graphene Suitable for Bio-Thermistor, Doctor of Philosophy thesis, Intelligent Polymer Research Institute, School of Chemistry, University of Wollongong, 2018. <https://ro.uow.edu.au/theses1/636>

Research Online is the open access institutional repository for the University of Wollongong. For further information contact the UOW Library: [research-pubs@uow.edu.au](mailto:research-pubs@uow.edu.au)



UNIVERSITY  
OF WOLLONGONG  
AUSTRALIA

# Developing Electrically and Thermally Conductive Hydrogel Based on Graphene Suitable for Bio- Thermistor

---

Mohammad Haj Seyed Javadi

Supervisors:

Dr. Stephen Beirne

Professor. Simon Moulton

Dr. Sina Naficy

Professor Gordon G. Wallace

This thesis is presented as part of the requirement for the conferral of the degree:

Doctor of Philosophy

The University of Wollongong

Australian Research Council Centre of Excellence for Electromaterials Science,  
Intelligent Polymer Research Institute and School of Chemistry, Faculty of Science,

Medicine and Health.

Dec 2018

## **Abstract**

This thesis focuses on the development of a family of flexible conductive hydrogels based on graphene and Poly (3, 4-ethylenedioxy thiophen):poly (styrenesulfonate) (PEDOT:PSS) as fillers of a polyurethane (PU) matrix. This thesis describes the novel modification of Liquid Crystal Graphene Oxide (LCGO) with chloride salts with an increase of the storage moduli, viscosity and thermal conductivity. Development of novel processable conductive hydrogel (PUHC) via blending LCGO and PEDOT:PSS within PU matrix is described, along with the processability and biocompatibility assessment. The PUHC was used in the fabrication of a temperature sensor, with the processability and performance of the developed PUHC temperature sensor (Ts-PUHC) discussed.

Study on the electrical and mechanical performance of PUHC was continued with an investigation of the thermal properties, thermal expansion, and the impact of prestrain on the PUHC properties. Finally, rheological behaviour and preparation of 3D printable PUHC ink is investigated and discussed. To the best of my knowledge, this is the first reported printable composite without any post-treatment that can offer negative temperature coefficient of resistance (NTC) behaviour under ambient conditions with adjustable thermal and electrical conductivity, and stretchability within the temperature range of the human body (25 - 45°C).

The thesis concludes with suggestions for further work that include both theoretical and practical areas.

## **Acknowledgements**

I would like to begin by thanking my supervisors Dr. Stephen Beirne, Professor. Simon Moulton, Dr. Sina Naficy and Professor Gordon G. Wallace for all their guidance, help, ideas and support throughout my project. I truly appreciate the time they have spent on my work, publications and thesis, as well as encouragement throughout my time in IPRI.

Thanks to Dr. Patricia Hayes for her assistance with Raman spectroscopy measurements, and Mr. Tony Romeo for his invaluable assistance with SEM microscopy. Thanks Dr. Rouhollah Jalili, Dr. Pawel Wagner, Ali Jeirani, and Prof. Morteza Aghmesheh for their help and comments toward my PhD process.

Thanks to all my friends in IPRI and AIIM, who are still here or have left for new adventures, for their support in both work and personal life.

Finally, and most important, I would like to thank my parents and my wife and son, Sara and Yasin. Thanks for your unconditional and endless love and support in all my life.

## **Certification**

I, Mohammad Haji Seyed Javadi, declare that this thesis, submitted in fulfilment of the requirements for awarding the degree of Doctor of Philosophy in the Intelligent Polymer Research Institute at the University of Wollongong, is entirely my own unless otherwise stated, referenced or acknowledged. This document has not been submitted for qualifications at any other academic institution.

Mohammad Haj Seyed Javadi

Dec 2018

---

## List of Names or Abbreviations

AgNW	Silver nanowire
CM	Carbonaceous materials
CuPc	Phthalocyanine
Cu	Copper
C <sub>6</sub> H <sub>8</sub> O <sub>6</sub>	Ascorbic acid
CNT	Carbon nanotubes
CVD	Chemical vapor deposition
CP	Conductive polymer
<i>d</i> -spacing	Layer-to-layer distance
Co	Cobalt
CaCl <sub>2</sub>	Calcium chloride
CRH	Critical relative humidity
DMF	Dimethylformamide
DBDA	4,5-dihydroxy-1,3-benzenedisulfonic acid
D	Dimensional
e-skin	Electronic-skin
ESD	Electrostatic discharge
EMI	Electromagnetic interference
EtOH	Ethanol
FS	Free standing
FET	field-effect transistor

GO	Graphene oxide
GICs	Graphite intercalation compounds
G'	Storage Modulus
G''	Loss modulus
HCl	Hydrogen chloride
H <sub>2</sub> SO <sub>4</sub>	Sulfuric acid
Hrs	Hours
HI	Hydrogen iodide
hs	Hard segment
hNSCs	Human neural stem cells
I <sub>D</sub>	Intensity of D band
I <sub>G</sub>	Intensity of G band
ICPs	Inherently conductive polymers
ITO	Indium-tin-oxide
I <sub>D</sub>	Drain current
ICs	Integrated circuits
KCl	Potassium chloride
LCGO	Liquid crystal graphene oxide
LC	Liquid crystal
MWCNTs	Multiple walls carbon nanotube
Modified LCGO	M-LCGO
MgCl <sub>2</sub>	Magnesium chloride

Mg	Manganese
MIM	Metal/insulator/metal
Ni	Nickel
NTC	Negative temperature coefficient of resistance
NH	Amine
NMP	Neutral mechanical plane
NaCl	Sodium chloride
N <sub>2</sub> H <sub>4</sub>	Hydrazine
OFET	Flexible organic field effect transistor
OMIm[PF <sub>6</sub> ]	Octyl-3-methylimidazolium hexafluorophosphate
PVDF	Pyroelectric poly(vinylidene fluoride)
PDMS	Polydimethylsiloxane
PTC	Positive temperature coefficient
PE	Polyethylene
PEO	Polyethylene oxide
PEDOT:PSS	Poly(3,4-ethylenedioxy thiophene):poly(styrenesulfonate)
PTCDI	Perylenetetracarboxylic-diimide
PTh	Polythiophenes
PPy	Polypyrrole
PAni	Polyaniline
PU	Polyurethanes
PET	Polyethylene terephthalate



PUHC	Polyurethane hybrid composite
PAni	Polyaniline
PPy	Polypyrrole
Pt	Platinum
PLA	Poly lactide
RTD	Resistive temperature detector
RFID	Radio frequency identification
R-GO	Reduced graphene oxide
RF	Radio frequency
RP	Rapid prototyping
SWCNT	Single wall carbon nanotube
SHP	Self-healing polymer
SEM	Scanning electron microscopy
ss	Soft segment
$T_g$	Glass transition temperature
TCR	Temperature coefficient of resistance
TRG	Thermally reduced graphene oxide
TLC	Thermochromic liquid crystals
TrFE	Trifluoroethylene
UV	Ultraviolet
w/w	Weight per weight
$W_0$	Weight of the films before drying

W	Weight of the films after drying
XRD	X-ray diffraction
$\zeta$	Zeta potential
$\kappa$	Thermal conductivity
$\sigma$	tensile strength
$\sigma$	conductivity
$\gamma$	shear rate
$\varepsilon$	breaking strain
$\eta$	apparent viscosity
$\dot{\eta}_l$	length efficiency factor
$\dot{\eta}_o$	orientation parameter factor
$\Phi$	critical volume fraction
$\varphi_{nem}$	nematic phase volume fraction
$\Omega$	Ohm
$\mu$	micro

## Table of Contents

1.1	Chapter 1: Introduction .....	2
1.2	The concept of a thermal (temperature) sensor .....	5
1.2.1	Negative Temperature Coefficient (NTC) thermistor.....	5
1.2.2	Resistance Temperature Detector (RTD).....	6
1.2.3	Thermocouple .....	6
1.2.4	Semiconductor-based (IC) sensors.....	7
1.3	Temperature sensor for health monitoring .....	8
1.3.1	Flexible and stretchable temperature sensor .....	9
1.4	Electrically active composite .....	23
1.5	Electrically Conducting Materials.....	25
1.5.1	Inherently Conducting Polymers .....	25
1.5.2	Polythiophene (PTh) .....	27
1.5.3	Polypyrrole (PPy).....	28
1.5.4	Polyaniline (PAni).....	30
1.5.5	Poly(3,4-ethylenedioxythiophene) poly(styrenesulfonate) (PEDOT:PSS)..	31
1.5.6	Carbonaceous Materials as Fillers .....	33
1.6	Hydrogels .....	41
1.6.1	Conductive Hydrogel .....	44
1.6.2	Polyurethanes .....	45

1.6.3	Polyurethane conducting polymers .....	<b>47</b>
1.7	3D Printing of Scaffolds.....	<b>52</b>
1.8	Thesis outline .....	<b>54</b>
2	Chapter 2: General Experimental .....	<b>56</b>
2.1	Material .....	<b>57</b>
2.1.1	Synthesis of Graphene Oxide.....	<b>57</b>
2.1.2	PEDOT:PSS dispersions .....	<b>58</b>
2.1.3	Synthesize of PUHC .....	<b>Error! Bookmark not defined.</b>
2.2	Experimental Techniques.....	<b>59</b>
2.2.1	Tensile test .....	<b>59</b>
2.2.2	Electrical conductivity .....	<b>60</b>
2.2.3	Scanning electron microscopy .....	<b>61</b>
2.2.4	X-ray diffraction .....	<b>61</b>
2.2.5	Raman spectroscopy .....	<b>62</b>
2.2.6	Rheological characterization.....	<b>62</b>
2.2.7	Preparation of PUHC Printed Scaffolds.....	<b>63</b>
3	Chapter 3: Ionic Interactions to Tune Mechanical, Electrical and Thermal Properties of Hydrated Liquid Crystal Graphene Oxide Films.....	<b>65</b>
3.1	Introduction .....	<b>66</b>
3.2	Experimental .....	<b>70</b>
3.2.1	Synthesis of modified liquid crystal graphene oxide (m-LCGO).....	<b>70</b>
3.2.2	Characterization of LCGO and m-LCGO dispersions and films.....	<b>71</b>

3.3	Results and Discussion.....	71
3.3.1	m-LCGO Dispersions and Rheology .....	71
3.3.2	m-LCGO dispersions, storage modulus ( $G'$ ) and loss modulus ( $G''$ ).....	74
3.3.3	Stability of m-LCGO dispersion .....	75
3.3.4	Morphology of m-LCGO Films .....	77
3.3.5	Raman Spectra of m-LCGO and LCGO .....	79
3.3.6	X-ray diffraction of m-LCGO .....	82
3.3.7	Mechanical properties of m-LCGO .....	83
3.3.8	Electrical property of m-LCGO .....	88
3.3.9	Thermal conductivity of m-LCGO .....	89
3.3.10	Comprising Hygroscopicity .....	90
3.3.11	Water Content .....	92
3.4	Conclusions .....	93
4	Chapter 4: Advanced Conductive Tough Hydrogel for Bio-applications .....	94
4.1	Introduction .....	95
4.2	Experimental .....	97
4.2.1	Characterization of PUHC .....	97
4.2.2	Cell culture and differentiation .....	98
4.2.3	Electrical stimulation .....	98
4.2.4	Immunocytochemistry and analysis .....	99
4.2.5	Reduction of PUHC .....	100

4.3	Results and Discussion.....	101
4.3.1	X-ray diffraction (XRD) .....	102
4.3.2	Correlation between mechanical and electrical properties .....	104
4.3.3	Mechanical Characterisation.....	105
4.3.4	Electrical conductivity .....	108
4.3.5	Water Content .....	111
4.3.6	Liquid Crystal Structure in PUHC .....	112
4.3.7	Morphology of PUHC.....	113
4.3.8	Reduction of LCGO .....	114
4.3.9	Raman spectra .....	119
4.3.10	hNSCs can be cultured and differentiated on PUHC.....	120
4.3.11	Electrical stimulation via PUHC enhances neuritogenesis of hNSCs .....	123
4.4	Conclusions .....	125
5	Chapter 5: PUHC Thermistor for Healthcare Applications A Preliminary Study	126
5.1	Introduction .....	127
5.2	Experimental .....	130
5.2.1	Rheological measurement and ink preparation.....	130
5.2.2	Thermal Expansion of PUHC .....	131
5.2.3	Thermal Transport Properties of Thin Films .....	135
5.2.4	Ts-PUHC design .....	137
5.2.5	Fabrication of scaffolds.....	138

5.2.6	Strain evaluation .....	140
5.2.7	Evaluating correlation between resistance and temperature in Ts-PUHC..	140
5.2.8	Paraffin oil treatment of Ts-PUHC .....	142
5.3	Result and Discussion .....	142
5.3.1	Optimization of filler ratio of PUHC .....	142
5.3.2	Impact of prestrain on PUHC film properties .....	145
5.3.3	Asymmetric Thermal Volume Expansion of Sample .....	148
5.3.4	Rheological Evaluation of PUHC Ink.....	151
5.3.5	3D printing of PUHC scaffolds (45 °C).....	154
5.3.6	Scanning electron microscopy .....	159
5.3.7	Effect of moisture on Ts-PUHC performance .....	160
5.3.8	Effect of pH on Ts-PUHC performance .....	162
5.3.9	Impact of Simulated Body Fluid on Ts-PUHC mechanical properties.....	165
5.4	Conclusions .....	168
6	Chapter 6: Conclusion and Recommendation .....	169
6.1	Conclusion.....	170
6.2	Future Recommendations.....	172
7	Reference .....	175

## List of Figures

- Figure 1.1* Examples of recently developed flexible and stretchable physical sensors for measuring parameters on the surface of the skin such as temperature, pressure and strain generated by human activities for personal healthcare monitoring.[4] .....**3**
- Figure 1.2* The advantages and disadvantages of four main types of commercially available temperature sensor devices.[27].....**8**
- Figure 1.3* a. Chemical structure of PVDF-TrFE. a.1) PVDF polymer chain and b: TrFE monomer structure, a.2) the principle of pyroelectric performance in temperature fluctuation. Pyroelectric is scavenging thermal energy from its working environment. Pyroelectric materials have the potential to convert temperature fluctuation into electric energy.....**10**
- Figure 1.4* a. Organic thin-film transistor structure with pyroelectric gate dielectric b. Temperature response data of the poled device in continuous measurements. [45].....**12**
- Figure 1.5* a) Optical images of temperature sensors based on Si nano membranes (top) and microheaters based on Au wires in a serpentine layout (bottom), both on a handle wafer. b) Optical image of a temperature sensor array based on Pt resistors, on a handle wafer. The two arrays have four sensors each, which are arranged in a bifacial configuration. c) Demonstrative temperature sensor on a plastic model of the human brain before (left frame) and after (right frame) dissolving a temporary silk substrate. d) Temperature monitoring experiment on an animal model using an instrumented suture strip based on a Pt thermistor



	on silk substrate.[50].....	1
		<b>4</b>
<i>Figure 1.6</i>	a) Stretchable sensors on top of a PDMS substrate with periodically buckled patterns. b) Tilted SEM view of the stretchable temperature sensor and the interface between the buckled sensor and PDMS. [52] c) Ultrathin, compliant, skin-like arrays of precision temperature sensors and heaters. Image of a 4×4 TCR sensor array after application to the skin using a water-soluble adhesive tape based on poly(vinyl alcohol). d) Similar device, deformed by pinching the skin in a twisting motion.[53].....	<b>15</b>
<i>Figure 1.7</i>	a) Schematic of transparent, flexible R-GO/PVDF-TrFE nanocomposite FET. The schematic illustrates structural, optical (transparent) and electrical (response to temperature) properties of the transparent, flexible R-GO/PVDF-TrFE nanocomposite FET. b) The ID response of the transparent, flexible nanocomposite FET to temperature after cyclic bending.[69].....	<b>17</b>
<i>Figure 1.8</i>	a,b) Schematic diagram and c,d) representative images of the stretchable graphene thermistors in relaxed and twisted states. Conductive AgNWs were used as electrodes, and resistive graphene was used as temperature sensing channels. [70].....	<b>19</b>
<i>Figure 1.9</i>	a) Schematic illustration of finite element modeling results for a device with a wireless heater under tensile strain, with magnified view of the Joule heating element (inset). b) Image of an active, wireless device collected while exposed to RF power in the air, with magnified view of the colour changes induced by the heater (inset). Scale bar, 3 cm.[74].....	<b>20</b>

*Figure 1.10* a) Thermal response of a single-channel-based ionic liquid sensor against the increase of temperature ranging from 35 °C to 45 °C with an interval of 1°C. b) On–off cycles of the thermal response of the self-healing sensor between 37 °C and room temperature. The SHP channel loading 1-Octyl-3-methylimidazolium hexafluorophosphate [OMIm][PF6] functions as c) self-healing circuit, and d) self-healing electronic sensor[76].....**22**

*Figure 1.11* a) Schematic diagram of hybrid composite filled with AgNWs and reduced graphene oxide (TRGs). Filler hybridization facilitates the formation of a conducting network.[87] b) Schematic of ionic electroactive polymer used for the force sensor.[88].....**24**

*Figure 1.12* Components of inherently conductive polymers. ICPs are organic polymers that conduct electricity and are not thermoplastic.....**26**

*Figure 1.13* Chemical structure of PTh. A, undoped and unsubstituted PTh (insoluble), B: doped and Alkyl substituted PTh (solution processable).....**28**

*Figure 1.14* Chemical structure of polypyrrole (a) and doping state (b). Conducting and reducing states of PPy can be electrochemically generated from the corresponding monomers. During electropolymerization, anions from the solution are inserted into the polymer matrix to maintain the material's electroneutrality, neutralizing the positive charges generated in the oxidized polymer threads.[120].....**29**

*Figure 1.15* Chemical structure of PANi.....**30**

<i>Figure 1.16</i>	Basic structure of PANi and different oxidation forms of PANi with its doped states.[127].....	<b>31</b>
<i>Figure 1.17</i>	Molecular structure of PEDOT:PSS complex.....	<b>32</b>
<i>Figure 1.18</i>	Hybridization of the carbon atom.....	<b>34</b>
<i>Figure 1.19</i>	Schematic of sp <sup>2</sup> hybridized carbon allotropes: graphite (3D), graphene (2D), carbon nanotubes (1D), and carbon fullerenes (0D).[158].....	<b>35</b>
<i>Figure 1.20</i>	Simplification of the graphite structure. The distance between the layers is around 2.5x of the distance between the atoms within one layer.....	<b>38</b>
<i>Figure 1.21</i>	Schematic of SWCNT and MWCNT.[174].....	<b>38</b>
<i>Figure 1.22</i>	a) Scanning electron micrograph of single-atom-thick sheets of graphene, (b) flat graphene crystal in real space (perspective view) and (c) the same for corrugated graphene.[188].....	<b>39</b>
<i>Figure 1.23</i>	Chemical structure of GO-hydrophilic groups are coloured red (carboxyl groups) and blue (hydroxyl and epoxy groups).[192].....	<b>40</b>
<i>Figure 1.24</i>	Representative applications of the hydrogels. (A) Bioelectrodes, (B) Biosensors, (C) Energy storage devices, (D) Drug delivery, (E) Neural electrodes, (F) Tissue engineering.[193].....	<b>42</b>
<i>Figure 1.25</i>	Schematic structure of PU a: soft segment and b: hard segment.....	<b>46</b>

<i>Figure 1.26</i>	Overview of RP technology that uses a layer by layer build up process.[284].....	<b>53</b>
<i>Figure 2.1</i>	a. Schematic of extrusion printing system (by Mr Rhys Cornock – University of Wollongong) and b. KIMM SPS1000 bio plotter extrusion printer.....	<b>64</b>
<i>Figure 3.1</i>	Functional groups of GO.[295].....	<b>67</b>
<i>Figure 3.2</i>	Doctor blade used for made the LCGO film and m-LCGO.....	<b>70</b>
<i>Figure 3.3</i>	(a) Scanning electron microscopy (SEM) image of large GO sheets obtained from the LCGO dispersion used in this work. The scale bar is 10 $\mu\text{m}$ . (b) Examples of viscosity curve of LCGO and m-LCGO (0.08 mM) dispersions as a function of shear rate.....	<b>72</b>
<i>Figure 3.4</i>	Effect of salts on (a) the storage modulus and (b) loss modulus of LCGO and m-LCGO dispersions as a function of interaction time at constant strain (0.01) and frequency (1 Hz). The salt concentration was fixed at 0.08 mM.....	<b>75</b>
<i>Figure 3.5</i>	Zeta potential of LCGO and m-LCGO dispersions, 5 min after treatment.....	<b>76</b>
<i>Figure 3.6</i>	Representative optical microscopy images of modified-LCGO a- d dispersions showing clear and non-agglomerated dispersions. b) LCGO, c) $\text{MgCl}_2$ , b) $\text{NaCl}$ , c) $\text{KCl}$ and d) $\text{CaCl}_2$ and polarized optical microscopy image (e) of an LCGO dispersion.....	<b>77</b>

- Figure 3.7* Low and high-resolution SEM images of m-LCGO, cross-section, modified by CaCl<sub>2</sub>, at a concentration of 0.08 mM (a-e), and 2 M (f). The SEM image, cross-section, in (f) clearly shows the formation of salt crystals within the film structure that potentially deteriorates the mechanical property. (g) SEM image of the surface of a CaCl<sub>2</sub>-LCGO film shows no agglomeration in the m-LCGO free standing films. The scale bars are 10 μm in panels (a), (d), (g) and (f), 100 nm in panel (c) and 1 μm in panels (b) and (e).....**78**
- Figure 3.8* Raman characterization of LCGO and m-LCGO films at a concentration of 0.08 mM, where m-LCGO films were treated with different salts as indicated. The broken lines indicate the location of D-band and G-band in LCGO film.....**80**
- Figure 3.9* The ID/IG ratio obtained from Raman spectroscopy for LCGO and m-LCGO films at a concentration of 0.08 mM.....**81**
- Figure 3.10* X-ray diffraction (XRD) patterns of hydrated m-LCGO films prepared from 0.08mM salt solutions compared with LCGO.....**82**
- Figure 3.11* (a) Stress-strain curves of the LCGO film and hydrated m-LCGO films formed from the salt treated dispersions (0.08 mM). (b) Photos show the flexibility and durability of a hydrated m-LCGO film modified with CaCl<sub>2</sub> (0.08 mM).....**84**
- Figure 3.12* Schematic model of the interaction between LCGO sheets and cations (Mg<sup>2+</sup>, Ca<sup>2+</sup>, K<sup>+</sup>, and Na<sup>+</sup>) in the presence of water.[341] Anionic counter ions are not shown here for clarity.....**87**
- Figure 3.13* Thermal conductivity of m-LCGO compared with LCGO.....**90**

<i>Figure 3.14</i>	Hygroscopicity of salts tasted in this study.....	<b>91</b>
<i>Figure 3.15</i>	Water content of LCGO and m-LCGO film.....	<b>92</b>
<i>Figure 4. 1</i>	A custom hNSC culture chamber and stimulation module comprising gold-coated Mylar film, G-film and platinum mesh counter electrode which was used for electrical stimulation of hNSCs.[364] .....	<b>100</b>
<i>Figure 4.3</i>	a) Homogeneous PUHC formulation immediately after preparation (i) and 6 months after preparation (ii), b) Chemical structure of PEDOT:PSS, LCGO and polyether-based liner polyurethane (abbreviation: ss - soft segment and hs - hard segment).....	<b>102</b>
<i>Figure 4.4</i>	X-ray diffraction (XRD) patterns of composite component and PUHC.....	<b>104</b>
<i>Figure 4.5</i>	The toughness and conductivity of the PUHC as a function of filler (PEDOT:PSS and LCGO) loading.....	<b>105</b>
<i>Figure 4.6</i>	Photos show as-prepared PUHC film in various forms, namely (a) free stand film, b) twisted free standing film and c) free standing film tied into a knot.....	<b>106</b>
<i>Figure 4.7</i>	a) Tensile stress-strain curve of the PUHC and control samples and b) Chemical structure of PU; ss) soft segment and hs) hard segment...	<b>107</b>
<i>Figure 4.8</i>	The electrical conductivity of PU composites containing a) PEDOT:PSS, b) reduced LCGO, and c) LCGO/PEDOT:PSS as a function of filler loading.....	<b>111</b>

- Figure 4.9* Water content (a) of PUHC (8 %w/w LCGO/PEDOT:PSS at 1:1), PU/LCGO (8%w/w), pure PU and PU/PEDOT:PSS (8%w/w). Photo images (b) of PUHC film (i), PU/LCGO (ii), PU (iii), and PU/PEDOT:PSS (iv) hydrogel films immersed for 5 min and 2 hr in 10 mL of EtOH-water (95-5%) solution.....**112**
- Figure 4.10* Representative polarized optical microscopy images of samples in solution phase. a) PU, b) LCGO (8% w/w), c) PEDOT:PSS (8% w/w) and d) PUHC (LCGO 4% w/w + PEDOT:PSS 4% w/w).....**114**
- Figure 4.11* SEM images of the PUHC. a) Surface SEM image b) Cross-section image of PUHC. The scale bar is 10  $\mu\text{m}$ .....**115**
- Figure 4.12* Conductivity of PUHC as a function of treatment time with 5% Hypophosphorous acid.....**118**
- Figure 4.13* Raman characterization of PU, PEDOT:PSS, LCGO, and PUHC. The broken line indicates the location of D and G-band in LCGO.....**119**
- Figure 4.14* Survival, maintenance and differentiation of hNSCs on PUHC. (a) Live (Calcein AM) and dead (PI) cell staining following 24 h culture. (b) Quantitative analysis of hNSC viability following 24 h culture. (c) Immunocytochemistry of hNSC markers SOX<sub>2</sub> and vimentin. (d) Immunocytochemistry of GFAP (astrocyte maker) and TUJ1 (neuronal marker) expression after differentiation of NSCs for 7 days.....**121**
- Figure 4.15* Neurite growth of hNSCs following culture for 3 days on PUHC with and without stimulation. (a, b) Immunocytochemistry of vimentin-expressing cells. (c) Assessment of neurite growth,

including the sum total length of neurites, mean neurite length, and maximum neurite length per cell  $\pm$  SD (for stimulated and unstimulated groups, n=11 and 40 respectively). “\*” Indicates statistical significance of  $\leq 0.05$ .....  
**...123**

*Figure 5.1* Rotary evaporation used to make viscous PUHC (contained in round bottom flask in the water bath) at 25 °C, 90 rpm in 10 mbar.....**129**

*Figure 5.2* a) Schematic drawing of the test set-up. b) Experimental illustration of dimension change in the sample operated in a silicone oil-filled glass beaker (radius  $R$ ); (1) calibration of oil thermal expansion having liquid height  $L_1$  at 25°C, and  $L_1'$  at 45°C, (2) Combined thermal expansion of oil with the immersed sample from an initial liquid level  $L$  raised to  $L'$  at 45 °C.....**131**

*Figure 5.3* Illustration of the microscopic measurement method used to analyze of the thermal dimensional changes of the sample (the figure represents the virtual concept, not the actual facilities).....**133**

*Figure 5.4* Sensor profile and illustration of thin film thermal conductivity measurement. (a) TPS thin film sensor 5501 composed of bifilar spiral structure with concentric equally spaced circular line sources; (b) cross-sectional view of the TPS test column including background materials, thin film specimens and TPS sensor (Insulation layers, adhesive materials and double spiral nickel wires); (c) demonstration of the experiment including background material (mild steel, SIS2343), and TPS sensor.....**135**

*Figure 5.5* a) KIMM SPS1000 printer which is used for this thesis. b) Printed extruded PUHC. (120 kpa was applied and 3cc plastic syringe was



used).....  
...137

*Figure 5.6* a).Experimental setup: temperature control via software managed rheometer hotplate. Thermistor recorded temperature on the top of the sample (b) Enclosed experimental setup to prevent impact on results from ambient air flow impact on results.....140

*Figure 5.7* a) The toughness, electrical and thermal conductivity of the PUHC as a function of filler (LCGO and PEDOT:PSS) b) The elastic recoveries at different applied strains (indicated in the graph) of PUHC as a function of filler loading.....143

*Figure 5.8* Impact of prestrain on PUHC film (8 %w/w LCGO/PEDOT:PSS at 1:1) properties. a) correlation between the percentage of prestrain on elastic recovery, b) Effect of 40% prestrain on toughness, the electrical and thermal conductivity of PUHC. A indicates the value before prestrain and B represents the value after prestrain. The tests were repetitively conducted 5 times for each sample, and the standard deviation is shown in the plot.....146

*Figure 5.9* Thermally induced expansion of the sample normalized from the overall expansion of sample-in-oil at 25°C and after heating to 45°C.....  
...148

*Figure 5.10* Thermally induced expansion of the samples a) dimension change (%) and b) normalized to the volume at 25°C and afterwards heated to 45°C.....  
...149

*Figure 5.11* PUHC ink preparation via rotary-evaporator. Viscosities were measured after rotary-evaporation at various times. The viscosity

of PUHC dispersions were measured in the shear rate ranging between 0.1 and 800 Hz.....151

*Figure 5.12* Rheological analysis of PUHC ink after use of rotary-evaporator to increase viscosity after 24 hrs, a) Temperature dependence of  $G'$  and  $G''$  for PUHC dispersion and b) the trend of  $\tan(\delta)$  between 25-45 °C.  $\tan(\delta) = G'' / G'$  .....153

*Figure 5.13* Optical image of extrusion printed 3D scaffolds PUHC ink (8%w/w LCGO/PEDOT:PSS at 1:1) after use of rotary-evaporator for 24 hrs. a) Multi-layer with dimensions of 10× 10 mm. b) 2 layers lattice structure's morphology.....154

*Figure 5.14* Solidworks images of 3 candidates stretchable design for PUHC a) Honeycomb design.[2], b) Star design.[412], and c) horseshoe design[432]. .....156

*Figure 5.15* Plot of normalized electrical resistivity of Ts-PUHC film and 3D printed star design of Ts-PUHC b) 3D printed star design of Ts-PUHC. The tests were repetitively conducted for 5 times for each sample and the standard deviation is shown in the plot. The scale bar represents 1 cm.....157

*Figure 5.16* SEM images of the surface of the 3D printed Ts-PUHC. The scale bar represents 1  $\mu\text{m}$ .....158

*Figure 5.17* Temperature sensing behaviour of a) 3D printed Ts-PUH b) Ts-PUHC submerged in SBF solution with pH 7.4 for 5 minutes and c) treated Ts-PUHC with paraffin oil and d) paraffin oil treated Ts-PUHC submerged in SBF solution with pH 7.4 for 5 minutes. The experiment was designed to test temperature in the range of

25 and 45° C for 5 cycles.....  
...**161**

*Figure 5.18* a) effects of pH on the electrical resistance of Ts-PUHC and treated Ts-PUHC with paraffin oil. b) SBF uptake at (pH 7.4) exposure time on Ts-PUHC and paraffin treated Ts-PUHC, measured by mass ratio analysis.....  
....**163**

*Figure 5.19* Tensile modulus (a) and elongation at break (b) of Ts-PUHC and paraffin treated Ts-PUHC in simulated body fluid (SBF) in 37°C for 15 days. All the measurements repeated on 5 different samples prepared in the same way. (The tests were repetitively conducted for 5 times for each sample and the standard deviation is shown in the plot).....  
...**165**

## List of tables

<i>Table 3.1</i>	Viscosity (Pa s) of m-LCGO dispersions as a function of salt concentration ( $\gamma=100$ s <sup>-1</sup> ). .....	<b>73</b>
<i>Table 3.2</i>	The d-spacing of GO sheets in LCGO and hydrated m-LCGO films obtained from XRD spectra.....	<b>82</b>
<i>Table 3.3</i>	Mechanical properties of LCGO film and hydrated m-LCGO films compared with data from the literature.....	<b>85</b>
<i>Table 3.4</i>	Surface electrical resistance ( $K\Omega m^{-2}$ ) of LCGO and m-LCGO films after drying and then over 120 hrs.....	<b>89</b>
<i>Table 4.1</i>	The effect of fillers on the mechanical properties of PU.....	<b>108</b>
<i>Table 4.2</i>	Conductive PU composites with a variety of conductive fillers (data from this study and literature).....	<b>109</b>
<i>Table 4.3</i>	The impact of reduction methods on each composite component separately.....	<b>117</b>
<i>Table 5.1</i>	Summary of 3D printer setting.....	<b>138</b>

# Chapter 1

## INTRODUCTION AND LITERATURE REVIEW

---

This literature review will begin with a brief introduction into the history of biomaterial applications in health monitoring and review of the literature on the following topics: concepts of thermal sensor devices, electrically conductive composites and their capability in sensing applications, and brief historical background of printable conductive hydrogels. These topics are discussed to highlight the implications from current literature and are used to develop the conceptual framework for the study reported in this thesis.

### **1.1 Introduction**

Discoveries in materials science are often the driving force behind the development of new sensing technologies. Humans have sensed physical and chemical parameters in our surroundings for many years with varying degrees of selectivity and resolution. Novel functional materials may allow us to increase the resolution at which we monitor our surrounding parameters or enable us to monitor parameters in new ways, but we first need to understand and characterise their material composition, response to stimuli, stability over time, and processability into practical devices.[1]

As graphically depicted in Figure 1.1, the field of wearable sensing devices is growing. Flexible and wearable sensors, with the ability to detect physical signals created by the human body, have received much attention due to their potential in electronic applications such as health monitoring, human interactive devices (such as artificial eye, and skin), and robotics.[2, 3]

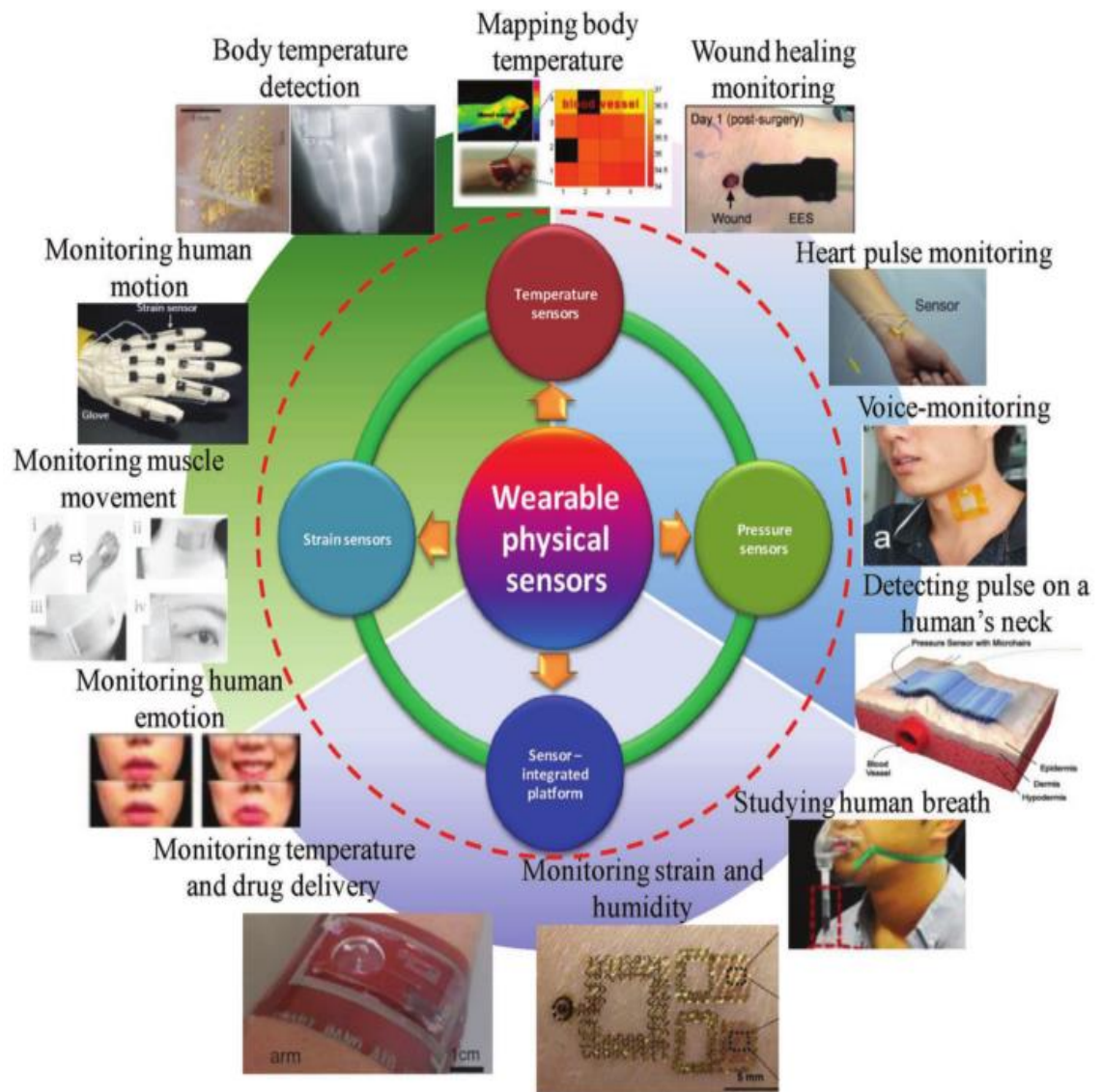


Figure 1.1 Examples of recently developed flexible and stretchable physical sensors for measuring parameters on the surface of the skin such as temperature, pressure and strain generated by human activities for personal healthcare monitoring.[4]

Body temperature is the basal index in physiology and is a key parameter in diagnosis and ongoing patient treatment [5, 6]. Therefore, the accurate monitoring of this parameter on a regular basis allows for a greater understanding of a patient's condition to be ascertained. An optimal sensing platform would facilitate continuous body temperature

monitoring, would be robust, respond rapidly to any change in temperature, and be indifferent to changes in the stimuli within and surroundings of the body environment, such as humidity, light, pH, and mechanical force.[7]

Materials for making temperature sensors for health monitoring, electronic-skin (e-skin), [8, 9] and human-activity monitoring, [10-13] must be capable of having at least one property that can be significantly changed by external temperature stimuli. Many different materials have been employed for making temperature sensing devices for health monitoring, such as inherently conductive polymers (ICPs), carbonaceous materials, pyroelectric materials and a combination of these materials with conductive polymers. [14-16] In view of the complexity of the temperature sensor application for health monitoring, it needs to be intelligently developed to adequately meet the requirements such as high sensitivity, light weight, flexibility, thinness, stretchability, biocompatibility, and low cost. [6, 17-19]

Hydrogels are three-dimensional, hydrophilic, porous polymeric networks capable of absorbing large amounts of water. Due to their soft consistency and porosity, they closely simulate natural living tissue, more so than any other class of synthetic biomaterials.[19] Combining the physical and mechanical properties of hydrogels with the electrical activity of an electroactive/conductive component can create unique opportunities for the next generation of materials, and hence a wide range of conductive fillers with different mechanical and biological properties can be used.[20] The use of conductive hydrogel in flexible microelectronic devices and three-dimensional (3D) fabrication is emerging. Commercial development and use of temperature sensors, based on conductive hydrogels, for health monitoring are at the early stages of research. However, there is a need for

continued combined improvement in material design aspects and fabrication methods to produce sustainable and sensitive conductive hydrogel-based sensors.

The limitations of these technologies will highlight the need for new materials possessing the required properties, including biocompatibility, for development of a thermistor suitable for human monitoring.

## **1.2 The concept of a thermal (temperature) sensor**

Temperature is the intensity or degree of the average kinetic energy of object or particles.[20] A thermal sensor is a device that is specifically used to measure temperature and is capable of providing a quantifiable way to describe the average kinetic energy of the molecules in a substance.

Sensors detect physical phenomena and translate these signals to corresponding electrical signals, which are capable of quantification. Several temperature sensor types are available; each one has its strengths and weaknesses. There are four commonly used temperature sensor types for continuous temperature measurement (Figure 1.2) as described below.

### **1.2.1 Negative Temperature Coefficient (NTC) thermistor**

A thermistor is a thermally sensitive resistor that exhibits a change in an electrical resistance correlated to change in temperature. An NTC thermistor delivers a high electrical resistance at low temperatures and as temperature rises, the resistance starts to decrease. The NTC thermistor's capability ensures a large change in electrical resistance per °C change. Therefore small changes in temperature can be detected with accuracy (0.001 to 1.0 °C) and working in a range of -50 to 1000°C.[21] However, thermistors are



non-linear in response. This leads to additional work to create a linear output and adds to the error of the final reading.[22]

### **1.2.2 Resistance Temperature Detector (RTD)**

An RTD, also known as a resistance thermometer, is a device that senses temperature by correlating the electrical resistance with temperature. An RTD usually contains a conductive film or a wire wrapped around a ceramic or glass core. The most widely used RTDs are made of platinum but lower cost RTDs can be made from nickel or copper. However, nickel and copper are not as stable nor have the ability to give the same output or reading under repeated identical conditions (repeatability). Platinum RTDs offer a more linear output than thermistors and are highly accurate (0.001 to 1 °C) across -200 to 600 °C. This improved accuracy leads to RTD's being more expensive than simpler thermistor sensors.[22, 23]

### **1.2.3 Thermocouple**

A thermocouple is a temperature sensing device that consists of two dissimilar metal wires connected at one point. The temperature dependent voltage between these two points reflects proportional changes in temperature. It is not easy to transform the voltage generated by a thermocouple into an accurate temperature reading for many reasons: the voltage signal is small, the temperature-voltage relationship is nonlinear, reference junction compensation is required, and thermocouples may pose grounding problems. The thermocouple accuracy is between 0.5 to 5 °C which is lower than NTC thermistors

and RTD's. There are several types of thermocouples, constructed from different metals with different temperature ranges and levels of accuracy. Nevertheless, they work across the broadest temperature range, from -200 to 1750 °C.[24, 25]

#### **1.2.4 Semiconductor-based (IC) sensors**

Semiconductor-based temperature sensors are placed on integrated circuits (ICs). These sensors are two identical diodes with temperature dependent voltage vs current characteristics that can be employed for temperature monitoring. They have a linear response but have the lowest accuracy in comparison to other temperature sensing devices, having an accuracy range from  $\pm 1$  to  $\pm 5$  °C. They also have the lowest sensitivity with a response rate of 5 to 60 s over a temperature sensing range of -70 to 150 °C.[26]




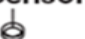
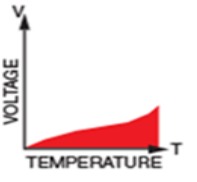
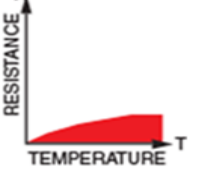
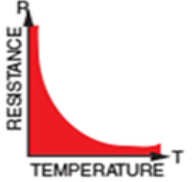
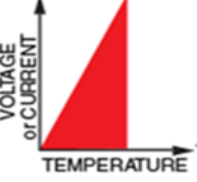
	 <b>Thermocouple</b>	 <b>RTD</b>	 <b>Thermistor</b>	 <b>I. C. Sensor</b>
				
<b>Advantages</b>	<ul style="list-style-type: none"> <li>• Self-powered</li> <li>• Inexpensive</li> <li>• Wide temperature range</li> </ul>	<ul style="list-style-type: none"> <li>• Most stable</li> <li>• Accurate</li> <li>• More linear than thermocouple</li> </ul>	<ul style="list-style-type: none"> <li>• High output</li> <li>• Fast</li> <li>• Most accurate</li> <li>• Flexible</li> <li>• Durable</li> <li>• Inexpensive</li> <li>• Large <math>\Delta R</math></li> </ul>	<ul style="list-style-type: none"> <li>• Linear</li> <li>• High output</li> <li>• Inexpensive</li> </ul>
<b>Disadvantages</b>	<ul style="list-style-type: none"> <li>• Non-linear</li> <li>• Low voltage</li> <li>• Least stable</li> <li>• Least sensitive</li> </ul>	<ul style="list-style-type: none"> <li>• Expensive</li> <li>• Current source required</li> <li>• Small <math>\Delta R</math></li> <li>• High self heating</li> </ul>	<ul style="list-style-type: none"> <li>• Non-linear</li> <li>• Current source required</li> <li>• Drift</li> </ul>	<ul style="list-style-type: none"> <li>• Power supply required</li> <li>• Slow</li> <li>• Self-heating</li> <li>• Limited configuration</li> </ul>

Figure 1.2 The advantages and disadvantages of four main types of commercially available temperature sensor devices.[27]

### 1.3 Temperature sensor for health monitoring

Amongst various health monitoring parameters, temperature is one of the most critical factors. This section attempts to review the current research and development on temperature sensors systems for health monitoring. A variety of materials, composites and system implementations are compared to identify the material shortcomings of the current state-of-the-art in temperature sensors for health monitoring.

### **1.3.1 Flexible and stretchable temperature sensor**

For applications of temperature sensors in wearable human-activity monitoring and personal healthcare, many types of temperature sensors embedded in a flexible and stretchable substrate have been developed.[1, 28] The most common temperature sensors are pyroelectric detectors, resistive temperature detectors, and thermistors.

#### **1.3.1.1 *Pyroelectric Temperature Detectors***

Pyroelectricity is the capability of a material to create a temporary voltage when subjected to a temperature gradient and has been detected in some ceramics [29-33] and semicrystalline polymers. [34-37] In particular, the pyroelectric poly(vinylidene fluoride) (PVDF) and its copolymer with trifluoroethylene (TrFE) (Figure 1.3a) is a good candidate for temperature sensor applications on flexible substrates and consequently has stimulated much research. [38-40] In a pyroelectric material, temperature fluctuation creates a change in remnant polarization (Figure 1.3b).

Due to the chemical structure of PVDF (Figure 1.3a), the difference of electronegativity between hydrogen and fluorine at opposite sides of the PVDF chain cause a large dipole moment oriented perpendicularly.

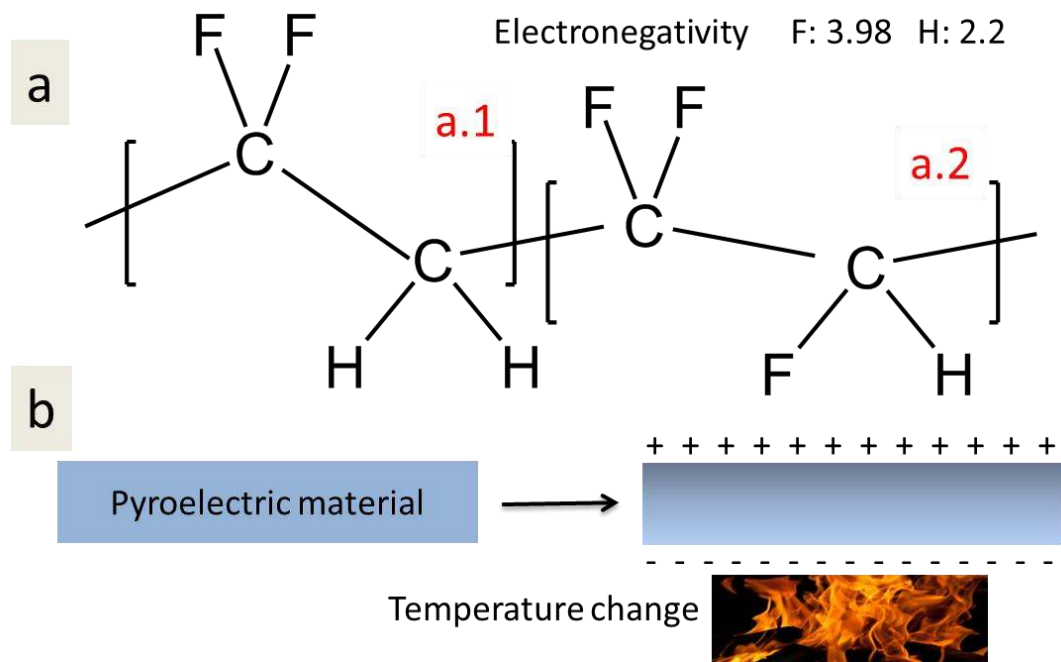


Figure 1.3 a. Chemical structure of PVDF-TrFE. a.1) PVDF polymer chain and a.2: TrFE monomer structure. b. The principle of pyroelectric performance in temperature fluctuation.

Pyroelectric material scavenges thermal energy from its working environment and has the potential to convert temperature fluctuation into electric energy. The significant difference in electronegativity between the component elements (hydrogen and fluorine) results in a strong dipole moment normal to the chain direction.[41]

One of the advantages of pyroelectric materials is that they can detect stimuli with a low amount of heat to maintain a temperature gradient, and have the ability to operate with a high thermodynamic efficiency for converting temperature changes into an electrical signal.[42] PVDF and its variants have been employed in a metal/PVDF/metal (MIM) sandwich structure which is very similar to a semiconductor diode that is capable of fast operation. Depending on the geometry and the material used for fabrication, the operation

mechanisms of temperature sensing are governed either by quantum tunnelling or thermal activation. Intensive studies have been done to improve the performance of pyroelectrics in the last century and are actively continued today owing to the multitude of applications of pyroelectrics in sensory and thermal imaging systems. The major disadvantage of these devices for human monitoring is the fact that they are fabricated on rigid substrates. [39, 43]

The operating mechanism of a MIM is provided by the negative pyroelectric coefficient (the electrodes which measure variation of polarisation with temperature are placed along a principal crystallographic direction, and therefore, the coefficient is often measured as a scalar, which is typically negative to represent a polarization falling with increasing temperature) of PVDF or (PVDF-TrFE) with a poor crystallinity originating from the thermal vibration of the dipoles in the amorphous phase at higher temperature causing a reduction of average dipole moment in the poling direction. [40, 44] Tine et al.[45] reported that direct incorporation of a highly crystalline PVDF-TrFE material with a large remnant structure (such as a pyroelectric gate-insulator layer) into a flexible organic field effect transistor (OFET) can be used for temperature-sensor application and exhibits a linear current-voltage relationship (Figure 1.4).

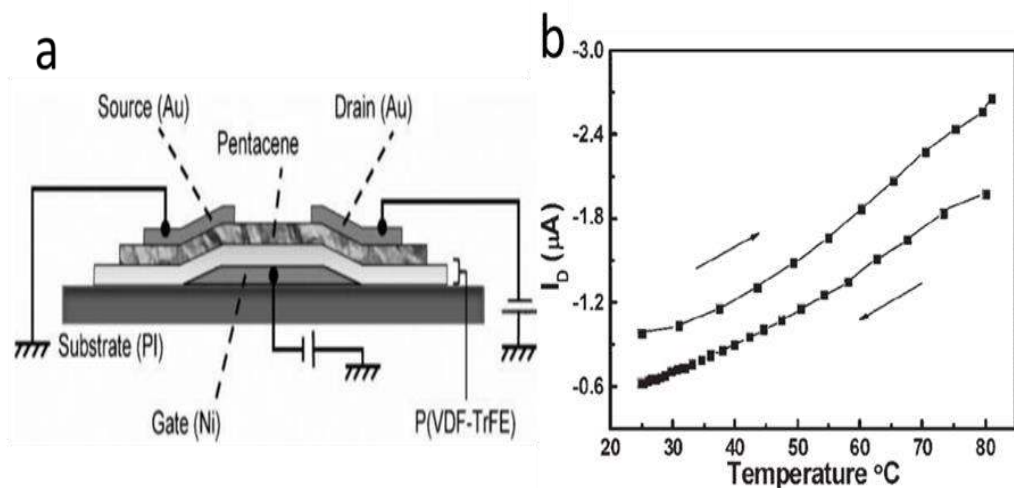


Figure 1.4 a. Organic thin-film transistor structure with pyroelectric gate dielectric b. Temperature response data of the poled device in continuous measurements. [45]

These temperature sensors operate based on oscillation in remnant polarization between the PVDF-TrFE, which varies under temperature fluctuation, and ultimately causes a growing density of accumulated holes at the surface of the PVDF-TrFE and semiconductor. Kim et al. and Tien et al. have shown that initial voltage, remnant polarization and the level of crystallinity of the PVDF-TrFE have a direct correlation with the temperature based on the thermal expansion of the crystalline phase.[45, 46] Furthermore, high resolution flexible and precise OFETs have been developed with PVDF-TrFE/BrTiO<sub>3</sub> nanocomposite on the substrate and display a precise response to temperature with a standard deviation between 6 mK to 12 mK.[46] While pyroelectric temperature sensors based on PVDF-TrFE show precise measurement and high resolution of temperature, their practical application is restricted by poor relaxation and slow response times.[4]

### 1.3.1.2 *Resistive Temperature Detectors*

A resistive temperature detector (RTD) or resistance thermometer sensor works based on an accurate temperature-resistance relationship. Pure metal elements such as copper (Cu), nickel (Ni), and platinum (Pt) are widely employed for the construction of RTDs.[47-49] Stretchable and flexible RTDs for healthcare monitoring such as wound monitoring and thermography of skin have been developed. [46, 50] A flexible Pt-RTD with a linear response to temperature integrated with suture strips has been proposed by Kim et al., [50] using a neutral mechanical plane (NMP) configuration and in an ultrathin design ( $< 3\mu\text{m}$ ). The NMP is a conceptual plane within a beam or cantilever. When loaded by a bending force, the beam bends so that the inner surface is in compression and the outer surface is in tension. The neutral plane is the surface within the beam between these zones, where the material of the beam is not under stress, either compression or tension.[51] The resultant suture strips displayed high durability, deformability, and stability under mechanical strain. Furthermore, this strip-sensor has been successfully implanted in animal models to monitor temperature (Figure 1.5).



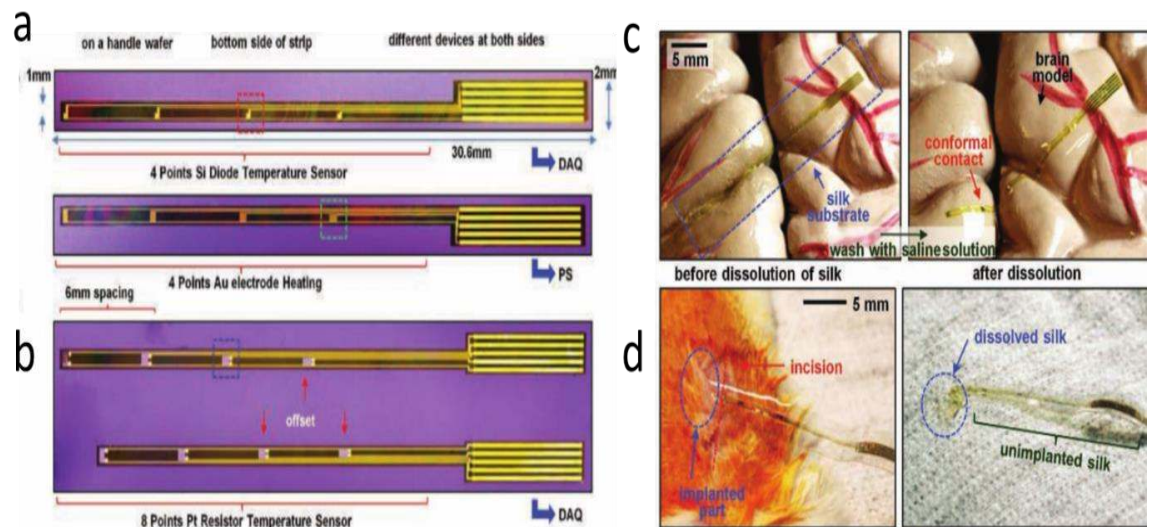


Figure 1.5 a) Optical images of temperature sensors based on Si nano-membranes (top) and microheaters based on Au wires in a serpentine layout (bottom), both on a handle wafer. b) Optical image of a temperature sensor array based on Pt resistors, on a handle wafer. The two arrays have four sensors each, which are arranged in a bifacial configuration. c) Demonstrative temperature sensor on a plastic model of the human brain before (left frame) and after (right frame) dissolving a temporary silk substrate. d) Temperature monitoring experiment on an animal model using an instrumented suture strip based on a Pt thermistor on silk substrate.[50]

For stretchable RTDs, Yu, et al. [52] developed a stretchable temperature sensor based on elastically buckled thin-film devices on an elastomeric polydimethylsiloxane (PDMS). The temperature sensor with a thin Cr/Au layer (5 nm/20 nm) was fabricated on a buckled PDMS substrate with a 30% of pre-strain. The fabrication began with spinning and patterning photoresist using standard lithography process on a silicon on insulator wafer. Moreover, the fabricated sensors can be reversibly compressed and stretched up to 30% without any sensor-performance degradation and fracture (Figure 1.6a and b).

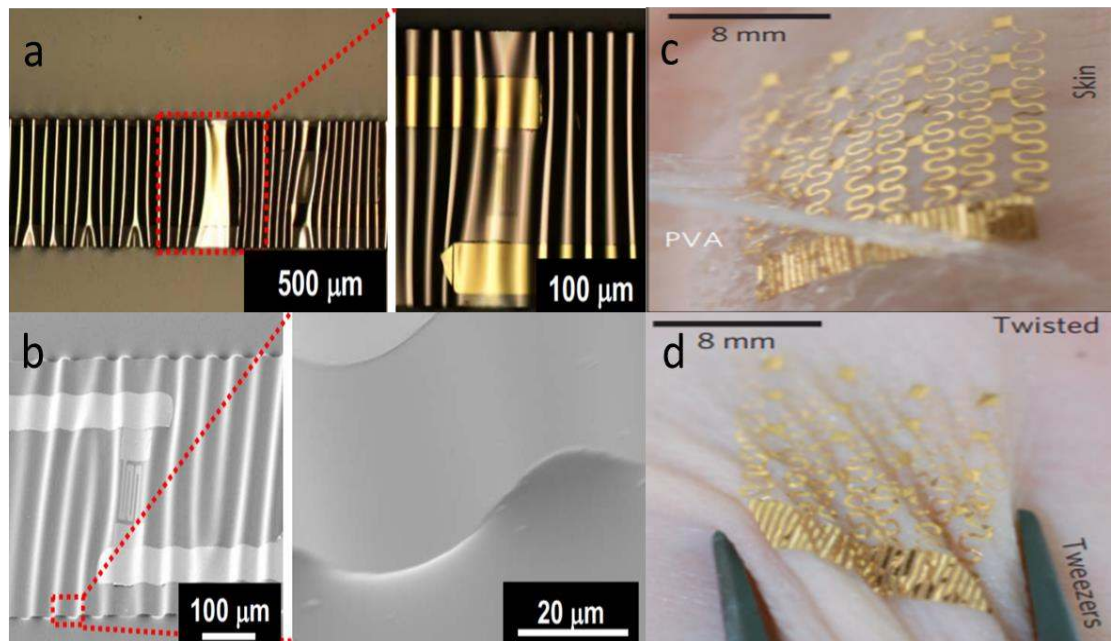


Figure 1.6 a) Stretchable sensors on top of a PDMS substrate with periodically buckled patterns. b) Tilted SEM view of the stretchable temperature sensor and the interface between the buckled sensor and PDMS. [52] c) Ultrathin, compliant, skin-like arrays of precision temperature sensors and heaters. Image of a 4×4 TCR sensor array after application to the skin using a water-soluble adhesive tape based on poly(vinyl alcohol). d) Similar device, deformed by pinching the skin in a twisting motion.[53]

Webb et al. [53] reported an RTD sensor with a compliant, ultrathin, and skin-like array. They introduced a temperature sensor with high precision in measurement, mapping capability, and non-invasiveness based on Cr/Au (5 nm/50 nm) with the surface of the skin. This temperature sensor was capable of attaching directly to the skin with twisting capability and was employed for mapping the temperature distribution (Figure 1.6c and d). The precision of this sensor can be adjusted through development of a sensor array with mapping capability and high precision which could find applications in the health monitoring and cognitive areas.[54]

### 1.3.1.3 *Thermistors*

A thermistor is another type of resistor sensor similar to the RTD. The electrical resistance of these devices is proportional to the temperature of their surrounding environment. Thermistors are capable of detecting small changes in temperature with accuracy ( $\pm 0.1^\circ\text{C}$  or  $\pm 0.2^\circ\text{C}$ ) and repeatability. There are two basic types of thermistors, each with different performance characteristics, namely positive temperature coefficient (PTC), and negative temperature coefficient (NTC) of resistance. For the NTC type, electrical resistance decreases with increased temperature, while for a PTC device resistance increases proportionally to increased temperature. Traditionally, semiconductor ceramic such as oxides of manganese (Mg), cobalt (Co), and nickel (Ni) are used to produce thermistor devices. These thermistors, based on oxide material, have a limited application in health monitoring because they are fabricated on a rigid substrate. As a result, stretchable and flexible thermistors based on nanocomposites, graphene, and organic semiconductors have been developed.[46, 55-65] Jeon et al. [66] developed a flexible and stretchable thermistor with a Ni binary polymer composite, with polyethylene (PE) and polyethylene oxide (PEO) as a matrix, with reproducibility and high sensitivity in the range of the human body temperature (from 25 to 45 °C). Results exhibit high performance of Ni binary polymer composite as a temperature sensor and show promise for applications in personal healthcare, and human activity monitoring. Another reported example of flexible temperature sensor development by Harada and co-workers [67] examines, microscale flexible and printable temperature sensor based on poly(3,4-ethylenedioxy thiophene):poly(styrenesulfonate) (PEDOT:PSS)–SWCNT film. The sensitivity and selectivity of the temperature was demonstrated using a 3×3 artificial skin array that senses temperature (from 21 to 80 °C) with a high sensitivity range from 0.25 to 0.63% /°C.

Trung et al. [68] reported a flexible temperature sensor through the incorporation of reduced graphene oxide (R-GO) and PVDF-TrFE nanocomposite as the sensing layer (Figure 1.7a and b).

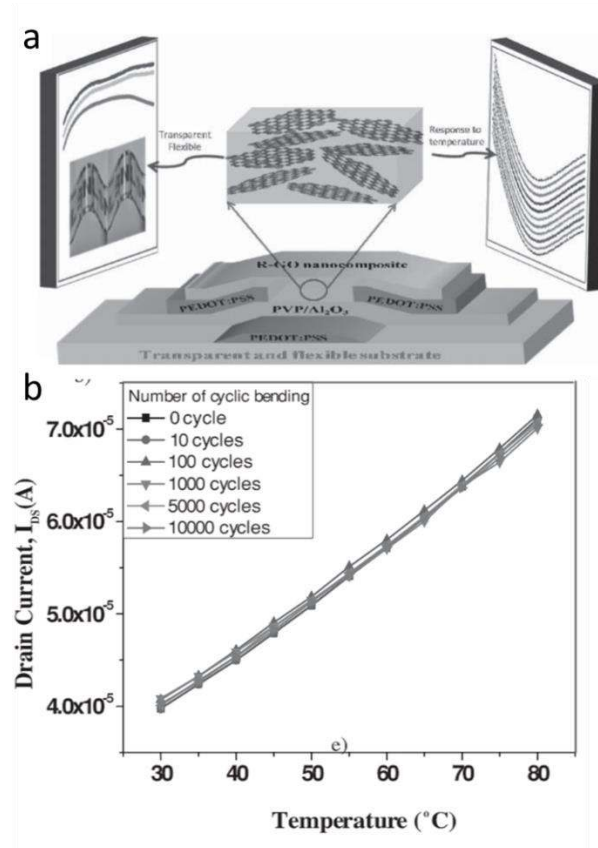


Figure 1.7 a) Schematic of transparent, flexible R-GO/PVDF-TrFE nanocomposite FET. The schematic illustrates structural, optical (transparent) and electrical (response to temperature) properties of the transparent, flexible R-GO/PVDF-TrFE nanocomposite FET. b) The  $I_D$  response of the transparent, flexible nanocomposite FET to temperature after cyclic bending.[69]

The combination of R-GO and PVDF-TrFE made the sensor highly responsive in the temperature range of 30 to 80 °C and is capable of detecting small temperature changes (0.1 °C).The temperature dependence of the conductivity of the R-GO/P(VDF-TrFE)

nanocomposite can be suggested to occur by two main mechanisms: the hopping transport mechanism and a tunnelling conduction mechanism.[69]

Yan et al.[70] developed a flexible and stretchable thermistor using graphene as a sensing channel and highly conductive silver nanowire (AgNW) as stretchable electrodes fully embedded inside a polydimethylsiloxane (PDMS) matrix for easy and consistent electrical measurements (Figure 1.8). This stretchable thermistor used crumpled Graviteum (Gr) as the temperature-sensor layer. By embedding three-dimensional crumpled Gr into an elastomer matrix, the Gr thermistor can be stretched up to 50%.

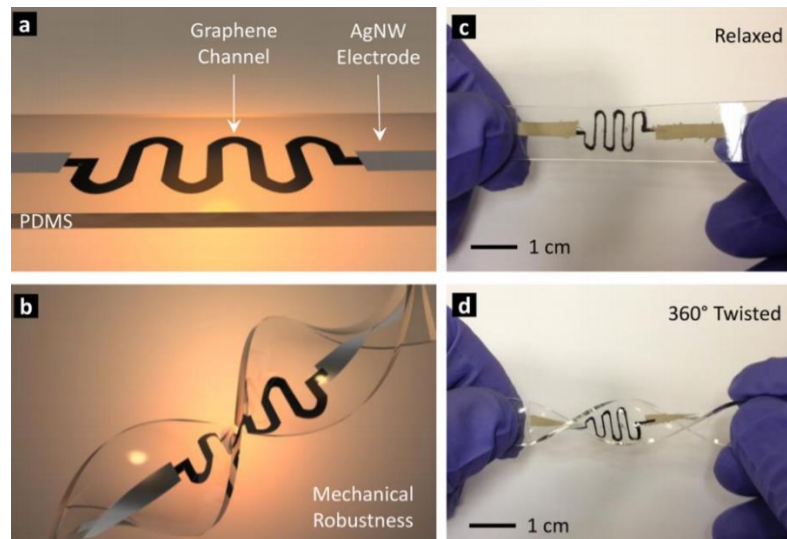


Figure 1.8 a and b) Schematic diagram, c and d) representative images of the stretchable graphene thermistors in relaxed (a and c) and twisted (b and d) states. Conductive AgNWs were used as electrodes, and resistive graphene was used as temperature sensing channels. [70]

#### 1.3.1.4 *Other Temperature Sensors*

Aside from the temperature sensors mentioned above, other research has been performed for making flexible and stretchable temperature sensors based on other common sensing mechanisms for health monitoring.[46] Some groups have reported flexible and stretchable temperature sensors based on colorimetric temperature indicators, Si diodes, polar groups of dielectric-induced charge-trapping, Si, and organic diodes.[71-73] Gao et al. [74] presented a stretchable colorimetric temperature sensor with wireless stretchable electronics. The temperature sensor arrays working with thermochromic liquid crystals (TLC) were fabricated on elastomeric substrates comprised of PVDF. These sensor arrays can find applications in monitoring the wound-healing process, core-body-temperature assessments, and cancer screening (Figure 1.9).

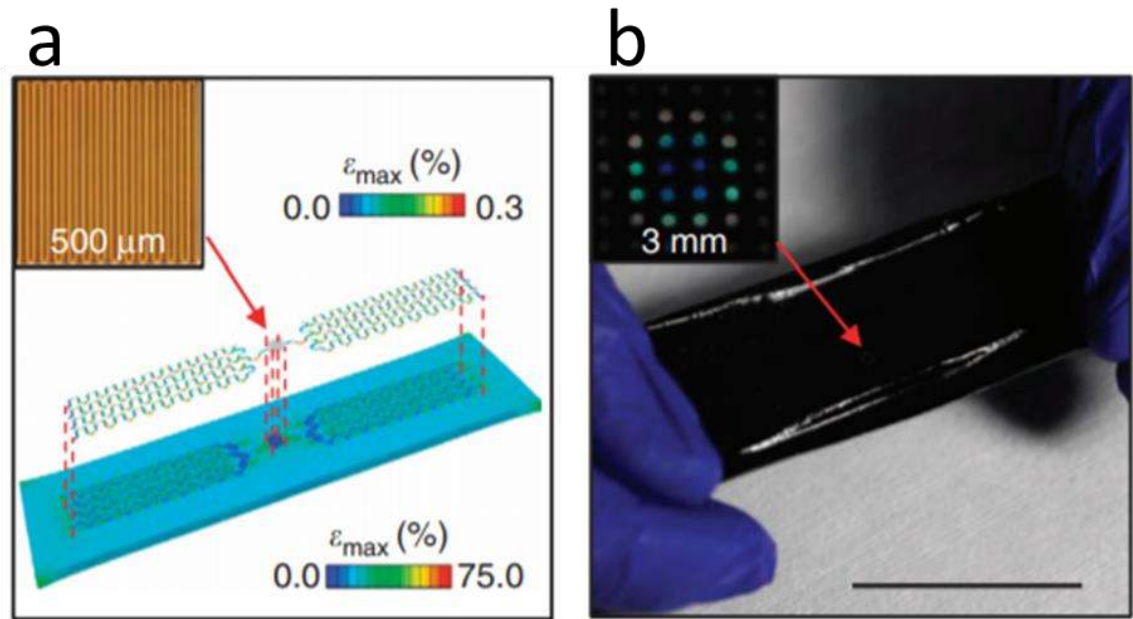


Figure 1.9 a) Schematic illustration of finite element modelling results for a device with a wireless heater under tensile strain, with magnified view of the Joule heating element (inset). b) Image of an active, wireless device collected while exposed to RF power in the air, with magnified view of the colour changes induced by the heater (inset). Scale bar, 3 cm.[74]

Wu et al. [75] fabricated a thermally stable, flexible and biocompatible polylactide (PLA) wound temperature monitoring sensor. Furthermore, they illustrated that the thermal sensitivity of the sensor could be enhanced by polar oxygen atoms which could form hydrogen bonds. The mechanism of the polar-group-induced thermal sensitivity can be described on the basis of the multiple trap and release (MTR) model. Someya et al. [48] demonstrated a flexible net-shaped structure of a temperature-sensor array based on an OTFT for an e-skin application. Organic diodes, as sheet-type thermal sensors, were connected to the drain contact of the transistors. The thermal sensor was manufactured on an indium-tin-oxide (ITO)-coated poly(ethylenephthalate) film. A p-type

semiconductor of copper phthalocyanine (CuPc) and an n-type semiconductor of 3,4,9,10-perylenetetracarboxylic-diimide (PTCDI) were deposited. Then, a gold film was deposited to form a cathode electrode. The film with the organic diodes was coated with a parylene layer and mechanically processed to form net-shaped structures. Finally, to complete the thermal sensor network, lamination of both the transistor and diode net films with silver paste patterned by a micro-dispenser was performed.[17]

He et al. [76] reported a temperature sensor incorporating thermally sensitive ionic liquids into a self-healing polymer (SHP). The sensitivity and repeatability of the fabricated devices were nearly the same after breaking and self-healing (Figure 1.10). Based on this feature, self-healing thermal sensors could be a next-generation application in human-activity monitoring and personal healthcare.



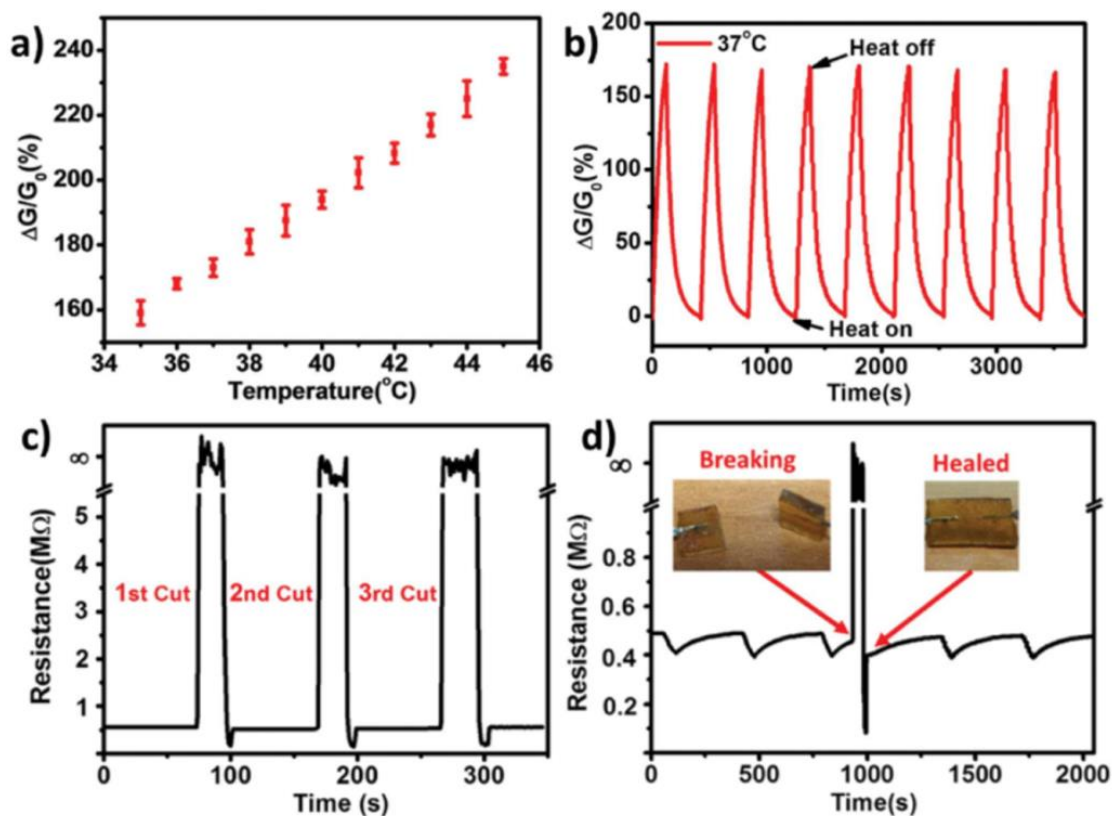


Figure 1.10 a) Thermal response of a single-channel-based ionic liquid sensor against the increase of temperature ranging from 35 °C to 45 °C with an interval of 1°C. b) On–off cycles of the thermal response of the self-healing sensor between 37 °C and room temperature. The SHP channel loading 1-Octyl-3-methylimidazolium hexafluorophosphate [OMIm][PF<sub>6</sub>] functions as c) self-healing circuit, and d) self-healing electronic sensor. [76]

Overall, numerous types of temperature sensors with wide ranges of thermally sensitive material have been developed with dynamic sensing ranges matching body-temperature, i.e., from 25 °C to 45 °C. Consequently, the critical necessities for stretchable and flexible temperature sensors in monitoring human health are high stability, repeatability, precision, sensitivity, and resolution in the range of human body temperature. Numerous materials have been used for making temperature sensors and insight into their variety

and properties can help candidate selection and employ them for developing new intelligent and advanced temperature sensors.

#### **1.4 Electrically active composite**

To make a thermistor, conducting materials are needed as fillers within the structure of the sensor device. Electrical conductivity is one of the important aspects of many sensor properties because measurement and quantifying stimulus is based on changes in electrical conductivity. Electrical conductivity can be provided by metals, but these have some restrictions on their resources, processability, and some applications such as biology to employ in/on body (biodegradability and biocompatibility). In this thesis, the main focus is the use of organic electronic conductors such as carbon materials and conducting polymers to replace metal as a temperature sensitive conductive filler suitable for fabricating a flexible temperature monitoring device.

Commonly, there are four primary categories of electrically conductive polymer systems, each with a different level of conductivity.[77] The first group is the electrically conductive composites in which an electrically insulating polymer matrix is rendered conductive with the inclusion of conductive particulate fillers (Figure 1.11a).[78, 79] Applications for such composites are widespread, and include interconnections, e-printed circuit boards, electrostatic discharge (ESD), heat sinks, conducting adhesives, electromagnetic interference (EMI) shielding, and sensor applications.[80-86]

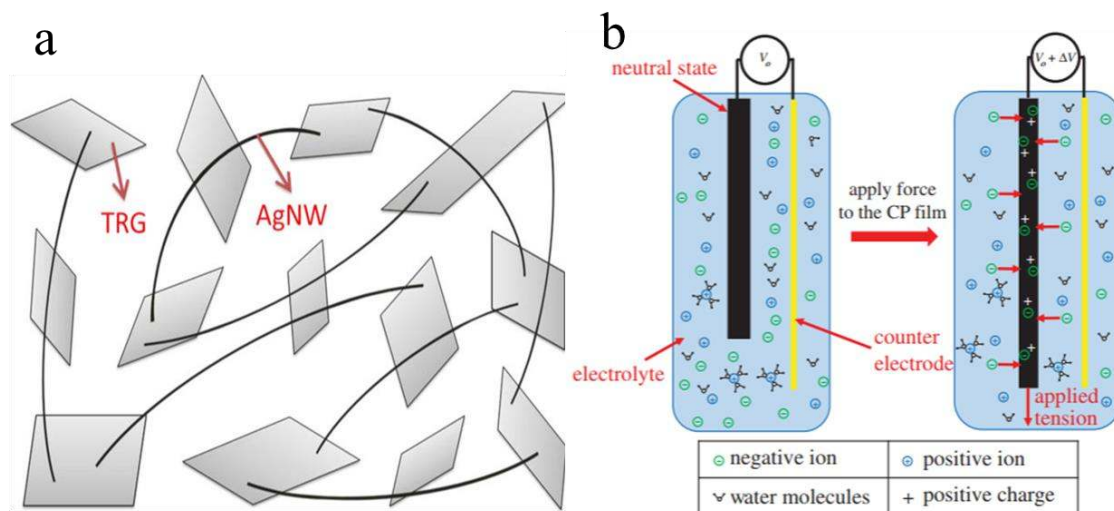


Figure 1.11 a) Schematic diagram of hybrid composite filled with AgNWs and reduced graphene oxide (TRGs). Filler hybridization facilitates the formation of a conducting network.[87] b) Schematic of ionic electroactive polymer used for the force sensor.[88]

The next group of polymers is ionically conducting polymers. The origin of electrical conductivity is a result of the movement of the ions in the system (Figure 1.11b). These types of electrically conductive polymers have practical applications in the battery industry. [89-93] The third group is redox polymers, their mechanism of operation is based on immobilized electroactive centres.[94] Though, these centres are not certainly in contact with the neighbouring centre but can result in charge transfer via electron transfer from one centre to another through the hopping mechanism.[95] During conduction, electrons tunnel from one redox centre to another through an insulating barrier.[96] Increasing the number of redox centres can increase this tunnelling effect. The fourth group of conducting systems is conjugated polymers. These inherently conductive polymers are made up of alternating double and single bonds, creating a conjugated network. The freedom of electron movement within this structure is the source of the electrical conductivity. However, conductive polymers have comparatively low

electrical conductivity and doping is compulsory to raise the level of the electrical conductivity. The conductivity of a filled conductive composite is subject to the concentration of conducting filler and matrix, type of polymer, distribution, and dispersion of the filler in the matrix.[97]

## **1.5 Electrically Conducting Materials**

For developing conductive composites, a conductive filler must be employed. Generally, for achieving a percolation threshold (the point at which charge can move throughout the composite), a higher loading of conducting fillers is required. A relatively low loading amount is needed for structures using fillers such as carbon black compared to isolated spherical metal fillers.[98] If short carbon fibre or carbon nanotubes are used in place of particulate carbon black, higher conductivity can be achieved by the addition of a relatively low level of conductive filler in the polymer matrix. Using metal as fillers in the insulating matrix has several limitations. For example, they impart poor mechanical properties, are heavy and easily degraded by oxidation.[99] Organic conductors possess excellent thermal and electrical conductivities as well as solution processability.

### **1.5.1 Inherently Conducting Polymers**

Since the discovery of Inherently Conducting Polymers (ICPs), or synthetic metals, [100-103] interest in and knowledge about this field of organic chemistry has grown dramatically and have been the subject of much research efforts. They are polymeric or oligomeric materials composed of phenylene rings and related units such as naphthalene, anthracene or heteroaromatic rings such as pyrrole and thiophene (Figure 1.12), which are connected to one another through carbon-carbon single bonds or through vinylene groups (-C=C-).

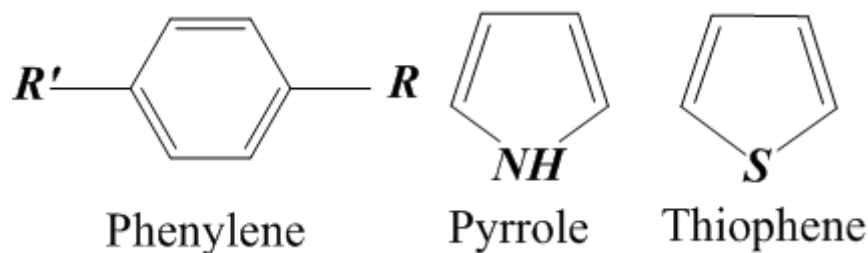


Figure 1.12 Examples of inherently conductive polymers. ICPs are organic polymers that conduct electricity and are not thermoplastic.

In contrast with metals, the electrical conductivity, electrochemical and physical properties of ICPs can be tailored for specific applications through the synthesis and doping processes. [104-106] These polymers have unique electrical and thermophysical properties and, due to the low hydrogen content and aromatic structure, they show fine chemical, thermal, and oxidative stability and are practically insoluble in all common solvents. Their conductivity could be increased to a similar level as that of metals mainly through 'p-doping' (oxidation), or 'n-doping' (reduction).[107] Due to the fully aromatic ring structure and absence of freely rotating groups, the mobility of the repeat units is highly restricted which results in high glass transition and melting temperatures. In fact, their melt viscosities are often so high that injection moulding and similar processing methods are not feasible or practical.

The doping process and the resultant conductivity of ICPs are a result of a number of processes. For instance, in non-conducting polymeric systems (i.e., polyurethane), the valence electrons are bound in  $sp^3$  hybridized covalent bonds. These "sigma-bonding electrons" do not have enough mobility to take part in the electrical conductivity of the material. However, in the case of ICPs, which are conjugated materials, the backbones of the polymers contain conjugated  $sp^2$  hybridized carbon centres. Therefore, there is a

valence electron on each centre in the  $p_z$  orbital, which is orthogonal to the other three sigma bonds. When ICPs are doped by oxidation (removing some of the delocalized electrons), the conjugated  $\pi$ -orbitals form a one-dimensional electronic band, and the electrons within this band become mobile. In theory, ICPs can also be doped by adding electrons to an otherwise unfilled band (reduction). However, practically, most ICPs are only doped by oxidation (giving p-type materials). The oxidative doping of ICPs is equivalent to the doping of silicon semiconductors, whereby a small fraction of silicon atoms is substituted by electron-rich atoms to create semiconductors.[107, 108]

A tremendous amount of intellectual efforts has been put into the development of different types of conducting polymers, namely characterization, stability (electrical, environmental, and thermal), processability, production costs, and applications. Among the many ICPs developed over the last 30 years are those based on polythiophenes, polypyrroles, and polyanilines.[98, 109, 110]

### **1.5.2 Polythiophene (PTh)**

Polythiophene (PTh) was first chemically synthesized in the early 1980s. However, the structure was not identified due to the lack of infusibility and solubility of the material.[111] Regardless of the synthesis method, PTh was found to be insoluble due to the strong  $\pi$ -stacking interaction between aromatic rings. Despite the lack of solubility, PTh films exhibited excellent thermal and environmental stability, high conductivity and biocompatibility which made it a highly popular material.[112] The doping/dedoping process can be achieved by a chemical or an electrochemical process. During the doping process, the conductivity of neutral PTh increases from an insulator to a highly conductive polymer in its doped form. Figure 1.13 shows the chemical structure and doping/dedoping process of PTh.[113] A soluble poly(phenylene) is achieved by the incorporation of

relatively flexible and long side chain or using radical polymerization (ester of 5,6-dihydroxycyclohexa-1,3-diene).[114]

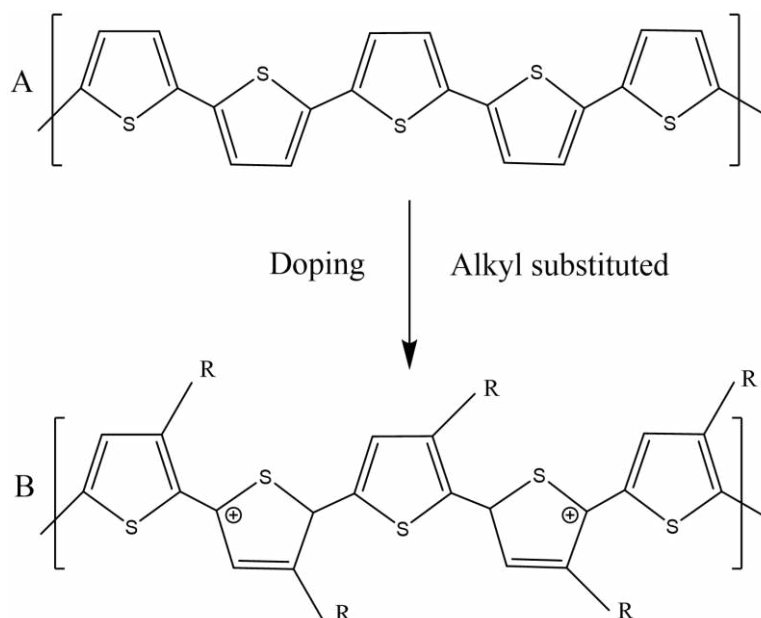


Figure 1.13 Chemical structure of PTh. A: undoped and unsubstituted PTh (insoluble), B: doped and Alkyl substituted PTh (solution processable).

To overcome problems with the solubility of PTh, various substituted derivatives of the polymer have been developed by adding side chains that carry alkyl, alkoxy, and other substituents along the polymer backbones.[115] A broad variety of properties such as aqueous/organic solvent solubility become available by the addition of side chains to the main PTh polymer backbone. However, the electronic properties of the parent ICP are degraded due to side chain substitution.[116, 117]

### 1.5.3 Polypyrrole (PPy)

Polypyrrole (PPy) is the most studied ICP; it can be easily processed, has good stimulus-responsive properties, and has many interesting electrical properties which make it a very

promising "smart" biomaterial. It is thermally and chemically stable and electrically conductive in an oxidized state. PPy has the potential to be fabricated in a large surface area with control of its porosity. Most of the conductive polymers compared to electrically conductive nonorganic materials have a low electrical conductivity, and PPy is no exception to this rule.[118] So to obtain higher electrical conductivity, a doping process is necessary (Figure 1.14).[119]

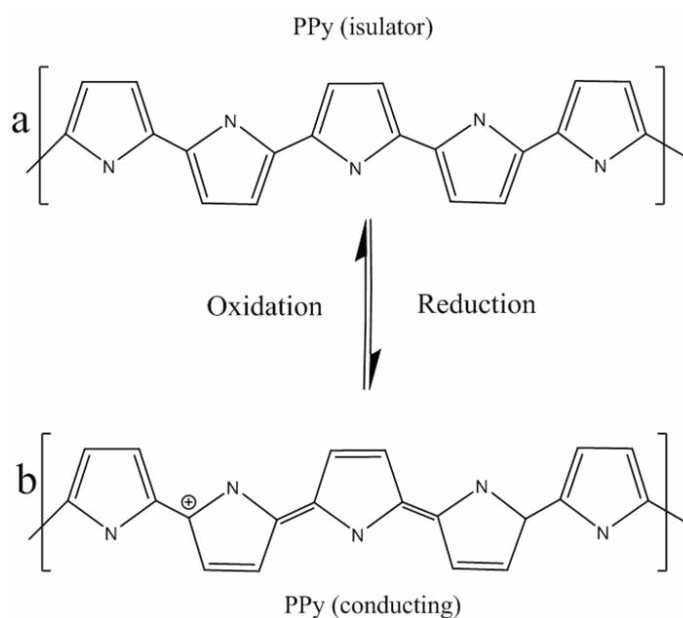


Figure 1.14 Chemical structure of polypyrrole (a) and doping state (b). Conducting and reducing states of PPy can be electrochemically generated from the corresponding monomers. During electropolymerization, anions from the solution are inserted into the polymer matrix to maintain the material's electroneutrality, neutralizing the positive charges generated in the oxidized polymer threads.[120]

The drawback of PPy is its low processability after synthesis, and also its molecular structure makes it a thermoset. Thermosetting polymers are generally non-flexible due to



the three-dimensional network of bonds (crosslinking) and are mechanically brittle, rigid and insoluble after synthesis.

#### 1.5.4 Polyaniline (PAni)

Polyaniline exists in different oxidation levels with different stability and conductivity (Figure 1.15). [121] It is a desirable conductive polymer because it is inexpensive, easy to synthesize, displays excellent environmental stability and can be easily chemically modified. [122] In the available literature reviewed, different ways to produce PAni have been demonstrated, including; chemical, electrochemical, enzymatic, photo, and plasma. [123-132] Chemical polymerization is again subdivided into heterophase, solution, interfacial, seeding, metathesis, self-assembling, and sonochemical polymerizations.[133]

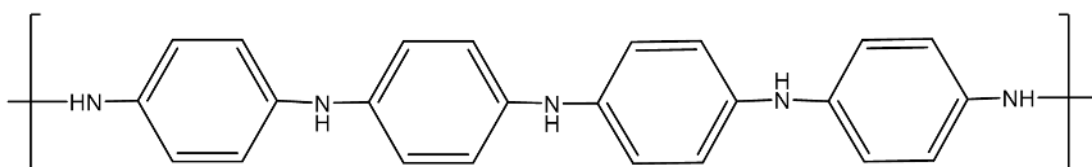


Figure 1.15 Chemical structure of polyaniline (PAni).

Its potential for biological application is restricted by its low flexibility, processability and also only conducting at low pH, well below physiological pH. Furthermore, PAni causes some chronic inflammation to the body. PAni has four different oxidation states and its physical properties change with respect to its oxidation state. The transition from one oxidation state to another is possible in PAni by simple redox methods electrochemically or chemically. PAni could be electrically conductive in Emeraldine salt oxidation state, i.e., when in a medium of  $\text{pH} < 2.5$  (Figure 1.16).[134]

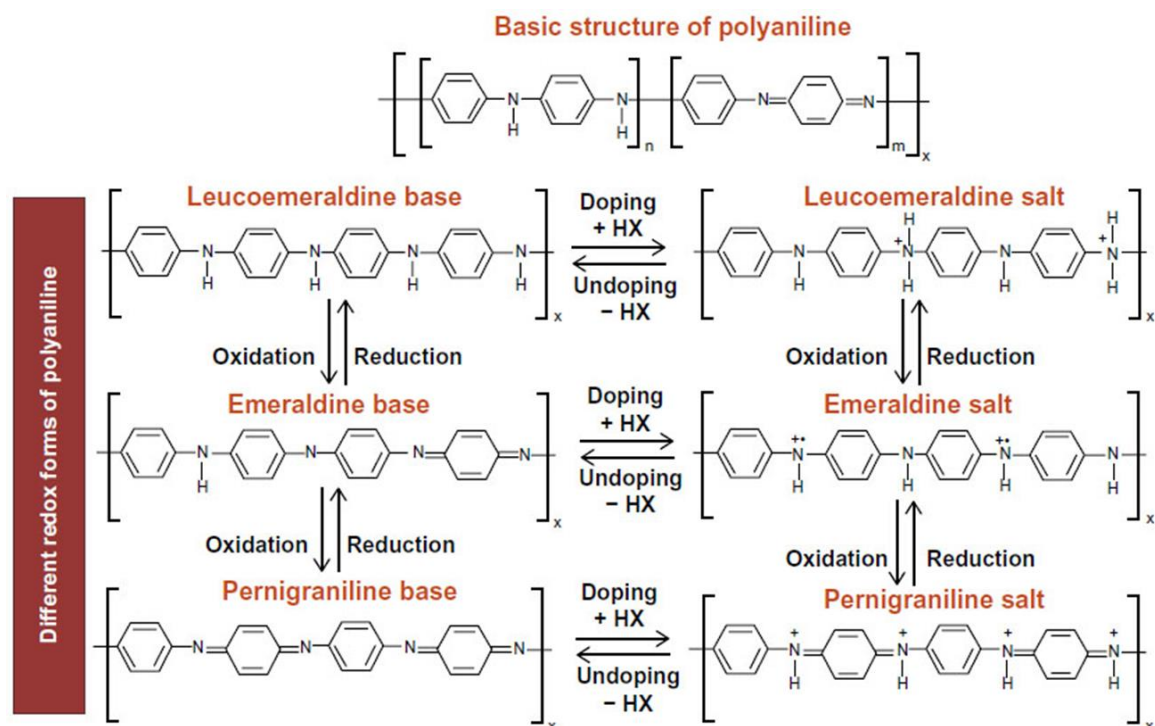


Figure 1. 16 Basic structure of PANi and different oxidation forms of PANi with its doped states.[127]

### 1.5.5 Poly(3,4-ethylenedioxythiophene) poly(styrenesulfonate) (PEDOT:PSS)

Of the soluble and processable polythiophene derivatives that have been developed, poly(3,4-ethylenedioxythiophene) poly(styrenesulfonate) (PEDOT:PSS) has been the most widely used and commercially successful since its development by Bayer in the late 1980s. [105] PEDOT:PSS has been used for several applications, such as sensors, transparent conducting electrodes, antistatic coatings, electrochromic devices, organic photovoltaic devices, ink jet printing, rechargeable batteries, supercapacitors, and in fibre spinning.[135-139] This widespread use of PEDOT:PSS stems from the fact that it is very stable and highly conductive in its cationic doped state, exhibits good thermal and

environmental stability, good optical transmission, and excellent processability from an aqueous dispersion. [140, 141]

PEDOT:PSS can be synthesized by oxidative polymerization of EDOT monomer in the presence of polystyrene sulfonic acid (PSS) as a template polymer. When synthesized by chemical oxidation of the monomer in solution, the PEDOT:PSS complex is a water processable dispersion when PEDOT is in its conductive oxidized state (Figure 1.17).

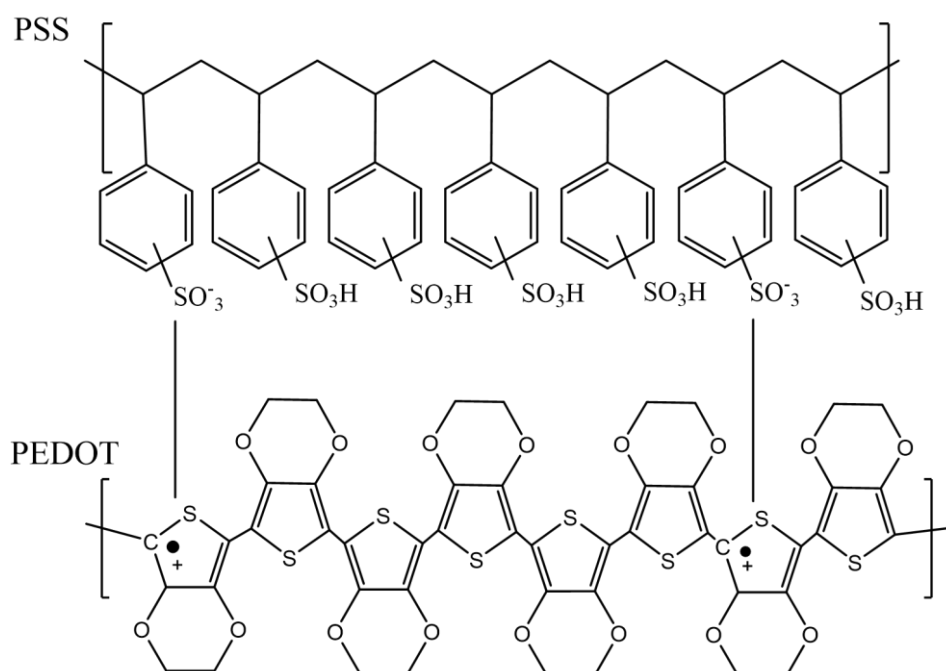


Figure 1.17 Molecular structure of PEDOT:PSS complex.

There are three main functions for PSS in the formation and stability of PEDOT:PSS complex; first, dispersing EDOT monomer in the aqueous polymerization medium. Second, acting as a charge balancing counterion for the PEDOT chain, and finally, PSS disperses PEDOT segments in water, which makes PEDOT:PSS complex dispersible in

water. This water processable dispersion is very stable and has an oligomeric nature containing 6 to 18 PEDOT repeating units. [141-144]

ICPs have been employed in various application such as sensors, batteries biosensors and catalysis.[145, 146] Conversely, their infusibility, and insolubility, and hence complex processability, made them problematic in commercial use. To improve processing, several approaches have been developed: **(1)** The 'precursor' method, in which a processable precursor ICP is initially prepared in the proper form and then chemically converted into the final ICP.[147] **(2)** The copolymerization method, in that graft, random or block conductive copolymers which are processable are prepared.[148] **(3)** the composite method, where an ICP is incorporated into an electrically insulating matrix. In the electrically conductive composites, the ICP is the source of electrical conductivity and the insulating matrix provides appropriate mechanical properties. Highly conductive materials could be prepared via method **1**; however not all ICPs can be prepared by this method. Generally, method **2** is detailed and complicated. The ICPs developed through method **3**, typically have reasonable electrical conductivity, with the resulting conductive composites affording the ability to adjust mechanical and electrical properties by varying the ratio of the conductive component to the insulating component. For this reason, the third method is most efficient. [149]

### **1.5.6 Carbonaceous Materials as Fillers**

Carbon has long been known as one of the most chemically multi-purpose elements. The capacity of carbon atoms to contribute to robust covalent bonds (C-C) in various hybridization states (Figure 1.18) or with non-metallic elements (nitrogen, oxygen, phosphorus, sulphur, etc.) enables them to form a wide range and size of structures.

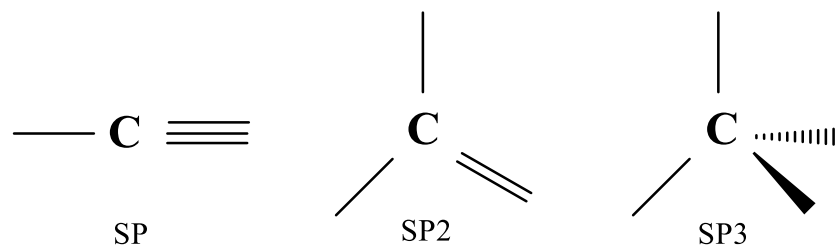


Figure 1.18 Hybridization of the carbon atom.

Carbonaceous materials (CM) have received much attention due to their extensive range of toughness, thermal, and electrical properties. These properties follow on in materials ranging from insulating diamond and diamond-like carbon to semiconducting fullerenes and carbon nanotubes, and low-cost conducting materials such as graphite and carbon black. With the varied range of molecular compounds present in different natural CM (from aliphatic to aromatic, with a variety of functional groups), these materials could be used in a wide range of thermal and electrical properties at very low cost. To use the potential of these materials, it is critical to develop compatible, low-cost methods of processing them. A wide range of biocompatible materials have already been used for developing structures for health monitoring applications. These have included, single wall carbon nanotubes (SWCNT), multiple walls carbon nanotubes (MWCNT), reduced graphene oxide (RGO), graphene oxide (GO), chemically converted graphene (CCG) and graphite.[150] However, it is hard to find a carbonaceous material that meets all the requirements such as repeatability, sensitivity, and processability for developing a perfect material for sensing applications.

Graphene oxide (GO), carbon nanotubes (CNT), fullerenes, graphite, and graphene have recently attracted the attention of researchers as composite fillers. The structure of the carbonaceous materials is based on a layer of  $sp^2$  hybridized carbon atoms covalently bonded in a honeycomb lattice which is known as graphene. [151-153] A physical analogy for graphene that has been put forward is “Atomic-scale chicken wire”. [154] The carbon-carbon bond length in graphene is about 0.142 nm. Graphene is the basic structural element of several carbon allotropes including graphite, carbon nanotubes and fullerenes. (Figure 1.19). [155-157]

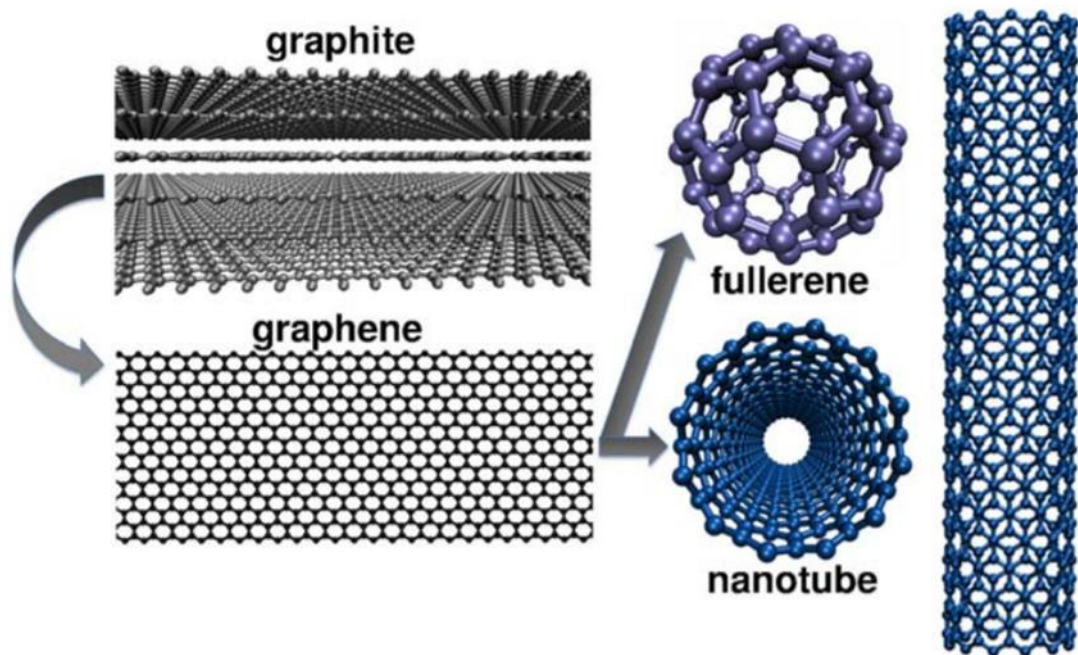


Figure 1.19 Schematic of  $sp^2$  hybridized carbon allotropes: graphite (3D), graphene (2D), carbon nanotubes (1D), and carbon fullerenes (0D). [158]

CMs show excellent mechanical, electrical, and thermal properties that make them suitable fillers to develop materials with high performance for sensor applications.

Furthermore, carbonaceous fillers such as graphene offer an additional advantage of displaying antibacterial properties. Combination of the sensing potential and antibacterial properties of these materials would be useful in the realization of wound healing patches. [159-161]

### 1.5.6.1 Graphite

Graphite is a crystalline carbon and has a layered structure. Figure 1.20 shows the arrangement of the atoms in each layer and the way the layers are spaced.[162]

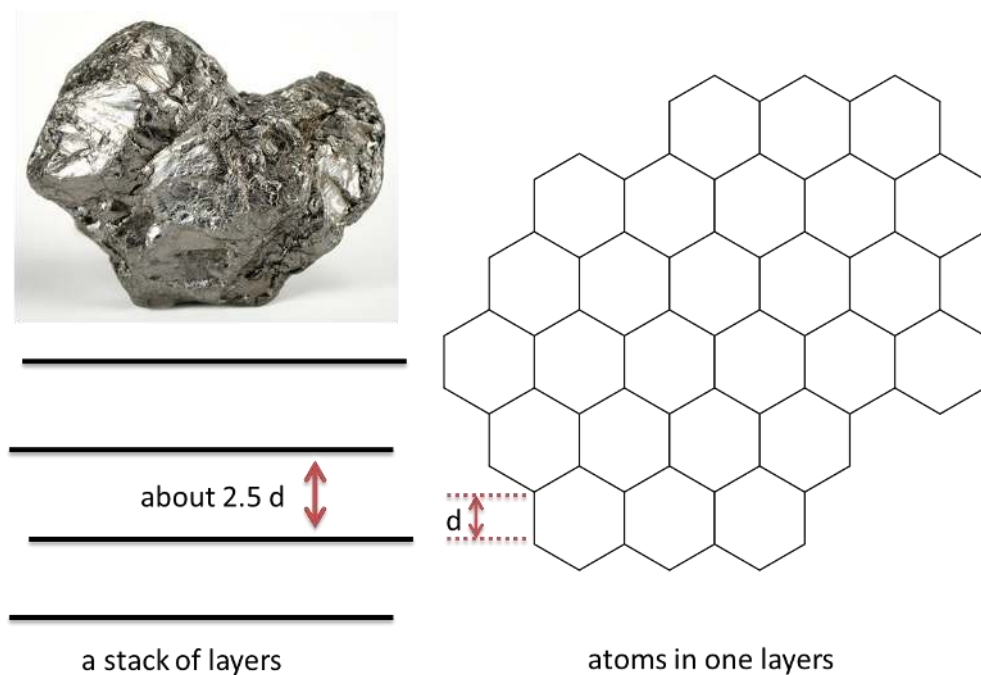


Figure 1.20 Simplification of the graphite structure. The distance between the layers is around 2.5x of the distance between the atoms within one layer.

Graphite has delocalized electrons that are not contributed in the covalent band. These delocalized electrons or free electrons in each carbon atom become delocalized and are free to move throughout and within the whole sheet, and not belong to one carbon.[163] In solid physics, delocalized electron that facilitates electrical conductivity also cause thermal conductivity.[164] Graphite has a soft, slippery feel, and high melting point. Graphite has sheets similar to a pack of cards in that each card (sheet) is robust and strong, but the sheets can slide over each other very easily.[162] It is insoluble in water and organic solvents due to the fact that the attractions between solvent molecules and carbon atoms will never be strong enough to overcome the strong covalent bonds in graphite.[165] The delocalized electrons are free to move throughout the sheets. If a piece of graphite is connected to a circuit, electrons can fall off one end of the sheet and be replaced with new ones at the other end.[166]

#### 1.5.6.2 *Carbon nanotubes (CNT)*

CNTs are attractive fillers for making electrically conductive nano composites because they exhibit excellent conductivity in the range 10<sup>5</sup> – 12000 S/cm.[167] Carbon nanotubes are tube-shaped carbon sheets bonded to each other via sp<sup>2</sup> bonds. There are two types of CNTs, namely single wall (SWCNTs) or multiple walls (MWCNTs) (Figure 1.21). The length of CNTs vary between 50 nm to 1 cm, and their diameters range from 1 – 2 nm for SWNTs and 10 – 100 nm for MWNTs.[168] CNTs are usually synthesized via carbon-arc discharge, laser ablation of carbon or chemical vapour deposition.[169] CNTs have been widely used in sensor applications, tissue engineering, drug delivery and regenerative medicine. [170-172] However, in the face of their excellent properties, the application of CNTs is very debated in biomedical fields, mainly due to their toxic nature,



high production cost, and physical powder form, which makes them difficult to handle.[173]

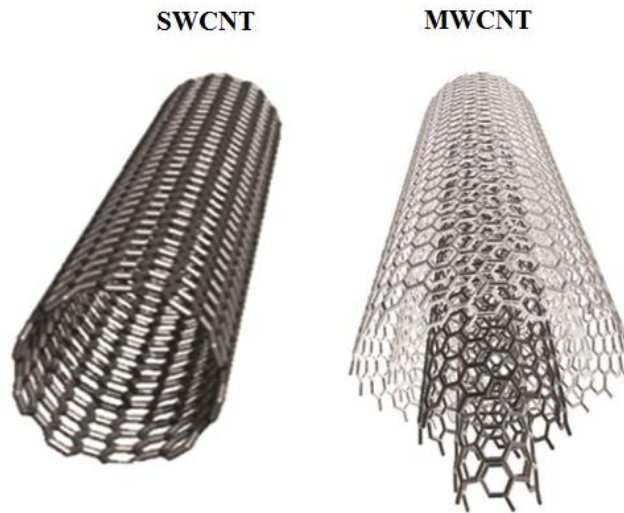


Figure 1.21 Schematic of SWCNT and MWCNT.[174]

### 1.5.6.3 *Fullerenes*

Carbon 60 or ‘Buckminsterfullerene’ is a zero-dimensional (0D) graphitic material containing 60 carbon atoms arranged in the form of a hollow ball.[175] Aside from its unique and interesting geometrical shape, it exhibits many properties such as superconductivity and ferromagnetism.[176] This material has been used to increase the thermal stability of polymers since its discovery by Kroto and Smalley in 1985.[177] It can be synthesized via, laser, chemical vapour deposition (CVD), electric arc discharge and plasma.[178-180] During the last decade, fullerene has been used in several sensor applications.[181, 182] However, the toxicity and biocompatibility of fullerene have continuously been questioned. Despite its remarkable properties, it is not a preferred filler for use in biomedical applications, due to its toxicity, high production costs, low water solubility and yield.[183, 184]

#### 1.5.6.4 Graphene

Graphene is the name of planer sheet of carbon, in a honeycomb lattice, with the two-dimensional sheet of  $sp^2$ -hybridized with a carbon-carbon bond length of 0.142 nm (Figure 1.22).[185] Its extended honeycomb network is the basic building block of other main allotropes; it can be stacked to form 3D graphite. Long-range  $\pi$ -conjugation in graphene produces extraordinary in-plane electrical ( $\sim 10^4 \Omega^{-1} \text{ cm}^{-1}$ ), thermal (3000-5000  $\text{W m}^{-1}\text{K}^{-1}$ ), and mechanical properties (with Young's modulus of  $\sim 1 \text{ TPa}$ ), which have long been the interest of many theoretical studies and more recently have become an exciting area for experimentalists.[186, 187]

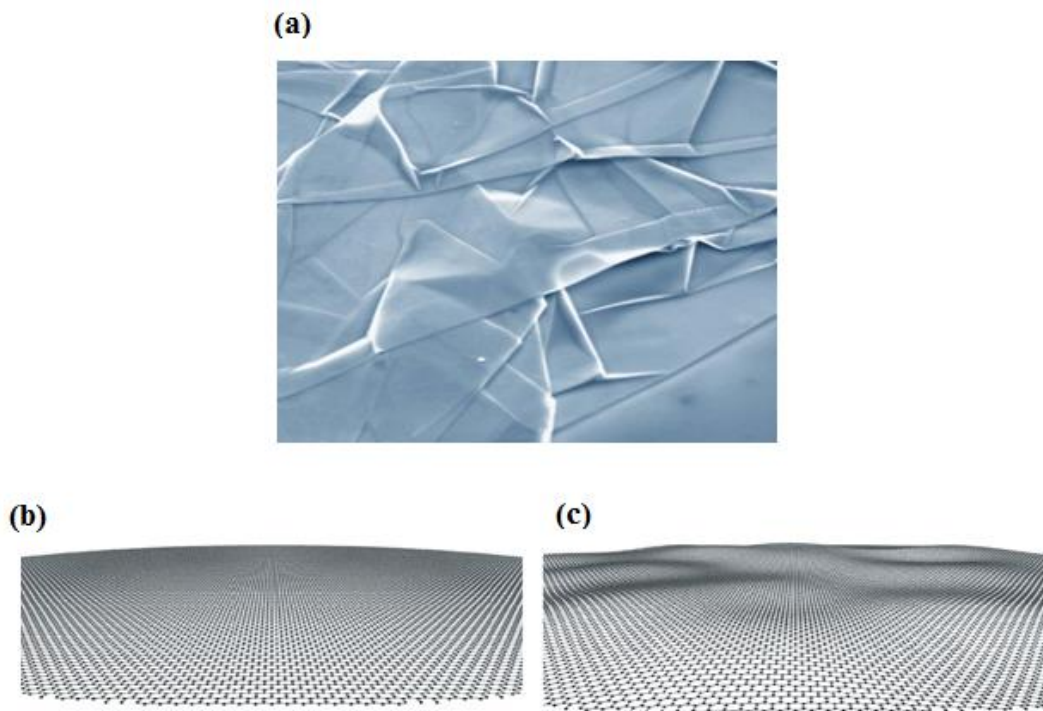


Figure 1.22 a) Scanning electron micrograph of single-atom-thick sheets of graphene, (b) flat graphene crystal in real space (perspective view) and (c) the same for corrugated graphene.[188]

Even though graphite has been used by humans for 6000 years, and graphite has been identified as a mineral for approximately 500 years. It was in the 1960s that graphene was studied for the first time via isolating as a single-atom plane of graphite. The electrical property of graphene attracted the attention of scientists at that time; but, research on graphene moved slowly as a synthesis of this nanosheet was found to be experimentally difficult.[189, 190] Different methods were taken to synthesize this honeycomb structure, including the same methods used for developing CNTs, but none of them were capable of preparing high-quality graphene. Revolution in graphene happened in 2004 when Konstantin Novoselov and Andre Geim successfully produced high-quality graphene crystals with the simple method of peeling off the graphite flakes via scotch tape.[191] Since then research on graphene has risen sharply, the synthesis and functionalization of graphene (Figure 1. 23) was further developed and optimized, and graphene has found application in different fields of science.

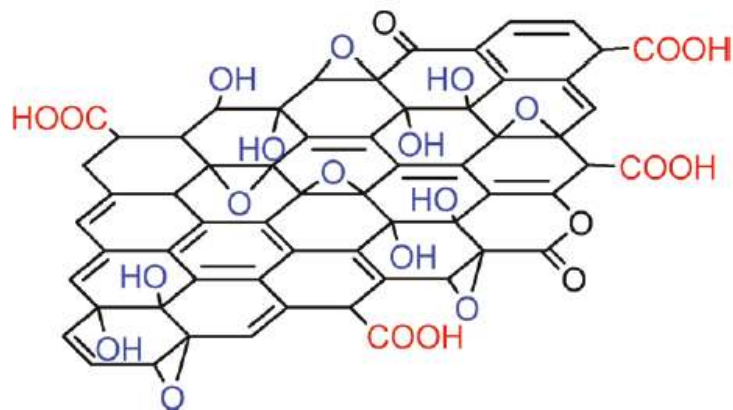


Figure 1. 23 Chemical structure of GO-hydrophilic groups are coloured red (carboxyl groups) and blue (hydroxyl and epoxy groups).[192]

Graphite has an anisotropy property [162] with the  $p_x$ ,  $s$ , and  $p_y$  atomic orbitals on each carbon hybridized able to form robust covalent  $sp^2$  bonds, giving growth to  $120^\circ$  C-C-C bond angles. The  $p_z$  orbital on each carbon overlaps with its three adjacent carbons to form a band of filled  $\pi$  orbitals, which is known as the valence band, and a band of empty  $\pi$  orbitals named the conduction band. Although three of the four valence electrons on each carbon has the  $\sigma$  (single) bonds, the fourth electron forms one-third of a  $\pi$  bond with each of its neighbours producing a carbon-carbon bond order in graphite of one and one-third. Lacking chemical bonding in the c-direction out-of-plane interaction is very weak and comprises the spread of thermal and charge carriers. This results in out-of-plane thermal and electrical conductivities that are both more than  $10^3$  times poorer than those of their in-plan analogues. The outstanding properties of graphene make it suitable for use as a reinforcing filler for the preparation of polymer composites.[162]

## 1.6 Hydrogels

Electrically conducting polymers suffer from mechanical limitations such as flexibility, so it is essential to use another material to address these limitations in a smart composite for sensing applications. An attractive candidate for this purpose is a class of materials known as hydrogels.

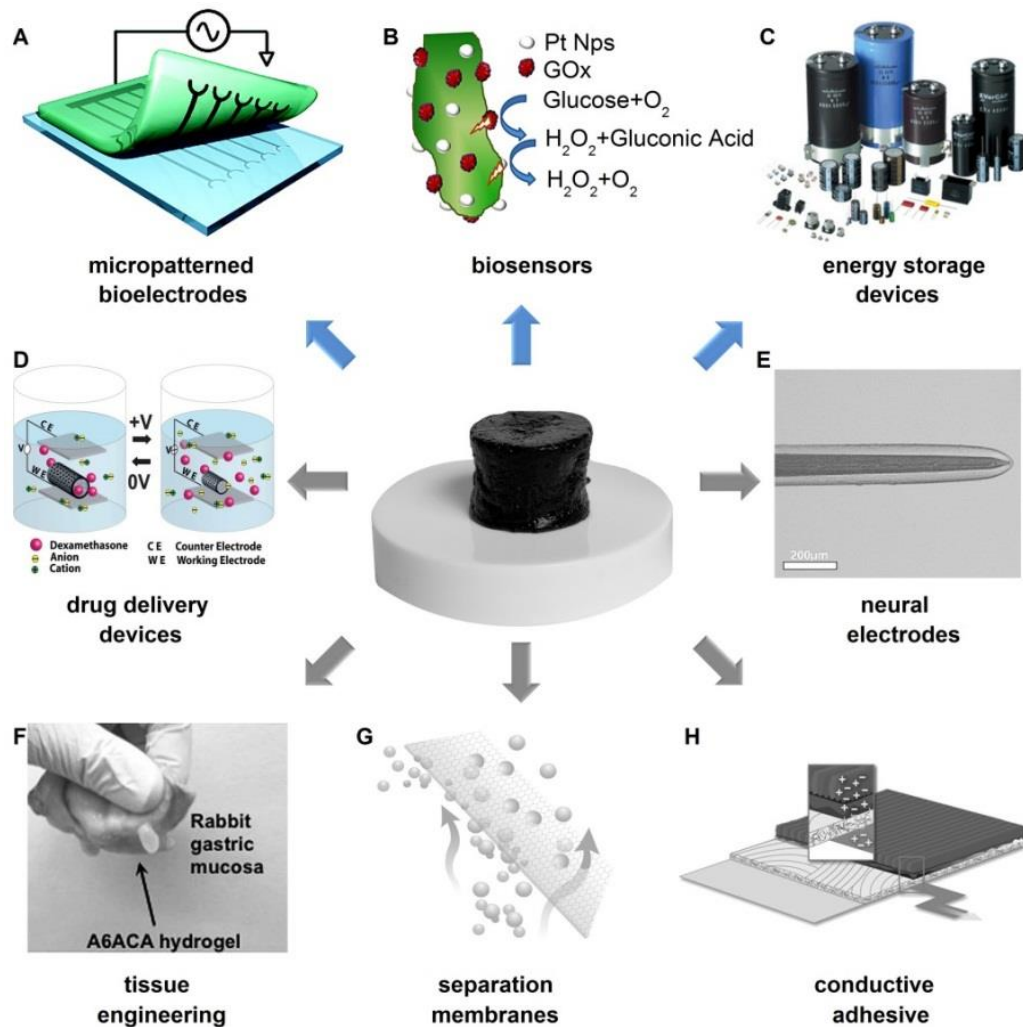


Figure 1.24 Representative applications of hydrogels. (A) Bioelectrodes, (B) Biosensors, (C) Energy storage devices, (D) Drug delivery, (E) Neural electrodes, (F) Tissue engineering.[193]

Hydrogels emerged in the early 1950's as being of great importance in the biomaterials field in part due to their ability to imbibe large amounts of water. Firstly, hydrogels found application in the agricultural and adsorbent industries, and then their applications were extended to other industries where an excellent water holding property was of prime importance.[194] Hydrogels are a class of cross-linked and water-swelling polymers with a three-dimensional network structure. Within this structure, the main chain or branched

chain contains a large number of hydrophilic groups. The result is an elastic network with water effectively filling the interstitial space of the network. When immersed and equilibrated in an aqueous medium, cross-linked hydrogels assume their final hydrated network structure which brings into balance the forces arising from the solvation of the repeat units of the macromolecular chains that leads to an expansion of the network (the swelling force) and the counterbalancing elastic force of the cross-linked structure (the retractive force).[195]

These characteristics have allowed hydrogels to be used in biomedical applications that include biosensors, drug delivery systems, and contact lenses (Figure 1.24). [195] Their unique characteristics, being of a soft elastomeric nature, serves to minimize mechanical and frictional irritation to the tissue bed, their low interfacial tension contributes to a reduction in protein adsorption and hence biofouling and cell adhesion, and their swelling capacity results in high permeability for low molecular weight drug molecules and metabolites. [196-203]

### 1.6.1 Conductive Hydrogel

Conducting polymers and hydrogels are macromolecular systems which present special and important characteristics that make them suitable for a broad range of practical applications. [204-210] The electric properties of conducting polymers make them suitable for devices driven by an external electric signal, such as a voltage or current [211] Whilst hydrogels are 3-dimensional structures formed by the cross-linking of hydrophilic polymeric chains, their swelling degree in solutions is dependent upon the chemical nature of the media, pH, ionic strength and temperature.[212] Hydrogels and conducting polymers are also called "smart materials" due to their change of volume or release of substances upon the application of an external signal.[213]

The combination of hydrogels and ICP permits both materials to preserve their unique responsive properties [195], and the resultant electrically conductive hydrogel is an intelligent hydrogel that can respond to electrical stimuli. Electroconductive hydrogels belong to the general class of multifunctional smart materials that seeks to combine the inherent properties of constituent materials to give rise to technologically relevant properties for devices and systems. [195, 214] The key applications of electro-conductive hydrogels are: biorecognition membranes for implantable biosensors, electrostimulated drug release devices for programme delivery sensors,[215] fuel cells,[206] supercapacitor,[216] dye sensitive solar cell [217] and rechargeable lithium batteries [195, 218] These applications provide new horizons for these stimuli-responsive, biomimetic polymeric materials. Moreover, combining the properties of hydrogels with conductive components allows the conductive polymer hydrogels to provide an excellent interface between the electronic-transporting phase (electrode) and the ionic-transporting phase (electrolyte), between biological and synthetic systems, as well as between soft and

hard materials.[219] While conductive hybrid polymer hydrogels have attracted the interest of researchers, there are intractable problems with these materials such as their complicated synthesis procedures and poor mechanical toughness.

### **1.6.2 Polyurethanes**

Polyurethane (PU) is a widely used polymer with numerous functional applications due to its unique property of possessing the elasticity of rubber combined with the durability and toughness of metal.[220] The origin of this material dates back to World War II where it was first developed as a supplement for rubber. The thermal and electrical conductivity of PU is varied from insulator to conductive via synthesis and/or compositing with a conductive material. [221-225] The resulting conductive composites of polyurethane are suitable for sensors, corrosion-resistance paints, electrostatic dissipaters, EMI shielding, and many other applications. [28, 226-229] PU's are reaction products of polyisocyanates ( $-N=C=O$ ) group with other species containing active hydrogens such as polycarbonates, hydroxyl-terminated polyesters, polyamines, polyethers, or polyols. The reaction leads to a unique polyurethane that is composed of diisocyanate-based hard polymer segments polyester or polyether soft segments. (Figure 1.25)



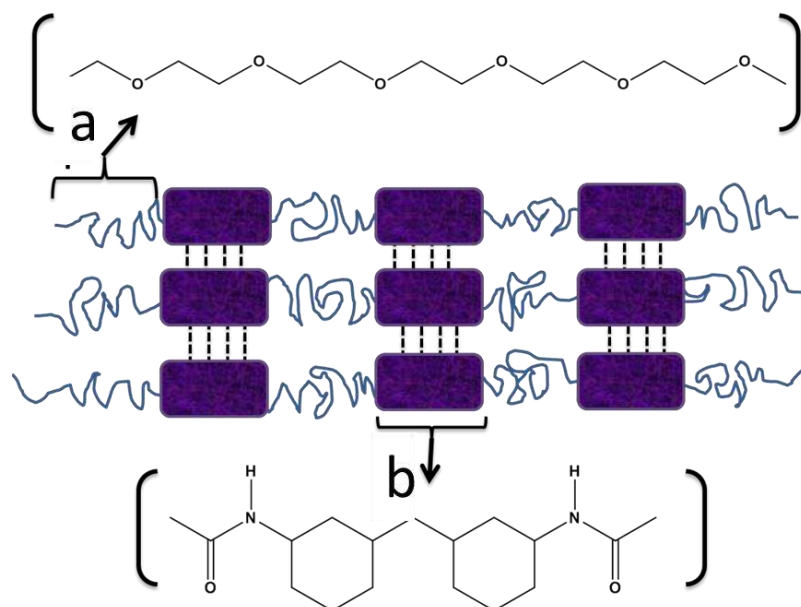


Figure 1.25 Schematic structure of PU; a: soft segment and b: hard segment.

During the past few decades, research on electrically conductive polyurethane composites has grown and resulted in the discovery of various applications for PU.[230] Binary composite systems, containing conductive fillers in the polymer matrix, resulted in materials that are electrically conductive, tough, and flexible. Despite these milestone improvements in PU composite properties, these composites suffer from the need of high levels of conductive fillers to reach a percolation threshold of sufficient electrical conductivity.[231, 232] The necessity to include a high percentage of fillers in search of electrical or thermal characteristics often leads to scarifying the mechanical properties of the matrix, so it is critical to obtain electrical and thermal conductivities with the minimum volume of fillers. The composite performance can be varied by varying the filler loading in order to satisfy the requirements dictated by the specific device demands. Electrically conductive PU composites with polyaniline, polypyrrole, or polythiophene are classified as tough conductive materials that have a combination of the electrical conductivity of intrinsically conducting polymers and the elasticity and toughness of PU.

### 1.6.3 Polyurethane conducting polymers

#### 1.6.3.1 *Polyurethane–polyaniline blends*

Among conductive polymers, polyaniline has many attractive processing properties. However, the chain stiffness renders processing difficult; meanwhile, the polymer in its doped form is insoluble in almost all organic solvents, and the mechanical properties are not processable. Conductive polyaniline and its derivatives were produced in several different ways; polyblend and block copolymers of PANi and poly(p-phenylene-terephthalamide) were spun from concentrated sulphuric acid [233]; poly(o-toluidine) was spun from sulphuric acid, m-cresol and N-methyl-2-pyrrolidinone (NMP); high molecular weight emeraldine base (EB) was spun from NMP and N,N'-dimethylproylene urea (DMPU); EB was spun from a melt, protonated with dodecylbenzenesulfonic acid (DBSA)[234]; and leucoemeraldine base (LB) was spun, post-oxidised, then doped to give the conductive emeraldine salt (ES). [92] In opposition to polyaniline, PU is a processable polymer [129] and it is expected that when both are blended, processability will be enhanced for PANi and electrical conductivity is attained for electrical insulating PU.[235] Since PANi is electrically conductive in its Emeraldine salt oxidation state, at  $\text{pH} < 2.5$ [127], to obtain PU-PAni composite, it is, therefore, necessary that PU must be stable at this pH. For tackling this problem, PANi was synthesized in an aqueous dispersion employing water soluble PU to make a conductive PU-PAni composite. [129, 130] Although this method was used for many studies regarding PU-PAni blending, it has disadvantages, namely the two phases of PU and PANi tend to separate during film formation leading to non-conductive and conductive regions in the film. Aside from the methodology mentioned above, grafting (functionalizing) the hard segment of the PU backbone with conductive polymer is an alternative means of synthesizing PU-PAni

composites.[132] Using this approach, amine-capped (NH) of PAni-EB was reacted with isocyanate attached to the PU soft segment.[236] It is likely that some crosslinking with emine / amine nitrogen in PAni backbone with PU forming networks occurs.[237, 238]

### 1.6.3.2 *Polyurethane-polypyrrole*

Considerable research has been undertaken into polypyrrole because of its high conductivity especially in its doped state, and easy electrochemical and chemical polymerization, which makes it a suitable candidate for various applications. However, PPy has poor mechanical properties and stability at ambient conditions, which restricts its possible applications.[232]

The solubility of PPy is highly restrained, owing to the extensive cross-linking of the polymer backbone. Neutral PPy is generally considered insoluble, but it can swell when exposed to some solvents. Therefore, the conventional methods for polymer processing, such as melt processing and solution casting, cannot typically be applied for PPy. For tackling these deficiencies of PPy several efforts have been made to improve the poor mechanical properties of PPy by making composites or blends with other polymers, e.g., PPy-poly(vinyl chloride), PPy-poly(tetrafluoroethylene), and PPy-poly(methyl methacrylate)[131], PPy-poly(ethylene terephthalate), PPy-poly(vinyl alcohol). Weiss et al. made electrically conductive PU-PPy ( $10^{-7}$  to  $10^{-2}$  S/cm) by adding ferric salts to the PU and then exposed it to Pyrrole vapors. In other work, polymerisation was performed in solutions containing either 4,5-dihydroxy-1,3-benzenedisulfonic acid (DBDA) or nitrate as dopants.[239]

### 1.6.3.3 *Composite of PU with CNTs*

Discovery of CNTs was one of the progressive milestones for making conductive polymer composites. These composites are attractive for use in electrostatic dissipation (ESD) and electromagnetic interference (EMI) shielding, and (at low CNT contents) transparent conductors.[240] The electrical conductivity of a composite is largely subject to the concentration of fillers. At a low loading ratio of conductive fillers, the conductivity of the composite is near to that of the host matrix (insulator matrix). At the percolation threshold, an increase in the filler concentration results in a significant increase in conductivity. After this level of increase, the conductivity levels off and approaches that of the filler material, as described by percolation theory.[167] Based on geometrical reflections, [241] the rate of the percolation threshold is dependent upon the ratio of length-to-diameter (aspect ratio) of the filler particles; (higher aspect ratio results in a decrease in the percolation threshold). [242] The percolation threshold of CNT-reinforced polymer nanocomposites is much lower than for composites containing conventional conducting fillers, such as metallic particles, carbon black, or carbon fibres, because of the high aspect ratio and high specific surface area of CNTs.[242] The most common method for formulating CNT-composites is from solution since it facilitates formation of CNT dispersions [243] with either water or organic solvents being used to produce CNT-composites.[244]

Solution processing is a suitable technique for electrically conductive composite formation. Nevertheless, melt processing is more applicable to scale up production, because of its simplicity and speed.[245] However, this approach is only applicable for blending a conductive polymer with a thermoplastic polymer with remoulding ability as the matrix polymer chains experiences a dramatic loss of conformational entropy during

this process.[246] In-situ polymerization, involving a chemical reaction resulting in the formation of a fine and thermodynamically stable conductive filler phase within the matrix is also employed for the making of CNT-composites, with the creation of a covalent bond between the matrix and the CNTs.[247-249]

A MWCNT/ PU composite, synthesized with chemical linkage of MWCNT with PU matrix has been reported. [250] The study on the mechanical properties of the composite material showed that the tensile strength and modulus were amplified by adding 2 wt% MWCNT into the PU matrix. The conductivity of the composite was  $10^{-5}$  S/cm at 0.5 wt% loading of MWCNTs. [251] The effect of cations such as NaCl on MWCNT-PU composite properties was investigated [252-255] and showed a 4x increase in electrical conductivity of the PU.[255] The percolation threshold of the MWCNT was found to be around 0.5 wt%. [256, 257] Furthermore, the thermal conductivity of the composite was enhanced by 86 % at 7 wt% of MWCNT. The properties of MWCNTs-PU such as thermal stability, tensile, and modulus could be improved via functionalization of MWCNTs.[258-262]

Much research has been performed to improve the mechanical strength of hydrogels through the inclusion of carbon conducting materials (e.g., graphite, carbon black and carbon nanotubes) to form carbon conductive composite hydrogels. These composite hydrogels can be strength-enhanced, however the preparation process typically involves the complicated methods of free radical polymerization and electrodeposition. Therefore, it is important to develop a facile method via blending carbon conducting substances with polymeric hydrogels directly to obtain conductive composite hydrogels.[263]

Due to the mechanical, electronic and thermal properties of graphene, it has been used in various applications, including field effect transistors, sensors, transparent electrodes,

batteries, supercapacitors, optoelectronics, biodevices, drug delivery systems, and composites.[264-273]

It is recognised that various noncovalent forces (including hydrogen bonding, ionic, and amphiphilic) exist in graphene-based hydrogels.[209, 274] Graphene materials are regarded as ideal fillers in the preparation of polymer composites due to their high aspect ratio and excellent mechanical, electrical, optical, thermal and magnetic properties. In contrast to other widely used nanomaterial fillers such as carbon nanotubes, the synthesis of graphene is facile, inexpensive and can easily be scaled up.[275] It has also been reported [276-278] that graphene/polymer composites exhibit improved thermal, electrical and mechanical properties compared with other nanostructured carbon fillers at similar volume fractions while retaining the processability of the polymer, thus allowing the fabrication of complex three-dimensional structures.

The combination of ICPs and liquid crystal graphene oxide (LCGO) has resulted in an advanced multifunctional composite. This kind of composite offers an attractive route to reinforce ICPs while enhancing electrochemical performance based on morphological modification or electronic interaction between ICPs and LCGO. It has been shown [281] that composites based on ICPs and graphene exhibit properties of each of the individual components with synergistic effect due to a facile charge transfer between the two constituents. This charge transfer, which is in contrast with composites containing non-conducting matrix, reduces the enhanced contact resistance between adjacent sheets. In the case of a non-conducting matrix, the efficiency of charge transfer within the adjacent sheets is strictly limited due to the insulator-coating of the sheets. Composite production using ICPs eliminates this resistive barrier and maximizes the electron transport among the LCGO sheets to improve the conductivity and electrochemical performance. The

addition of LCGO to ICPs is also attractive because of the limited conductivity of ICPs in their reduced state; the state in which graphene can function as the conducting platform for charge delivery.[281]

## **1.7 3D Printing of Scaffolds**

More than three decades since its introduction by Charles Hull, 3D printing technology has revolutionized research processes. It is also commonly referred to as solid freeform fabrication (SFF), rapid prototyping (RP), or additive manufacturing (AM).[282] 3D printing has only recently been applied to biomedical engineering and applications. In this decade scientists have been developing 3D printers with the ability to fabricate complex 3D biomedical devices.[283] 3D extrusion printing is an attractive method of scaffold formation in the biomedical field due to reasonable accuracy and the capability of printing a varied range of biomaterials. Extrusion printing is based on extrusion of a melt or solution through a nozzle and X, Y, Z movements via a predefined 3D CAD (Computer Aided Design) generated pattern to create a 3D structure. 3D models are typically sliced into vertical sections or 'layers' via a chosen slicing software allowing for the structure to be printed layer by layer (Figure 1. 26).

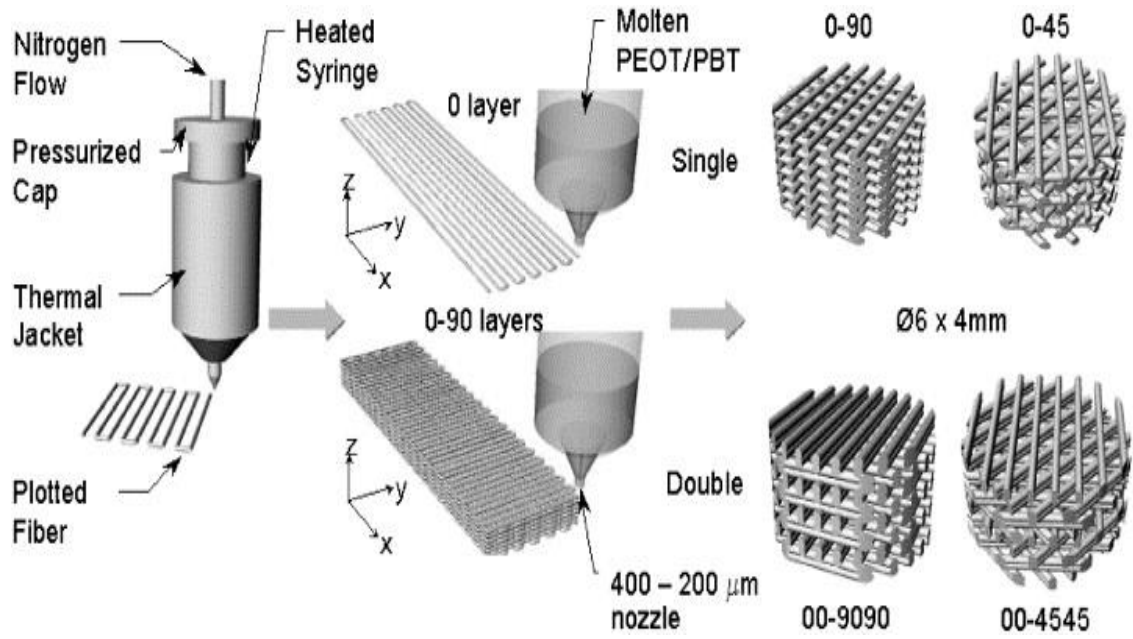


Figure 1.26 Overview of RP technology that uses a layer by layer build up process.[284]



## 1.8 Thesis outline

From the literature survey reported in the preceding sections, the most promising aspects of current research have been given due consideration for the basis of the work of this PhD thesis. Therefore, this PhD study focuses on the development of a flexible and stretchable conductive hydrogel material based on graphene and PEDOT:PSS for temperature sensing. This thesis describes the novel modification of LCGO with chloride salts to increase the storage moduli, viscosity and thermal conductivity properties. Development of a novel processable conductive hydrogel via inclusion of LCGO and PEDOT:PSS within a PU matrix has subsequently been undertaken to develop a flexible material, referred to as polyurethane hybrid composite (PUHC), for temperature sensing applications. The processability of the PUHC was investigated via the printing of 3D structures. Furthermore, the biocompatibility of the synthesized conductive hydrogel was examined through cell study. The structure of the thesis is as follows.

**Chapter 1** describes the motivation of the work and reviews the related literature describing the background work already published in this field of research.

**Chapter 2** describes general experimental methods used in this work such as synthesis of modified liquid crystal graphene oxide (m-LCGO), polyurethane hybrid composite (PUHC), mechanical, electrical, thermal, and rheological characterisation.

**Chapter 3** describes the work undertaken to form electrically and thermally conductive LCGO. The review of the literature highlighted the lack of a comprehensive study on the use of simple and low-cost methods to improve the electrical and thermal conductivity of LCGO and impact of cations post-treatment on mechanical and rheological properties of LCGO. Therefore, the development of modified LCGO (m-LCGO) is investigated here.

**Chapter 4** develops a conductive hydrogel. PU, an electrical isolator, is a promising material for the development of biomaterials. However, the lack of data about the conductive polyurethane conductive hybrid composite (PUHC) with LCGO/PEDOT:PSS composites in the literature motivated a comprehensive study on this subject here. The mechanical, electrical and biocompatibility properties of PUHC composite and the optimization of the ratio of the filler is presented in this chapter.

**Chapter 5** presents work performed to develop a preliminary thermistor sensor based on the developed PUHC. Sensor characterization tests, mechanical properties, and impact of other ambient physical stimuli are described. Finally, PUHC was employed as an ink for extrusion 3D printing. Design, rheological and morphological properties of the 3D printed PUHC temperature sensor are discussed.

**Chapter 6**, Conclusions and recommendations.

Each chapter contains a short introduction, followed by experimental, results, discussion and conclusions.

## **Chapter 2**

# General Experimental

---

This chapter describes the general materials, syntheses, and characterization methods which have been used in this Thesis. Specific experimental procedures of each chapter will be described in more detail in the relevant chapters.

## 2.1 Material

Sodium chloride (NaCl) was obtained from Aladdin-reagent. Potassium chloride (KCl), calcium chloride ( $\text{CaCl}_2 \cdot 2\text{H}_2\text{O}$ ), 50 wt.% hypophosphorous acid ( $\text{H}_3\text{PO}_2$ ) and magnesium chloride ( $\text{MgCl}_2 \cdot 6\text{H}_2\text{O}$ ) were purchased from Sigma-Aldrich and used without further purification. All chemicals were analytical grade and their solutions were prepared using Milli-Q water (18.2 MOhms) (Nanopure water, Barnstead). Expandable graphite used as the precursor for synthesizing ultra-large GO sheets was obtained from Asbury Carbon (3772). Orgacon™ DRY re-dispersible PEDOT:PSS pellets were from Agfa. Ethanol and DMF were purchased from Sigma-Aldrich and used as supplied. HydroMed D3 (AdvanSource, USA; referred to as PU-D3 hereafter) was used as the base polyurethane material (PU-D3).

### 2.1.1 Synthesis of Graphene Oxide

Graphene oxide (GO) was synthesized from natural graphite powder using a modified Hummers' method in two steps to achieve better oxidation of graphite. The whole procedure was performed in a fume hood and the temperature of the reaction was controlled accurately by a digital thermometer. In the preoxidation step,  $\text{K}_2\text{S}_2\text{O}_8$  (5g) and  $\text{P}_2\text{O}_5$  (5 g) were added successively into an 80 °C solution of concentrated  $\text{H}_2\text{SO}_4$  (30 ml), followed by addition of 10 g graphite powder. The reaction was carried out in a three neck flask located into a dish containing silicone oil to be able to accurately control the reaction temperature. The mixture was stirred at 80 °C for 4.5 hrs. After cooling to room temperature, the mixture was carefully diluted through dropwise addition of cold distilled water with continuous monitoring of the temperature. Then, the resultant sample was filtered and washed until the washings became pH neutral and air-dried. In the second oxidation step, the graphite powder was put into 230 ml cold (0 °C) concentrated  $\text{H}_2\text{SO}_4$

and 30 g  $\text{KMnO}_4$  was added gradually with stirring and cooling, so that the temperature of the mixture was kept below  $12\text{ }^\circ\text{C}$ . The reaction was carried out by putting the reaction flask into an ice bath to control the temperature and ensure the exothermic reaction was controlled. The temperature of the mixture was increased to  $35\text{ }^\circ\text{C}$  by gradual addition of warm deionised (DI) water to the ice bath, stirred for 2 hrs and followed by careful addition of 920 mL DI water maintaining the temperature at  $35\text{ }^\circ\text{C}$ . The mixture was then diluted with 0.5 L DI water and stirred for 15 min. Successively, 1.5 L of DI water was added to the mixture to terminate the reaction followed by dropwise addition of 30%  $\text{H}_2\text{O}_2$  (25 ml). The colour of the mixture changed to bright yellow at this stage. The mixture was washed and centrifuged with 1 M HCl solution (2.5 L) in order to remove metal ions. Finally, the GO product was washed with DI water through centrifugation (at 13,200 rpm by Eppendorf Centrifuge 5415D) until the washings became neutral.

### **2.1.2 PEDOT:PSS dispersions**

Aqueous dispersions were prepared from the PEDOT:PSS pellets (Orgacon DRY re-dispersible PEDOT:PSS pellets were from Agfa) with concentrations of up to  $30\text{ mg ml}^{-1}$ . The dispersions were prepared by homogenizing at 11,000 rpm for 10 min (Labtek IKA® T25 homogenizer) followed by 1 hr bath sonication (Branson B5500R-DTH). DMF and EtOH were directly added to the formulation and then homogenized at 11,000 rpm for 2 min followed by 10 min bath sonication.

### **2.1.3 Development of An Easy To Produce; An Electrical Conducting Tough Hydrogel**

For making LCGO dispersions in EtOH, 10 ml of the stock aqueous LCGO was poured into a 50 ml centrifuge tube (Nalgene, Thermofisher, USA) to which 20 ml of the EtOH was added and then mixed vigorously by vortex shaking. After centrifugation, 30 ml of the supernatant was extracted, replaced with 30 ml of the EtOH and then mixed vigorously by vortex shaking. This process was repeated 10 times to replace the water with the EtOH. PU/LCGO/PEDOT:PSS composite (PUHC) formulations were prepared as follows: various amount of LCGO dispersion in EtOH were added to a 1:1 mixture of DMF and water. PEDOT:PSS (10 mg ml<sup>-1</sup>) was then added to this mixture. Separately, PU-D3 solution (5 % w/w) was prepared by dissolving PU in a 95:5 mixture of EtOH:water. This PU-D3 solution was added to the LCGO/PEDOT:PSS dispersion in DMF:water. The final concentration of PU in this mixture was 92 % w/w. Subsequently, the mixtures were stirred by a vortex mixer (45 °C for 24 hrs) in a round-bottom flask. Hydrogel films from these formulations were formed via solution casting in glass Petri dishes. Solvents were removed using a vacuum oven (70 °C, -80 Kpa, 12 hrs) to obtain uniform films. After evaporation of solvent mixture, films were rehydrated by adding water on top of the films, allowing them to fully swell and subsequently release from the Petri dish.

## **2.2 Experimental Techniques**

### **2.2.1 Tensile test**

The samples for mechanical testing were prepared by laser cutting films (Versa Laser VLS4.60) into strips of 5 mm wide and 15 mm long. The tensile properties of sample

strips were measured at a constant strain rate of 0.01 mm min<sup>-1</sup>, and tests were performed on at least 7 replicates of each sample. The tensile strength, elongation at break and Young's modulus were reported as the average of all measurements.

### 2.2.2 Electrical conductivity

The electrical conductivity of the samples was measured using both two-point probe and four-point probe methods. The bulk conductivity of the samples was measured by a two-point probe method using a multimeter (Fluke 287 True-RMS). The film was cut into specific dimensions and was fixed on a glass slide. A line of silver paint was then painted at the edges of the film to ensure better contact between the film and the probes. The sheet resistance was then measured by putting the probes on the silver painted edges of the opposite sides. The conductivity was then calculated using the following equation:

$$\rho = R \frac{A}{l} \quad \dots\dots \text{(Equation 2.1)}$$

$$\sigma = \frac{l}{\rho} \quad \dots\dots \text{(Equation 2.2)}$$

Where  $\rho$  is the resistivity ( $\Omega/\square$ ),  $R$  is the resistance ( $\Omega$ ),  $A$  is the cross-sectional area of the specimen ( $\text{cm}^2$ ),  $l$  is the length of the specimen (cm), and  $\sigma$  is the conductivity ( $\text{S cm}^{-1}$ ).

The electrical conductivities of the LCGO and m-LCGO hydrogel films were measured using a four-point probe resistivity measurement system (JG 293015 Jandel) with a linear four-point probe having a 0.65 mm pin distance at ambient temperature. The conductivity values reported here are the averages of 10 consecutive measurements across different locations of each sample with measurements repeated on 3 different samples prepared in the same way.

### **2.2.3 Scanning electron microscopy**

Scanning electron microscopy (SEM) images were taken with a field-emission SEM instrument (JEOL JSM-7500FA). Samples were frozen in liquid nitrogen, fractured and sputter-coated (EDWARDS Auto 306) with a thin layer of gold (12 nm thickness).

#### **2.2.3.1 *Graphene oxide sheets***

SEM analyses were carried out by first depositing LCGO sheets from their dispersions on pre-cleaned and salinized silicon wafer (300 nm SiO<sub>2</sub> layer). Silane solution was prepared by mixing 3-Aminopropyltriethoxysilane (Aldrich) with water (1:9 v/v) and one drop of hydrochloric acid (Sigma–Aldrich). Pre-cut silicon substrates were salinized by immersing in aqueous silane solution for 30 min and then washed thoroughly with Millipore water. LCGO sheets were deposited onto salinized silicon substrates by immersing a silicon substrate into the LCGO dispersion (50 µg ml<sup>-1</sup>) for 5 seconds, then into a second container containing Millipore water for 30 seconds and then air-dried. Prior to SEM analysis, LCGO sheets were observed under an optical microscope to ensure uniform LCGO sheet deposition was achieved. As-deposited LCGO sheets were directly examined by scanning electron microscopy.

### **2.2.4 X-ray diffraction**

X-ray diffraction (XRD) analysis of the LCGO and m-LCGO was conducted using a GBC MMA diffraction instrument (GBC Scientific Equipment Pty Ltd, Australia) with Cu K $\alpha$  radiation ( $\lambda = 0.154$  nm), operating at 40 keV and with a cathode current of 20 mA. The spectra were obtained between angles of 5° and 40° with typical scan speeds of 0.5° min<sup>-1</sup>.



<sup>1</sup> utilised. The sample was prepared through depositing 500µl DMF-dispersed dispersion with 0.5 mg ml<sup>-1</sup> concentration on a quartz substrate followed by evaporating the solvent at room temperature. For m-LCGO and PUHC films and their composites, a 1.5 × 1.5 cm film was mounted on the quartz substrate using ethanol.

### 2.2.5 Raman spectroscopy

Raman and polarized Raman spectra were recorded on a Jobin Yvon Horiba HR800 Raman microscope using a 632 nm laser line and a 300-line grating to achieve a resolution of ± 1.25 cm<sup>-1</sup>/pixel. In the case of polarized Raman mode, samples were fixed on a substrate and a set of reference spectra was recorded, referred to as P0°. Another set of spectra was then recorded after the laser was polarized by 90° and referred to as P90°. The qualitative orientation parameter, P-qualitative, was then derived from their respective Raman intensities at 1426 cm<sup>-1</sup> (relative to the Raman intensity at 1000 cm<sup>-1</sup>) using equation 4 and tests were performed on at least 3 replicates of each sample.

$$P\text{-qualitative} = 1 - (IP90^\circ / IP0^\circ) \quad \dots \quad (\text{Equation 2.3})$$

### 2.2.6 Rheological characterization

Rheological properties of aqueous LCGO, m-LCGO, and PUHC dispersions were investigated in a rheometer (AR-G2 TA Instruments) with a conical shaped spindle (angle: 2°, diameter: 40 mm). Approximately 600 µl of sample dispersions was loaded into the rheometer with great care taken not to shear or stretch the sample. Shear stress and viscosity were measured at shear rates between 0.01 to 10 using logarithmic steps (total 200 points) for two complete (ascending and descending) cycles. Shear rate was kept constant at each point for 2 minutes with the data recorded during the last 15 seconds being reported.

Time sweep oscillation tests were carried out at 25 °C and constant strain and frequency (0.01 and 1 Hz), using the same cone-plate geometry set up. The rheological values reported here are the averages of 5 repeats of each samples prepared in the same way.

### **2.2.7 Preparation of PUHC Printed Scaffolds**

PUHC composites were extrusion printed into scaffold structures using a KIMM SPS1000 bio plotter extrusion printing system (Figure. 2.1), in which the extrusion assembly is mounted on a three-axis stepping system above a level stage for full mechanised control of its XYZ axes via an associated computer system with customised software. Materials are extruded through interchangeable tips with internal diameters of 100-500 µm attached to a pressurised stainless-steel barrel enclosed in a temperature controlled jacket. For extrusion of these composite materials, the barrel temperature was set to 45 °C and the applied pressure varied between 250-500 kpa (120 kpa was applied for fabrication of polyurethane hybrid composite temperature sensor which is discussed in Chapter 5) .

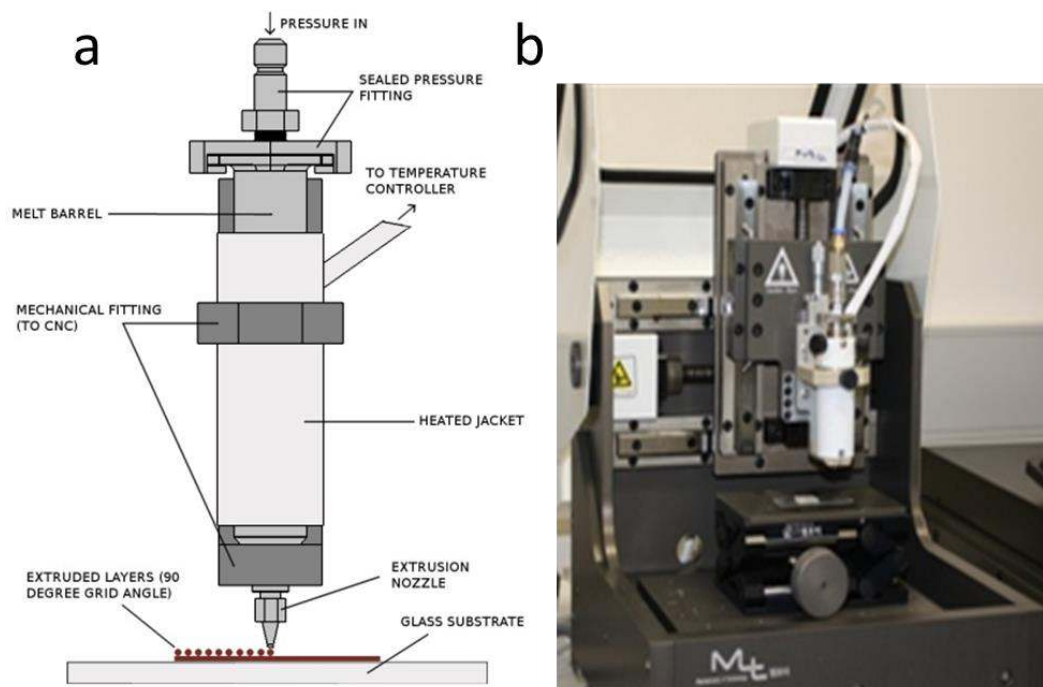


Figure 2.1 a. Schematic of extrusion printing system (by Mr Rhys Cornock – University of Wollongong) and b. KIMM SPS1000 bio plotter extrusion printer.

## **Chapter 3**

# **Ionic Interactions to Tune Mechanical, Electrical and Thermal Properties of Hydrated Liquid Crystal Graphene Oxide Films**

---

This chapter has been adapted from the published article “Mohammad Javadi, Sina Naficy, Stephen Beirne, Sepidar Sayyar, Rouhollah Jalili, and Simon E. Moulton. "Ionic Interactions to Tune Mechanical and Electrical Properties of Hydrated Liquid Crystal Graphene Oxide Films." *Materials Chemistry and Physics* 186 (2017): 90-97.”

The introduction section of this chapter is a modified version compared with the published article to avoid duplication with the comprehensive literature review of Chapter 1.

### 3.1 Introduction

As described in Chapter 1, the development of a flexible biocompatible temperature sensor will require the addition of a conductive filler material to an elastomeric matrix. Graphene has opened new pathways for developing a broad range of novel functional composite materials. [285] Theory suggests that single graphene sheet may have unusually high thermal conductivity, but there is gap of knowledge about thermal conductivity between the adjacent sheets of graphene and impact of oxygen groups on thermal conductivity.[286]

Graphite, a planar structure made of multi-layered graphene sheets, is the main source of processable graphene derivatives such as graphene oxide (GO). GO is a unique, unconventional soft material [287-291], which is one of the most scalable derivatives of graphene (Figure 3.1). It is a monolayer material consisting of a hydrophilic graphenic sheet bearing oxygen functional groups on its basal plane and edges.[292] Through the process of oxidation, different functional groups form on the graphenic sheets, which results in their exfoliation and render the individual sheets dispersible in polar solvents.[293, 294]

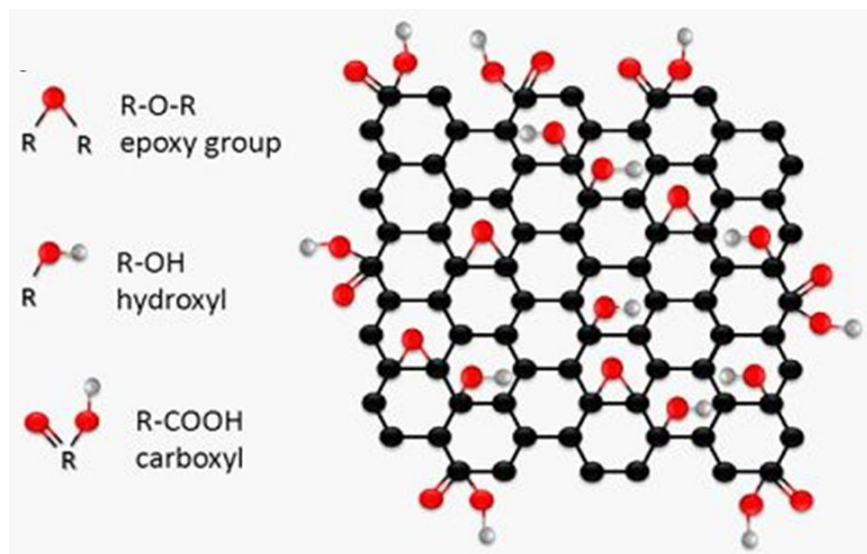


Figure 3.1 Functional groups of GO[295]

It has been discovered that the electrical and thermal properties of graphene strongly depend on its unique structure and morphology. Namely, the size of graphene and its derivatives plays an important role in their electrical and thermal conductivities.[296-300]

The thermal conductivity ( $\kappa$ ) of graphene is dominated by phonon transport, namely diffusive conduction at high temperature and ballistic conduction at sufficiently low temperature.[302] Large GO sheets exhibit fascinating properties, such as the ability to form liquid crystalline dispersions, known as Liquid Crystalline Graphene Oxide (LCGO). Liquid crystal (LC) could be defined as a “mesomorphic ordered state of anisotropic particles that bears liquid-like fluidity as well as crystal-like ordering”.[301] Within current research, LCGO is viewed as a promising component for advanced conductive devices.

LCGO dispersions can improve the processability and induce order in the resulting composite materials at atomic levels [303, 304] and can be used to construct high strength, highly conducting, self-assembled layer-by-layer composites after reduction[305], and to

make the high surface area in sensor applications.[306, 307] By reducing graphene oxide, oxidized functional groups are removed, to obtain a graphene material. The ability to produce LCGO in large scale and fabricate it into various functional structures, in a cost-effective manner, is crucial for enabling realisation of its potential applications.[308, 309] In this regard, LCGO obtained by chemical exfoliation of natural graphite has a great potential for use as a filler material in thermistor based temperature sensing applications. The properties of LCGO dispersion permits using scalable techniques.[310] However, the development of large-area graphene-based free-standing films using LCGO or GO with high mechanical properties, flexibility, stability (in water and another organic solvent), and conductivity, is still an ongoing challenge.

The development of free-standing (FS) films based on GO and/or LCGO have been achieved using a variety of techniques such as solvent-casting and filtration.[311] Utilizing these one-step fabrication approaches to make FS films is very appealing due to their low processing cost, and has potential for bulk production of graphene films for numerous applications. Although a variety of substrates such as indium tin oxide (ITO), polyethylene terephthalate (PET), glass slide, and thin copper films have been used to develop FS-GO films, none of them resulted in a film with appropriate mechanical properties, especially when in a wet environment.[312] Furthermore, films made of large-sized graphene sheets break easily during transfer from the casting substrate onto the target substrate via lift-off techniques.[313] Hence, there are still critical needs for simple, environmentally friendly, and cost-effective approaches that are scalable for the preparation of bulk quantities of high fidelity FS-LCGO films with robust mechanical performance.

Hydrated GO films made by filtration of GO dispersions have been reported.[314] Whilst there are published reports on the chemical interaction of divalent cations on GO paper, little investigation has been undertaken to study the effect of mono and divalent salts on the mechanical and electrical properties of FS GO-based structures in their hydrated state. This chapter describes the gelation behaviour of LCGO dispersion with significant enhancements in the mechanical properties and electrical conductivity of resulting FS-LCGO films upon modification with low quantities of the chloride salt of monovalent alkali metals ( $\text{Na}^+$ ,  $\text{K}^+$ ) and divalent alkaline earth metals ( $\text{Mg}^{2+}$  and  $\text{Ca}^{2+}$ ). Salt treated LCGO dispersions and films are referred to as m-LCGO, where LCGO represents liquid crystal graphene oxide and m is to highlight modification by chloride salts. These observations can be described in terms of the interactions between the functional groups of the LCGO sheets and the metals ions [315] and also could be interpreted by the salts physical properties such as ions size and the valency of positive charge of the cations, ratio of charge and cations size and/or hygroscopic nature that influences the ability to take up and retain moisture. [316-319]



## 3.2 Experimental

### 3.2.1 Synthesis of modified liquid crystal graphene oxide (m-LCGO)

m-LCGO hydrogel films were prepared by adding required amounts of salt solution (e.g., NaCl, KCl, MgCl<sub>2</sub> or CaCl<sub>2</sub>) to 15 ml of the LCGO aqueous dispersion (7.1 mg ml<sup>-1</sup>). Milli-Q water was added where required to maintain the final concentration of LCGO at 3 mg ml<sup>-1</sup>, while the salt concentration ranged from 0.001 mM to 2 M. As a priority of this study was making of free stand film of LCGO via modified LCGO with chloride salts, the ability to peel off the m-LCGO film was an important property for choosing the salt concentration for this investigation. All of the m-LCGO prepared with a salt concentration  $\geq 0.08\text{mM}$  provide the ability to remove the m-LCGO film. The mixtures were stirred by a vortex mixer for 2 min and then directly used to form films using a doctor blade device (K-CONTROL-COATER-System K 303, Model 625) (Figure 3.2).

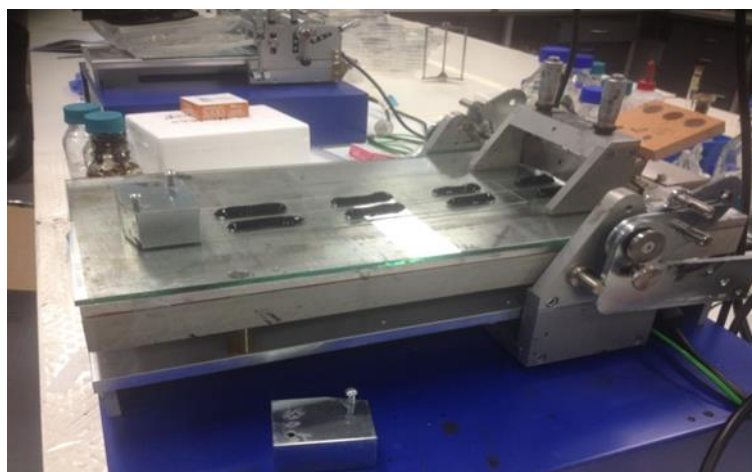


Figure 3.2 Doctor blade used for making the LCGO film and m-LCGO.

The films were formed on ITO substrates at a coating speed rate of 0.5 m min<sup>-1</sup> at RT then dried in an oven for 10 hrs at 50 °C. Unmodified LCGO films were prepared as

controls following the same procedure as above without inclusion of the salts. In the control specimens, Milli-Q water was used instead of the salt solution to obtain the same LCGO concentration in final dispersions ( $3 \text{ mg ml}^{-1}$ ). To remove the m-LCGO hydrogel films and LCGO films from their substrate, samples were placed in Milli-Q water for 1 hr then carefully peeled off from the substrate surface.

### **3.2.2 Characterization of LCGO and m-LCGO dispersions and films**

Zeta potential measurements were performed on LCGO and m-LCGO dispersions with a Malvern Zeta sizer Nano series instrument. The electrical conductivity of the LCGO and m-LCGO hydrogel films was measured using a four-point probe resistivity measurement system (JG 293015 Jandel) at ambient temperature. The conductivity values reported here are the averages of 10 consecutive measurements across different locations of each sample with measurements repeated on 3 different samples prepared in the same way.

## **3.3 Results and Discussion**

### **3.3.1 m-LCGO Dispersions and Rheology**

The aqueous LCGO dispersion used here contained large GO sheets with a lateral size as large as  $10 \text{ }\mu\text{m}$  (Figure 3.3a). Rheological tests performed on the LCGO and m-LCGO dispersions revealed a power-law pattern for viscosity as a function of shear rate (Figure 3.3b). This is in agreement with previous reports [320] showing a non-Newtonian behaviour for LCGO dispersions. The viscosity of m-LCGO dispersions was found to increase dramatically against salt concentration until a peak was reached, followed by a gradual decrease as more salt was added (Table 3.1). For all salt concentrations

considered here, however, the viscosity of m-LCGO dispersions remained higher than that of LCGO.

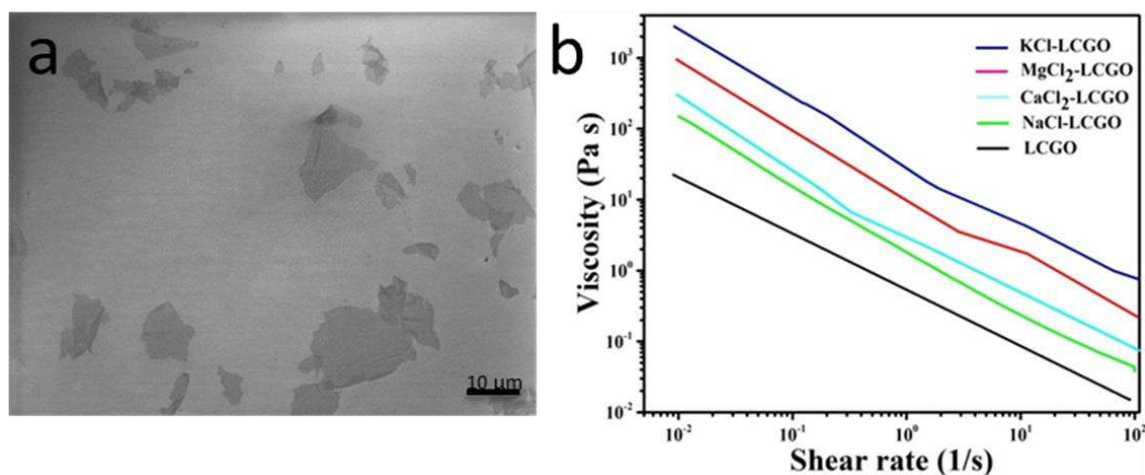


Figure 3.3 (a) Scanning electron microscopy (SEM) image of large GO sheets obtained from the LCGO dispersion used in this work. The scale bar is 10 μm. (b) Examples of viscosity curve of LCGO and m-LCGO (0.08 mM) dispersions as a function of shear rate.

The increase in viscosity observed upon addition of salts is indicative of an interaction between ionic species and charged LCGO sheets. Considering that LCGO sheets are negatively charged, cations can directly interact with them, establishing ionic bonds.[321, 322] These bonds allow the formation of the network facilitating the formation of free-standing films. Furthermore, ionic bonds between an adjacent sheet of GO potentially could increase thermal diffusivity via the photonic mechanism.[323]

Table 3. 1 Viscosity (Pa s) of m-LCGO dispersions as a function of salt concentration ( $\dot{\gamma} = 100 \text{ s}^{-1}$ ).

Salt Concentration (mM)	KCl-LCGO	NaCl-LCGO	CaCl <sub>2</sub> -LCGO	MgCl <sub>2</sub> -LCGO
0	0.021 <sup>a)</sup>	0.021 <sup>a)</sup>	0.021 <sup>a)</sup>	0.021 <sup>a)</sup>
0.001	0.91	0.034	0.052	0.12
0.005	5.84	0.23	0.37	1.26
0.01	8.21	0.73	0.64	3.50
0.08	6.87	0.67	0.86	3.79
500	3.25	0.56	0.45	1.84
1000	0.64	0.41	0.23	0.32
2000	0.21	0.23	0.18	0.16

<sup>a)</sup> These values are for the LCGO dispersion.

There appears to be an optimal salt concentration at which maximum viscosity was achieved (approximately 0.08 mM). The addition of ions alters the ionic strength of the sheets surrounding, reducing the repulsive electrostatic force between negatively charged sheets. This process results in destabilization of dispersions. The viscosity of the graphene oxide dispersions modified with the salt changes in response to this destabilization due to two phenomena. Namely, i) a quasi-network begins to form through van der Waals interactions between nanosheets [311] and ii) as destabilisation progresses the suspension will eventually break down into larger solid gels (as was observed experimentally in this research). The first phenomenon leads to an increase in viscosity and storage modulus while the second part results in a reduction in viscosity and storage modulus. LCGO

treated with salt concentration  $\leq 0.01$  mM were not able to provide free standing films, so salt concentration 0.08 mM was chosen as an optimum point for further investigation.

### 3.3.2 m-LCGO dispersions, storage modulus ( $G'$ ) and loss modulus ( $G''$ )

At this optimum salt concentration of 0.08 mM, the structural integrity of the m-LCGO dispersions was found to be time-dependent and controlled by the type of added salt. To monitor the gel formation in the m-LCGO dispersions, storage modulus ( $G'$ ) and loss modulus ( $G''$ ) were determined as a function of time at a constant strain (0.01) and frequency (1 Hz), immediately after salts were added to the LCGO dispersion (Figure 3.4). Interestingly, regardless of the type of salt, the storage modulus (Figure 3.4a) of m-LCGO dispersions was considerably higher than that of LCGO (200-1200 Pa vs. 40 Pa). The dominance of  $G'$  means that the ink behaves like a fluid with insufficient  $G''$  to hold the shape of the printed ink. The increase in storage modulus makes m-LCGO more printable. Furthermore, while the storage modulus of LCGO dispersion remained constant over time, a gradual increase in storage modulus was observed for all m-LCGO dispersions. This indicates an immediate network formation in m-LCGO dispersions, followed by continuous network development over time. Overall, KCl had the most profound effect on  $G'$  and  $G''$ , followed by  $MgCl_2$ ,  $CaCl_2$  and NaCl. This trend is similar to the viscosity trend against shear rate (Figure 3.4b).

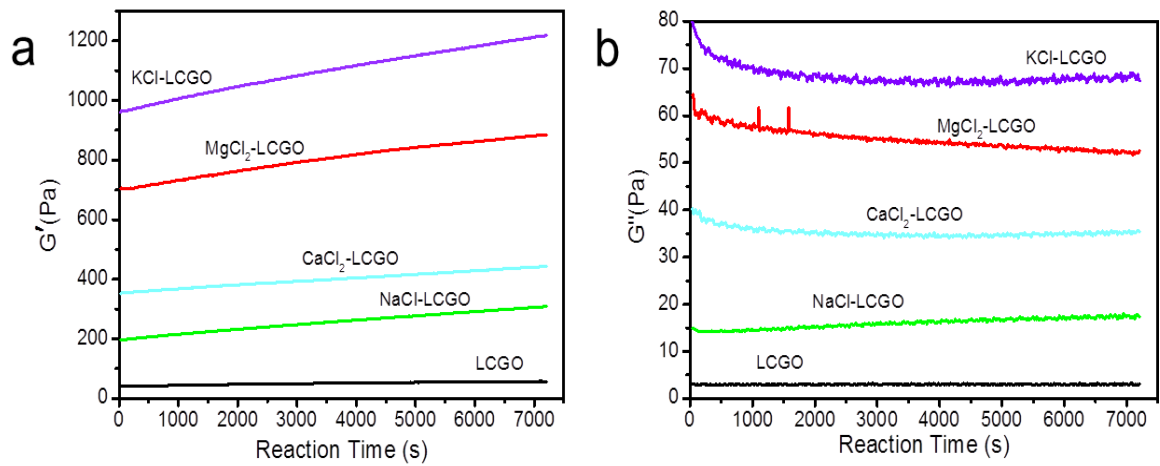


Figure 3.4 Effect of salts on (a) the storage modulus and (b) loss modulus of LCGO and m-LCGO dispersions as a function of interaction time at constant strain (0.01) and frequency (1 Hz). The salt concentration was fixed at 0.08 mM.

### 3.3.3 Stability of m-LCGO dispersion

It is believed that the LCGO sheets form a stable colloidal suspension as long as the electrostatic repulsion between LCGO sheets, resulting from their ionized functional groups, prevents their aggregation in an aqueous medium. The zeta potential is an important factor for characterizing the charged layer around the colloid particle.[324] Particles with zeta potentials more positive than +30 mV or more negative than -30 mV are considered to form stable dispersions due to interparticle electrostatic repulsion [325]. As shown in Figure 3.5, the zeta potential ( $\zeta$ ) of m-LCGO dispersions was very sensitive to the nature of the added salt. Based on these observations, the LCGO sheets form stable dispersions where  $\zeta$  was -34.3 mV. The zeta potential of m-LCGO dispersion treated with KCl showed a slight decrease to -36.2 mV, while the addition of other salts had a more destabilizing effect on the dispersion as indicated by an increase in the zeta potential.

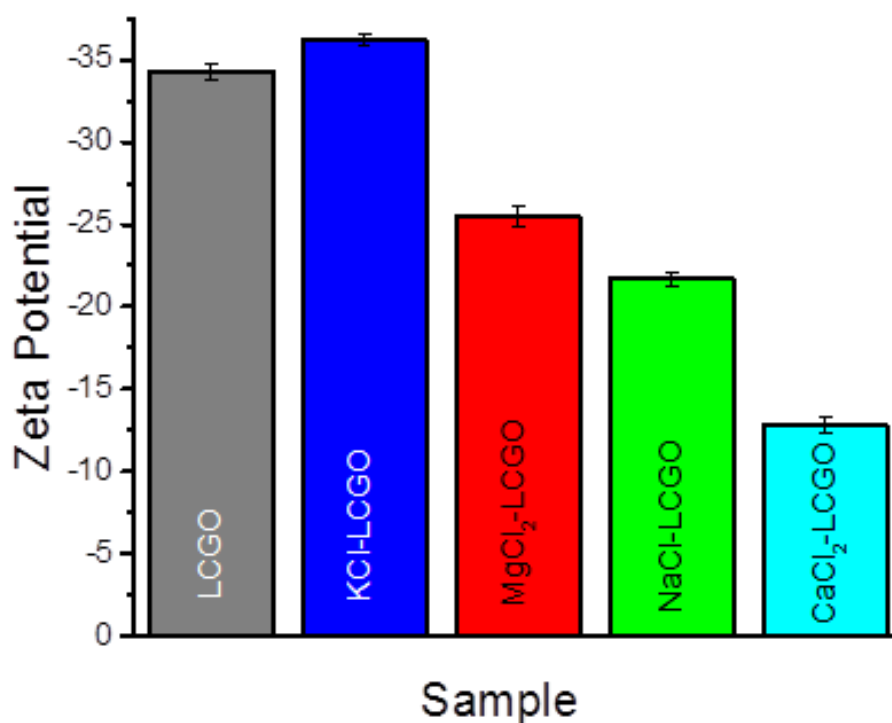


Figure 3.5 Zeta potential of LCGO and m-LCGO dispersions, 5 min after treatment. The salt concentration was fixed at 0.08 mM.

The effect of salts on destabilization of LCGO dispersion was also evident from the phase separation and precipitation of LCGO from dispersions modified with NaCl, CaCl<sub>2</sub> and MgCl<sub>2</sub> salts over the course of one week, while LCGO and m-LCGO dispersion treated with KCl remained fully dispersed after 3 months. The trend observed in the destabilizing effect of MgCl<sub>2</sub>, NaCl, and CaCl<sub>2</sub> confirms the trend observed in the rheological characterization of m-LCGO dispersions. As discussed above, the destabilization of m-LCGO dispersions will result in a change in dispersions viscosity and viscoelasticity due to two competing factors. As observed here and reported elsewhere, the screening effect of NaCl is larger than KCl [326], while it is larger for CaCl<sub>2</sub> than MgCl<sub>2</sub>. [327] Consequently, the m-LCGO dispersions modified with CaCl<sub>2</sub> or NaCl form mechanically

isolated gel particles (crashing out), which results in a decrease in viscosity and storage modulus. In contrast, the m-LCGO dispersions modified with KCl or  $\text{MgCl}_2$  remain in the quasi-network phase exhibiting a higher viscosity and storage modulus.

### 3.3.4 Morphology of m-LCGO Films

The m-LCGO films prepared by casting of dispersions treated with a low concentration of salt (0.08 mM), dispersions showing clear and non-agglomerated (Figure 3.6), had a multilayered microstructure as shown in Figure 3.7.

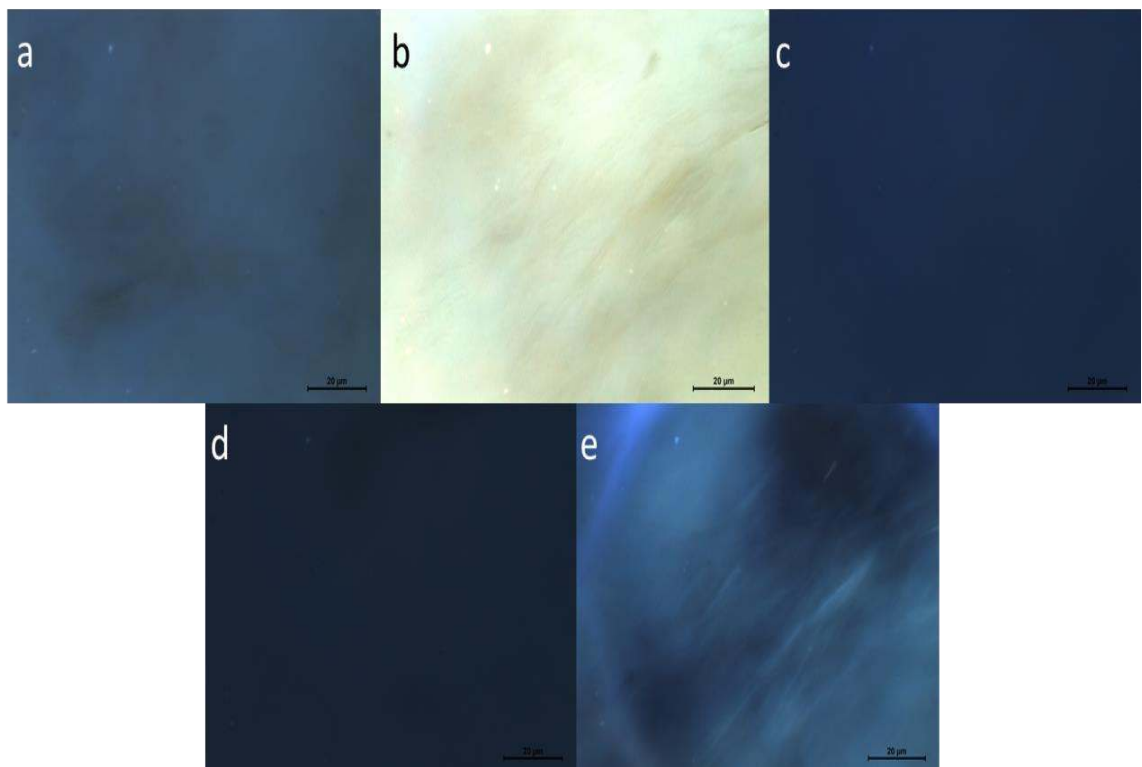


Figure 3.6 Representative optical microscopy images of modified-LCGO a-d dispersions showing clear and non-agglomerated dispersions. b) LCGO, c)  $\text{MgCl}_2$ , b) NaCl, c) KCl and d)  $\text{CaCl}_2$  and polarized optical microscopy image (e) of an LCGO dispersion. The salt concentration was fixed at 0.08 mM.



On the other hand, SEM images of m-LCGO films made from dispersions treated with high concentration (2 mM) of salt revealed salt crystals are separating layers of LCGO sheets (Figure 3.7f).

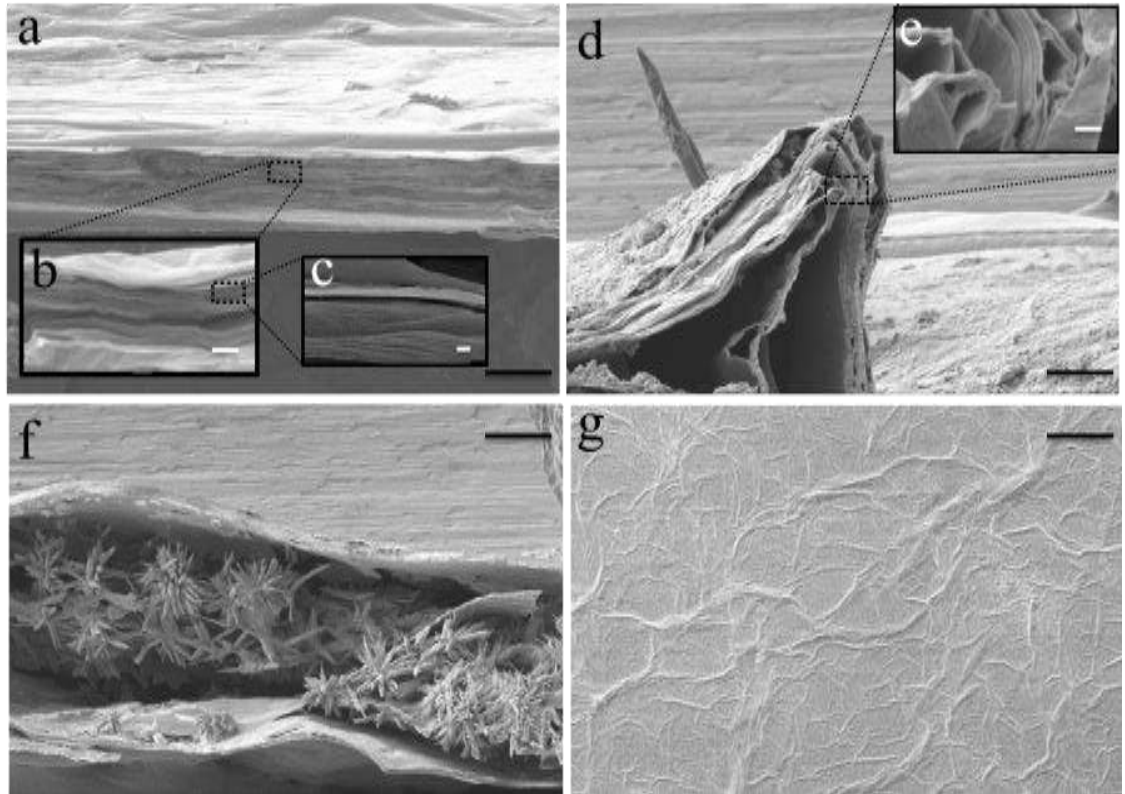


Figure 3.7 Low and high-resolution SEM images of m-LCGO, cross-section, modified by  $\text{CaCl}_2$ , at a concentration of 0.08 mM (a-e), and 2 M (f). The SEM image, cross-section, in (f) clearly shows the formation of salt crystals within the film structure that potentially deteriorates the mechanical property. (g) SEM image of the surface of a  $\text{CaCl}_2$ -LCGO film shows no agglomeration in the m-LCGO free standing films. The scale bars are 10  $\mu\text{m}$  in panels (a), (d), (g) and (f), 100 nm in panel (c) and 1  $\mu\text{m}$  in panels (b) and (e). The salt concentration was fixed at 0.08 mM.

The addition of higher concentrations of salts also resulted into a dramatic loss of mechanical properties. Considering the adverse effect of salt concentration on the

integrity of m-LCGO films along with the observed peak in viscosity of m-LCGO dispersions at a concentration less than 0.08 mM, m-LCGO films were prepared from dispersions with 0.08 mM salt concentration.

### **3.3.5 Raman Spectra of m-LCGO and LCGO**

Figure 3.8 shows the Raman spectra of LCGO and hydrated m-LCGO films containing 9.65-26.3% water (Figure 3.14). The spectra showed the existence of the D-band and the G-band for LCGO and m-LCGO films. The down-shift of D and G bands to the lower wavenumbers in GO indicates an increase in  $sp^2$  carbon-carbon bonds in the structure. For the LCGO film, the G-band was located at  $1609\text{ cm}^{-1}$ , while for the m-LCGO films the G-band shifted to lower values between  $1606\text{ cm}^{-1}$  and  $1595\text{ cm}^{-1}$ , depending on the modifying salt. The location of the D-band also decreased from  $1337\text{ cm}^{-1}$  for LCGO films to  $1333\text{ cm}^{-1}$  for m-LCGO films.

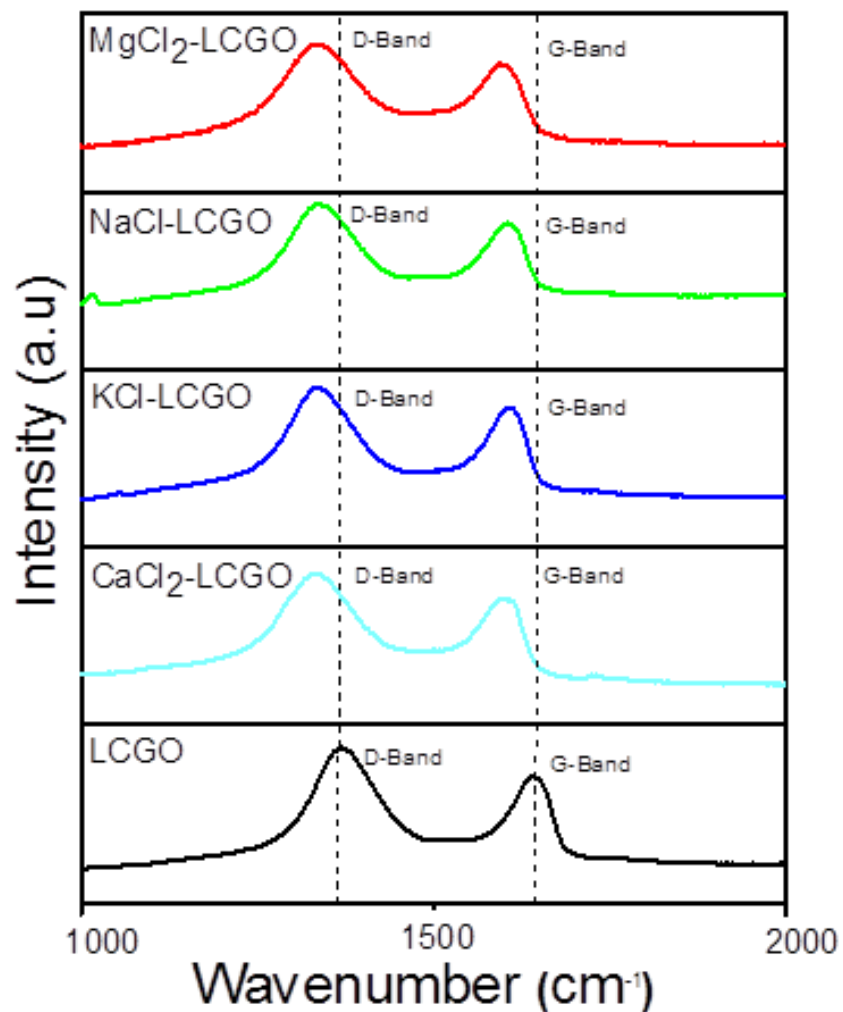


Figure 3.8 Raman characterization of LCGO and m-LCGO films at a concentration of 0.08 mM, where m-LCGO films were treated with different salts as indicated. The broken lines indicate the location of D-band and G-band in LCGO film. The salt concentration was fixed at 0.08 mM.

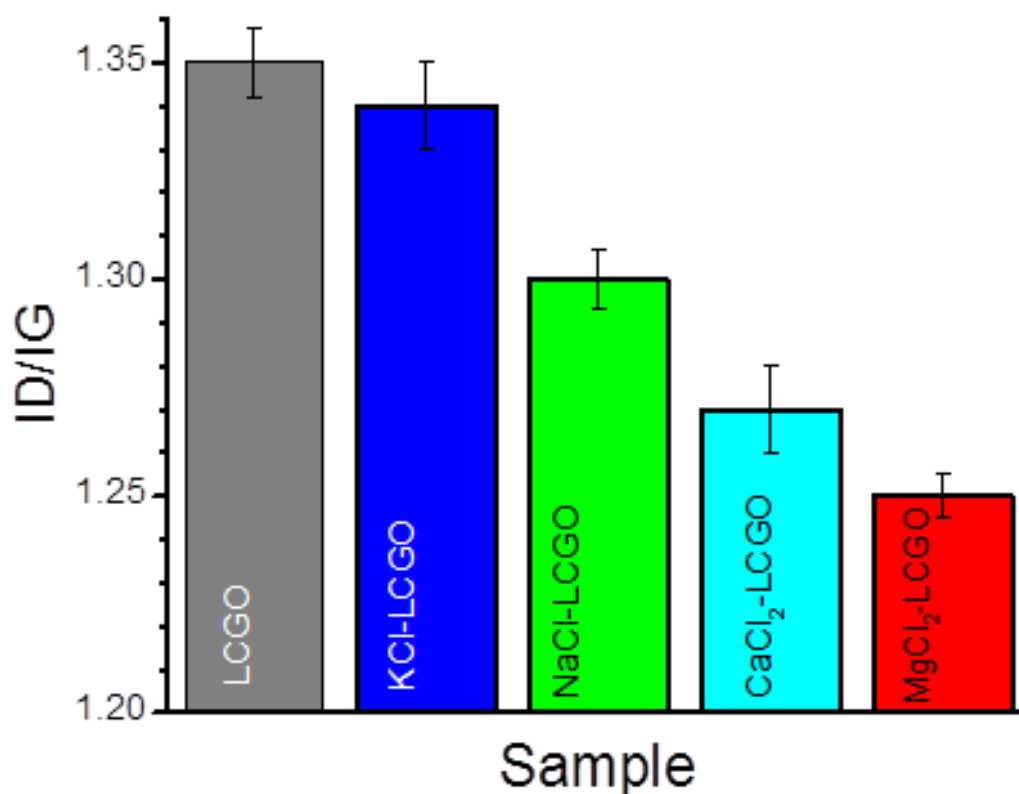


Figure 3.9 The ID/IG ratio obtained from Raman spectroscopy for LCGO and m-LCGO films at a concentration of 0.08 mM.

Depending on the salt, the intensity ratio of the D-band to the G-band ( $I_D/I_G$ ) reduced when LCGO was treated, as shown in Figure 3.9. This reduction in  $I_D/I_G$  indicates that graphenic sheets within the LCGO are more ordered after modification by salt [328, 329], and based on Raman spectra; some of the  $sp^2$  bonds have been restored.[330-332] The observed decrease in  $I_D/I_G$  was more pronounced in the case of divalent salts ( $CaCl_2$  and  $MgCl_2$ ) than the monovalent salts ( $NaCl$  and  $KCl$ ). Downshift of D-and G-bands can be caused by various reasons. As the only difference between the control sample and M-LCGO films was treatment via chloride salts, so it's logical acceptable that difference between the  $sp^2$  carbon-carbon bonds in the m-LCGO structures were because of the ionic interaction with LCGO functional groups not because of the other reason.

### 3.3.6 X-ray diffraction of m-LCGO

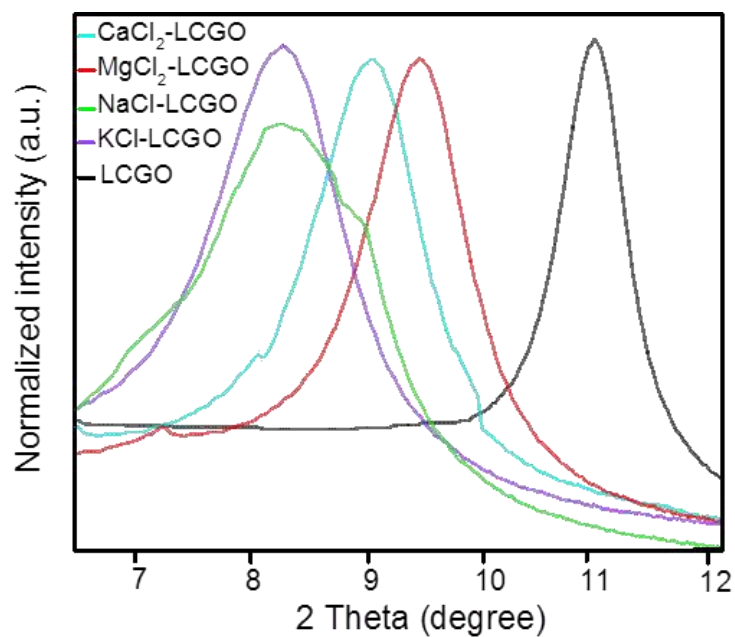


Figure 3.10 X-ray diffraction (XRD) patterns of hydrated m-LCGO films prepared from 0.08mM salt solutions compared with LCGO.

Table 3.2 The *d*-spacing of GO sheets in LCGO and hydrated m-LCGO films obtained from XRD spectra. The salt concentration was fixed at 0.08 mM.

Sample	LCGO	KCl-LCGO	NaCl-LCGO	CaCl <sub>2</sub> -LCGO	MgCl <sub>2</sub> -LCGO
Cation species ionic diameter (pm)		152	116	114	86

<i>d</i> -spacing (nm)	0.76	1.06	1.07	0.98	0.96
------------------------	------	------	------	------	------

---

The X-ray diffraction (XRD) patterns of the hydrated m-LCGO films showed a shift of the  $2\theta$  peak to the lower values (Figure 3.10) compared to LCGO which indicates an increase in layer-to-layer distance (*d*-spacing) of the LCGO sheets within the samples. Also, the *d*-spacing seems to broaden in the presence of added salts. While the XRD peak of the LCGO film showed a *d*-spacing peak of 0.76 nm, a considerable shift to higher *d*-spacing values was observed in m-LCGO films, correlating with the ionic size of cationic species. The sodium and potassium cations have an ionic diameter of approximately 116 pm and 152 pm, respectively, while magnesium has an ionic radius of 86 pm and calcium's ionic radius is 114 pm. The correlation between the size of cationic species and *d*-spacing is highlighted in Table 3.2, where m-LCGO films treated with NaCl and KCl had a *d*-spacing of 1.06 nm and 1.07 nm, respectively, followed by CaCl<sub>2</sub> (0.98 nm) and MgCl<sub>2</sub> (0.96 nm). The observed increase in *d*-spacing indicates the intercalation of these cationic alkali and alkaline earth metals with LCGO sheets basal planes. However, it is important to note that this increase in *d*-spacing is considerably larger than the size of individual cationic species, suggesting the LCGO sheets are not simply stacked up by cations. Instead, the LCGO sheets are likely to remain solvated, separated by a large amount of water.[333]

### 3.3.7 Mechanical properties of m-LCGO

The typical stress-strain curves for LCGO and hydrated m-LCGO films are presented in Figure 3.11. Since the LCGO films were not stable in the wet state, mechanical tests were

performed on dry LCGO films. All hydrated m-LCGO films were tested at their fully swollen state. Regardless of the salt used to treat the corresponding m-LCGO dispersions, considerable enhancement was observed in the films Young's modulus, tensile strength and elongation at break (Table 3.3) compared to the untreated LCGO films. The average Young's modulus, tensile strength, and elongation at break of dry LCGO film was  $6.2 \pm 0.9$  GPa,  $84.3 \pm 3.4$  MPa and  $2.5 \pm 0.21$  %, respectively.

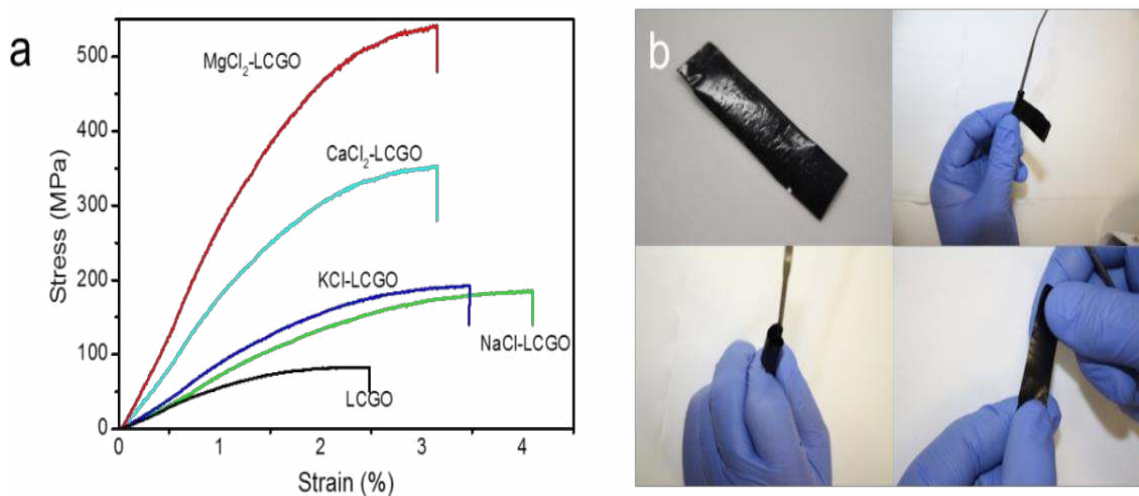


Figure 3.11 (a) Stress-strain curves of the LCGO film and hydrated m-LCGO films formed from the salt treated dispersions (0.08 mM). (b) Photos show the flexibility and durability of a hydrated m-LCGO film modified with CaCl<sub>2</sub> (0.08 mM).

The m-LCGO films treated with MgCl<sub>2</sub> exhibited the highest Young's modulus (32.7 GPa) and tensile strength (547.2 MPa), followed by m-LCGO films treated with CaCl<sub>2</sub> (23.6 GPa and 354.4 MPa, respectively). The m-LCGO films treated with KCl and NaCl performed lower than the divalent salts but still exhibited at least a two-fold improvement in Young's modulus and tensile strength compared to the LCGO film. Compared to other GO or reduced GO-based systems reported in the literature, the hydrated m-LCGO films developed here exhibited considerable mechanical enhancement (Table 3.3). On the other

hand, dried LCGO film prepared from untreated LCGO dispersion performed similarly to GO films and fibres described by others.

Table 3.3 Mechanical properties of LCGO film and hydrated m-LCGO films compared with data from the literature.

Sample	Young's modulus (GPa)	Tensile strength (MPa)	Elongation at break (%)	Reference
LCGO film (dry)	$6.2 \pm 0.9$	$84.3 \pm 3.4$	$2.5 \pm 0.21$	This thesis
KCl-LCGO film (hydrated)	$11.4 \pm 2.2$	$195.5 \pm 17.4$	$3.5 \pm 0.12$	This thesis
NaCl-LCGO film (hydrated)	$10.0 \pm 2.1$	$187.3 \pm 20.4$	$4.1 \pm 0.52$	This thesis
CaCl <sub>2</sub> -LCGO film (hydrated)	$23.6 \pm 1.4$	$354.4 \pm 19.5$	$3.1 \pm 0.28$	This thesis
MgCl <sub>2</sub> -LCGO film (hydrated)	$32.7 \pm 2.7$	$547.2 \pm 32.8$	$3.2 \pm 0.35$	This thesis
Treated GO film	~28	~65-140	~0.30-0.50	[25]
GO film	36	~ 117	~ 0.43	[334]
GO film	~ 14.83	~ 178	~ 0.47	[335]
GO fibre	5.4	102	6.3	[336]
rGO film (heated at 220 °C)	42	300	0.8	[337]



Reduced giant GO +divalent ions cross- linking	11.2	501.5	6.7%	[338]
Reduced giant GO	12.8 ± 0.8	360.1 ± 12.7	~2.5%	[339]

The interaction between alkali metals and alkaline earth metals with LCGO sheets can occur at different levels. The key to understanding the mechanical properties of hydrated m-LCGO films lies in examining the collective behaviour of stacked platelets along with the interlayer water molecules. The individual LCGO sheets can be interlinked via a non-uniform network of ionic bonds mediated by cationic species and polar and charged groups on the LCGO edges and surface.

The observed trend in Figure 3.11a, in which mechanical properties of hydrated m-LCGO films increase differently with various salts, correlates well with the charge density of cations in the system, where  $KCl < NaCl < CaCl_2 < MgCl_2$ . This indicates that the ionic interaction between charged cations and LCGO's functional groups play an important role in the enhancement of the mechanical properties of hydrated m-LCGO films. Given the expected chemical functionalities that are present on LCGO sheets, two modes of interactions for cations with the LCGO sheets in m-LCGO samples are possible: i) bridging the edges of the sheets through carboxylate chelates to the cation; ii) intercalating between the basal planes and cations through weak alkoxide, carbonyl and hydroxyl groups [25]. Moreover, changes in the mechanical properties of the hydrated m-LCGO film are also linked to the attendance of water molecules in the space between GO sheets which enhance the mechanical properties through hydrogen bonding to the functional groups on adjacent sheets in the film structure (Figure 3.11 and Figure 3.12).[340]

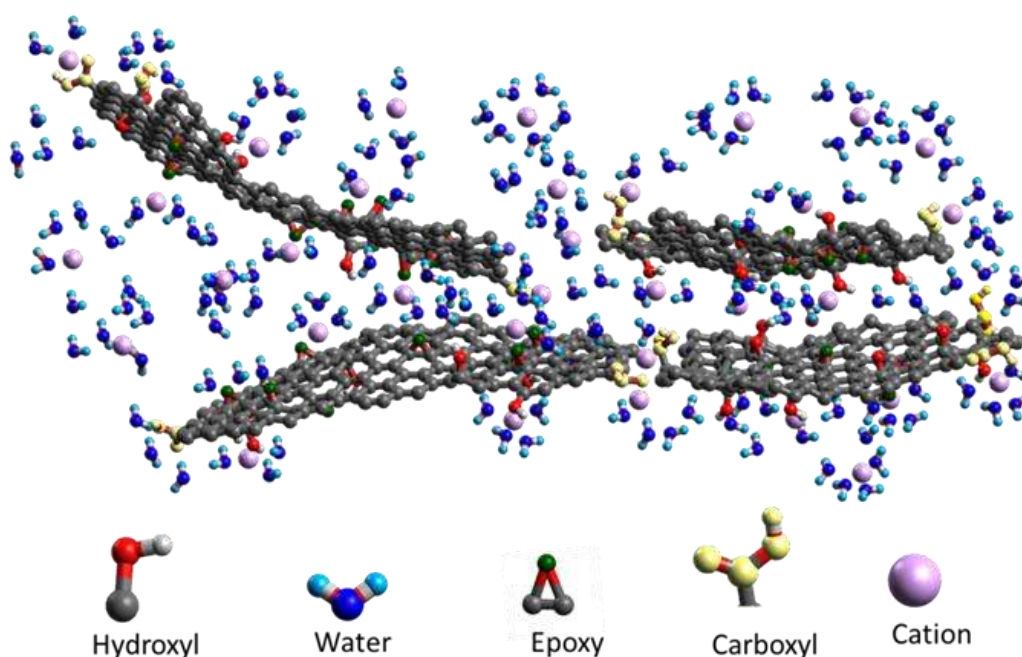


Figure 3.12 Schematic model of the interaction between LCGO sheets and cations ( $\text{Mg}^{2+}$ ,  $\text{Ca}^{2+}$ ,  $\text{K}^+$ , and  $\text{Na}^+$ ) in the presence of water.[341] Anionic counter ions are not shown here for clarity.

The XRD data (Figure 3.10 and Table 3.2) shows that the  $d$ -spacing between LCGO sheets had increased when salt was added to the system. The ionic interaction between cations and functionalized groups of LCGO may be mainly through the edges and parts of the basal planes of two adjacent LCGO sheets which are close enough for ionic interactions, while the majority of spacing between LCGO sheets is filled with water molecules. Thus, in addition to ionic interaction, hydrogen bonding between the water molecules filling the space between LCGO sheets and the oxygen-containing functional groups of LCGO can contribute to the observed increase in mechanical properties of salt treated m-LCGO films.[47] This is particularly true for monovalent cations. The importance of water in the observed mechanical enhancement of hydrated m-LCGO films was highlighted when fully dried m-LCGO films (120 °C, 10 hrs) demonstrated poor

mechanical properties similar to those of dry LCGO films. It was also observed that the dry m-LCGO films were able to absorb water from ambient air and regain their enhanced mechanical performance, due to the hygroscopic nature of added salts (Figure 3.11b).

### 3.3.8 Electrical property of m-LCGO

The ability of m-LCGO in absorbing water from the environment not only contributed to the mechanical improvement of hydrated m-LCGO films but also assisted the enhancement of their conductivity. Table 3.4 lists the surface resistivity of LCGO and m-LCGO films directly after drying at 50 °C for 10 hrs, along with the surface resistivity of the same films after being stored under laboratory conditions for 5, 24, 72 and 120 hrs, respectively. For measurements taken immediately after drying process, the surface resistivity of all salt-treated films was lower than that of the LCGO film, while CaCl<sub>2</sub> and MgCl<sub>2</sub> had the most significant effect on reducing the resistivity up to, 3 and 1 order of magnitude, respectively. This can be due to restoring of the  $\pi$ -conjugated bonds from LCGO sheets upon reduction in the presence of cations.[209] Interestingly, the resistivity of m-LCGO samples continued to decrease until no further change in resistivity was detected. This time-dependent reduction in surface resistivity was more profound for MgCl<sub>2</sub> and CaCl<sub>2</sub>, followed by NaCl and KCl.

Table 3.4 Surface electrical resistance ( $K\Omega m^{-2}$ ) of LCGO and m-LCGO films after drying and then over 120 hrs.

Sample	LCGO	KCl- LCGO	NaCl- LCGO	CaCl <sub>2</sub> - LCGO	MgCl <sub>2</sub> - LCGO
Dry					
50 °C for 10 hrs	2050	1240	984	1.8	124
After drying in laboratory condition					
5 hrs	2050	1210	970	0.58	73
24 hrs	2050	1200	932	0.53	32
72 hrs	2050	1210	810	0.52	32
120 hrs	2050	1210	790	0.52	31

This trend is similar to the hygroscopic behaviour of these salts (Figure 3.13). The hygroscopic nature of the salts could result in water absorption until equilibrium was reached and thus improved ionic mobility within the sample.

### 3.3.9 Thermal conductivity of m-LCGO

There are many factors affecting the thermal conductivity of graphene filler in the composite. For example, the defect on graphene, the graphene loading, the orientation of graphene sheets in the composite and the surface modification, etc.[342] Raman results in Figure 3.8 showed the down-shift of D and G bands to the lower wavenumbers in m-LCGO and that indicates an increase in  $sp^2$  carbon-carbon bonds in the structure and increase in degree of crystallinity. It is expressing more order in graphite crystallinity and

higher crystallinity causes an increase in thermal conductivity. Figure 3.13 showed the impact of ionic salts treatment on LCGO. The thermal conductivity of all m-LCGO show significant increase in comparison with LCGO.

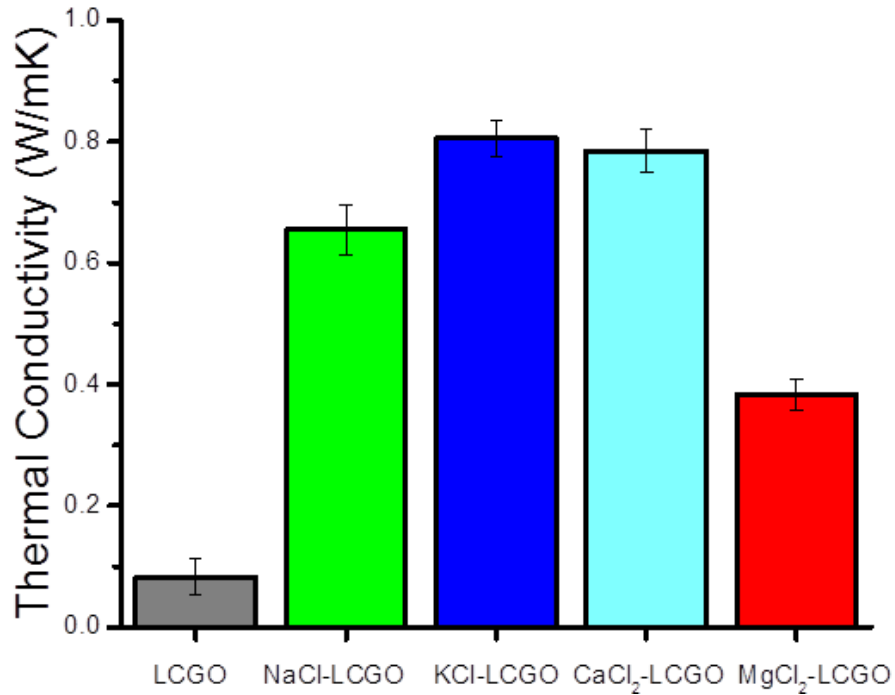


Figure 3.13 Thermal conductivity of m-LCGO compared with LCGO. The salt concentration was fixed at 0.08 mM and samples radius were 6.4 mm and thickness of  $100\pm 12$   $\mu\text{m}$ .

### 3.3.10 Comprising Hygroscopicity

Critical relative humidity (CRH) of salt is an index for comparing hygroscopic property at the relative humidity of the surroundings at which the material begins to absorb moisture. From Table 3.4 it is clear that the NaCl, CaCl<sub>2</sub> and MgCl<sub>2</sub> salts decrease the resistivity, with the alkaline earth metal demonstrating the greatest decrease. This

variation in the extent of resistivity decrease can be attributed to the extent of each salt's hygroscopic nature. (Figure 3.14)

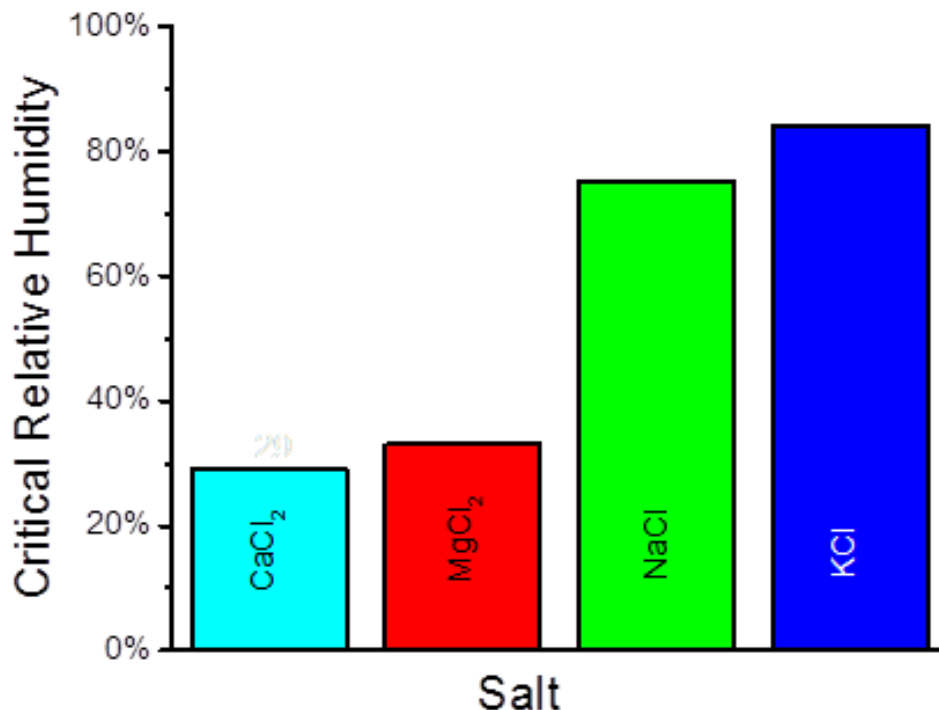


Figure 3.14 Hygroscopic nature of salts tested in this study.

The positive impact of adding chloride salts to the LCGO dispersion on the mechanical properties and electrical conductivity of the resulting m-LCGO films presents a simple method to utilize GO-based structures when the mechanical performance is important in the presence of water. The enhancement observed in the mechanical properties of the hydrated m-LCGO films, especially in their strength and elongation at break, guarantees their flexibility and stability water. Furthermore, the hygroscopic nature of the salts in the film structure leads to absorption of water from the environment. This absorbed water is sufficient enough to keep the m-LCGO films fully hydrated outside of water, with hydrated m-LCGO films retaining their enhanced mechanical performance. The

sensitivity of conductivity of m-LCGO films to environmental humidity can also be useful in sensory applications and electronic applications.

### 3.3.11 Water Content

To measure the water content (Equation 3.1) of the LCGO and m-LCGO hydrated films, the samples were dried to a constant weight in a vacuum at 60 °C (Figure 3.15). The water content was calculated as follows:

$$\text{Water content\%} = (W_0 - W)/W_0 \times 100\% \quad (\text{Equation 3.1})$$

Where  $W_0$  and  $W$  are the weight of the films before and after drying respectively.

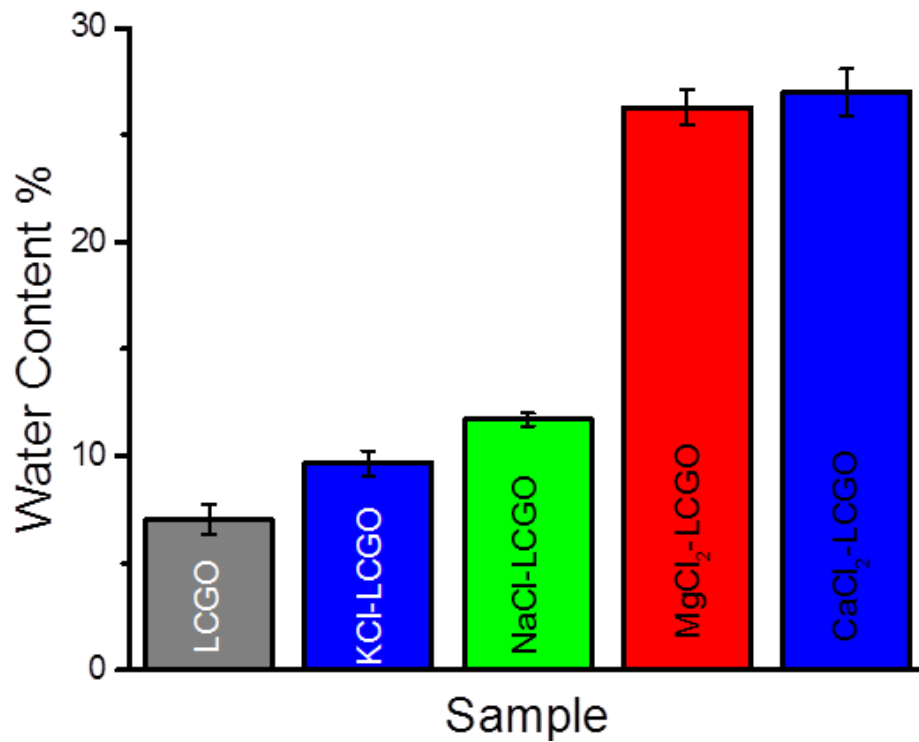


Figure 3.15 Water content of LCGO and m-LCGO film. The salt concentration was fixed at 0.08 mM.

### 3.4 Conclusions

Ionic interactions of chloride salts with LCGO dispersions result in an improvement in mechanical and electrical properties of free-standing films formed from these salts treated LCGO dispersions. The interaction of the cationic component of the ionic solution with the charged functional groups of the LCGO sheets facilitates the formation of “cation bridges” that cross-link LCGO sheets and causes an increase in the m-LCGO dispersion viscosity and storage modulus. The free-standing films formed from the m-LCGO dispersions show considerable improvement in their mechanical properties and remain robust and stable in aqueous solutions. The presence of water in the structure of m-LCGO films is also crucial for hydrogen-bonding and enhancement of mechanical properties. Also, the hygroscopic properties of salts used to treat the LCGO dispersion lead to an increase in conductivity by the absorption of ambient moisture. When left exposed to the environment, fully dried m-LCGO films are capable of absorbing water from their surroundings, becoming hydrated and retaining their enhanced mechanical properties. The significance of the work is that it provides a wide range of properties that can be adopted based on the application. For example, the  $\text{MgCl}_2$ -LCGO samples provide a suitable material when high mechanical properties in contact with water and moderate conductivity are required. While the KCl-LCGO samples, due to the high viscosity of their dispersions, offer a suitable material for various fabrication techniques. This new route of treating LCGO dispersions with hygroscopic salts to create high-quality LCGO films could provide practical solutions to the fabrication of a wide range of devices where mechanical robustness in a wet environment is required.



## **Chapter 4**

# **Advanced Conductive Tough Hydrogel for Bio-applications**

---

This chapter has been adapted from the published article “Javadi M, Gu Q, Naficy S, Farajikhah S, Crook JM, Wallace GG, Beirne S, Moulton SE. Conductive Tough Hydrogel for Bioapplications. *Macromolecular Bioscience*. 2018, 18, 1700270. The introduction section in this chapter is a modified version compared with the submitted article to avoid duplication with the comprehensive literature review of Chapter 1.

## 4.1 Introduction

As described in Chapter 1, for applications of temperature sensors in wearable human-activity monitoring and personal healthcare we need a thermally sensitive conductive material with a dynamic range matching body temperature, flexibility, stretchability, and biocompatibility. Practically, graphene materials could not solely cover the entire physical requirement for making a thermistor for health monitoring application. In this chapter, the development of conductive hydrogel based on polyurethane with adjustable properties is presented and discussed.

Over the last two decades, conductive hydrogels have been of interest to both academic researchers and commercial organisations. Hydrogels are polymeric materials, with a hydrophilic structure that renders them capable of holding large amounts of water or other polar solvents in their 3D networks.[343] Conductive hydrogels incorporate an additional functionality by enabling the conduction of electricity. Such materials have great potential for use in wearable and implantable sensors for healthcare, mimicry of neural networks, soft robotics, and electro-stimulated drug release.[344-347]

Electrically conductive hydrogels have previously been produced by combining a hydrophilic matrix with conductive fillers [348] such as metallic particles, conductive polymers (CP), or carbon-based fillers.[211, 311, 349] Composite materials of the polymeric matrix and randomly dispersed metal particles are considered as heterogeneous disordered systems and have low durability.[350, 351] Among all CPs, potentially PEDOT:PSS is the most promising because of its dispersibility (high stability in its p-doped form) in polar solvents and hence excellent processability, and the high conductivity, attainable. Therefore, PEDOT:PSS has been widely used as a conductive

component in many hybrid systems to enhance electrical conductivity.[352-354] In this regard, the discovery of graphene and its derivatives has opened new pathways for developing conductive composites. Graphene-based fillers have a high surface area, large aspect ratio, and excellent thermal and electrical conducting properties that can be imported to composites containing them.[222] The antibacterial activity of graphene and its derivatives make it appealing for biomedical application.[159, 355] Notwithstanding, it is technically impractical to produce scaffolds solely from graphene[356], and so graphene-based fillers are typically dispersed in processable polymers.[357]

Although graphene sheets exhibit high in-planar (intra-sheet) electrical conductivity, their trans-planar (inter-sheet) conductivity greatly diminishes for low loading of graphene in an insulating matrix.[153, 243] The efficiency of charge transfer between adjacent sheets is normally limited by the insulating coating of the graphene sheets by the matrix material. While the problem can be addressed by increasing the ratio of fillers to the matrix, this in turn negatively impacts on the matrix flexibility and stretchability whereby the hydrogel composites are brittle, possess relatively low flexibility and are unable to undergo elongational deformations. [358]

In the human body, endogenous electric fields generated from the membranes of cells serve as important cues to direct cell migration during embryonic development and wound healing.[359] Accordingly, it has been well documented that externally applied electric fields during cell culture can improve the growth of electro-responsive cells such as nerve and muscle cells.[360] Electrically stimulated tissue engineering is dependent on the identification and development of novel electrode materials that are processable, electrochemically stable, soft, and biocompatible.[361-363] To date, the development of an easy to produce conductive and biocompatible hydrogel with the ability to sustain large

dimensional deformations without any mechanical failure, while remaining stable in aqueous and dry ambient conditions has proved challenging. Consequently, progress in the field has been slow due to the limited development of conductive hydrogel formulations that contain well-dispersed conducting fillers.

Here, the production of an electrical conducting tough polyurethane hybrid composite (PUHC) hydrogel by a simple method that possesses excellent mechanical performance and biocompatibility is reported. The PUHC is made from well-dispersed PEDOT:PSS, liquid crystalline graphene oxide (LCGO) and a hydrophilic polyurethane matrix (PU). The optimized formulations used to prepare the PUHC are easy to process via solution casting to produce films with high conductivity and stretchability. Biocompatibility is demonstrated through culture and differentiation of clinically-relevant human neural stem cells (hNSCs) to neurons and supporting neuroglia on the films, with electrical stimulation enhancing neuritogenesis.

## **4.2 Experimental**

PUHC used in this study is also employed in Chapter 5, therefore in order to avoid repetition, the materials and methods of PUHC formulation is described in Chapter 2, Section 2.1.3.

### **4.2.1 Characterization of PUHC**

The water content was calculated as follows:

$$\text{water content (\%)} = \frac{(W_o - W)}{W_o} \times 100\% \quad \text{.....(Equation 4.1)}$$

Where  $W_0$  and  $W$  are the weight of the films before and after drying respectively.

#### **4.2.2 Cell culture and differentiation**

Working stocks of human neural stem cells (hNSCs, ReNcell CX, SCC007, Millipore) were maintained under 5% CO<sub>2</sub>, seeding at a density of  $2 - 3 \times 10^6$  cells in self-renewal medium consisting of NeuroCult NS-A (#5751, Stem Cell Technologies) with 2 $\mu$ g/ml Heparin (Sigma), basic fibroblast growth factor (FGF2, 20ng/ml; Peprotech) and epidermal growth factor (EGF, 20ng/ml; Peprotech) on laminin (Life Technologies) coated 6-well plates (Greiner Bio-One). Cells were passaged every 5-7 days by digesting in Triple (Life Technologies) for 3 min at 37 °C. hNSCs were similarly cultured on PUHC-film that was fixed to the bottom of culture plate wells. Differentiation of hNSCs was performed in a differentiated neural medium comprising two parts DMEM F-12: one part Neurobasal supplemented with 0.5% N2 (Gibco), 2% StemPro (Life Technologies) and 50 ng/mL brain-derived neurotrophic factor (BDNF; Peprotech) for 7 days.

#### **4.2.3 Electrical stimulation**

hNSCs were seeded on PUHC films formed within a 4-well culture chamber customized for concomitant electrical stimulation (Figure 4. 2). Cells were seeded at a density of  $5 \times 10^4$  cells/cm<sup>2</sup> in self-renewal medium, allowed to adhere for 24 h, and subsequently stimulated for 8 h per 24 h at 37 °C under CO<sub>2</sub> for 3 days. The stimulation paradigm was  $\pm 0.25$  mA/cm<sup>2</sup> using a biphasic waveform of 100  $\mu$ s pulses with 20  $\mu$ s interphase at 250Hz on a Digital Stimulator DS8000 and A365 Isolator units (World Precision Instruments) interfaced with an e-corder system (eDAQ). Stimulation was performed in self-renewal medium to determine an effect independent of standard medium-directed differentiation on hNSC-neuritogenesis.

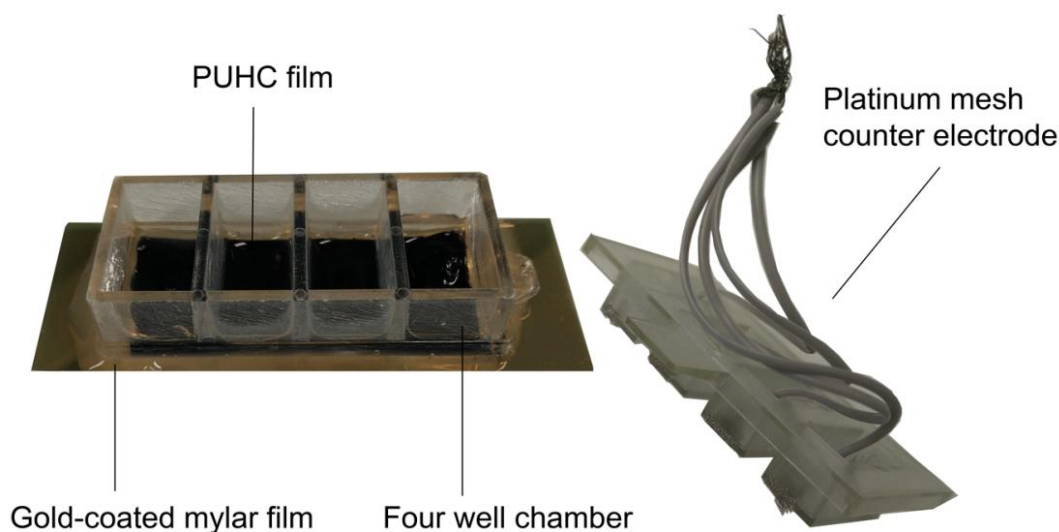


Figure 4. 2 A custom hNSC culture chamber and stimulation module comprising gold-coated Mylar film, G-film and platinum mesh counter electrode which was used for electrical stimulation of hNSCs.[364]

#### 4.2.4 Immunocytochemistry and analysis

Cell samples were fixed with 3.7% paraformaldehyde solution in PBS for 10 min and then blocked and permeabilized in 0.3% Triton X-100 containing 10% donkey serum for 1h at 37 °C. The cells were incubated with primary antibodies against SOX2 (1:500, rabbit; Millipore), Vimentin (1:1000, chicken; Millipore), TUJ1 (1:1000, chicken; Millipore) or glial fibrillary acidic protein (GFAP, 1:1000, rabbit; Millipore) overnight at 4 °C. After rinsing with PBS containing 0.1% Triton X-100, the samples were incubated with Alexa 647, 594 or 488 (1:1000; Invitrogen) secondary antibody for 1h at room temperature. A further wash was undertaken followed by 5 min incubation at RT with 1 mg/mL DAPI in PBS. Imaging was performed using a Leica confocal microscope (Leica

TSC SP5 II), and neurite studies were completed using MetaMorph software V 7.8 with the neurite analysis plugin.

#### **4.2.5 Acid treatment of PUHC**

The acid treatment of the PUHC films was carried out by immersing the hydrogel films into a 5% aqueous solution of  $\text{H}_3\text{PO}_2$  acid (50 °C for 12 hrs) in a round-bottom flask. Afterwards, samples were then thoroughly rinsed with Milli-Q water to remove the remaining acid (wash cycle was 10 times 30 min each cycle). Reduced graphene oxide (RGO) is the form of GO that is processed by chemical, thermal and other methods in order to reduce the oxygen content, while graphiteoxide is a material produced by oxidation of graphite which leads to increased interlayer spacing and functionalization of the basal planes of graphite. For comparison of the acid treatment process other reduction methods such as chemical reduction with other reduction agents, reduction via UV, annealing, and microwave were evaluated (Table 4. 3)

### 4.3 Results and Discussion

Stable dispersions of PEDOT:PSS, LCGO, and PU were prepared by dissolving PEDOT:PSS in water and DMF (50:50), followed by addition of LCGO dispersion in EtOH and PU. The difference in dispersibility of PU, LCGO, and PEDOT:PSS in various organic solvents is expected to influence the ability to prepare homogeneous PUHC formulations for composite film formation purposes. (Figure 4.3)

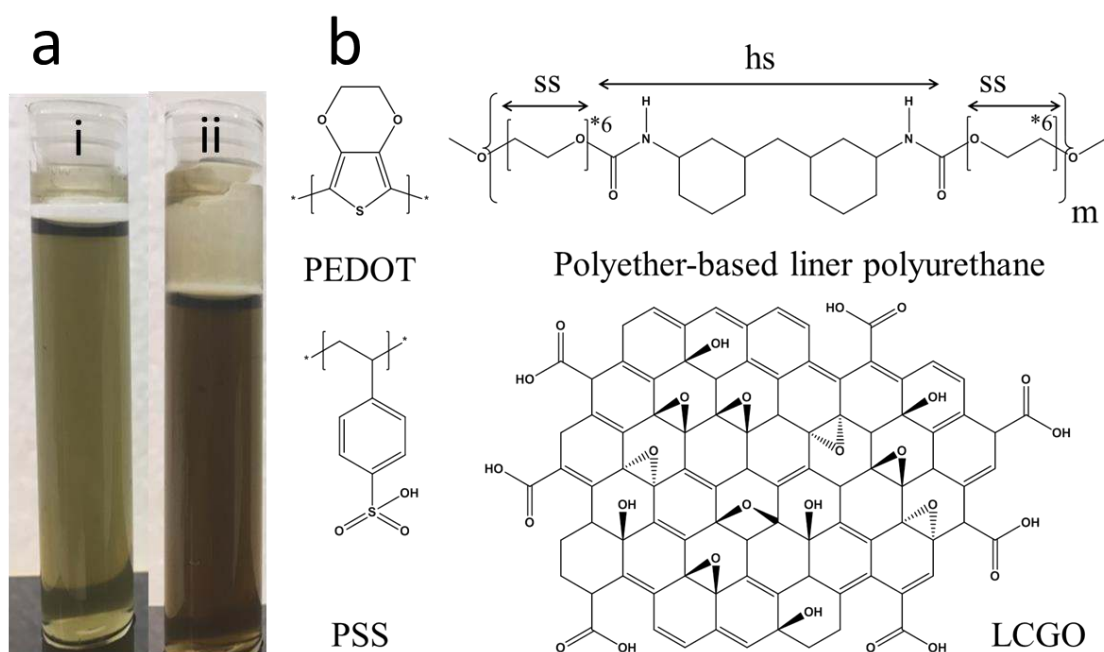


Figure 4.3 a) Homogeneous PUHC formulation immediately after preparation (i) and 6 months after preparation (ii), b) Chemical structure of PEDOT:PSS, LCGO and polyether-based liner polyurethane (abbreviation: ss - soft segment and hs - hard segment).

DMF and ethanol solvents provided the best dispersibility for both PU and PEDOT:PSS and were therefore used to compare the processability of the composite formulations. The use of DMF and water in making PEDOT:PSS formulations resulted in dispersions that



are stable for one month and displayed a higher electrical conductivity than that of the equivalent dispersion prepared in water. The addition of PEDOT:PSS and LCGO to PU dispersions resulted in homogeneous PUHC formulation that was stable for at least six months after preparation (Figure 4.3a).

#### **4.3.1 X-ray diffraction (XRD)**

The crystalline structure of PUHC and other composite components were analysed by XRD and reveal that XRD patterns of PUHC do not show any characteristic signals for LCGO. This lack of XRD signal may be due to the high dispersion of graphene sheets within PU matrix.

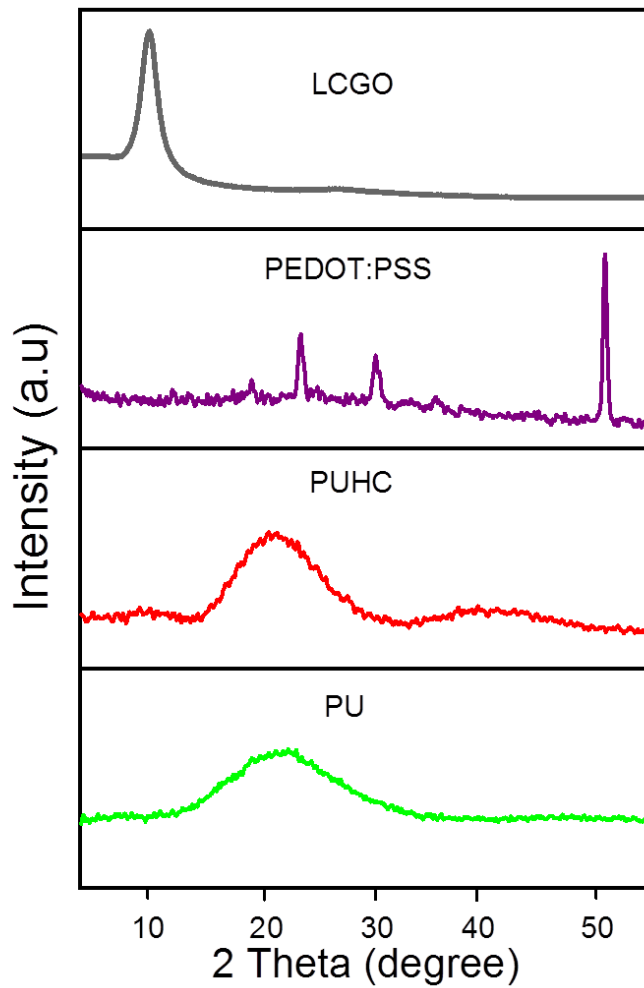


Figure 4.4 X-ray diffraction (XRD) patterns of composite component and PUHC (8%w/w LCGO/PEDOT:PSS at 1:1 and treated with a 5% aqueous solution of  $H_3PO_2$  acid) and PUHC do not show any characteristic signals for LCGO.

As shown in Figure 4.4, the XRD pattern of the LCGO shows a diffraction peak at  $2\Theta = 10.32^\circ$ , corresponding to its interlayer spacing of 0.654nm. The intensity of this peak sharply decreases for reduced LCGO, and a new weak peak (hump) will appear approximately  $2\Theta = 23.15^\circ$ . The XRD patterns of PUHC do not show any obvious characteristic signals for LCGO, indicating the uniform dispersion of graphene sheets in PU matrix.

### 4.3.2 Correlation between mechanical and electrical properties

Free standing reduced PUHC films were prepared by incorporating a range of filler (PEDOT:PSS/LCGO at 1:1 ratio) % w/w into the PU (in a solvent mixture of ethanol, water, and DMF) followed by casting in glass Petri dishes. Solvents were removed using a vacuum oven (70 °C, -80 Kpa, 12 hrs) to obtain uniform films. Then the reduction agents employed as described in the experimental section. The electrical and mechanical properties of these films are presented in and show that the electrical conductivity of the PUHC increases with increasing filler ratio, indicating enhanced electrical conductivity of PUs.

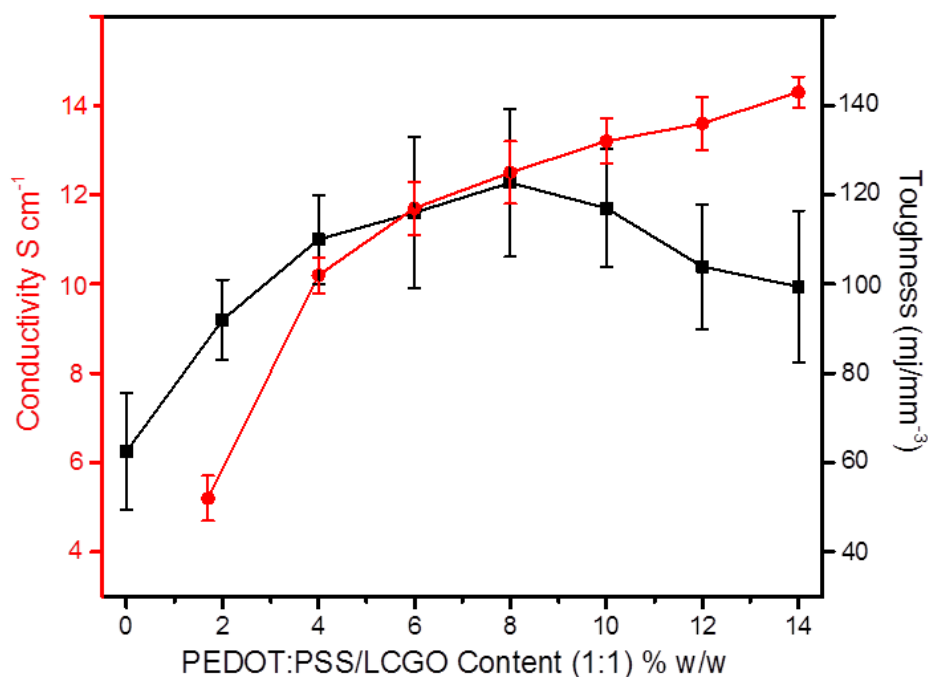


Figure 4.5 The toughness and conductivity of the PUHC as a function of filler (PEDOT:PSS and LCGO at 1:1 ratio and treated with a 5% aqueous solution of H<sub>3</sub>PO<sub>2</sub> acid) % w/w loading into the PU.

It can also be seen that the toughness of the PU is increased and reaches a maximum at an incorporation of 8 % w/w of filler. Therefore 8 % w/w ratio of filler was chosen as optimal weight percent for further PUHC formulation evaluation. These PUHC films displayed flexibility and remained stretchable after solvent removal as evidenced in photographic representations of Figure 4.6.

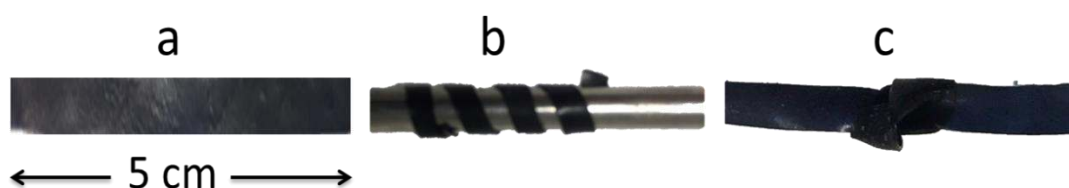


Figure 4.6 Photos show as-prepared PUHC film in various forms, namely (a) free stand film, b) twisted free standing film and c) free standing film tied into a knot. (PEDOT:PSS and LCGO at 1:1 ratio and treated with a 5% aqueous solution of  $H_3PO_2$  acid)

### 4.3.3 Mechanical Characterisation

Typical stress-strain curves of the PUHC and control samples are presented Figure 4.5a and shows the improvement in the tensile modulus, and yield strength but a decrease in elongation at break compared to the base PU material, PU-LCGO, and PU-PEDOT:PSS film. The data in Table 4.1 summarizes that the average tensile modulus and yield strength rather than control samples (with the same ratio of fillers) are greater than the control samples by a factor of approximately 1.6 times.

The elastomeric properties of PU and its composites are derived from the presence of the hard and soft copolymer segments of the polymer chains (Figure 4.7b). The soft segments, which are normally linear chains in their rubbery state (glass transition temperature ( $T_g$ ) lower than room temperature), are flexible and mobile. These flexible segments are

covalently coupled to the hard segments ( $T_g$  above room temperature) via urethane linkages (R-NH-CO-O-).

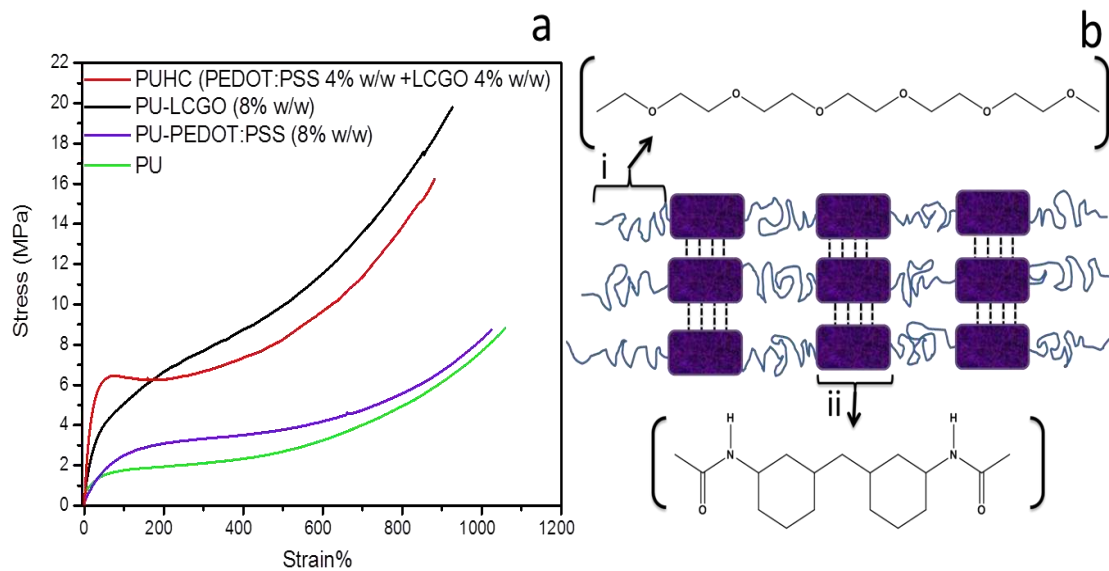


Figure 4.7 a) Tensile stress-strain curve of the PUHC and control samples and b) Chemical structure of PU; i) soft segment and ii) hard segment.

Table 4.1 The effect of fillers on the mechanical properties of PU.

	Tensile Modulus (MPa)	Ultimate Strength (MPa)	Yield Strength (MPa)	Elongation at break %	Filler % w/w*
PU	1.02 ± 0.3	7.32 ± 1.2	0.42 ± 0.12	1084 ± 96	0
PU/PEDOT PSS	2.31 ± 0.26	10.42 ± 0.8	2.37 ± 0.3	1127 ± 115	8.0*
PU/LCGO	3.45 ± 0.22	19.8 ± 1.3	3.98 ± 0.24	936 ± 76	8.0*
PUHC	5.64 ± 0.34	16.21 ± 1.02	6.23 ± 0.53	891 ± 93	PEDOT: PSS 4.0  LCGO 4.0

\*Note: The % w/w of the PEDOT:PSS and LCGO were chosen to be 8% in order to have the same amount of filler in these samples as is in the PUHC sample.

When stress is applied to the PU composites, a portion of the soft segments is stressed by uncoiling, and the hard segments become aligned in the stress direction. Therefore, the soft segments provide high elongation while hard segments provide stiffness in PUHC. Previous work has shown that growth in hard segment content gives rise to an increase in tensile modulus, ultimate strength and yield strength, and a decrease in elongation to break.[226] After adding each of the components to the PU, an increase in tensile strength was observed that agrees with other published results.[139, 221]

#### 4.3.4 Electrical conductivity

The electrical conductivity of PUHC films was investigated (Figure 4.8). The onset of conductivity occurred at  $\approx 3.8$ , 2.2 and 1.7 % w/w loadings of PEDOT:PSS, LCGO, and PEDOT:PSS/LCGO (1:1) respectively, above these loadings the composite conductivity increased almost monotonically with filler loading. PUHC (Figure 4.8) showed an increase in conductivity after addition of 1.7 % w/w of a 1:1 blend of PEDOT:PSS and LCGO.

Table 4.2 Conductive PU composites with a variety of conductive fillers (data from this study and literature).

Filler	Conductivity (S/cm)	Ref.
LCGO + PEDOT:PSS (8 % w/w)	12.5	This thesis
PAni (34 wt%)	$8 \times 10^{-2}$	[365]
PPy	$10^{-7}$ – $10^{-2}$	[366]
PPy(30 wt%)	$2.6 \times 10^{-1}$	[367]
MWCNTs (5 wt%)	$1 \times 10^{-3}$	[368]
SWCNT + PPy (2.5wt%)	$9.8 \times 10^{-3}$	[369]
Graphene (2 wt%)	$10^{-5}$ , $10^{-8}$	[370, 371]
Graphite (6.5 vol.%)	0.01	[372]
PEDOT:PSS (8 wt.%)	4.8	[373]

PU: Polyurethane, PPy: polypyrrole, PAni: polyaniline, MWCNT: Multi-walled carbon nanotube, and SWCNT: Single-walled carbon nanotube;

This correlates to an individual filler content of 0.85 % w/w PEDOT:PSS and 0.85 % w/w LCGO. These values are lower than the individual amounts of 3.8 % w/w and 2.2 % w/w indicated above for PEDOT:PSS and LCGO respectively and indicates a synergistic effect when these two fillers are combined that facilitates an increase in composite conductivity. The conductivity of the optimal PUHC composite is compared to previous reports conducting PU composites in Table 4.2. The increase in conductivity may be due to the establishment of LC structure in PUHC (transfer isotropic to nematic structure).[374] Percolation threshold results comparing the electrical behaviour of LCGO and PEDOT:PSS/LCGO composites suggested that lower amounts of filler are needed to create conducting paths in an isolating matrix of PU. At ratios below the percolation threshold, the composite conductivity is almost the same as the polymer matrix, and therefore charge carrier transport cannot occur. By increasing the filler loading, the average distance between conducting filler particles decreases and below a certain threshold, charge carrier transport can occur via electrical field assisted tunneling or hopping between neighbouring fillers.[375] At the percolation threshold, the amount of filler is enough to begin the formation of a continuous conductive network throughout the polymer matrix.



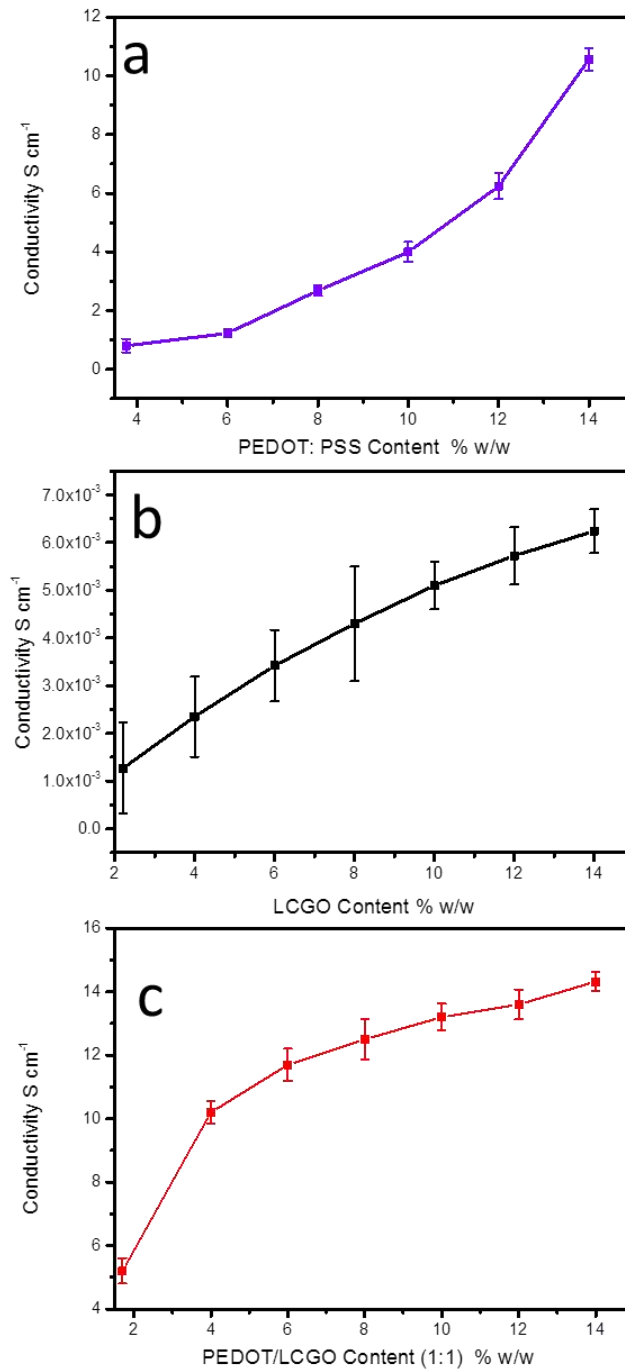


Figure 4.8 The electrical conductivity of PU composites containing a) PEDOT:PSS, b) reduced LCGO, and c) LCGO/PEDOT:PSS as a function of filler loading. PUHC showed an increase in conductivity after addition of 1.7 % w/w of a 1:1 blend of PEDOT:PSS and LCGO. (PEDOT:PSS and LCGO at 1:1 ratio and treated with a 5% aqueous solution of  $H_3PO_2$  acid)

As indicated above PU polymer chains have hard and soft segments. (Figure 4.7b) The urethane hard segment domains are physically cross-link via hydrogen bonding between the amorphous polyether soft segment domains.

### 4.3.5 Water Content

The polyether segments define the amount of water that the PU can hold since they are hydrophilic and therefore interact with water. While the water content of pure PU is close to 60%, this gradually decreases by the addition of other less hydrophilic components such as PEDOT:PSS and LCGO (Figure 4.9a).

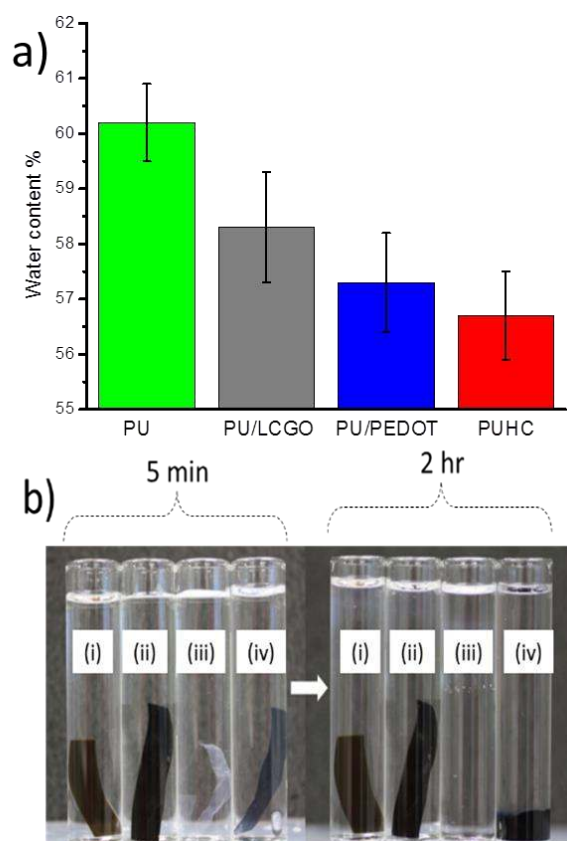


Figure 4.9 Water content (a) of PUHC (8 %w/w LCGO/PEDOT:PSS at 1:1), PU/LCGO (8%w/w), pure PU and PU/PEDOT:PSS (8%w/w). Photo images (b) of PUHC

film (i), PU/LCGO (ii), PU (iii), and PU/PEDOT:PSS (iv) hydrogel films immersed for 5 min and 2 hr in 10 mL of EtOH-water (95:5%) solution.

It is well documented that the water content has a positive effect on elongation at break and negative effects on tensile modulus, ultimate strength, and yield strength.[376] The data presented in Table 4.1 is in agreement (within the error range) of this phenomenon. Interactions between the filler and PU were investigated by forming free standing films and observing their behaviour in an EtOH:water (95:5%) solvent. It was found that neither PU/LCGO or PUHC were soluble in the solvent, while both pure PU and its composite with PEDOT:PSS were readily soluble (Figure 4.9b). The hard segment of polyurethane is a key segment for determining solubility and interaction between hard segment and other active group can decrease solubility of polyurethane composites. This observation indicates that the addition of LCGO prevents the PU chains from dissolving in its solvent. This effect is most likely due to the documented interaction between LCGO and the hard segment of PU. [376]

#### **4.3.6 Liquid Crystal Structure in PUHC**

The liquid crystal (LC) nature of these materials (Figure 4.10) provides the ability to have the fillers aligned and maintain alignment between LCGO nanosheets within the composite that has been shown to result in increased mechanical [226] and electrical [12] properties. The LC phases may offer a dynamic anisotropy at molecular scale [377] as it is pivotal to control the orientation and spatial ordering of graphene sheets in a precise manner [26] in order to translate individual graphene sheet into high-performance macroscopic materials. The LCGO dispersions in ethanol exhibited a nematic liquid crystalline phase at concentrations above 1.5 % w/w. It was found that the minimum concentration of LCGO that is required to obtain LC structure in PUHC solution is

approximately 4% w/w.[378] This increase in LCGO concentration required to invoke LC structure may be due to the forces imposed on the LCGO by the PU that prevents the spontaneous formation of LC domains at lower concentrations. The data in Figure 4.10 suggests that once a critical concentration of LCGO is incorporated these restrictive forces are overcome.

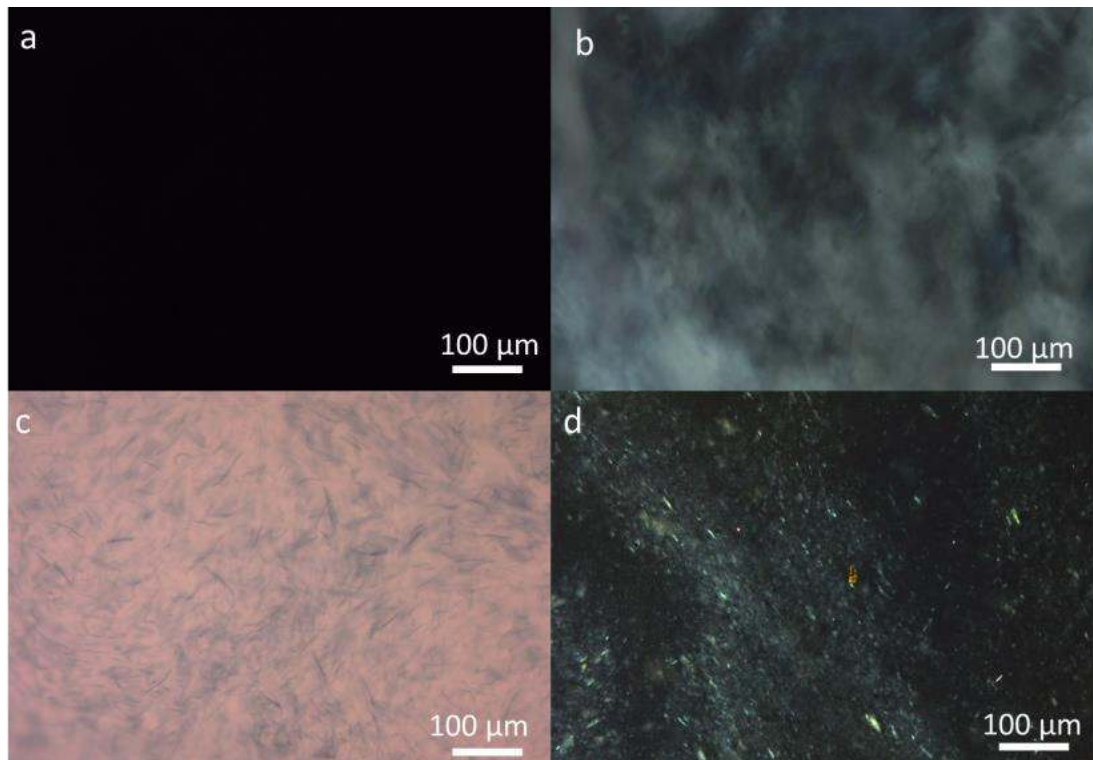


Figure 4.10 Representative polarized optical microscopy images of samples in solution phase. a) PU, b) LCGO (8% w/w), c) PEDOT:PSS (8% w/w) and d) PUHC (LCGO 4% w/w + PEDOT:PSS 4% w/w and treated with a 5% aqueous solution of  $H_3PO_2$  acid) .

#### 4.3.7 Morphology of PUHC

The SEM image shown in Figure 4.11a illustrates the uniformity of PUHC surface and layered microstructure of composite across the cross section (Figure 4.11b). This

highlights the aligned structure of LCGO nanosheets within the PUHC. The LC structure of graphene causes the sheets to reassemble forming a sandwich structure in the polymer matrix (Figure 4.11b). The PEDOT:PSS phase is believed to be dispersed between these parallel nanosheets, which can explain the synergistic effect of LCGO and PEDOT:PSS in increased conductivity. This ordered structure also helps to explain the higher mechanical properties observed for composites containing LCGO. The nematic orientation of fillers within the PU matrix provides a facile pathway for electrons inside the isolated matrix compared to the isotropic orientation and explains why PUHC's with self-assembly structure have a lower percolation threshold compared to the control samples (Figure 4.8).

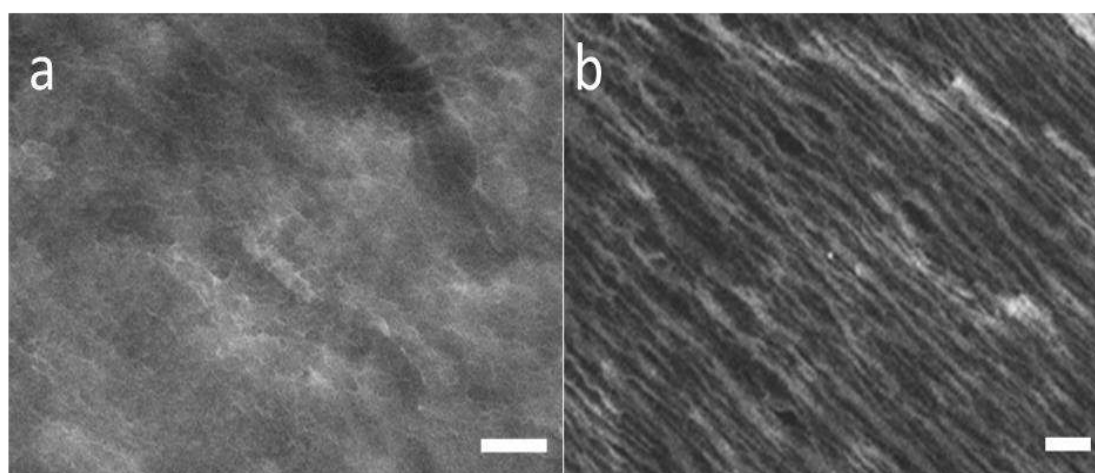


Figure 4.11 SEM images of the PUHC (8%w/w LCGO/PEDOT:PSS at 1:1). a) Surface SEM image b) Cross-section image of PUHC which shows aligned structure of LCGO nanosheets within the PUHC. The scale bar is 10  $\mu\text{m}$ .

#### 4.3.8 Reduction of LCGO

LCGO has a similar layered structure to graphite, but the plane of carbon atoms in LCGO is heavily decorated by oxygen-containing groups (carbonyl (C=O), hydroxyl (-OH),

phenol), which not only expand the interlayer distance but also make the atomic-thick layers hydrophilic.[379, 380] So LCGO can be exfoliated in water under moderate ultrasonication. The most attractive property of LCGO is that it can be partially reduced to graphene-like sheets by removing the oxygen-containing groups with the recovery of a conjugated structure.[381] The reduced LCGO sheets are usually considered as one kind of chemically derived graphene.[382] The most straightforward goal of any reduction protocol is to produce graphene-like materials both in properties and structure and also without any negative effect on composite properties.[383]

Methods for reducing LCGO include chemical, thermal or electrochemical means.[384-386] Some of those techniques are able to produce very highly reduced GO with high conductivity similar to pristine graphene. In choosing the reduction method for PUHC, it is important to consider the impact on other components of the composite, namely PU and PEDOT:PSS. For example, almost all of the thermal treatment methods disrupt the mechanical properties of PU. Furthermore, some of the chemical agents such as hydrazine, and sulphuric acid make the composite brittle or form a paste-like consistency (Table 4. 3).

Optimization of the conductivity and the mechanical properties of the PUHC was achieved using hypophosphorous acid as the reducing agent (Figure 4.5). Hypophosphorous acid is a powerful reducing agent with molecular formula  $H_3PO_2$ . The electronic structure of hypophosphorous acid is such that it has only one hydrogen atom bound to oxygen, and it is thus a monoprotic oxyacid. It is a weak acid and is used as an industrial non-toxic reducing agent. Therefore, it has been used as a cheap and safe reducing agent [387] The PUHC became conductive following chemical reduction using 5% v/v hypophosphorous acid at 50 °C. From Figure 4.12 it appears that reduction times

greater than 6 hrs are not necessary as maximum conductivity is reached at this time. PUHC samples after treatment with chemical agent immersing in the Milli-Q water for 3 hrs followed by washing with Milli-Q water to avoid any residual acid agent in the samples and then samples' electrical conductivity directly measured after drying on the oven over 120 hrs under vacuum condition. It has been reported that the partial removal of PSS, due to the treatment of composite containing PEDOT:PSS with acid, could be considered as another reason for the increase in electrical conductivity of the PUHC. [388]

Table 4.3 The impact of reduction methods on each composite component separately.

Reduction method		Conductivity (S cm <sup>-1</sup> ) A*, B*, C* and D*	Mechanical properties
No treatment		A: Insulator B: Insulator C: 345±32.4 D: 0.286±0.05	A: Flexible, stretchable B: Free standing film, brittle C: Free standing film D: Free standing film
Chemical reduction	H <sub>2</sub> SO <sub>4</sub> (5% ,50 °C for 12 hrs)	A: Insulator B: 89±26.2 C: 425± 48 D: 0.59±0.11	A: Paste B: Brittle C: Free standing film D: Paste
	N <sub>2</sub> H <sub>4</sub> (5% ,50 °C for 12 hrs)	A: Insulator B: 548±32 C: 320±66 D: 15.23±2.8	A: Paste B: Brittle C: Free standing film D: Paste
	HCl (5%, 50 °C for 12 hrs)	A: Insulator B: 48±3.5 C: 370±102.8 D: 3.24±1.4	A: Paste B: Brittle C: Free standing film, D: Paste
	HI (5% ,50 °C for 12 hrs)	A: Insulator B: 195±32.0 C: 320±71 D: 488±104	A: Paste B: Brittle C: Free standing film D: Paste`



	Ascorbic acid (5% ,50 °C for 12 hrs)	A: Insulator B: 0.35±0.45 C: 312±17 D: 0.056±0.012	A: Flexible, stretchable B: Free standing film, brittle C: Free standing film D: Flexible, stretchable
	H <sub>3</sub> PO <sub>2</sub> (5% ,50 °C for 12 hrs)	A: Insulator B: 84±13.1 C: 370±54.8 D: 12.84±1.7	A: Flexible, stretchable B: Brittle C: Free standing film D: Flexible, stretchable
Physical reduction	UV light (Oriel 450 W xenon arc lamp, 3 h)	A: Insulator B: 0.98±0.36 C: 118±97.2 D: 0.023±0.005	A: Flexible B: Brittle C: Free standing film, brittle D: Flexible
	Annealing (250 °C 48 hrs)	A: Insulator B: 56±14.2 C: 184±9.5 D: None	A: Decompose B: Brittle C: Free standing film, D: Decompose
	Microwave (1000 w, 5 s for 10 repeats)	A: Insulator B: 21±9.4 C: 0.95±1.2 D: 0.0087±0.00037	A: Flexible B: Brittle C: Free standing film, brittle D: Flexible

A: PU film

B: LCGO film

C: PEDOT:PSS film

D: PUHC (LCGO 4% w/w + PEDOT:PSS 4 % w/w)

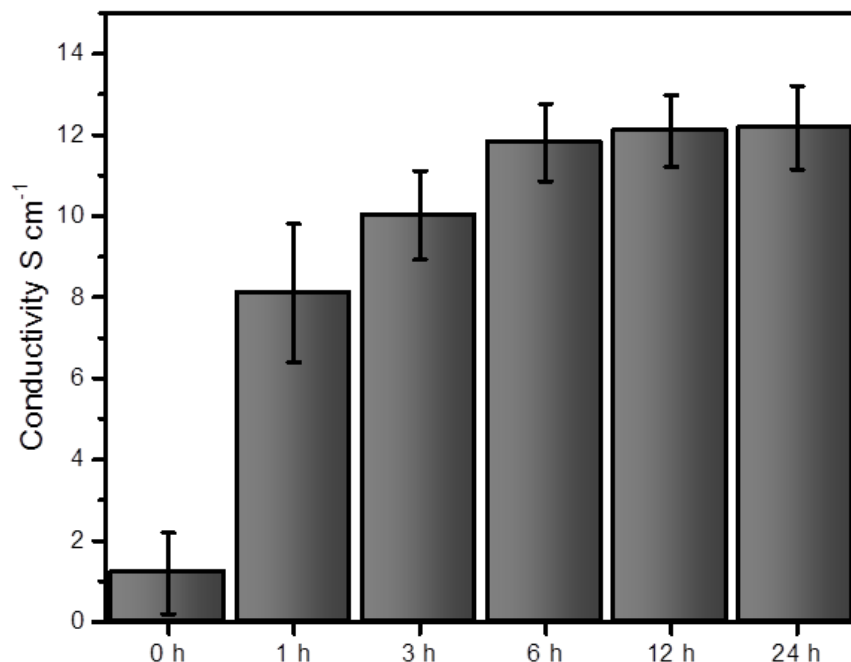


Figure 4.12 Conductivity of PUHC (8%w/w LCGO/PEDOT:PSS at 1:1 and treated with a 5% aqueous solution of  $\text{H}_3\text{PO}_2$  acid) as a function of treatment time with 5% v/v Hypophosphorous acid at 50 °C and treatment times greater than 6 hrs are not necessary as maximum conductivity is reached at this time.

#### 4.3.9 Raman spectra

In the Raman spectra (Figure 4.13) bands at  $\sim 1590 \text{ cm}^{-1}$  are assigned to the symmetric stretch of C=C. Compared to LCGO, this peak for PUHC is shifted towards a higher frequency from 1588 to  $1595 \text{ cm}^{-1}$ , suggesting the  $\pi$ - $\pi$  interaction between LCGO and PEDOT:PSS in PUHC.[389, 390] The ratio of the D band intensity ( $I_D$ ) to the G-band intensity ( $I_G$ ) which is called the R values ( $I_D/I_G$ ), indicates the amount of structural order in graphene oxide. From Figure 4.13 the R-value of LCGO (1.47) is reduced compared

to that of PUHC (1.36) and indicates that graphene sheets within the LCGO are more ordered and some of the  $sp^2$  bonds have been restored.[391]

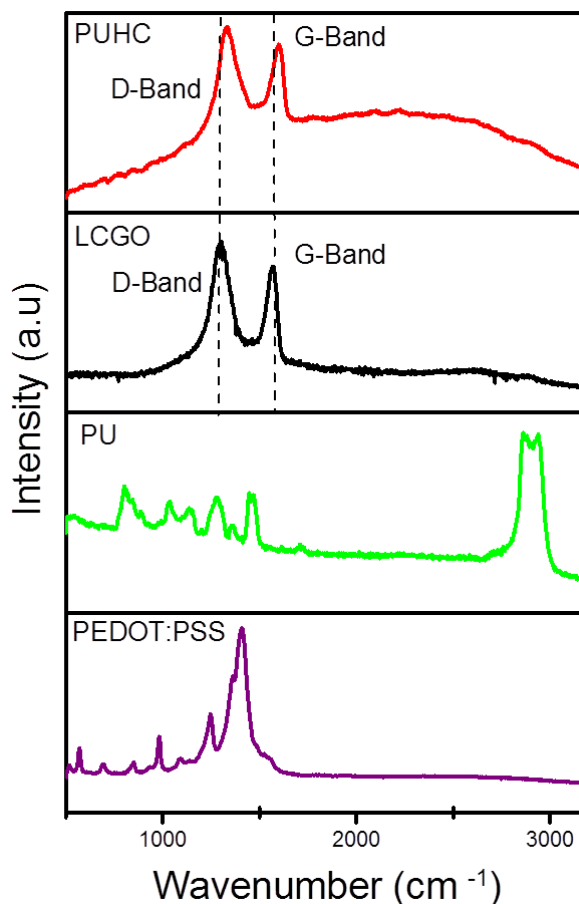


Figure 4.13 Raman characterization of PU, PEDOT:PSS, LCGO, and PUHC (PEDOT:PSS and LCGO at 1:1 ratio and treated with a 5% aqueous solution of  $H_3PO_2$  acid). The broken line indicates the location of D and G-band in LCGO and this peak for PUHC is shifted towards a higher frequency from 1588 to 1595  $cm^{-1}$ .

#### 4.3.10 hNSCs can be cultured and differentiated on PUHC

The biocompatibility of PUHC with hNSCs was initially tested by evaluating cell viability following 24 h culture (Figure 4.14a, b). Live/dead cell analysis indicated robust cell survival (>80%) similar to standard plate-based controls (Figure 4.14b). Importantly, hNSCs expressed neural stem/progenitor cell markers SOX2 and Vimentin and exhibited

small immature and sparsely arranged neurites, typical of hNSC culture (Figure 4.14c). After two weeks culture under differentiation conditions, cell morphology and immunophenotyping was consistent with advanced neuronal cell induction (Figure 4.14d), with TUJ1 immuno-labelling revealing neurons with extensive networks of neurites, and GFAP labelling indicated supporting neuroglia (Figure 4.14d). These data support PUHC biocompatibility and more specifically hNSC survival, proliferation, and differentiation.

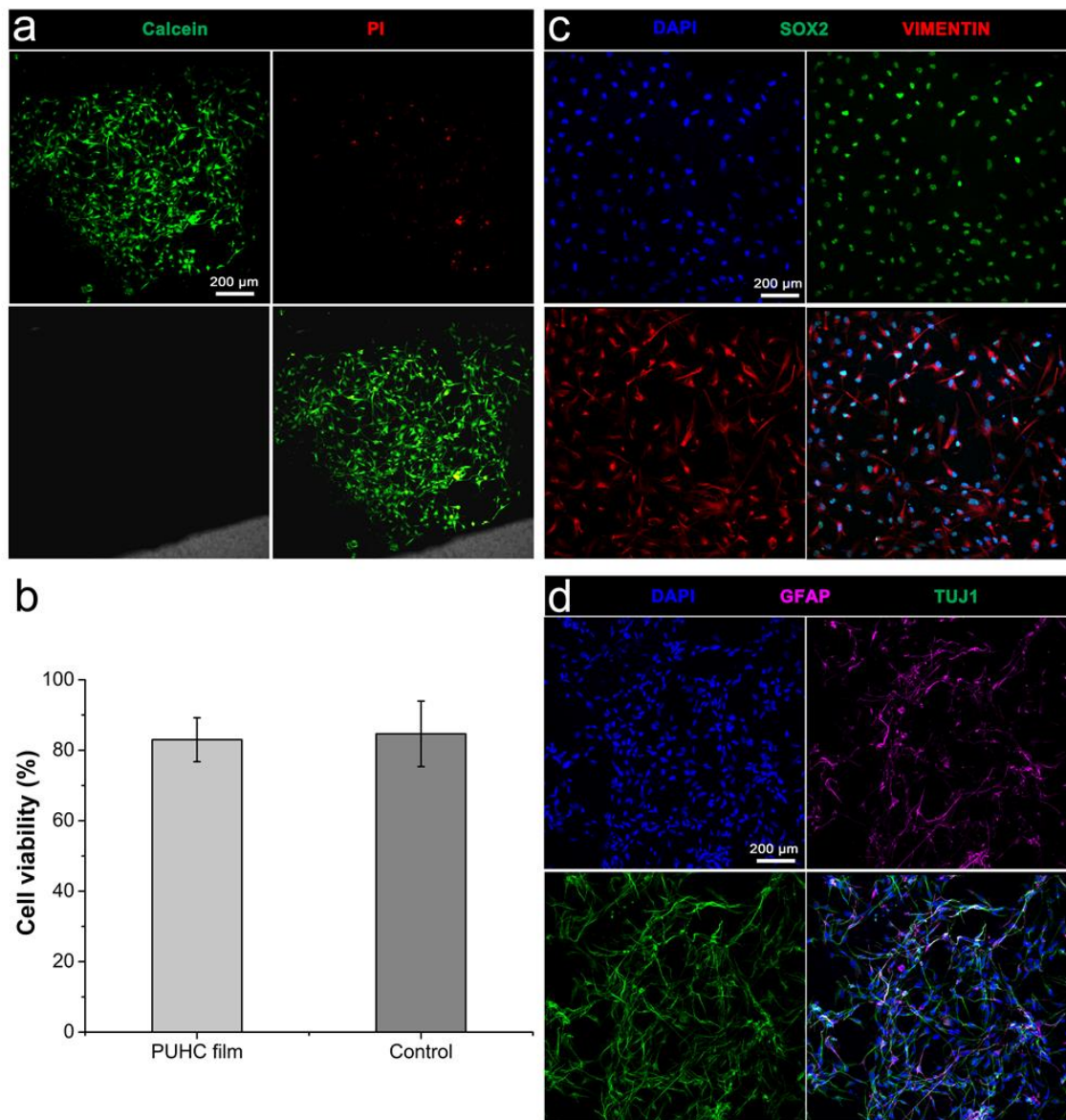


Figure 4.14 Survival, maintenance and differentiation of hNSCs on PUHC (PEDOT:PSS and LCGO at 1:1 ratio and treated with a 5% aqueous solution of  $H_3PO_2$  acid). (a) Live (Calcein AM) and dead (PI) cell staining following 24 hrs culture. (b) Quantitative analysis of hNSC viability following 24 hrs culture. (c) Immunocytochemistry of hNSC markers SOX2 and vimentin. (d) Immunocytochemistry of GFAP (astrocyte maker) and TUJ1 (neuronal marker) expression after differentiation of NSCs for 7 days.

#### **4.3.11 Electrical stimulation via PUHC enhances neuritogenesis of hNSCs**

Since electrical signals are implicated in a diversity of biological events, electrically conductive biomaterials are increasingly being used to modulate cell and tissue behaviour for research and biomedical applications, including tissue engineering and implantable bio-electrodes.[392] Having initially shown PUHC biocompatibility with hNSCs (Figure 4.14), the effect of electrical stimulation via the hydrogel on the cells was investigated.

Compared to unstimulated controls (Figure 4.14a, c), electrical stimulation of hNSCs via PUHC enhanced early neuritogenesis (Figure 4.14b, c), manifest as greater total neurite length, mean neurite length, and maximum neurite length per cell (Figure 4.14c). These findings are consistent with a previous report of increased hNSC neuritogenesis following electrical stimulation using conductive polymer polypyrrole (PPy).[393] Data corroborates these initial PUHC cell-biocompatibility studies, substantiating the use of electroactive-substrates for neural cell support [394], and verifies the application of electroactive-PUHC for tissue engineering where electrical stimulation, mechanical softness and other properties of the biomaterial presently shown are deemed important.

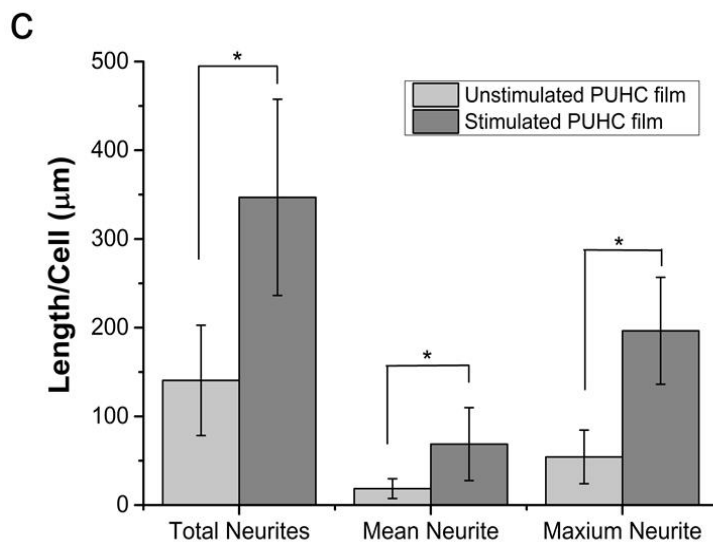
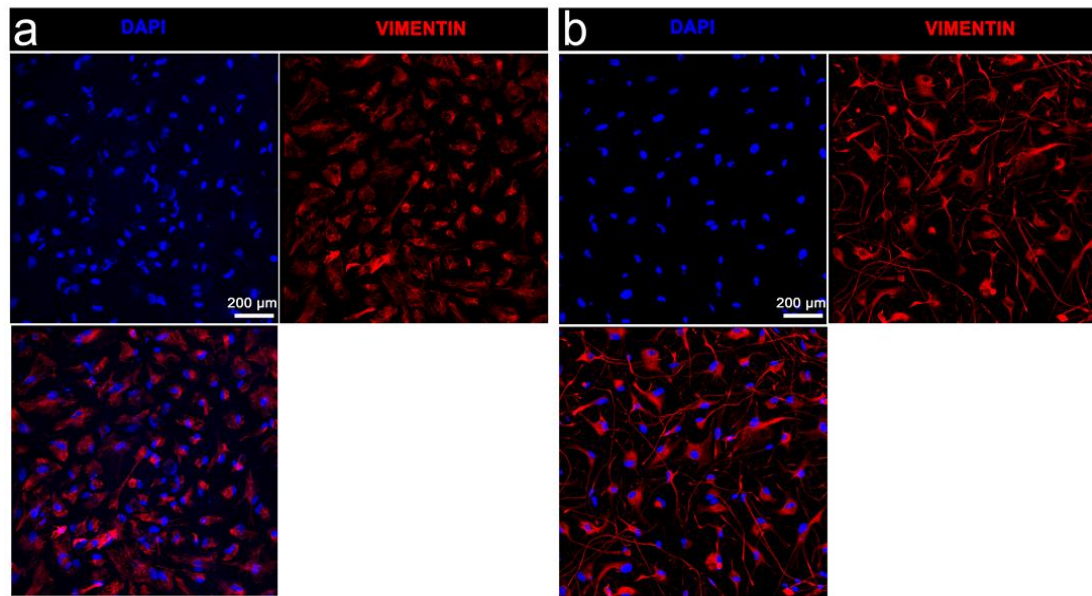


Figure 4.15 Neurite growth of hNSCs following culture for 3 days on PUHC (PEDOT:PSS and LCGO at 1:1 ratio and treated with a 5% aqueous solution of  $H_3PO_2$  acid) with and without stimulation. (a, b) Immunocytochemistry of vimentin-expressing cells. (c) Assessment of neurite growth, including the sum total length of neurites, mean neurite length, and maximum neurite length per cell  $\pm$  SD (for stimulated and unstimulated groups,  $n=11$  and  $40$  respectively). “\*” Indicates statistical significance of  $\leq 0.05$

## 4.4 Conclusions

As discussed in this chapter, our experimental results provide evidence for chemical interaction between the fillers (LCGO and PEDOT:PSS) giving rise to the synergic behaviour in mechanical and electrical properties of PUHC. This phenomenon in PUHC properties can be explained 1) physical influence of the LC structure in the composite solution, 2) chemical interaction between LCGO and PEDOT:PSS and these are as a filler with the PU's hard segment to create a synergic filler impacts on PUHC composite and 3) post-treatment of PUHC by acid agent. This chapter has demonstrated the production of PUHC with conductivity, stability, and elastomeric and biocompatible features. It could, therefore, be considered for use as an advanced material in sensor application for health monitoring. In the next chapter, the development of a preliminary thermistor sensor based on the PUHC will be presented and discussed. Sensor characterization tests, mechanical properties, biodegradability, and impact of other ambient physical stimuli are described. Finally, PUHC is employed as an ink for extrusion 3D printing. Design, rheological and morphological properties of the 3D printed PUHC temperature sensor are investigated.



## **Chapter 5**

# PUHC Thermistor for Healthcare Applications A Preliminary Study

---

## 5.1 Introduction

This chapter describes the work undertaken in the development of a thermistor temperature sensor based on the novel polyurethane hybrid composite (Ts-PUHC) described in Chapter 4 and its subsequent characterization required for use in body temperature monitoring. Intelligent polymers have found themselves in amongst a large number of applied fields including sensing, tissue engineering, drug delivery, cell culture and soft robotics to name a few. [395-397] Although considerable achievements have been made in the area of composite formation, there is still work to be done in order to tackle the various fundamental challenges associated with smart composites in regards to hysteresis and fatigue, which heavily underpin commercialization viability for a final product. [398] Hysteresis for a sensor can be defined as a dynamic lag between an input and output parameter of a sensor and is dependent on the state of a system, such as fatigue due to the weakening of the sensor material through repeatedly applied physical changes (such as temperature and stress/strain).

Among smart composites, thermally and electrically conductive polymer composites (TECPCs) have received considerable attention due to their multi-functional applications in many engineering and electronic fields. TECPCs are excellent materials for developing thermistors for healthcare monitoring due to the ability to match their thermal, electrical and mechanical properties with the human body. [396]

Thermal expansion is the tendency of a material to evolve in shape and volume due to a change in temperature and it causing the material to take up more or less space. Materials that contract on heating are unusual and have the potential to find previously unexplored applications with materials showing NTE behaviour usually being anisotropic.[400] From a scientific viewpoint, it is interesting to understand materials that contract while

heating as this understanding may provide a means to extend the relatively small family of materials that show negative thermal expansion (NTE).[399]

Thermal expansion is an important feature of thermal sensor technology especially when different materials with different thermal expansion behaviour are employed together to make a sensing structure. When a complex structure with positive thermal expansion (PTE) is heated it will tend to expand, which creates an increase in the structures volume. So, consideration must be taken when designing a sensing device to account for the thermal expansion of the material and consider potential impact on the cyclic performance of the device due to hysteresis and fatigue. For example, in order to use PUHC as a thermistor for healthcare monitoring, it is important to design junctions in the thermistor to allow for this volume change under expected operating conditions. These junctions will provide enough freedom of movement for repeatable and stable expansion and contraction.

After the development of the TECPC, the last important step is the fabrication method. Conventional methods such as salt leaching, solvent casting, fibre spinning or freeze-drying have been used to fabricate TECPC structures.[401] However, the most promising fabrication method is 3D printing as it provides more control over the printed structural parameters. In particular, extrusion printing which provides advantages, such as the ability to customize final products, increase productivity and be cost-effective.[402] The extrusion-based method can continuously dispense materials layer-by-layer from a movable dispensing head to create predefined structures. Developing homogeneous inks with appropriate rheological property and cohesion of subsequent layers onto each other are critical for successful 3D extrusion printing. These advantages have made 3D

extrusion printing a preferred method for the fabrication of 3D structures from organic material in recent years.

Depending on the material and technology, processing a 3D printed object can be time-consuming and complicated. In some cases, an integral method of the printing technique can make the 3D printing process complex. For example, in order to create 3D hydrogel structures for health monitoring, it would be necessary that the printed material would be stable at both room temperature (i.e., during the printing process) and at human body temperature (i.e., when in use). It is common practice to modify hydrogels and composites that include photo or thermal crosslinkable acrylate groups to enable cross-linking of the hydrogel during the printing process.[403, 404]

In this body of work, a simple method to prepare a 3D printable structure onto a flat substrate from a PUHC ink was employed without post-treatment. This was achieved by removing some of the solvent from the ink prior to printing.

In this chapter, the earlier work on electromechanical characterization of PUHC (Chapter 4) is continued with investigation of the material's rheological behaviour in the preparation of a 3D printable PUHC ink. Finally, the thermal properties, conductivity, expansion, and impact of prestrain on 3D printed PUHC properties are reported.

To the best of this author's knowledge, this is the first report investigating a printable composite without post-treatment, apart from drying time, that can offer NTE behaviour at ambient conditions with biocompatibility and stretchability in the window of human body temperature range (between 25 and 45 °C), so it is a promising material for this thesis application for body temperature monitoring.

## 5.2 Experimental

Development of the PUHC material utilised in this chapter has been described in detail in Chapter 4.

### 5.2.1 Rheological measurement and ink preparation

In order to obtain a PUHC solution suitable for printing it was necessary to partially remove the PUHC solvents via rotary-evaporator. Rotary evaporation is a technique commonly used in organic chemistry to remove a solvent, and with this method (for 24 hours @ 25 °C, 90 rpm in 10 mbar), liquid solvents can be removed without excessive sample heating with reduced pressure (Figure 5.1).



Figure 5.1 Rotary evaporation used to make viscous PUHC (contained in round bottom flask in the water bath) at 25 °C, 90 rpm in 10 mbar.

The dynamic rheological properties of the PUHC ink solution were analysed using an AR-G2 rheometer (TA Instruments, DE) equipped with a Peltier plate thermal controller. The plate geometry with the diameter of the 40 mm and angle 2° was used in all

measurements. The solutions were placed on the plate to reach the equilibrium temperature for 5 min prior to performing the experiments. Storage modulus ( $G'$ ) and loss modulus ( $G''$ ) were measured as a function of temperature and frequency. Sample volumes of 0.9 ml were placed on the plate and temperature sweep experiments were conducted at a rate of  $3\text{ }^{\circ}\text{C min}^{-1}$  from  $25\text{ }^{\circ}\text{C}$  to  $45\text{ }^{\circ}\text{C}$ , at a fixed strain and frequency of 1% and 1 Hz respectively. Frequency sweep experiments were conducted at a fixed strain of 1% from 0.01 to 10 Hz.

### **5.2.2 Thermal Expansion of PUHC**

For measuring the thermal expansion of PUHC two methods were adopted, 1) thermally induced volume change and 2) change in the diameter of the samples (tests were performed on 3 replicates of each sample). The reason for conducting two test methods was to verify the volume change results in context of each other.

#### **5.2.2.1 Method 1: Thermally Induced Volume Change**

PUHC films were made from the formulations discussed in Section 2.1.3 via solution casting in glass Petri dishes. Solvents were removed using a vacuum oven ( $70\text{ }^{\circ}\text{C}$ , -80 Kpa, 12 hrs) to obtain PUHC films. Thermally induced volume change of the PUHC film was investigated by heating it within a silicone oil-filled beaker. This characterisation method is based on that employed by Aziz *et al.*[406] Silicone oil has high thermal stability and is particularly suitable as a high-temperature heat transfer liquid.[407] The sample was placed into the silicone oil in order to measure the volume changes of both the oil and the sample. Figure 5.2a is a visual representation of the experimental set-up used to measure changes in the volume of the sample before and after heating. A laser beam displacement analyzer was used to accurately measure the change in liquid level

and sample volume. Figure 5.2b shows the illustration of a test procedure with silicone oil only as a control (section 1) and sample immersed in silicone oil.[406]

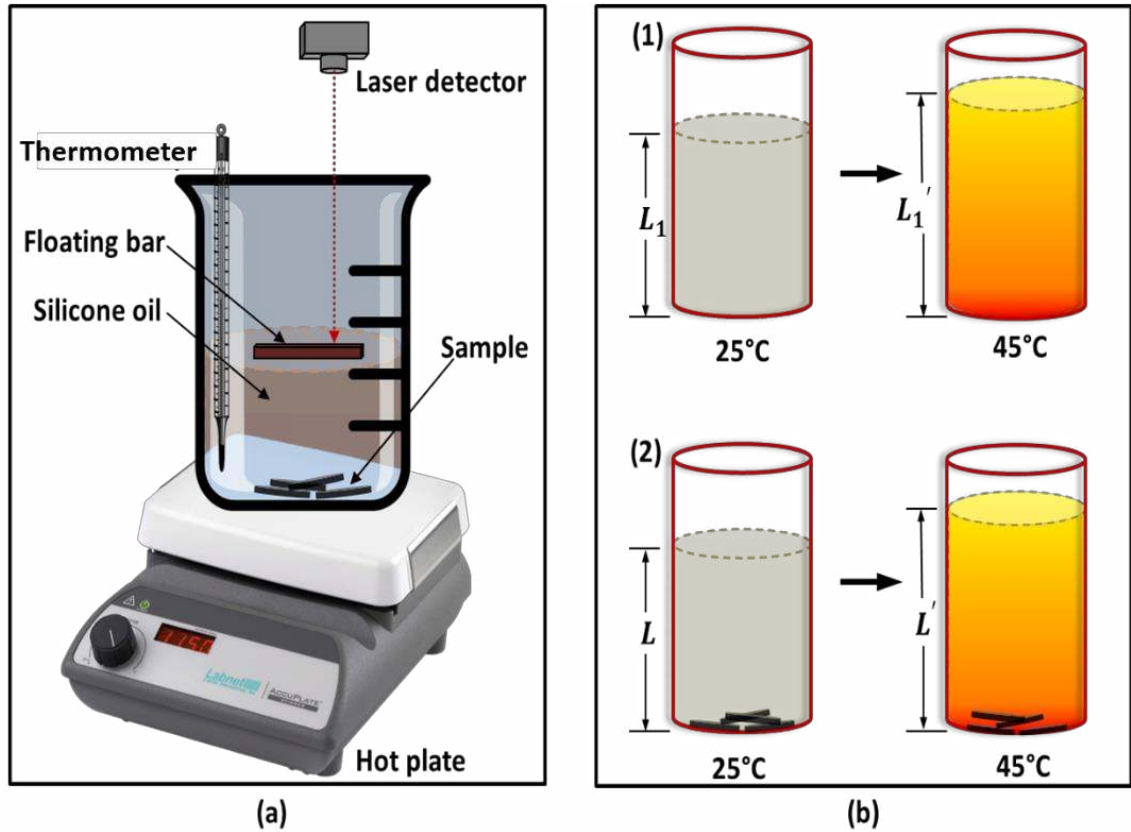


Figure 5.2 a) Schematic drawing of the test set-up. b) Experimental illustration of dimension change in the sample operated in a silicone oil-filled glass beaker (radius  $R$ ); (1) calibration of oil thermal expansion having liquid height  $L_1$  at  $25^\circ\text{C}$ , and  $L_1'$  at  $45^\circ\text{C}$ , (2) Combined thermal expansion of oil with the immersed sample from an initial liquid level  $L$  raised to  $L'$  at  $45^\circ\text{C}$ .

Starting with the same initial volume of oil, the volume changes for the oil-only ( $\Delta V_1$ ) and sample-in-oil cases ( $\Delta V$ ) can be written as:

$$\Delta V_1 = \pi \cdot R^2 \cdot (L_1' - L_1) \quad \text{(Equation 5.1)}$$

V: volume of oil

R: radius of glass beaker

L: liquid height

$$\Delta V = \pi \cdot R^2(L' - L) \quad (\text{Equation 5.2})$$

The change in glass beaker's diameter over the change in volume is considered negligible.

Subtracting equation (5.1) from (5.2), gives the volume change of sample ( $\Delta v$ ):

$$\Delta v = \pi \cdot R^2[(L' - L) - (L_1' - L_1)] \quad (\text{Equation 5.3})$$

#### 5.2.2.2 *Method 2: Measurement of radial change*

To enable confirmation of the physical changes induced by exposure of the sensor sample to elevated temperatures a second test technique was used. A series of images captured from a rigidly mounted microscope camera were used to measure the changes in width and thickness of the sample upon heating. A lever arm transducer was used to measure the length change under a nominal tensile force of ~10 mN in order to keep the sample straight without applying a significant strain. The sample was heated by using an infrared light source, and the temperature change recorded by a thermal imaging camera (Figure 5.3).



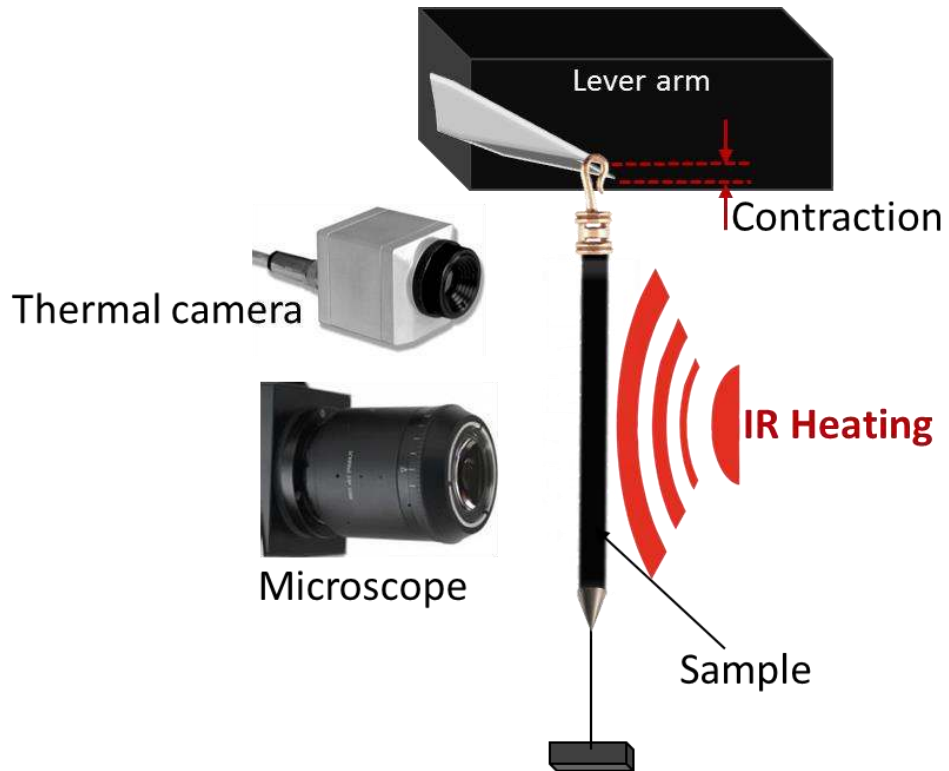


Figure 5.3 Illustration of the microscopic measurement method used to analyze of the thermal dimensional changes of the sample (the figure represents the virtual concept, not the actual facilities).

The volume change induced via thermal expansion was calculated using Equation 5.4 obtained from reference [408]:

$$\Delta v = v_1 - v_0 = (l_1 * w_1 * t_1) - (l_0 * w_0 * t_0) \quad (\text{Equation } 5.4)$$

Here,  $v$ ,  $l$ ,  $w$  and  $t$  are sample's volume, length, width and, thickness, respectively. The subscripts represent the conditions before (0) and after (1) heating, respectively.

### 5.2.3 Thermal Transport Properties of Thin Films

#### 5.2.3.1 *The hot disk thermal constants analyser*

The Hot Disk Thermal Constants Analyzer, (Hot Disk AB, Gothenburg, Sweden and ThermTest Inc.) employs transient plane source (TPS) technique which can measure the in-plane and through-plane thermal conductivity of isotropic/anisotropic material in the same test.[409, 410] In this study, a Hot Disk 500 S was used to measure the thermal conductivity of thin PUHC films that were prepared as mentioned in Section 5.2.2.1. The sensor employed in this test, shown in Figure 5.4a consists of a 10  $\mu\text{m}$  thick double spiral nickel element embedded between two 25  $\mu\text{m}$  thick layers of Kapton polyimide film with an adhesive which gives the total thickness of the sensor of approximately 80  $\mu\text{m}$ . The nickel foil was wound in a double spiral form and had a radius of 6.4 mm. Given the existing TPS method for thin films, the sensor is sandwiched between two identical pieces of a sample supported by a background material, as shown in Figure 5.4b. The background material should be at least ten times more conductive compared to the film specimen.[411] Standard background material (mild steel, SIS2343) provided with Hot Disk TPS analyzer with a thermal conductivity of 13.78 (W/m·K), (Figure 5.4C) was used.

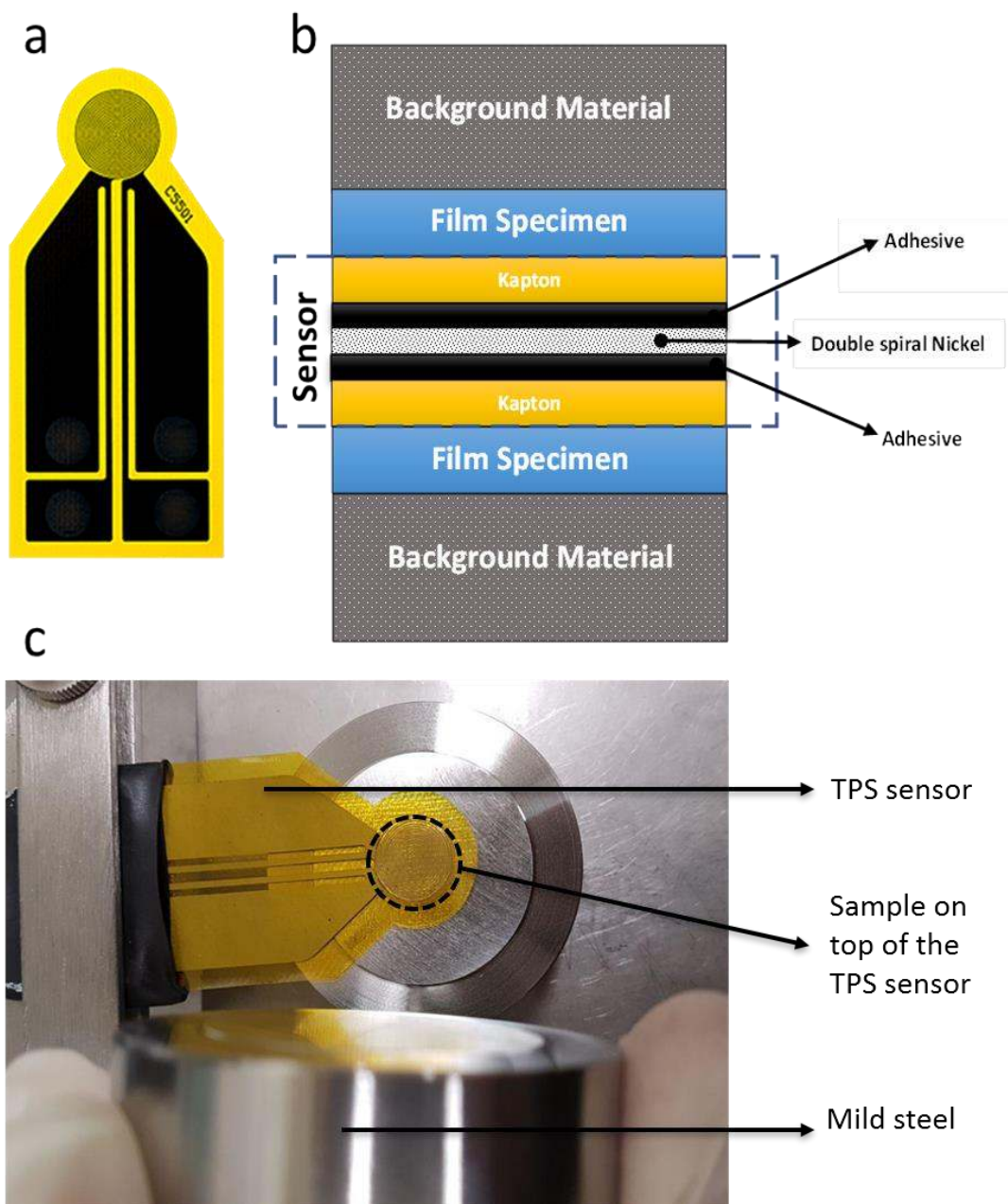


Figure 5.4 Sensor profile and illustration of thin film thermal conductivity measurement. (a) TPS thin film sensor 5501 composed of bifilar spiral structure with concentric equally spaced circular line sources; (b) cross-sectional view of the TPS test column including background materials, thin film specimens and TPS sensor (Insulation layers, adhesive materials and double spiral nickel wires); (c) demonstration of the experiment including background material (mild steel, SIS2343), and TPS sensor.

#### **5.2.4 Ts-PUHC design**

Sensors can be classified into two categories, rigid and flexible. Rigid sensors are utilized in a wide range of applications in the control automation industry. The flexible sensor is fabricated from materials which are malleable to a certain extent without changing its properties and are utilized especially in healthcare monitoring and soft-robotic applications. A sensing system associated with monitoring physiological parameters of the human body involves prominent stress on the sensor, thus potentially leading to damage during normal operation. It is critical to keep this in mind when developing novel sensor materials, prior to fabricating them into a functional device. In order to obtain a PUHC temperature sensor (Ts-PUHC) with the ability to stretch without compromising the performance of the sensor, a range of structural designs were assessed.

Initially, the Ts-PUHC shape was designed in a feature based, parametric solid modelling CAD design software, Solidworks™. As with all modern computer-aided design packages, the next step in producing a printable file is to save a surface based representation of the defined structure as a Standard Tessellation Language (STL) file. This file type is then read by a “Slicer” software tool, in the case of the research an open source product called Slic3r. The purpose of this tool is to take the input .STL data, orientate it in space relative to the proposed build surface and then based on user input variables slice the geometry into incremental layers built upon each other. Typically layers are defined as an outer boundary, the outer contour of the structure to be reproduced, and a corresponding infill within the defined boundary.

The output of the slicer tool is a set of sequential G-code instruction commands (originally developed as an automated means of instructing computer numerically controlled machine tools) that can be read by 3D printing hardware and define the path that has to

be taken by a printer head (extruder) so that the defined geometry can be produced layer-by-layer. In the case of the KIMM SPS1000 system utilised in this body of work, a MACH3 control interface customised to the settings of the pneumatic based extruder system, was used to interpret the generated G-code (porous lattice scaffolds and structures defined simply as a boundary) and translate these instructions to the printer hardware with the most promising being the star shape adapted from Jiang et.al.[412]

### 5.2.5 Fabrication of scaffolds

The scaffolds were printed using the optimized PUHC ink formulation, as described in Section 4.2, on a KIMM SPS1000 biplotter extrusion printing system (Figure 5.5a). The biplotter was equipped with an attachment for syringe deposition connected to a controllable gas pressure regulator.

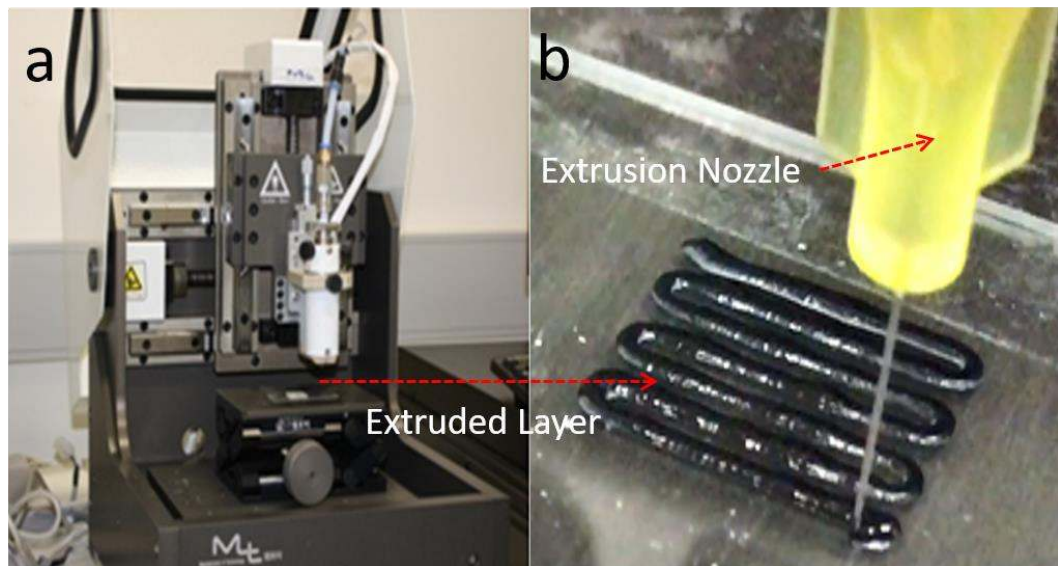


Figure 5.5 a) KIMM SPS1000 printer which is used for this thesis. b) Printed extruded PUHC. (120 kpa was applied and 3cc plastic syringe was used)

The PUHC ink was extruded through a 100  $\mu\text{m}$  diameter nozzle fitted to a disposable syringe (Nordson EFD) at a feed rate of 100 mm/min. These settings produced consistent prints and were applied to all 3D printing undertaken for this study in order to eliminate any variation in parameters and orientation that could influence morphological properties of the printed structure (Table 5.1).

Table 5.1 Summary of 3D printer setting.

<b>Printing setting</b>	<b>Value</b>
<b>Layer thickness</b>	0.1 mm
<b>Distance between lines</b>	1 mm
<b>Feed Rate</b>	100 mm/min
<b>Corner velocity</b>	80% of line acceleration
<b>Nozzle Inner Diameter</b>	0.10 mm
<b>Nozzle Outer Diameter</b>	0.24 mm
<b>Ink temperature</b>	45°C
<b>Print-bed temperature</b>	Lab temperature
<b>Gas pressure (nitrogen)</b>	120 kPa

### **5.2.6 Strain evaluation**

Ts-PUHC film with the dimension of 9 x 20 mm and thickness of 100  $\mu\text{m}$  and the Ts-PUHC 3D printed shapes were prepared and the impact of strain on resistivity was tested in 5 steps between 10% and 50% of strain using a Shimadzu mechanical tester. An Agilent multimeter was connected to a computer and used to measure electrical resistivity of samples. The sample was held for 30 seconds at each step to evaluate the stability of electrical resistivity at a constant strain. The Agilent multimeter was connected to a computer and used to record electrical resistivity of the sample.

### **5.2.7 Evaluating correlation between resistance and temperature in Ts-PUHC**

A rheometer plate was used to change the composite sample temperature and a multimeter used to measure the resistivity of the composite. The temperature was measured via a wire  $\pm 5\%$  10K $\Omega$  thermistor which was integrated with an Arduino setup (Jaycar Australia). Since monitoring body temperature is one of the potential applications for the Ts-PUHC, the experiment was designed to test temperature in the range of 25 to 45 °C.[413]

Ts-PUHC resistance data was collected via Keysight BV0001A and BenchVue Digital Multimeter Pro App (Figure 5.6).

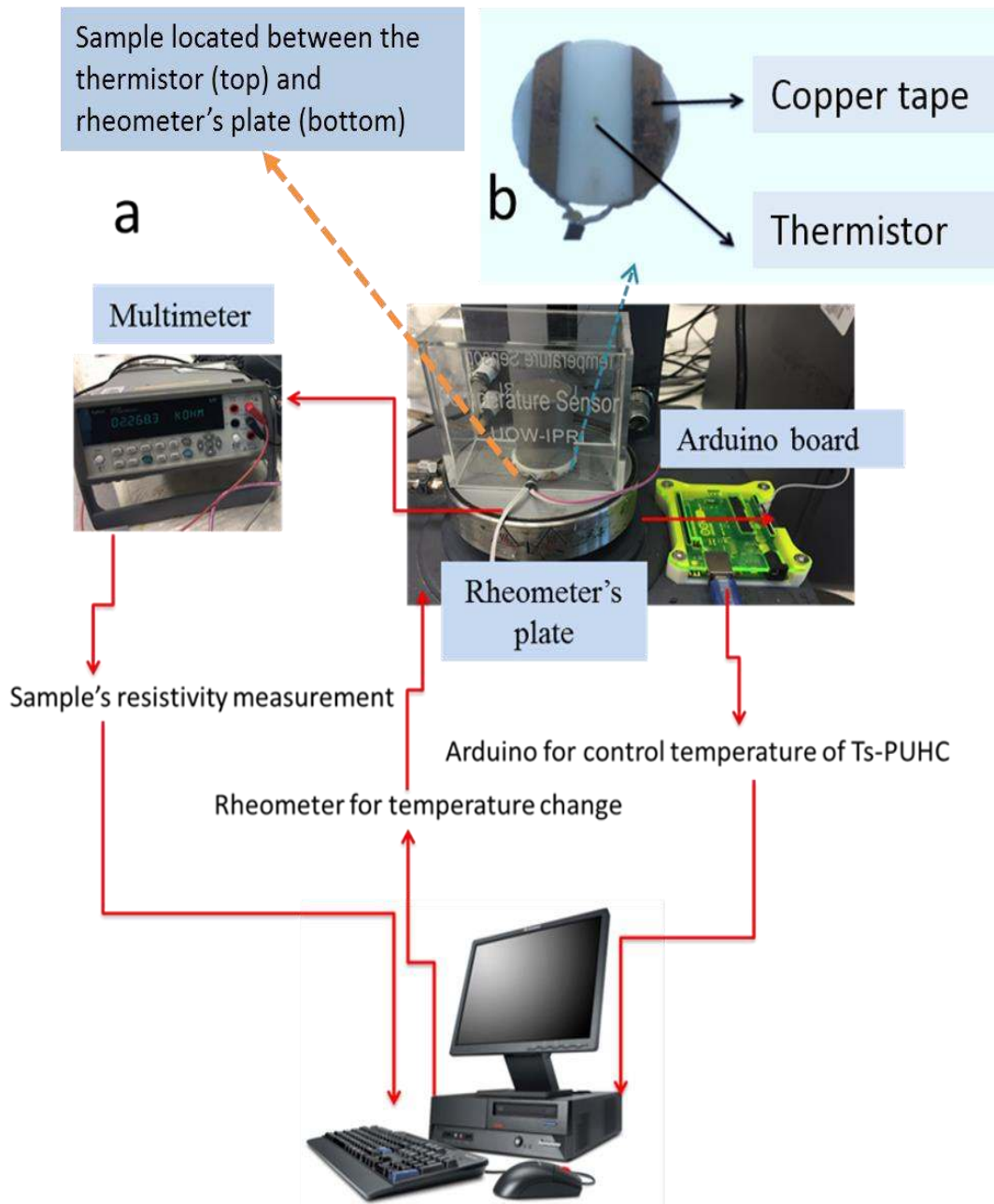


Figure 5.6 a. Experimental setup: temperature control via software managed rheometer hotplate. Thermistor recorded temperature on the top of the sample (b) Enclosed experimental setup to prevent impact on results from ambient air flow impact on results.



## 5.2.8 Paraffin oil treatment of Ts-PUHC

### 5.2.8.1 *Ts-PUHC Stability Evaluation*

The impact of moisture on the electrical and mechanical properties of the Ts-PUHC was evaluated in simulated body fluid (SBF - has the ion concentrations and osmolarity of the solutions that match those of the human body) at 37 °C at various times during 15 days. To prepare 1 L of SBF with pH 7.4, 5.403 g of NaCl, 0.225 g of KCl, 0.504 g of NaHCO<sub>3</sub>, 0.228 g of K<sub>2</sub>HPO<sub>4</sub>·3H<sub>2</sub>O, and 0.312 g of MgCl<sub>2</sub>·6H<sub>2</sub>O were dissolved in 750 mL of Milli-Q water. Then, 3.34 mL of hydrochloric acid (concentrated solution) was added to the solution; 0.071 g of Na<sub>2</sub>SO<sub>4</sub> and 0.388 g of CaCl<sub>2</sub>·2H<sub>2</sub>O, 6.057 g of tris (hydroxymethyl) aminomethane were sequentially dissolved in the solution. Finally, the solution was diluted to 1 L and the pH of SBF was adjusted between 4 and 9 by using hydrochloric acid and sodium hydroxide.[414]

Degradation stability was also measured via monitoring the tensile modulus and elongation at break for Ts-PUHC samples after 3, 5 and 15 days of incubation in SBF at 37 °C.

## 5.3 Result and Discussion

### 5.3.1 Optimization of filler ratio of PUHC

Optimization of the PUHC filler content with respect to thermal and electrical conductivity was performed. Figure 5.7 shows that the thermal conductivity of the PUHC increases sharply with increasing filler ratio until 4% w/w ratio. Increasing the filler ratio to more than 4% w/w shows a marginal increase in thermal conductivity. It can also be

seen that the toughness of the PUHC increases with an increase in filler and reaches a maximum at 8% w/w. Furthermore, the onset of conductivity occurred at ~ 2% w/w loading of fillers and above this loading, the composite conductivity increased almost monotonically with filler loading (Figure 5.7a). Since the thermal conductivity and toughness is at a maximum at 8% w/w ratio of filler and a modest conductivity is also demonstrated, this 8% w/w value was chosen as a candidate weight percent for further PUHC formulation evaluation.

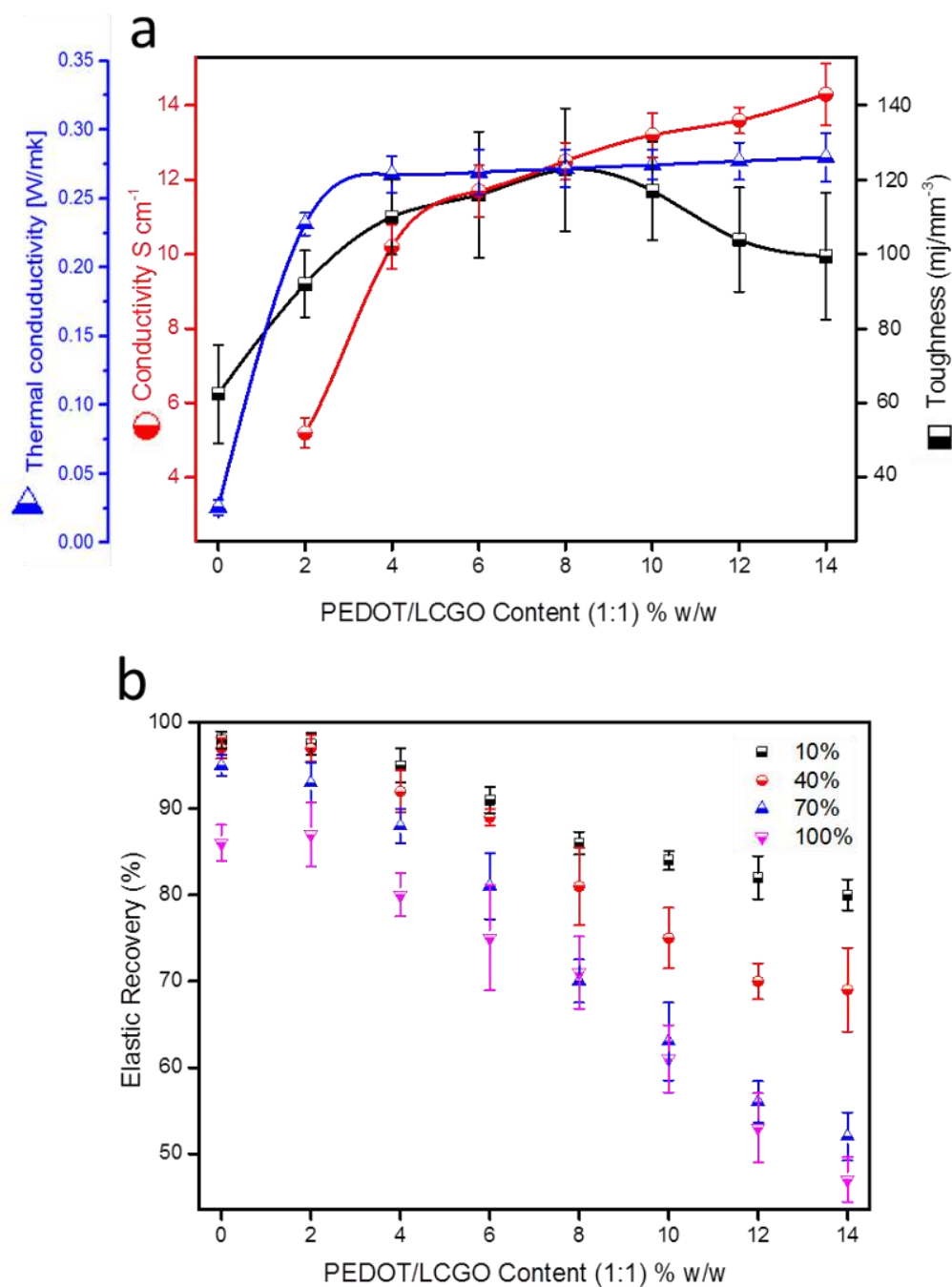


Figure 5.7 a) The toughness, electrical and thermal conductivity of the PUHC after treatment with a 5% aqueous solution of  $H_3PO_2$  acid as a function of filler (LCGO and PEDOT:PSS), b) The elastic recoveries at different applied strains (indicated in the graph) of PUHC as a function of filler loading.

The increase in conductivity may be due to the establishment of LC structure in PUHC (transfer isotropic to nematic structure). Percolation threshold results (discussed in Section 4.3.4 - electrical conductivity of PUHC) comparing the electrical behaviour of LCGO and PEDOT:PSS/LCGO composites suggested that lower amounts of filler are needed to create conducting paths in an insulating matrix of PU. Interestingly, correlation of electrical conductivity with filler ratio does not match with thermal behaviour of PUHC.

It is well documented that at ratios below the percolation threshold the composite conductivity is almost the same as the polymer matrix, and therefore charge carrier transport cannot occur.[415, 416] By increasing the filler loading, the average distance between conducting filler particles in the matrix decreases and below a certain filler loading threshold, charge carrier transport can occur via electrical field assisted tunnelling or hopping between neighbouring fillers.[417, 418] At the percolation threshold, the amount of filler materials is enough to begin the formation of a continuous conductive network throughout the polymer matrix. Combination of complementary conducting fillers such as PEDOT:PSS and LCGO offer an attractive route to enhancing electrochemical performance based on orientation or electronic interaction between PEDOT:PSS and LCGO.

### **5.3.2 Impact of prestrain on PUHC film properties**

The influence of filler content on the mechanical properties of the PUHC film was investigated. The elastic recovery of a material is defined as a non-permanent deformation with the capability of returning to its original shape upon the release of the mechanical stress. The elastic recovery property of PUHC was compared as a function of filler loading and applied strain between 10% to 100% (between the elastic deformation region

of PUHC). Figure 5.8 shows that for all applied strains, the elastic recovery of PUHC decreased with increasing filler loading. For example, at 40% applied strain PU film (no filler) has an elastic recovery of  $\approx 97\%$ . However, significant reduction in elastic recovery to values of  $\approx 89\%$  and  $\approx 69\%$  for the filler ratio of 4% and 8% respectively was observed. Research on the effects of prestrain on molecular orientation in different segments of the block-polymer chain provides a basis for the interpretation of mechanical property data. [419, 420] PU has a hetero-phase microstructure [421] and by monitoring the behaviour of N-H (hard segment) and C-H (soft segment) infrared stretching absorptions, it has been shown that the orientation of both segments strongly depends upon strain history. Upon initial straining, both segments orient similarly but after relaxation, the hard segments remain oriented to a substantially higher degree than soft segments.[422, 423] The orientation of the soft segment groups is unaffected by the prestrain.[424] The elastic recovery of PUHC was investigated as a function of the percentage of prestrain (Figure 5.8a) and shows the elastic recovery of PUHC increased with increasing prestrain until 40% and dropped at 50% prestrain. Figure 5.9b showed the impact of prestrain on toughness (from 124.6 to 79.8 mJmm<sup>-3</sup>), electrical (from 12.15 to 6.71 Scm<sup>-1</sup>) and thermal conductivity (from 0.2512 to 0.3024 W/(m.K)) of PUHC after 40% prestrain equating to 24% and 46% decrease in toughness and electrical conductivity respectively and 8% increase in thermal conductivity. Reduction of electrical conductivity may be explained by the fact that conductive paths have been destroyed during the prestrain. Phonons are quantized modes of vibration in a rigid crystal lattice, which is the fundamental mechanism of heat conduction in most polymers.[425] Polymers in the amorphous state are usually considered to have many defects that contribute to numerous phonons scattering, leading to low thermal conductivity. So, the increase in thermal conductivity

after prestrain can be explained by the increase in the degree of hard segments orientation (i.e., an increase of the degree of crystallinity in PUHC).

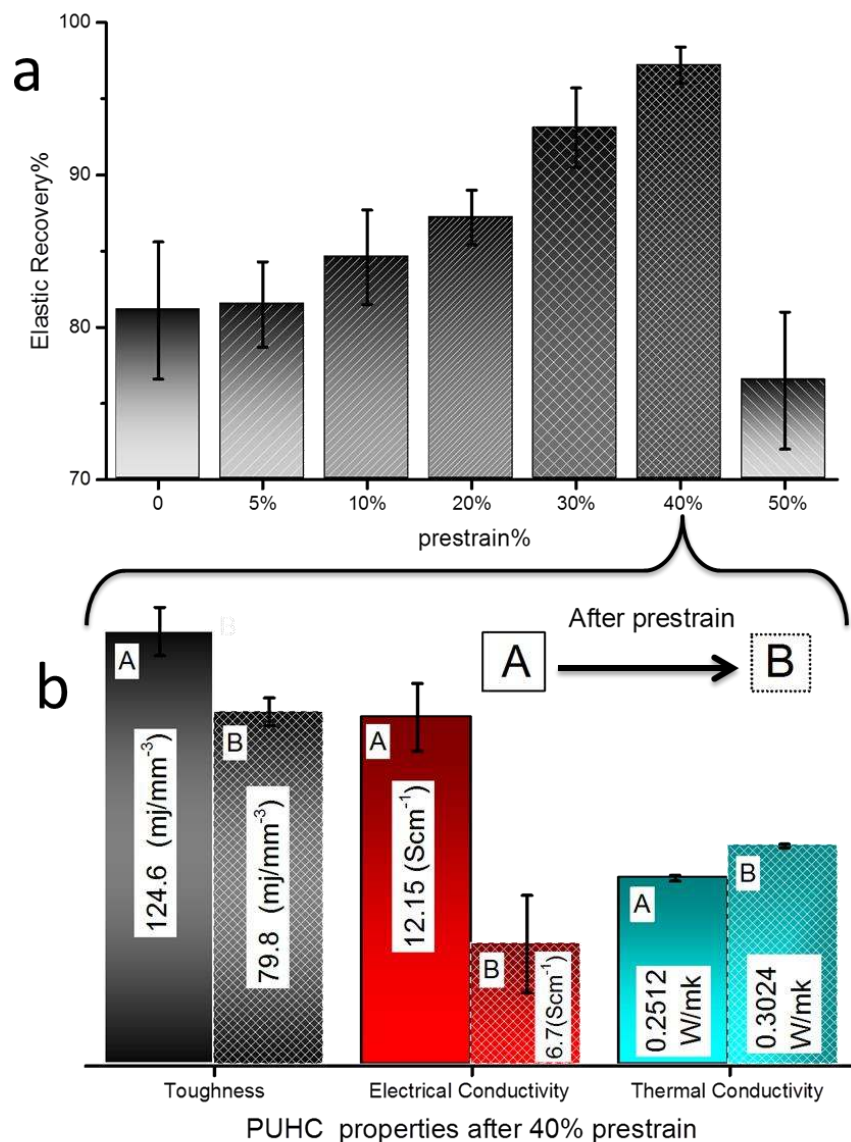


Figure 5.8 Impact of prestrain on PUHC film (8 %w/w LCGO/PEDOT:PSS at 1:1 and treated with a 5% aqueous solution of  $\text{H}_3\text{PO}_2$  acid) properties. a) correlation between the percentage of prestrain on elastic recovery, b) Effect of 40% prestrain on toughness, the electrical and thermal conductivity of PUHC. A indicates the value before prestrain and B represents the value after prestrain. The tests were repetitively conducted 5 times for each sample, and the standard deviation is shown in the plot.

### **5.3.3 Asymmetric Thermal Volume Expansion of Sample**

Thermal expansion is defined as the fractional change in dimension of a composite under heating or cooling through a given temperature range. It is a key material property especially when a composite structure works in a temperature-changing environment. However, although rare, some materials contract upon heating under constant pressure and are referred to as negative thermal expansion (NTE) materials. For measuring the thermal expansion of the PUHC two methods were adopted, 1) thermally induced volume change and 2) change in the diameter of the samples. In order to gain confidence in the data obtained regarding thermal expansion, these two methods were employed as a comparison.

#### **5.3.3.1 *Thermally Induced Volume Change***

Method 1 is described in Section 5.2.3.1. Samples were heated slowly in an oil-filled glass beaker to experimentally measure the volume change as shown in Figure 5.9. A negative thermal volume expansion (or, thermal contraction) of ~6.4% was observed over a 20 °C range from 25 °C to 45 °C.

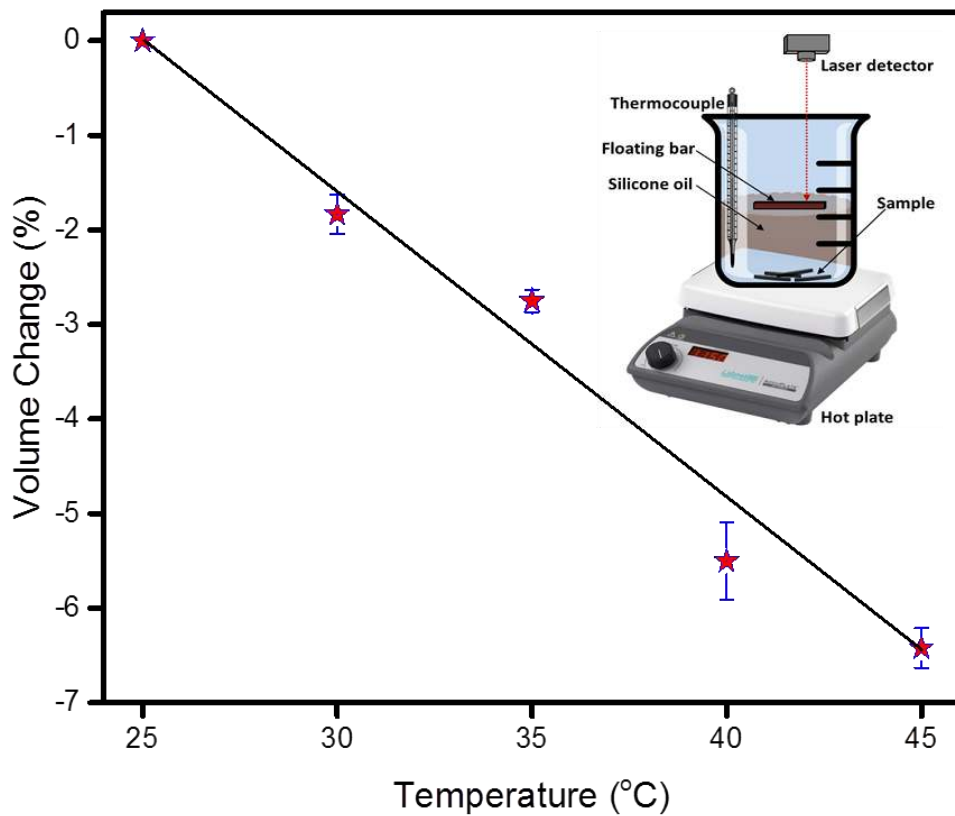


Figure 5.9 Thermally induced expansion of the sample normalized from the overall expansion of sample-in-oil at 25°C and after heating to 45°C.

The method used to measure the radial change of the sample is described in Section 5.2.2.2. Experimentally measured volume contraction of the sample was found to be ~5.2% by using the results extracted from three-dimensional volume changes when heated from 25°C to 45°C (Figure 5.10 shows the results for heating range from 25°C to 45°C).



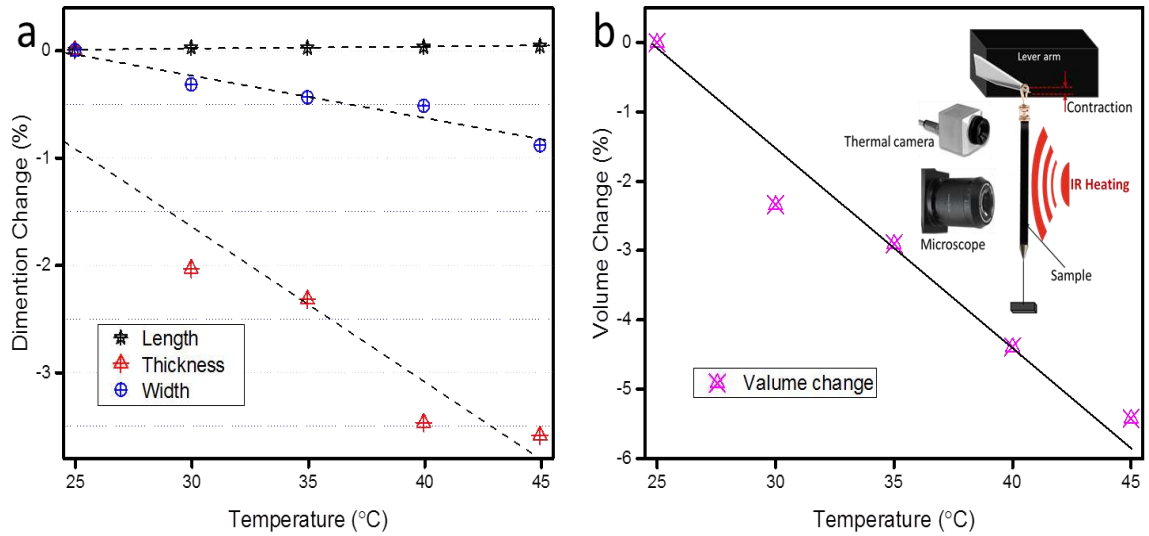


Figure 5.10 Thermally induced expansion of the samples a) dimension change (%) and b) normalized to the volume at 25°C and afterwards heated to 45°C.

PUHC demonstrates NTE behaviour. Computational results suggest that in-plane expansion, bond stretching, and bond bending effects in graphene sheet cancel each other out, leading to a negative thermal expansion coefficient in the plane of orientated graphene sheets.[426-427] The elastomeric PU is semi-crystalline in structure and exhibits a little volumetric change when heated to the melting temperature. The effect of thermal expansivity of PU is not so obvious within the nominate testing range (25-45°C) under which PUHC was examined. A notable negative thermal expansion coefficient was demonstrated previously when the PU is heated over 50 °C. However, applying such high temperature to the PUHC is not practically feasible in the field of wearable sensor technology. [428]

### 5.3.4 Rheological Evaluation of PUHC Ink

The rheological and thermo-rheological properties of the PUHC ink was determined as a function of ink composition. Understanding the rheological behaviour of the material is important in order to ensure successful processing of the ink during a manufacturing process, such as 3D printing.

Figure 5.11 illustrates the viscosity values of PUHC (8 %w/w LCGO/PEDOT:PSS at 1:1) composites as a function of shear rate. The samples underwent a period of rotary evaporation as indicated in the Figure 5.11 (2, 5, 12 and 24hrs) which were compared to an untreated sample (original solution). All samples show shear-thinning behaviour as the shear rate increased. At higher shear rates, the viscosity of all the samples became less shear rate-dependent due to a reduction of polymer chain entanglements and drop in viscosity.

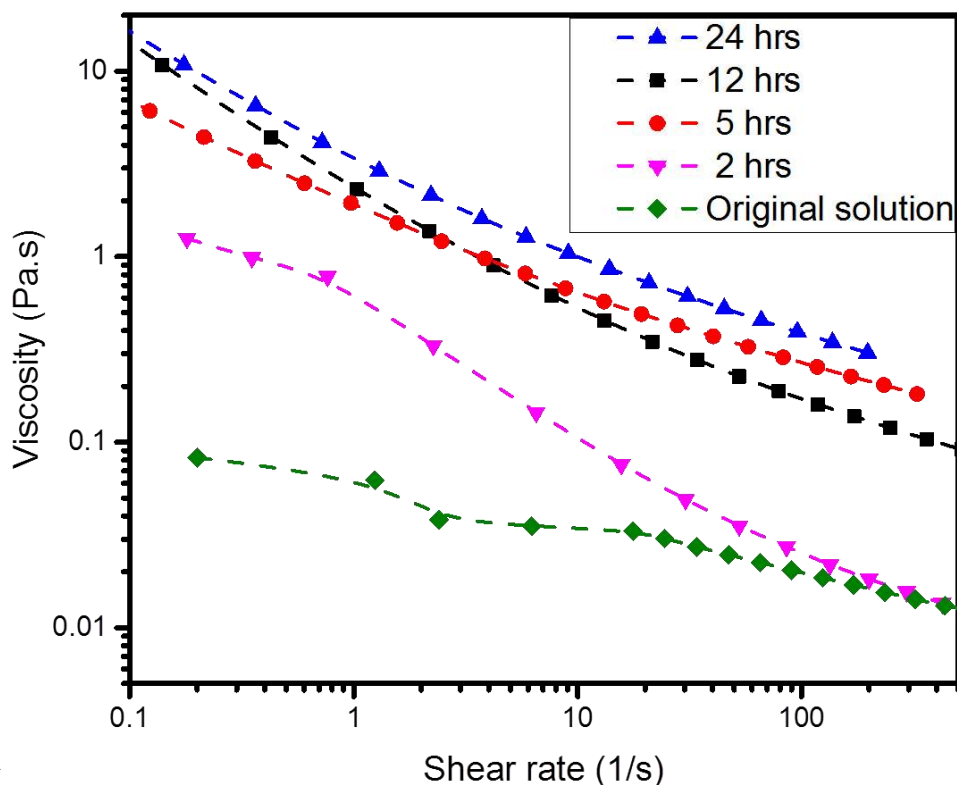


Figure 5.11 PUHC (8%w/w LCGO/PEDOT:PSS at 1:1) ink preparation via rotary-evaporator. Viscosities were measured after rotary-evaporation at various times. The viscosity of PUHC dispersions were measured in the shear rate ranging between 0.1 and 800 Hz.

Monitoring of the thermo-rheological behaviour of the composites during processing is a key factor in their ability to be 3D fabricated. Mechanically, the ink requires sufficient strength and stiffness to maintain structural integrity during and after printing. In order to successfully build 3D structures, the first layer needs to have structural integrity before the second layer is deposited. Consequently, parameters such as polymer rheology and the gel-forming mechanism are critically important; polymer solutions must be either viscous and viscoelastic initially, and then become a self-supporting structure before additional layers are added. To evaluate the printing processability of the PUHC (8 %w/w LCGO/PEDOT:PSS at 1:1) samples, their rheological properties were investigated.

Samples that underwent rotary evaporation for a period greater than 24hrs were not readily printable due to a high viscosity, requiring extrusion pressures in excess of 400kPa and providing inconsistent print results in combination with frequent extrusion tip blockages. Samples which underwent rotary evaporation for a period of 24hrs displayed a consistent viscosity and predictable shear thinning behaviour leading to reliable and repeatable printing

Storage modulus ( $G'$ ) and the loss modulus ( $G''$ ) of PUHC inks were measured as a function of temperature (Figure 5.12). It was observed that samples behave as viscous fluids, where  $G'$  is more dominant than  $G''$ . The dominance of  $G'$  means that the ink behaves like a fluid with insufficient  $G''$  to hold the shape of the printed ink. An increase is observed in  $G'$  and decreases in  $G''$  of PUHC with increasing temperature until 45 °C. The ratio  $G''/G'$  which is  $\tan(\delta)$ , is a measure of the internal friction of the material. When  $G''$  is higher than  $G'$  then  $\tan(\delta)$  is  $> 1$  and one can say that the sample is more viscous than elastic, and vice versa when  $G'$  is higher than  $G''$  and  $\tan(\delta)$  is  $< 1$ . The results indicate that temperature can be utilized effectively to develop 3D printable gels with controllable properties.

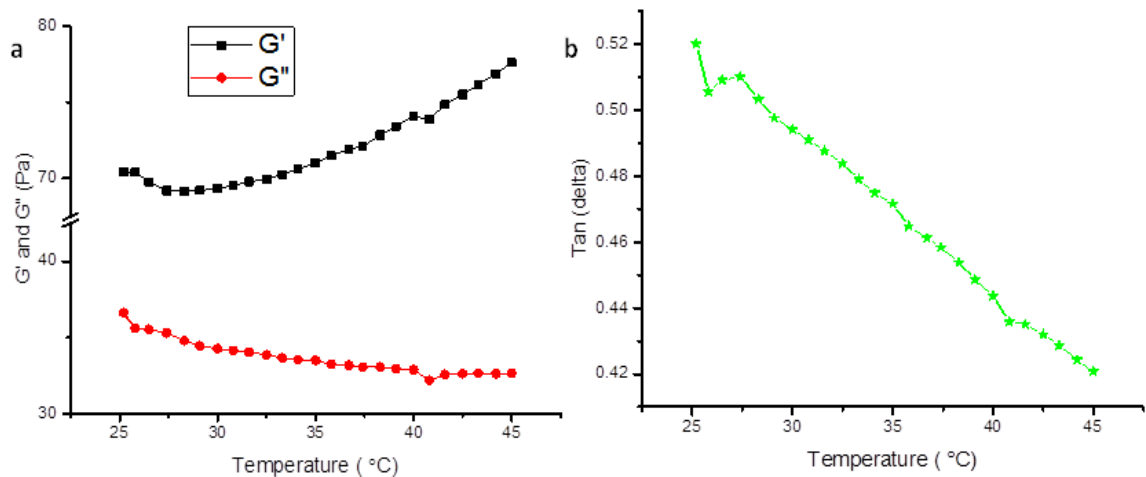


Figure 5.12 Rheological analysis of PUHC ink (8%w/w LCGO/PEDOT:PSS at 1:1) after use of rotary-evaporator to increase viscosity after 24 hrs, a) Temperature dependence of  $G'$  and  $G''$  for PUHC dispersion and b) the trend of  $\tan(\delta)$  between 25-45 °C.  $\tan(\delta) = G'' / G'$

### 5.3.5 3D printing of PUHC scaffolds (45 °C)

As demonstrated above, remarkable improvements in the rheological properties of PUHC ink compared to the original PUHC solution were achieved, however, it is also crucial to obtain excellent materials processability for practical application. The processability of the PUHC composites was therefore investigated through printing the 2 layers and multilayer lattice structure at 45 °C (Figure 5.13). The feasibility and materials behaviour was initially studied during the printing of the first layer. It was noticed that the physical properties (viscosity and storage modulus) of PUHC ink is significantly robust (Section 5.3.3), and it is not necessary to go through any post-treatment of 3D printed structure such as reinforcement, post-print cross-linking or photo-cured steps. Solution printing process was adopted, and PUHC with 8%w/w LCGO/PEDOT:PSS at 1:1 content was able to be printed successfully into scaffolds of 10 mm × 10 mm × 700 μm height

dimension with pore size of approximately 500  $\mu\text{m}$  (Figure 5.14a) and  $15 \times 15 \text{ mm} \times 100 \mu\text{m}$  height dimension with pore sizes of around 589  $\mu\text{m}$  (Figure 5. 13b).

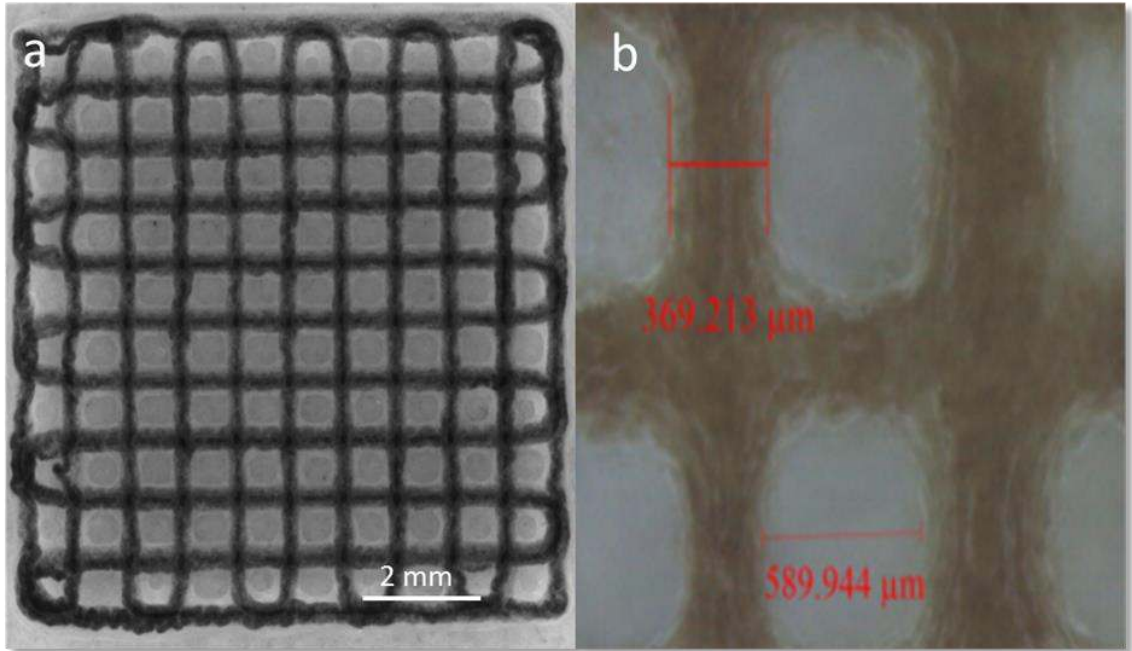


Figure 5.13 Optical image of extrusion printed 3D scaffolds PUHC ink (8%w/w LCGO/PEDOT:PSS at 1:1) after use of rotary-evaporator for 24 hrs. a) Multi-layer with dimensions of  $10 \times 10 \text{ mm}$ . b) 2 layers lattice structure's morphology.

#### 5.3.5.1 3D printing of the stretchable design

Flexible and stretchable sensors hold several advantages compared to current wearable sensors based on rigid substrates, and may eventually lead to revolutionary changes in the field of continuous and long-term health monitoring devices to tackle social health challenges.[429, 430] Flexible and stretchable temperature sensors offer maximum compliance to the skin. Thus, the minimum reaction force is produced from the sensor due to structural deformation. Since skin deformation can vary a sensor dimensions by up to 30% [431], it is important to evaluate the stretchability, sensing stability, precision, and repeatability parameters of Ts-PUHC when employed as temperature sensor for

direct placement on skin. Stretching the Ts-PUHC causes a change in the distance between the conductive filler particles contained in the nonconductive matrix. Furthermore, materials used in skin sensors follow a rule that the bending strain of the materials decreases linearly with a thickness of materials. So, in this circumstance resistance changes are affected by temperature and the amount of stretch. This change could be reversible or non-reversible based on the quantity of stretch and composite mechanical properties and therefore demands alternative approaches to obtain stretchable sensors for health monitoring. Several designs were proposed to achieve the fabrication of a stretchable Ts-PUHC. For this thesis, three different structural designs (Figure 5.14) were investigated which were previously developed by others.[2, 432-434] The star-shaped Ts-PUHC (Figure 5.14b) had reversible resistance values (within experimental error) (Figure 5.15a). The resistance change values were taken from 5 samples and shows that it was possible to perform repeat experiments from the same sample in the strain range shown. This star shaped structural strategy was considered for further characterization in the context of this thesis. The honeycomb and horseshoe design of the printed Ts-PUHC did not show shape reversibility with this composite (Figure 5.14a and c).

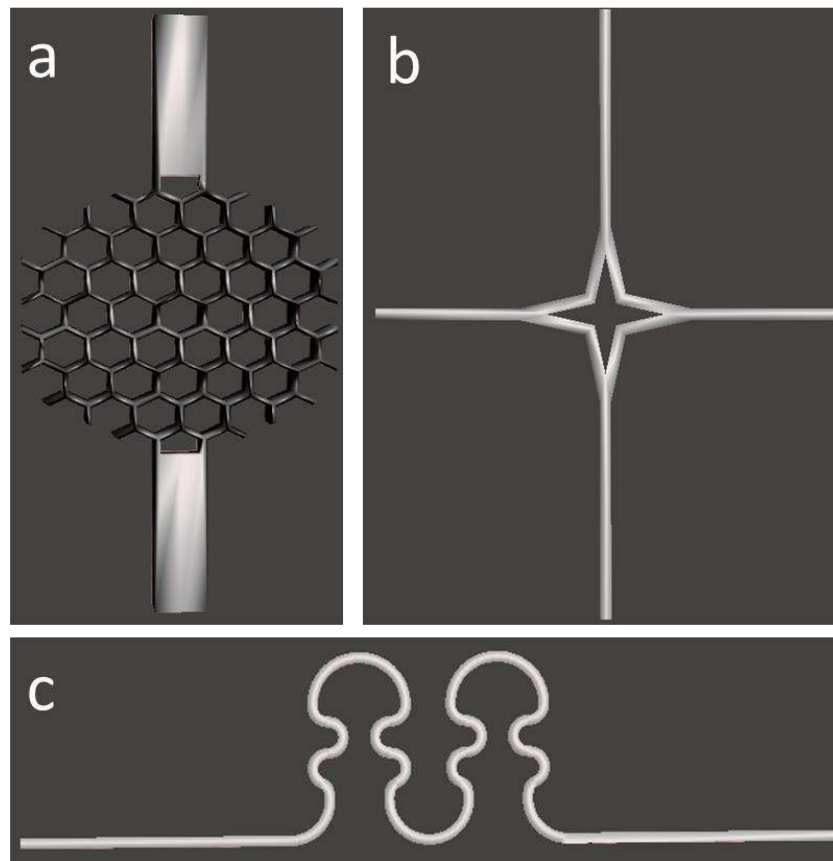


Figure 5.14 Solidworks images of 3 candidates stretchable design for PUHC a) Honeycomb design.[2], b) Star design.[412], and c) horseshoe design[432].

Stretching the Ts-PUHC film in the range of 10 – 50 % causes an increase in the distance between the conductive filler particles, PEDOT:PSS and LCGO, contained in the nonconductive matrix (Figure 5.15) while the star designed structure for Ts-PUHC demonstrated considerable tolerance to the deformation. The experimental data show that for stretching  $\geq 40\%$  along both x and y-axes of star Ts-PUHC that there is an increase in electrical resistance under strain. It should be noted that when the strain is  $\leq 40\%$ , there is no difference in the resistance increase as strain % is increased. This is likely due to the star design being tolerant to geometric changes of  $\geq 40\%$ . However, at strains greater than 40% a significant increase in resistance is observed. This may be due to this strain causing



an increase in the distance between the conductive filler particles, therefore decreasing the electronic pathways (percolation). This property attributed to the elasticity property of Ts-PUHC and cause reversible extension in response to the strain forces up to 40% in both x and y-axis.

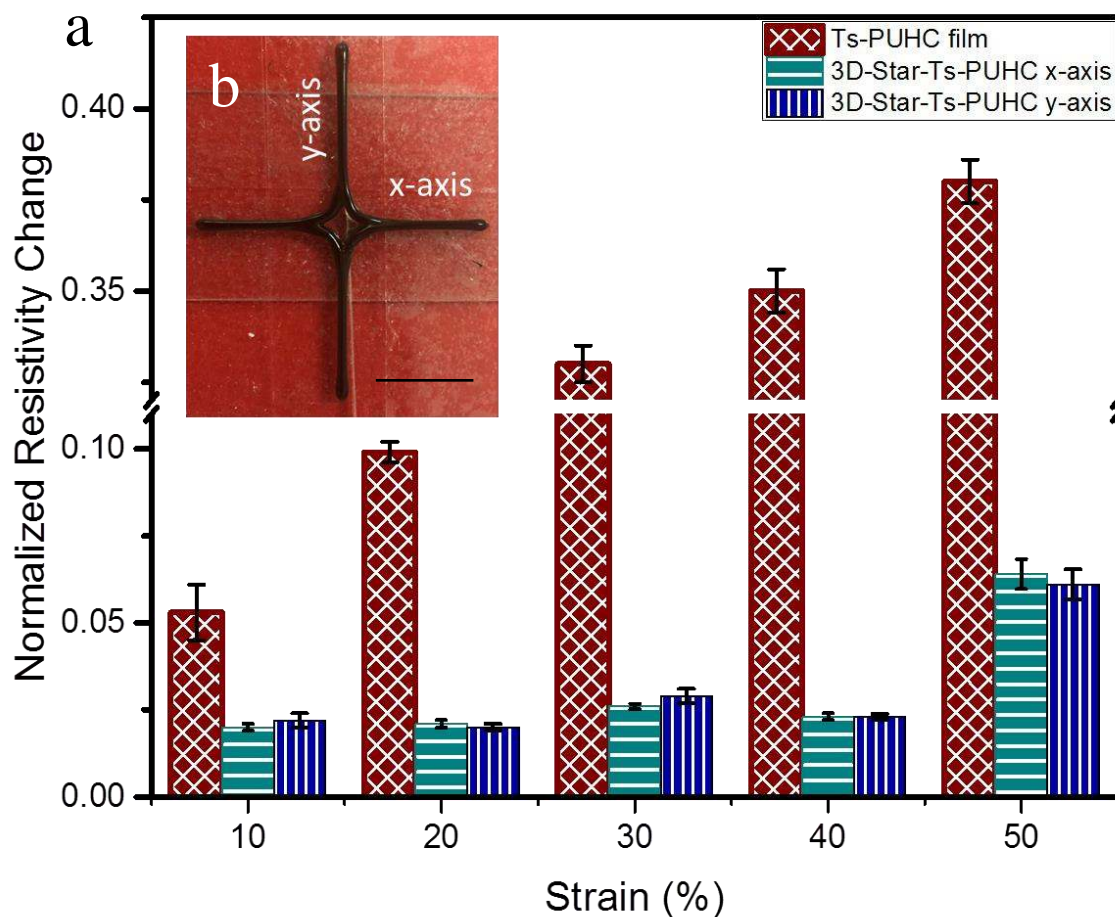


Figure 5.15 Plot of normalized electrical resistivity of Ts-PUHC (8%w/w LCGO/PEDOT:PSS at 1:1 and treated with a 5% aqueous solution of  $H_3PO_2$  acid) film and 3D printed star design of Ts-PUHC b) 3D printed star design of Ts-PUHC. The tests were repetitively conducted for 5 times for each sample and the standard deviation is shown in the plot. The scale bar represents 1 cm.

### 5.3.6 Scanning electron microscopy

Scanning electron microscopy (SEM) was used to determine the quality of the dispersion of fillers in the polymer matrix and impact of the 3D printing process on the composite structure. Figure 5.16 shows that the surface of the PUHC are uniform without any observable fillers agglomeration or aggregation, indicating a homogenous dispersion of PEDOT:PSS and LCGO within the PUHC matrix.

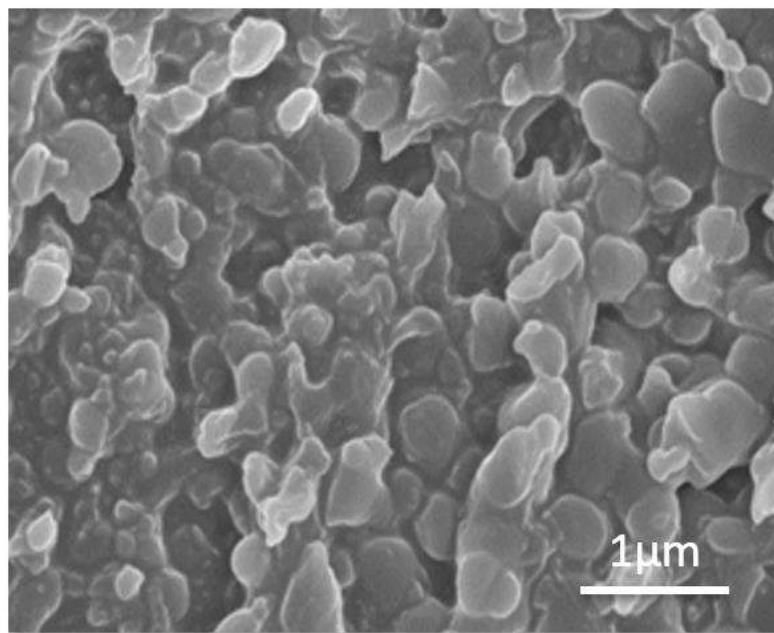


Figure 5.16 SEM images of the surface of the 3D printed Ts-PUHC (8%w/w LCGO/PEDOT:PSS at 1:1 and treated with a 5% aqueous solution of H<sub>3</sub>PO<sub>2</sub> acid). The scale bar represents 1 μm.

### 5.3.7 Effect of moisture on Ts-PUHC performance

Temperature sensors based on electrically conductive composites are challenged by environmental moisture. In this section, the effect of moisture on the printed Ts-PUHC performance (Figure 5.17a) was investigated through exposure of the material to simulated body fluid (SBF). The ultimate goal of the Ts-PUHC is for monitoring body temperature, therefore, to allow for continuous body temperature assessment and monitoring it is critical to design a sensor whose performance is not affected by moisture. The change of electrical resistance with temperature of the Ts-PUHC is presented in Figure 5.17. The temperature was changed between 25 and 45 °C for 5 cycles. Ts-PUHC (Figure 5.17a) electrical resistance at 25 °C was 28.3 MOhms. As the temperature increased up to 45 °C electrical resistance decreased to 11.82 MOhms and showed NTC behaviour, electrical resistance decreases with increased temperature. It was observed that the performance of the Ts-PUHC was affected by moisture (Figure 5.17b). This instability in resistance is typically accompanied by an increase in volume and can cause significant change in sensor response. One of the key factors for making stable and predictable temperature sensors is preventing the influence of changes in ambient humidity and pH on temperature sensing performance. This could be achieved by encapsulating the sensor in a coating that is pH resistant, electrically isolated, has a higher or equal thermal diffusivity and equal or lower heat capacity compared to Ts-PUHC.

To provide this encapsulating coating, Ts-PUHC samples were submerged in 10 cm<sup>3</sup> of paraffin oil at room temperature for 10 s ensuring complete coverage of the sample surface. Coated samples were then air dried for 24 hrs on a coarse mesh to allow excess oil to be removed via gravity. In Figure 5.17c the impact of this paraffin oil treatment on Ts-PUHC performance was investigated and it shows that there is no detrimental effect

on Ts-PUHC behaviour after paraffin treatment (compare responses in Figure 5.17a and 5.17c). The data in Figure 5.17d shows paraffin oil treated Ts-PUHC in presence of SBF had a predictable performance, namely, increase in resistance upon cooling. Covering the Ts-PUHC with a hydrophobic material such as paraffin oil appears to stabilise the Ts-PUHC performance (Figure 5.17d)

Moreover, immersion of Ts-PUHC in paraffin as a technique for protection from humidity variation is also compatible with the flexible structures proposed earlier and would have limited impact on the stretch properties of the material, paraffin oil is electrically isolated, has a high thermal conductivity ( $0.133 \text{ w/m}^\circ\text{k}$ ), and heat capacity ( $1.67 \text{ kj/kg}^\circ\text{k}$ ).

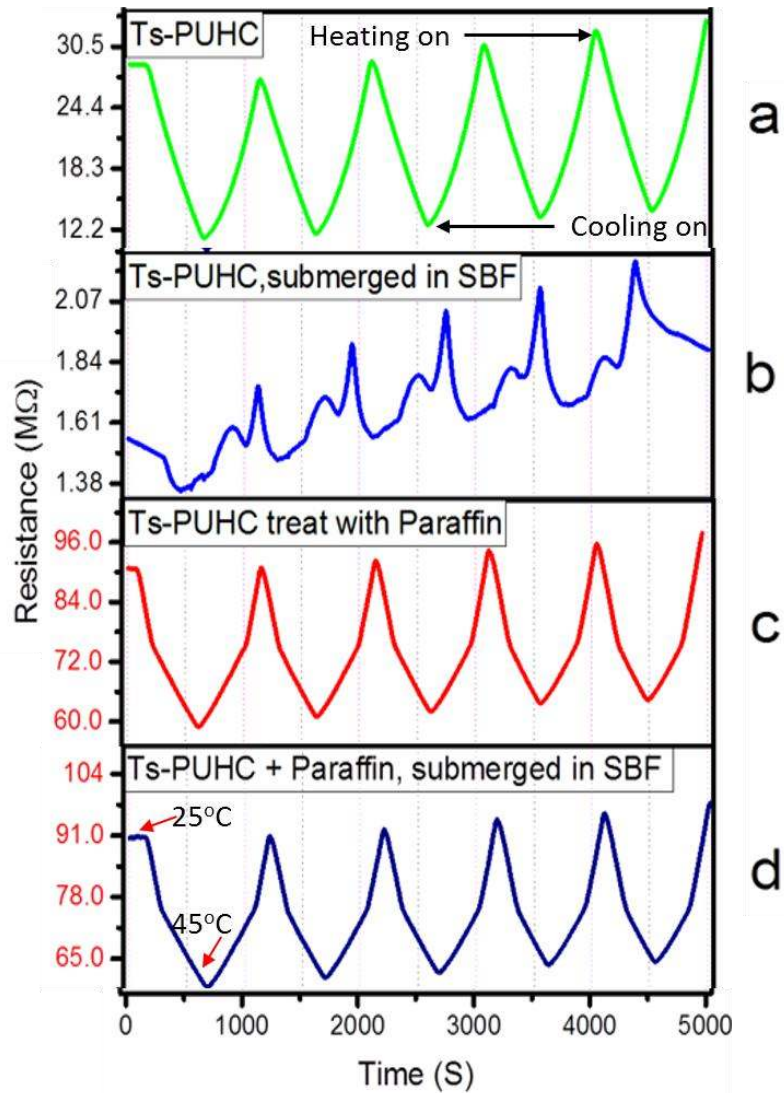


Figure 5.17 Temperature sensing behaviour of a) 3D printed Ts-PUH b) Ts-PUHC submerged in SBF solution with pH 7.4 for 5 minutes and c) treated Ts-PUHC with paraffin oil and d) paraffin oil treated Ts-PUHC submerged in SBF solution with pH 7.4 for 5 minutes. The experiment was designed to test temperature in the range of 25 and 45° C for 5 cycles.

### 5.3.8 Effect of pH on Ts-PUHC performance

Another key factor for making a stable and predictable Ts-PUHC sensor is stability at various pH. Coating or encapsulating the sensor could be employed to protect against

potential pH variation.[435, 436] Skin, is influenced by pH. The pH of healthy skin is mildly acidic (pH 4–6). However, when the skin is damaged this acidic environment is disturbed as the body's internal pH of 7.4 is exposed.[437] The pH of the unhealthy or healing skin can reach as high as 9.0.[438] Due to these factors, the effects of exposing the TS-PUHC to moisture at a variety of pH was evaluated.

To investigate the Ts-PUHC performance at various pH samples were exposed to three different pH levels. Figure 5.18 shows the effect of pH and SBF intake into paraffin oil treated and untreated Ts-PUHC films. Untreated Ts-PUHC shows significant resistance change in the presence of moisture (Figure 5.18a) at various pH. When paraffin treated, the resistance of the Ts-PUHC was greater at all pH levels compared to the untreated. However, there was no variation in the resistance for the treated Ts-PUHC as pH was varied. This result shows electrical and SBF uptake stability of paraffin coated Ts-PUHC. Figure 5.18b shows stability of paraffin treated Ts-PUHC in the presence of SBF.

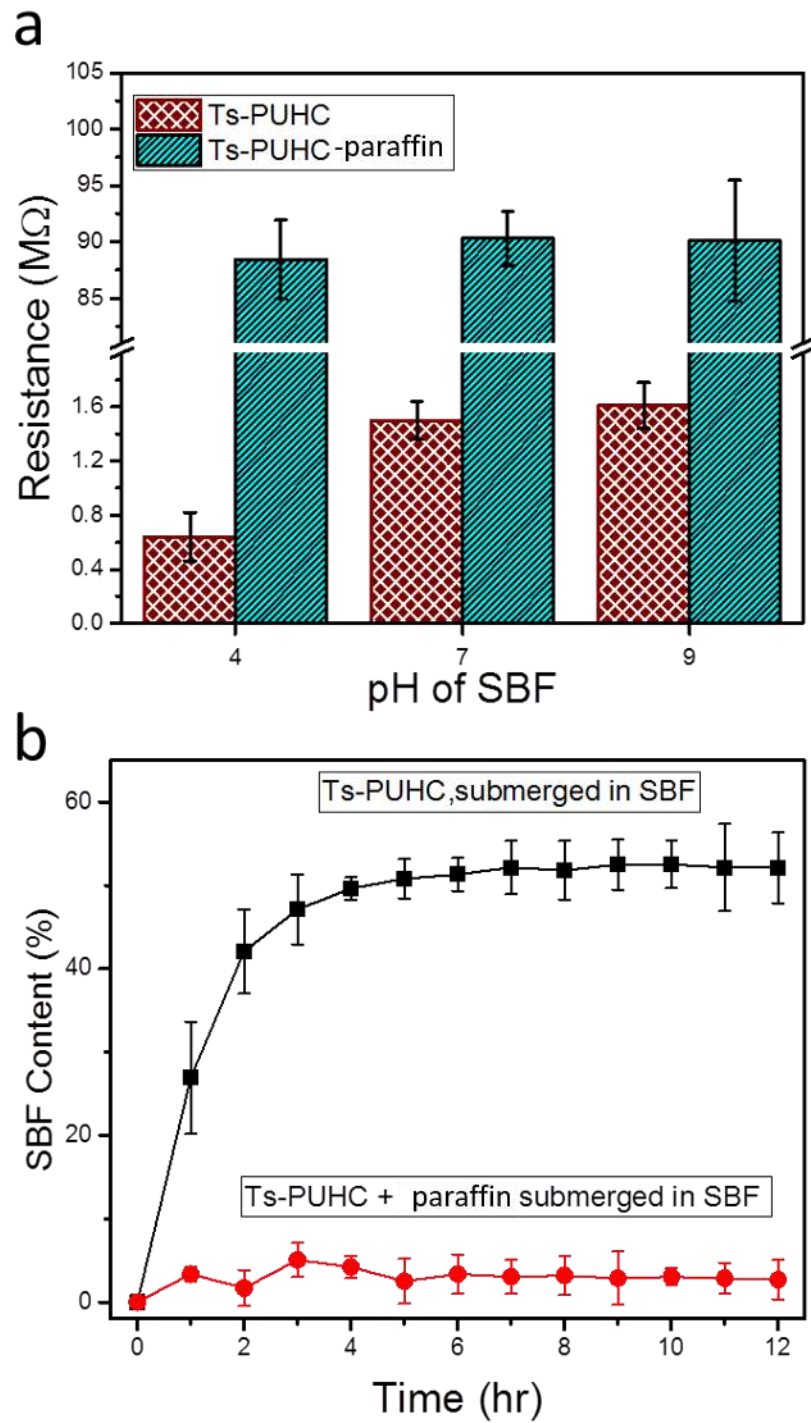


Figure 5.18 a) effects of pH on the electrical resistance of Ts-PUHC and treated Ts-PUHC with paraffin oil. b) SBF uptake at (pH 7.4) exposure time on Ts-PUHC and paraffin treated Ts-PUHC, measured by mass ratio analysis.

Coating of the Ts-PUHC with paraffin appears to stabilise the response at different pH levels and moisture contents however it does significantly increase the resistance measured. It should be noted that whilst the treatment process achieves stability it may cause the sensor resistance to be too high and thus outside the operable range of a sensor.

### **5.3.9 Impact of Simulated Body Fluid (SBF) on Ts-PUHC mechanical properties**

The degradation behaviour of Ts-PUHC and paraffin treated Ts-PUHC in SBF at pH 7.4 (37 °C) for 15 days in vitro was investigated through changes in Ts-PUHC stiffness and elongation at break and results compared with control samples (Ts-PUHC) in SBF. There were no noticeable differences between the control samples elongation at break and stiffness when compared to paraffin treated Ts-PUHC samples.

The stiffness as a function of time and the values of elongation at break at each time point are presented in Figure 5.19a and 5.19b respectively. The tensile modulus and elongation at break for Ts-PUHC-paraffin remains constant while a significant drop in stiffness and elongation at break in uncoated Ts-PUHC were evident over the testing period.



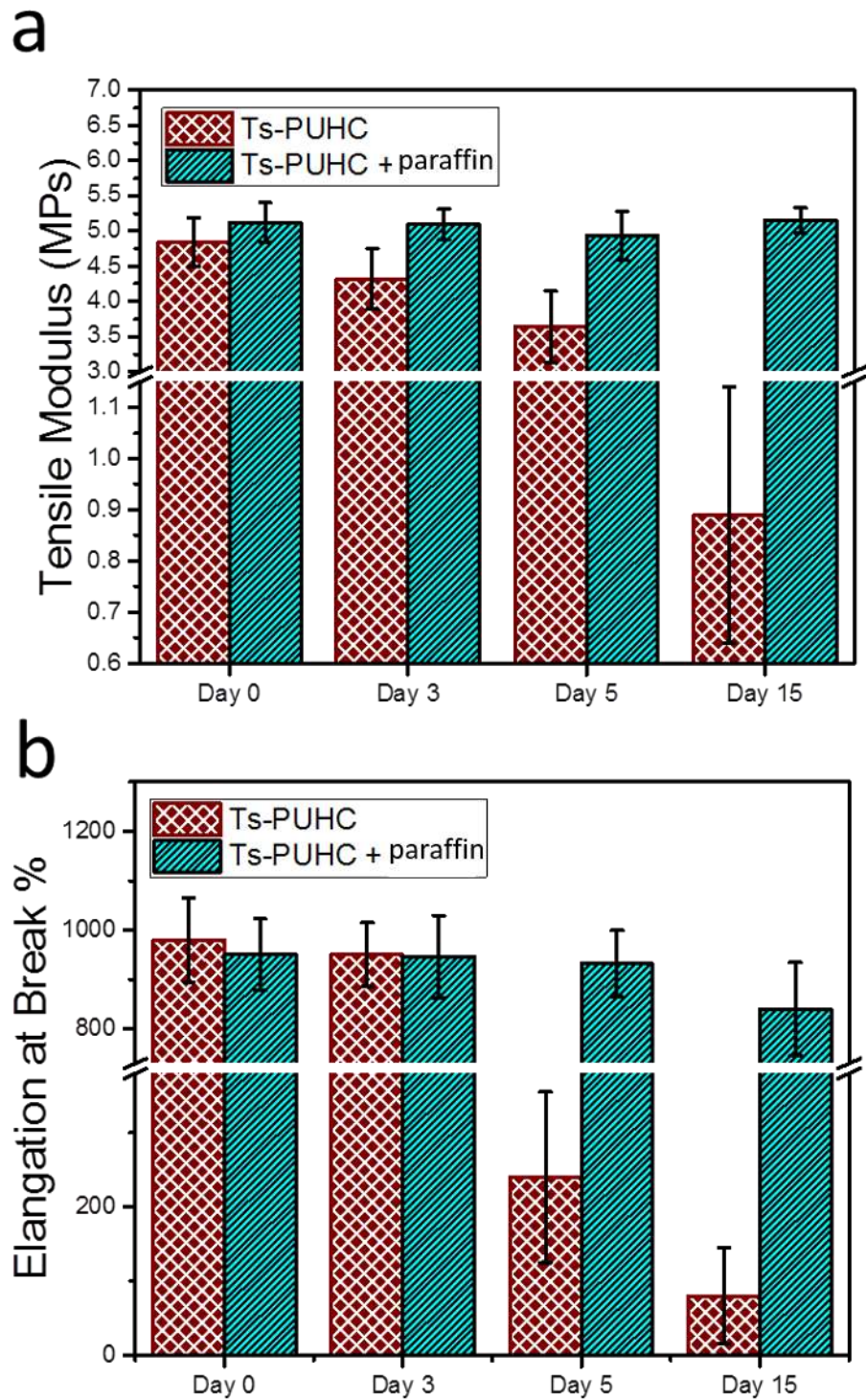


Figure 5.19 Tensile modulus (a) and elongation at break (b) of Ts-PUHC and paraffin treated Ts-PUHC in simulated body fluid (SBF) in 37 °C for 15 days. All the measurements repeated on 5 different samples prepared in the same way. (The tests were repetitively conducted for 5 times for each sample and the standard deviation is shown in the plot).

In general, a trend of decreasing tensile modulus with time can be seen for Ts-PUHC samples. Ts-PUHC samples also showed a lower elongation at break compared to paraffin treated Ts-PUHC at each time point measured which can be due to the hydrophobic properties of paraffin oil. With all the Ts-PUHC samples showing close to 5x and 12x drop in tensile modulus and elongation at break after 15 days respectively in SBF (Figure 5.19a and b), while there is no significant change observed in the overall mechanical properties in paraffin treated Ts-PUHC. It has been discussed in Section 4.3.3 that the interaction between PEDOT:PSS with the diol part of polyurethane could be causing this loss of mechanical property of Ts-PUHC in SBF over time.[439, 440]

## 5.4 Conclusions

This work has demonstrated the production of a thermistor temperature sensor based on the polyurethane hybrid composite (Ts-PUHC) with strain ability, stability in various pH between 4 and 9, and NTE behaviour in the window of human body temperature range (between 25 and 45 °C), so it is a promising material for this thesis application for body temperature monitoring. The rheological and thermo-rheological properties of the PUHC ink were measured as a function of ink modification using rotary evaporation to obtain sufficient strength and stiffness to maintain structural integrity during and after 3D printing. The combination of Ts-PUHC design treated with paraffin oil can be engineered to accommodate enhanced elastic strain along a selected dimension and to support biaxial deformation modes. It could, therefore, be considered for use as an advanced material in wearable bionics and stretchable electronics, and soft robotics. Apart from sensing application, PUHC is lightweight, with excellent processability, flexibility, variety and could be customised for their properties based on applications for healthcare monitoring.

## **Chapter 6**

# **Conclusion and Recommendation**

---

## 6.1 Conclusion

The aim of this PhD project was the development of conductive hydrogels incorporating graphene with the capability to be utilized for the development of a thermistor temperature sensor for health monitoring. Body temperature is the basal index in physiology, as temperature affects the rate of the chemical reactions in physiological activities. Materials for making temperature sensors must be capable of having at least one property that can be significantly changed by change in external temperature stimuli. The aims of the thesis were achieved in a progression of four steps.

The first aim of the research documented in this thesis, Chapter 3, was to synthesize highly electrically and thermally conductive LCGO. Review of the literature highlighted the lack of a comprehensive study on the use of simple and low-cost methods to improve the electrical and thermal conductivity of LCGO and impact of cations post-treatment on mechanical and rheological properties of LCGO in their hydrated state, by modification of LCGO dispersions with a low quantity of chloride salts. The properties of m-LCGO were studied with four different chloride salts. Addition of salts to LCGO dispersions result in an increase of the storage and loss moduli and viscosity through the interaction between cations and functional groups of LCGO, with the magnitude of increase being dependent upon the concentration of the salt added. A viscosity increase of between 30× and 300× (depending on the salt type) is recorded when salt is added at a concentration as low as 80 mM while storage and loss moduli increase up to 23× and 29×, respectively. Free standing films made from the salt treated LCGO dispersions contained up to 26% water in their structure and were observed to have significantly improved mechanical (2× to 5× increase) and electrical properties (decreased surface resistance up to approximately 670×) compared to free-standing films prepared without chloride salts. The influence of

the salts on properties of LCGO dispersions and their hydrated free-standing films is postulated as a complex interplay of many factors such as the size of cations, the valency of positive charge of the cations, the ratio of charge and cations size, as well as the hygroscopic nature of the salts.

The second aim of this research project, discussed in Chapter 4, was to develop a conductive hydrogel. PU, an electrical isolator, is a promising material for the development of biomaterials. However, the lack of data about the conductive polyurethane hybrid composite (PUHC) with LCGO/PEDOT:PSS composites in the literature motivated a comprehensive study in this area. A simple method was developed, to achieve a self-assembled tough elastomeric composite structure that is biocompatible, conductive, and with high flexibility. The hydrogel comprises polyether-based linear polyurethane (PU), poly (3,4-ethylenedioxythiophene) (PEDOT) doped with poly(4-styrenesulfonate) (PSS) and liquid crystal graphene oxide (LCGO). The polyurethane hybrid composite (PUHC) containing the PEDOT:PSS, LCGO, and PU has a higher electrical conductivity (10×), tensile modulus (>1.6×) and yield strength (>1.56×) compared to respective control samples.

Furthermore, the PUHC is biocompatible and can support human neural stem cell (NSC) growth and differentiation to neurons and support neuroglia. Moreover, the stimulation of PUHC enhances NSC differentiation with enhanced neuritogenesis compared to unstimulated cultures. A model describing the synergistic effects of the PUHC components and their influence on the uniformity, biocompatibility and electromechanical properties of the hydrogel was presented.

The third aim of this research project was to develop and optimize a thermistor based on the PUHC. Sensor characterization tests, mechanical properties, biodegradability,

biocompatibility and impact of the other ambient physical stimuli is described in Chapter 5. The elastic recovery properties of PUHC and PU as a function of filler loading and under strain between 10% to 100% was compared. The elastic recovery of PUHC decreased with increasing filler loading. For example, at 40% applied strain PU film shows an elastic recovery of ~97% whereas this decreased to ~89% and ~69% for the filler ratio of 4% and 8% respectively in PUHC. The results showed that the presence of a lower ratio of filler reduced the plastic deformation, i.e., elastic recovery was enhanced compared to the PU matrix.

The fourth and final aim of this research was to use PUHC as ink for extrusion 3D printing. Design, rheological and morphological properties of the 3D printed PUHC temperature sensor were described at the end of Chapter 5. Considering the remarkable improvements achieved in the rheological properties of PUHC via rotary evaporator, the processability of the PUHC composite was investigated by printing a multilayer scaffold. The sufficient rheological properties of the composite allow direct printing of ink at room temperature and without any post-treatment on 3D printed structure. The processability of the PUHC composites was therefore obtained through printing the single and multilayer scaffold. The feasibility and materials behaviour of PUHC was initially studied during the printing. It was noticed that the physical properties (viscosity and storage modulus) of PUHC ink is significantly robust.

## **6.2 Future Recommendations**

In this thesis, a composite which potentially could be employed as a thermistor based on polyurethane matrix with LCGO and PEDOT:PSS as fillers was developed. The impact of filler ratio on mechanical properties, electrical and thermal conductivity and eventually

fabricated the preliminary thermistor via 3D printing was highlighted. The impact of strain and moisture on sensor performance was also investigated in the thesis. However, Ts-PUHC has hysteresis and fatigue which may be a limitation in practical applications over extended periods. Several areas of direct extension of this work include:

- The further investigation of the impact of the ratio of polyurethane hard segment on thermistor performance.

The polyurethane is composed of diisocyanate-based hard polymer segments polyester and polyether soft segments. Phonons are quantized modes of vibration in a rigid crystal lattice, which is the fundamental mechanism of heat conduction in polyurethane and most polymers.[425] Polymers in the amorphous state are usually considered to have many defects that contribute to numerous phonons scattering, leading to low thermal conductivity. So, the higher in thermal conductivity can be obtained by the increase in the ratio of polyurethane hard segment (i.e., an increase of the degree of crystallinity in PUHC).

- Investigation of the impact of graphene sheet size on thermal expansion and thermal diffusivity of PUHC.

The aqueous LCGO dispersion used in this thesis contained GO sheets with a lateral size as large as 10  $\mu\text{m}$  (Section 3.11). Several physical properties, such as the thermal conductivity and stability, electrical conductivity, number of graphene particles per unit volume of composite, mechanical properties and surface area, vary with the graphene sheet size. I think LCGOs' with bigger sheet size potentially have a higher thermal and electrical conductivity and could boosting the thermal conductivity throughout the composite.



Furthermore, in polymer composites such as PUHC, the fillers can have the potential to induce or alter polymer structure and morphology. The liquid crystal (LC) nature of LCGO with bigger sheet size provides the different ability to have the fillers aligned and maintain alignment between LCGO nanosheets within the composite.

- Investigation of using another polymer as a matrix with a higher degree of crystallinity such as Polysarcosine and poly-L-proline.

The degree of crystallinity in polymers plays an essential role in determining the final properties of structural composite material, especially on thermal properties. Polymers with a higher degree of crystallinity such as polysarcosine and poly-L-proline have a higher thermal conductivity. More investigation would be done to make an electrically conductive composite with suitable mechanical properties based on these highly thermally conductive polymers, and the morphology, thermal and mechanical properties of the composites should be investigated and compared.

## Reference

1. Pantelopoulos, A. and N.G. Bourbakis, *A survey on wearable sensor-based systems for health monitoring and prognosis*. IEEE Transactions on Systems, Man, and Cybernetics, Part C (Applications and Reviews), 2010. **40**(1): p. 1-12.
2. Zhao, Y. and X. Huang, *Mechanisms and Materials of Flexible and Stretchable Skin Sensors*. Micromachines, 2017. **8**(3): p. 69.
3. Mainwaring, A., et al., *Wireless sensor networks for habitat monitoring*, in *Proceedings of the 1st ACM international workshop on Wireless sensor networks and applications*. 2002, ACM: Atlanta, Georgia, USA. p. 88-97.
4. Trung, T.Q. and N.-E. Lee, *Flexible and Stretchable Physical Sensor Integrated Platforms for Wearable Human-Activity Monitoring and Personal Healthcare*. Advanced Materials, 2016. **28**(22): p. 4338-4372.
5. Inpil, K., et al., *A carbon nanotube strain sensor for structural health monitoring*. Smart Materials and Structures, 2006. **15**(3): p. 737.
6. Park, J., et al., *Tactile-Direction-Sensitive and Stretchable Electronic Skins Based on Human-Skin-Inspired Interlocked Microstructures*. ACS Nano, 2014. **8**(12): p. 12020-12029.
7. Casa, D.J., et al., *Validity of devices that assess body temperature during outdoor exercise in the heat*. Journal of athletic training, 2007. **42**(3): p. 333.
8. Hammock, M.L., et al., *25th Anniversary Article: The Evolution of Electronic Skin (E-Skin): A Brief History, Design Considerations, and Recent Progress*. Advanced Materials, 2013. **25**(42): p. 5997-6038.

9. Wang, C., et al., *User-interactive electronic skin for instantaneous pressure visualization*. Nat Mater, 2013. **12**(10): p. 899-904.
10. Kahn, P., et al., *Human activity monitoring device*. 2010, Patent No. 7,647,196.
11. Kahn, P., et al., *Chest strap having human activity monitoring device*. 2010, Patent No. 7,753,861.
12. Najafi, B., et al., *Ambulatory system for human motion analysis using a kinematic sensor: monitoring of daily physical activity in the elderly*. IEEE Transactions on Biomedical Engineering, 2003. **50**(6): p. 711-723.
13. Yang, C.-C. and Y.-L. Hsu, *A Review of Accelerometry-Based Wearable Motion Detectors for Physical Activity Monitoring*. Sensors, 2010. **10**(8): p. 7772.
14. Carroll, R., et al., *Continua: An Interoperable Personal Healthcare Ecosystem*. IEEE Pervasive Computing, 2007. **6**(4): p. 90-94.
15. Leonhardt, S., A. Aleksandrowicz, and M. Steffen. *Magnetic and Capacitive Monitoring of Heart and Lung Activity as an Example for Personal Healthcare*. in *2006 3rd IEEE/EMBS International Summer School on Medical Devices and Biosensors*. 2006.
16. Katz, J.E. and R.E. Rice, *Public views of mobile medical devices and services: A US national survey of consumer sentiments towards RFID healthcare technology*. International Journal of Medical Informatics, 2009. **78**(2): p. 104-114.
17. Someya, T., et al., *Conformable, flexible, large-area networks of pressure and thermal sensors with organic transistor active matrixes*. Proceedings of the National Academy of Sciences of the United States of America, 2005. **102**(35): p. 12321-12325.

18. Wang, X., et al., *Silk-Molded Flexible, Ultrasensitive, and Highly Stable Electronic Skin for Monitoring Human Physiological Signals*. *Advanced Materials*, 2014. **26**(9): p. 1336-1342.
19. Pang, C., C. Lee, and K.-Y. Suh, *Recent advances in flexible sensors for wearable and implantable devices*. *Journal of Applied Polymer Science*, 2013. **130**(3): p. 1429-1441.
20. Cossins, A., *Temperature biology of animals*. 2012: Springer Science & Business Media.
21. Feteira, A., *Negative temperature coefficient resistance (NTCR) ceramic thermistors: an industrial perspective*. *Journal of the American Ceramic Society*, 2009. **92**(5): p. 967-983.
22. Park, K. and D. Bang, *Electrical properties of Ni–Mn–Co–(Fe) oxide thick-film NTC thermistors prepared by screen printing*. *Journal of Materials Science: Materials in Electronics*, 2003. **14**(2): p. 81-87.
23. De Györgyfalva, G.C. and I. Reaney, *Decomposition of NiMn<sub>2</sub>O<sub>4</sub> spinel: an NTC thermistor material*. *Journal of the European Ceramic Society*, 2001. **21**(10): p. 2145-2148.
24. Riffat, S.B. and X. Ma, *Thermoelectrics: a review of present and potential applications*. *Applied thermal engineering*, 2003. **23**(8): p. 913-935.
25. Shaddix, C.R., *Correcting thermocouple measurements for radiation loss: a critical review*. 1999, Sandia National Labs., Livermore, CA (US).
26. Ren, F. and S.J. Pearton, *Semiconductor-based Sensors*. 2016: World Scientific.
27. Wilson, J.S., *Sensor technology handbook*. 2004: Elsevier.

28. Kanao, K., et al., *Highly selective flexible tactile strain and temperature sensors against substrate bending for an artificial skin*. RSC Advances, 2015. **5**(38): p. 30170-30174.
29. APC International, L., *Piezoelectric ceramics: principles and applications*. 2002: APC International.
30. Shrout, T.R. and S.J. Zhang, *Lead-free piezoelectric ceramics: Alternatives for PZT*. Journal of Electroceramics, 2007. **19**(1): p. 113-126.
31. Yoshii, K., et al., *Electrical properties and depolarization temperature of  $(Bi_{1/2}Na_{1/2})TiO_3-(Bi_{1/2}K_{1/2})TiO_3$  lead-free piezoelectric ceramics*. Japanese journal of applied physics, 2006. **45**(5S): p. 4493.
32. Takenaka, T. and K. Sakata, *Dielectric, piezoelectric and pyroelectric properties of  $(BiNa)_{1/2}TiO_3$ -based ceramics*. Ferroelectrics, 1989. **95**(1): p. 153-156.
33. Whatmore, R., *Pyroelectric ceramics and devices for thermal infra-red detection and imaging*. Ferroelectrics, 1991. **118**(1): p. 241-259.
34. Bune, A., et al., *Piezoelectric and pyroelectric properties of ferroelectric Langmuir-Blodgett polymer films*. Journal of Applied Physics, 1999. **85**(11): p. 7869-7873.
35. Levi, N., et al., *Properties of polyvinylidene difluoride- carbon nanotube blends*. Nano Letters, 2004. **4**(7): p. 1267-1271.
36. Lovinger, A.J., *Ferroelectric polymers*. Science, 1983. **220**(4602): p. 1115-1121.
37. Mark, J.E., *Physical properties of polymers handbook*. Vol. 1076. 2007: Springer.
38. Lang, S. and S. Muensit, *Review of some lesser-known applications of piezoelectric and pyroelectric polymers*. Applied Physics A, 2006. **85**(2): p. 125-134.

39. Dietze, M. and M. Es-Souni, *Structural and functional properties of screen-printed PZT–PVDF-TrFE composites*. Sensors and Actuators A: Physical, 2008. **143**(2): p. 329-334.
40. Ploss, B., et al., *Pyroelectric activity of ferroelectric PT/PVDF-TRFE*. IEEE transactions on dielectrics and electrical insulation, 2000. **7**(4): p. 517-522.
41. Zhu, R., K. Jenkins, and R. Yang, *Degradation and nano-patterning of ferroelectric P (VDF-TrFE) thin films with electron irradiation*. RSC Advances, 2015. **5**(129): p. 106700-106705.
42. Zhang, Y., et al., *Enhanced pyroelectric and piezoelectric properties of PZT with aligned porosity for energy harvesting applications*. Journal of Materials Chemistry A, 2017. **5**(14): p. 6569-6580.
43. Ploss, B., et al., *Pyroelectric or piezoelectric compensated ferroelectric composites*. Applied Physics Letters, 2000. **76**(19): p. 2776-2778.
44. Tien, N.T., et al., *Utilizing highly crystalline pyroelectric material as functional gate dielectric in organic thin-film transistors*. Advanced Materials, 2009. **21**(8): p. 910-915.
45. Tien, N.T., et al., *Utilizing Highly Crystalline Pyroelectric Material as Functional Gate Dielectric in Organic Thin-Film Transistors*. Advanced Materials, 2009. **21**(8): p. 910-915.
46. Trung, T.Q. and N.E. Lee, *Flexible and Stretchable Physical Sensor Integrated Platforms for Wearable Human-Activity Monitoring and Personal Healthcare*. Advanced materials, 2016. **28**(22): p. 4338-4372.
47. Kang, X., et al., *A sensitive nonenzymatic glucose sensor in alkaline media with a copper nanocluster/multiwall carbon nanotube-modified glassy carbon electrode*. Analytical biochemistry, 2007. **363**(1): p. 143-150.

48. Lopatin, S. and A.H. Nickel, *Method of reducing electromigration in a copper line by Zinc-Doping of a copper surface from an electroplated copper-zinc alloy thin film and a semiconductor device thereby formed*. 2003, Patent No. 6,624,075.
49. Cho, B.-O., M.-S. Lee, and T. Yasue, *Non-volatile organic resistance random access memory device and method of manufacturing the same*. 2006, Patent Application No. 11/465,040.
50. Kim, D.H., et al., *Thin, flexible sensors and actuators as 'instrumented' surgical sutures for targeted wound monitoring and therapy*. *Small*, 2012. **8**(21): p. 3263-3268.
51. Chu, K., et al., *Direct measurement of the spectral phase of femtosecond pulses*. *Optics Letters*, 1995. **20**(8): p. 904-906.
52. Yu, C., et al., *A stretchable temperature sensor based on elastically buckled thin film devices on elastomeric substrates*. *Applied Physics Letters*, 2009. **95**(14): p. 141912.
53. Webb, R.C., et al., *Ultrathin conformal devices for precise and continuous thermal characterization of human skin*. *Nature materials*, 2013. **12**(10): p. 938-944.
54. Webb, R.C., et al., *Ultrathin conformal devices for precise and continuous thermal characterization of human skin*. *Nature materials*, 2013. **12**(10): p. 938.
55. Joshi, G.M. and K. Deshmukh. *Conjugated polymer/graphene oxide nanocomposite as thermistor*. in *AIP Conference Proceedings*. 2015. AIP Publishing.
56. Jung, H.-M. and S. Um, *Thermo-electrical properties of composite semiconductor thin films composed of nanocrystalline graphene-vanadium oxides*. *Journal of nanoscience and nanotechnology*, 2014. **14**(12): p. 9051-9059.

57. Al-Juaid, S.S., et al., *Novel functional nitrile butadiene rubber/magnetite nano composites for NTCR thermistors application*. Journal of Applied Polymer Science, 2011. **121**(6): p. 3604-3612.
58. Nguyen, T.P., *Applications of Polymer-Based Nanocomposites*. Polymer Composites, Nanocomposites, 2013. **2**.
59. Kong, D., et al., *Temperature-dependent electrical properties of graphene inkjet-printed on flexible materials*. Langmuir, 2012. **28**(37): p. 13467-13472.
60. Hu, B., W. Chen, and J. Zhou, *High performance flexible sensor based on inorganic nanomaterials*. Sensors and Actuators B: Chemical, 2013. **176**: p. 522-533.
61. Fan, X. and D. Zhao, *On the spaces  $L_p(x)(\Omega)$  and  $W_{m,p}(x)(\Omega)$* . Journal of Mathematical Analysis and Applications, 2001. **263**(2): p. 424-446.
62. Rusu, G.I., G.G. Rusu, and M.E. Popa, *Studies on the electronic transport properties of some organic semiconductors in thin films*. Materials Research Innovations, 2003. **7**(6): p. 372-380.
63. Fischer, A., et al., *Feel the heat: Nonlinear electrothermal feedback in organic LEDs*. Advanced Functional Materials, 2014. **24**(22): p. 3367-3374.
64. Rusu, G., et al., *Studies on the electronic transport properties of some aromatic polysulfones in thin films*. Acta materialia, 2001. **49**(3): p. 553-559.
65. Rusu, M. and G. Rusu, *High-field electrical conduction in thin-film sandwich structures of the metal/organic semiconductor/metal type*. Applied surface science, 1998. **126**(3): p. 246-254.
66. Jeon, J., H.B.R. Lee, and Z. Bao, *Flexible wireless temperature sensors based on Ni microparticle-filled binary polymer composites*. Advanced Materials, 2013. **25**(6): p. 850-855.



67. Harada, S., et al., *Fully printed flexible fingerprint-like three-axis tactile and slip force and temperature sensors for artificial skin*. ACS nano, 2014. **8**(12): p. 12851-12857.
68. Trung, T.Q., S. Ramasundaram, and N.E. Lee, *Infrared detection using transparent and flexible field-effect transistor array with solution processable nanocomposite channel of reduced graphene oxide and P (VDF-TrFE)*. Advanced Functional Materials, 2015. **25**(11): p. 1745-1754.
69. Trung, T.Q., et al., *Flexible and Transparent Nanocomposite of Reduced Graphene Oxide and P (VDF-TrFE) Copolymer for High Thermal Responsivity in a Field-Effect Transistor*. Advanced Functional Materials, 2014. **24**(22): p. 3438-3445.
70. Yan, C., J. Wang, and P.S. Lee, *Stretchable graphene thermistor with tunable thermal index*. ACS nano, 2015. **9**(2): p. 2130-2137.
71. Carpi, F. and D. De Rossi, *Electroactive polymer-based devices for e-textiles in biomedicine*. IEEE transactions on Information Technology in biomedicine, 2005. **9**(3): p. 295-318.
72. Sahoo, B.N., et al., *Hybrid functional microfibers for textile electronics and biosensors*. Journal of Semiconductors, 2018. **39**(1): p. 011009.
73. Rohrbaugh, N., et al., *Stability and Reliability of III-Nitride Based Biosensors*, in *Semiconductor-Based Sensors*. 2017, World Scientific. p. 149-196.
74. Gao, L., et al., *Epidermal photonic devices for quantitative imaging of temperature and thermal transport characteristics of the skin*. Nature communications, 2014. **5**: p. 4938.

75. Wu, X., et al., *Thermally Stable, Biocompatible, and Flexible Organic Field-Effect Transistors and Their Application in Temperature Sensing Arrays for Artificial Skin*. *Advanced Functional Materials*, 2015. **25**(14): p. 2138-2146.
76. He, Y., et al., *A Self-Healing Electronic Sensor Based on Thermal-Sensitive Fluids*. *Advanced Materials*, 2015. **27**(31): p. 4622-4627.
77. Zhang, W., A.A. Dehghani-Sani, and R.S. Blackburn, *Carbon based conductive polymer composites*. *Journal of Materials Science*, 2007. **42**(10): p. 3408-3418.
78. Pötschke, P., T.D. Fornes, and D.R. Paul, *Rheological behavior of multiwalled carbon nanotube/polycarbonate composites*. *Polymer*, 2002. **43**(11): p. 3247-3255.
79. Jiang, H., et al., *Surface Functionalized Silver Nanoparticles for Ultrahigh Conductive Polymer Composites*. *Chemistry of Materials*, 2006. **18**(13): p. 2969-2973.
80. Mamunya, Y.P., et al., *Electrical and thermal conductivity of polymers filled with metal powders*. *European Polymer Journal*, 2002. **38**(9): p. 1887-1897.
81. Andrews, R., et al., *Multiwall Carbon Nanotubes: Synthesis and Application*. *Accounts of Chemical Research*, 2002. **35**(12): p. 1008-1017.
82. Che, G., et al., *Metal-Nanocluster-Filled Carbon Nanotubes: Catalytic Properties and Possible Applications in Electrochemical Energy Storage and Production*. *Langmuir*, 1999. **15**(3): p. 750-758.
83. Tee, B.C.K., et al., *An electrically and mechanically self-healing composite with pressure- and flexion-sensitive properties for electronic skin applications*. *Nat Nano*, 2012. **7**(12): p. 825-832.
84. Chung, D.D.L., *Electromagnetic interference shielding effectiveness of carbon materials*. *Carbon*, 2001. **39**(2): p. 279-285.

85. Bönnemann, H. and Ryan M. Richards, *Nanoscopic Metal Particles – Synthetic Methods and Potential Applications*. European Journal of Inorganic Chemistry, 2001. **2001**(10): p. 2455-2480.
86. Li, Y. and C.P. Wong, *Recent advances of conductive adhesives as a lead-free alternative in electronic packaging: Materials, processing, reliability and applications*. Materials Science and Engineering: R: Reports, 2006. **51**(1): p. 1-35.
87. He, L. and S.-C. Tjong, *Electrical behavior and positive temperature coefficient effect of graphene/polyvinylidene fluoride composites containing silver nanowires*. Nanoscale research letters, 2014. **9**(1): p. 375.
88. Wang, T., et al., *Electroactive polymers for sensing*. Interface focus, 2016. **6**(4): p. 20160026.
89. Rosenmeier, L. and B.C. Knutz, *Ion-conductive polymers*. 1998, Patent No. 5,789,106.
90. Yoshio, M., et al., *One-Dimensional Ion-Conductive Polymer Films: Alignment and Fixation of Ionic Channels Formed by Self-Organization of Polymerizable Columnar Liquid Crystals*. Journal of the American Chemical Society, 2006. **128**(16): p. 5570-5577.
91. Noda, A. and M. Watanabe, *Highly conductive polymer electrolytes prepared by in situ polymerization of vinyl monomers in room temperature molten salts*. Electrochimica Acta, 2000. **45**(8): p. 1265-1270.
92. Cao, Y., P. Smith, and A.J. Heeger, *Counter-ion induced processibility of conducting polyaniline and of conducting polyblends of polyaniline in bulk polymers*. Synthetic Metals, 1992. **48**(1): p. 91-97.

93. Yang, Y., et al., *Improving the Performance of Lithium–Sulfur Batteries by Conductive Polymer Coating*. ACS Nano, 2011. **5**(11): p. 9187-9193.
94. Skotheim, T.A., Y. Okamoto, and P.D. Hale, *Electrochemical biosensor based on immobilized enzymes and redox polymers*. 1992, Patent No. 5,089,112.
95. Barrière, F., et al., *Targetting redox polymers as mediators for laccase oxygen reduction in a membrane-less biofuel cell*. Electrochemistry Communications, 2004. **6**(3): p. 237-241.
96. Factor, A. and G.E. Heinsohn, *Polyviologens – a novel class of cationic polyelectrolyte redox polymers*. Journal of Polymer Science Part B: Polymer Letters, 1971. **9**(4): p. 289-295.
97. Keiichi, K., Y. Katsumi, and I. Yoshio, *Electrical Properties of Conducting Polymer, Poly-Thiophene, Prepared by Electrochemical Polymerization*. Japanese Journal of Applied Physics, 1982. **21**(9A): p. L567.
98. Zotti, G., et al., *Conductive and Magnetic Properties of 3,4-Dimethoxy- and 3,4-Ethylenedioxy-Capped Polypyrrole and Polythiophene*. Chemistry of Materials, 2000. **12**(10): p. 2996-3005.
99. Meincke, O., et al., *Mechanical properties and electrical conductivity of carbon-nanotube filled polyamide-6 and its blends with acrylonitrile/butadiene/styrene*. Polymer, 2004. **45**(3): p. 739-748.
100. Hatchett, D.W. and M. Josowicz, *Composites of Intrinsically Conducting Polymers as Sensing Nanomaterials*. Chemical Reviews, 2008. **108**(2): p. 746-769.
101. MacDiarmid, A.G., *Synthetic metals: a novel role for organic polymers*. Synthetic Metals, 2001. **125**(1): p. 11-22.

102. MacDiarmid, A.G., "*Synthetic Metals*": *A Novel Role for Organic Polymers (Nobel Lecture)*. *Angewandte Chemie International Edition*, 2001. **40**(14): p. 2581-2590.
103. Wang, Y. and X. Jing, *Intrinsically conducting polymers for electromagnetic interference shielding*. *Polymers for Advanced Technologies*, 2005. **16**(4): p. 344-351.
104. Cho, S.I. and S.B. Lee, *Fast Electrochemistry of Conductive Polymer Nanotubes: Synthesis, Mechanism, and Application*. *Accounts of Chemical Research*, 2008. **41**(6): p. 699-707.
105. Elschner, A., [*electronic resource*] : *PEDOT principles and applications of an intrinsically conductive polymer / Andreas Elschner*. 2011: Boca Raton, FL : CRC Press, c2011.
106. Kumar, D. and R.C. Sharma, *Advances in conductive polymers*. *European Polymer Journal*, 1998. **34**(8): p. 1053-1060.
107. A. G. MacDiarmid, a., et al., *The Concept of 'Doping' of Conducting Polymers: The Role of Reduction Potentials [and Discussion]*. *Philosophical Transactions of the Royal Society of London. Series A, Mathematical and Physical Sciences*, 1985(1528): p. 3.
108. Chiang, C.K., et al., *Electrical Conductivity in Doped Polyacetylene*. *Physical Review Letters*, 1977. **39**(17): p. 1098-1101.
109. Zotti, G., S. Cattarin, and N. Comisso, *Electrodeposition of polythiophene, polypyrrole and polyaniline by the cyclic potential sweep method*. *Journal of Electroanalytical Chemistry and Interfacial Electrochemistry*, 1987. **235**(1): p. 259-273.

110. Keiichi, K., T. Shinji, and Y. Katsumi, *Characteristics of Heterojunction Consisting of Conducting Polymers of Polythiophene and Polypyrrole*. Japanese Journal of Applied Physics, 1985. **24**(7A): p. L553.
111. Laforgue, A., et al., *Polythiophene-based supercapacitors*. Journal of Power Sources, 1999. **80**(1): p. 142-148.
112. Ong, B.S., et al., *High-performance semiconducting polythiophenes for organic thin-film transistors*. Journal of the American Chemical Society, 2004. **126**(11): p. 3378-3379.
113. Furukawa, Y., M. Akimoto, and I. Harada, *Vibrational key bands and electrical conductivity of polythiophene*. Synthetic Metals, 1987. **18**(1): p. 151-156.
114. Bao, Z. and A.J. Lovinger, *Soluble Regioregular Polythiophene Derivatives as Semiconducting Materials for Field-Effect Transistors*. Chemistry of Materials, 1999. **11**(9): p. 2607-2612.
115. Talmage, D. and R. Talmage, *Calcium homeostasis: how bone solubility relates to all aspects of bone physiology*. Journal of Musculoskeletal and Neuronal Interactions, 2007. **7**(2): p. 108.
116. Kim, et al., *Titration Behavior and Spectral Transitions of Water-Soluble Polythiophene Carboxylic Acids*. Macromolecules, 1999. **32**(12): p. 3964-3969.
117. Wudl, F. and S. Hoyer, *Highly organic solvent soluble, water insoluble electroluminescent polyphenylene vinylenes having pendant steroid groups and products and uses thereof*. 1997, Patent No. 5,679,757.
118. Skotheim, T.A., *Handbook of conducting polymers*. 1997: CRC press.
119. Neri, G., *First Fifty Years of Chemosensitive Gas Sensors*. Chemosensors, 2015. **3**(1): p. 1.

120. Núñez, R., et al., *Icosahedral boron clusters: a perfect tool for the enhancement of polymer features*. Chemical Society Reviews, 2016. **45**(19): p. 5147-5173.
121. Oyama, N., et al., *Dimercaptan-polyaniline composite electrodes for lithium batteries with high energy density*. Nature, 1995. **373**(6515): p. 598-600.
122. Bhadra, S., et al., *Progress in preparation, processing and applications of polyaniline*. Progress in Polymer Science, 2009. **34**(8): p. 783-810.
123. Bowman, D. and B.R. Mattes, *Conductive Fibre Prepared From Ultra-High Molecular Weight Polyaniline for Smart Fabric and Interactive Textile Applications*. Synthetic Metals, 2005. **154**(1): p. 29-32.
124. Chaudhari, H.K. and D.S. Kelkar, *Investigation of Structure and Electrical Conductivity in Doped Polyaniline*. Polymer International, 1997. **42**(4): p. 380-384.
125. Dhand, C., et al., *Recent advances in polyaniline based biosensors*. Biosensors and Bioelectronics, 2011. **26**(6): p. 2811-2821.
126. Feng, X.-M., et al., *One-Step Electrochemical Synthesis of Graphene/Polyaniline Composite Film and Its Applications*. Advanced Functional Materials, 2011. **21**(15): p. 2989-2996.
127. Lai, J., et al., *Review: Polyaniline-based glucose biosensor: A review*. Journal of Electroanalytical Chemistry, 2016. **782**: p. 138-153.
128. Li, M., et al., *Electrospinning polyaniline-contained gelatin nanofibers for tissue engineering applications*. Biomaterials, 2006. **27**(13): p. 2705-2715.
129. Masters, J.G., et al., *Polyaniline: Allowed oxidation states*. Synthetic Metals, 1991. **41**(1): p. 715-718.

130. Meng, Y., et al., *Hierarchical Porous Graphene/Polyaniline Composite Film with Superior Rate Performance for Flexible Supercapacitors*. *Advanced Materials*, 2013. **25**(48): p. 6985-6990.
131. Njuguna, J. and K. Pielichowski, *Recent developments in polyurethane-based conducting composites*. *Journal of Materials Science*, 2004. **39**(13): p. 4081-4094.
132. Yan, J., et al., *Preparation of a graphene nanosheet/polyaniline composite with high specific capacitance*. *Carbon*, 2010. **48**(2): p. 487-493.
133. Xia, H. and Q. Wang, *Ultrasonic Irradiation: A Novel Approach To Prepare Conductive Polyaniline/Nanocrystalline Titanium Oxide Composites*. *Chemistry of Materials*, 2002. **14**(5): p. 2158-2165.
134. Gospodinova, N. and L. Terlemezyan, *Conducting polymers prepared by oxidative polymerization: polyaniline*. *Progress in Polymer Science*, 1998. **23**(8): p. 1443-1484.
135. Dimitriev, O.P., et al., *PEDOT:PSS films—Effect of organic solvent additives and annealing on the film conductivity*. *Synthetic Metals*, 2009. **159**(21–22): p. 2237-2239.
136. Stöcker, T., A. Köhler, and R. Moos, *Why does the electrical conductivity in PEDOT:PSS decrease with PSS content? A study combining thermoelectric measurements with impedance spectroscopy*. *Journal of Polymer Science Part B: Polymer Physics*, 2012. **50**(14): p. 976-983.
137. Chang, C.-L., K. Fix, and W.-C. Wang. *Reliability of PEDOT-PSS strain gauge on foam structure*. 2010.
138. Chen, T., et al., *Ultra high permittivity and significantly enhanced electric field induced strain in PEDOT:PSS-RGO@PU intelligent shape-changing electro-active polymers*. *RSC Advances*, 2014. **4**(109): p. 64061-64067.



139. Saleem, H., et al., *Mechanical and Thermal Properties of Thermoset–Graphene Nanocomposites*. *Macromolecular Materials and Engineering*, 2016. **301**(3): p. 231-259.
140. Seyedin, M.Z., et al., *Sensors: Strain-Responsive Polyurethane/PEDOT:PSS Elastomeric Composite Fibers with High Electrical Conductivity (Adv. Funct. Mater. 20/2014)*. *Advanced Functional Materials*, 2014. **24**(20): p. 3104-3104.
141. Strankowski, M., et al., *Thermal and Mechanical Properties of Microporous Polyurethanes Modified with Reduced Graphene Oxide*. *International Journal of Polymer Science*, 2016. **2016**: p. 8.
142. Huang, J., et al., *Influence of thermal treatment on the conductivity and morphology of PEDOT/PSS films*. *Synthetic Metals*, 2003. **139**(3): p. 569-572.
143. Ouyang, J., et al., *On the mechanism of conductivity enhancement in poly(3,4-ethylenedioxythiophene):poly(styrene sulfonate) film through solvent treatment*. *Polymer*, 2004. **45**(25): p. 8443-8450.
144. Xu, Y., et al., *A hybrid material of graphene and poly (3,4-ethyldioxythiophene) with high conductivity, flexibility, and transparency*. *Nano Research*, 2009. **2**(4): p. 343-348.
145. Chiang, C.K., et al., *Electrical conductivity in doped polyacetylene*. *Physical review letters*, 1977. **39**(17): p. 1098.
146. Heeger, A.J., et al., *Solitons in conducting polymers*. *Reviews of Modern Physics*, 1988. **60**(3): p. 781.
147. Basescu, N., et al., *High electrical conductivity in doped polyacetylene*. *Nature*, 1987. **327**(6121): p. 403-405.
148. Kanatzidis, M., *Conductive polymers*. *C&EN special report*, 1990: p. 36.

149. Sun, Y. and E. Ruckenstein, *Polypyrrole-bearing conductive composite prepared by an inverted emulsion pathway involving nonionic surfactants*. *Synthetic Metals*, 1995. **72**(3): p. 261-267.
150. Jin, H., Y.S. Abu-Raya, and H. Haick, *Advanced Materials for Health Monitoring with Skin-Based Wearable Devices*. *Advanced Healthcare Materials*, 2017: p. 1700024.
151. Wang, Y., et al., *High-quality reduced graphene oxide-nanocrystalline platinum hybrid materials prepared by simultaneous co-reduction of graphene oxide and chloroplatinic acid*. *Nanoscale Research Letters*, 2011. **6**(1): p. 241.
152. Bagri, A., et al., *Structural evolution during the reduction of chemically derived graphene oxide*. *Nat Chem*, 2010. **2**(7): p. 581-587.
153. Loh, K.P., et al., *Graphene oxide as a chemically tunable platform for optical applications*. *Nat Chem*, 2010. **2**(12): p. 1015-1024.
154. Emtsev, K.V., et al., *Towards wafer-size graphene layers by atmospheric pressure graphitization of silicon carbide*. *Nature materials*, 2009. **8**(3): p. 203.
155. Yang, M.-Q., N. Zhang, and Y.-J. Xu, *Synthesis of Fullerene-, Carbon Nanotube-, and Graphene-TiO<sub>2</sub> Nanocomposite Photocatalysts for Selective Oxidation: A Comparative Study*. *ACS Applied Materials & Interfaces*, 2013. **5**(3): p. 1156-1164.
156. Georgakilas, V., et al., *Broad Family of Carbon Nanoallotropes: Classification, Chemistry, and Applications of Fullerenes, Carbon Dots, Nanotubes, Graphene, Nanodiamonds, and Combined Superstructures*. *Chemical Reviews*, 2015. **115**(11): p. 4744-4822.

157. Huertas-Hernando, D., F. Guinea, and A. Brataas, *Spin-orbit coupling in curved graphene, fullerenes, nanotubes, and nanotube caps*. Physical Review B, 2006. **74**(15): p. 155426.
158. Kuc, A., *Low-dimensional transition-metal dichalcogenides*. 2014.
159. Liu, S., et al., *Antibacterial activity of graphite, graphite oxide, graphene oxide, and reduced graphene oxide: membrane and oxidative stress*. ACS nano, 2011. **5**(9): p. 6971-6980.
160. Hu, W., et al., *Graphene-Based Antibacterial Paper*. ACS Nano, 2010. **4**(7): p. 4317-4323.
161. Liu, S., et al., *Lateral Dimension-Dependent Antibacterial Activity of Graphene Oxide Sheets*. Langmuir, 2012. **28**(33): p. 12364-12372.
162. Pierson, H.O., *Handbook of carbon, graphite, diamonds and fullerenes: processing, properties and applications*. 2012: William Andrew.
163. Terrones, M., et al., *Graphene and graphite nanoribbons: Morphology, properties, synthesis, defects and applications*. Nano Today, 2010. **5**(4): p. 351-372.
164. Dresselhaus, M.S., G. Dresselhaus, and P.C. Eklund, *Science of fullerenes and carbon nanotubes: their properties and applications*. 1996: Academic press.
165. Oganov, A.R. and C.W. Glass, *Crystal structure prediction using ab initio evolutionary techniques: Principles and applications*. The Journal of chemical physics, 2006. **124**(24): p. 244704.
166. Enoki, T., M. Suzuki, and M. Endo, *Graphite intercalation compounds and applications*. 2003: Oxford University Press.
167. Sandler, J., et al., *Ultra-low electrical percolation threshold in carbon-nanotube-epoxy composites*. Polymer, 2003. **44**(19): p. 5893-5899.

168. Ren, Z.F., et al., *Synthesis of Large Arrays of Well-Aligned Carbon Nanotubes on Glass*. Science, 1998. **282**(5391): p. 1105-1107.
169. O'Connell, M.J., et al., *Band Gap Fluorescence from Individual Single-Walled Carbon Nanotubes*. Science, 2002. **297**(5581): p. 593-596.
170. Tans, S.J., A.R.M. Verschueren, and C. Dekker, *Room-temperature transistor based on a single carbon nanotube*. Nature, 1998. **393**(6680): p. 49-52.
171. Zhang, D., et al., *Transparent, Conductive, and Flexible Carbon Nanotube Films and Their Application in Organic Light-Emitting Diodes*. Nano Letters, 2006. **6**(9): p. 1880-1886.
172. Fan, Z., et al., *A Three-Dimensional Carbon Nanotube/Graphene Sandwich and Its Application as Electrode in Supercapacitors*. Advanced Materials, 2010. **22**(33): p. 3723-3728.
173. White, A.A., S.M. Best, and I.A. Kinloch, *Hydroxyapatite–Carbon Nanotube Composites for Biomedical Applications: A Review*. International Journal of Applied Ceramic Technology, 2007. **4**(1): p. 1-13.
174. Choudhary, V. and A. Gupta, *Polymer/carbon nanotube nanocomposites*, in *Carbon nanotubes-Polymer nanocomposites*. 2011, Intech.
175. Prato, M. and M. Maggini, *Fulleropyrrolidines: A family of full-fledged fullerene derivatives*. Accounts of chemical research, 1998. **31**(9): p. 519-526.
176. Friedman, S.H., et al., *Inhibition of the HIV-1 protease by fullerene derivatives: model building studies and experimental verification*. Journal of the American Chemical Society, 1993. **115**(15): p. 6506-6509.
177. Kroto, H., et al., *This Week's Citation Classic*. Nature, 1985. **318**: p. 162-3.
178. Bosi, S., et al., *Fullerene derivatives: an attractive tool for biological applications*. European journal of medicinal chemistry, 2003. **38**(11): p. 913-923.

179. Guldi, D.M. and M. Prato, *Excited-state properties of C60 fullerene derivatives*. *Accounts of chemical research*, 2000. **33**(10): p. 695-703.
180. Da Ros, T. and M. Prato, *Medicinal chemistry with fullerenes and fullerene derivatives*. *Chemical Communications*, 1999(8): p. 663-669.
181. Sherigara, B.S., W. Kutner, and F. D'Souza, *Electrocatalytic properties and sensor applications of fullerenes and carbon nanotubes*. *Electroanalysis*, 2003. **15**(9): p. 753-772.
182. Fendler, J.H., *Nanoparticles and nanostructured films: preparation, characterization, and applications*. 2008: John Wiley & Sons, 2008.
183. Troshin, P.A., et al., *Material Solubility-Photovoltaic Performance Relationship in the Design of Novel Fullerene Derivatives for Bulk Heterojunction Solar Cells*. *Advanced Functional Materials*, 2009. **19**(5): p. 779-788.
184. Wu, H., et al., *Construction of a zinc porphyrin–fullerene-derivative based nonenzymatic electrochemical sensor for sensitive sensing of hydrogen peroxide and nitrite*. *Analytical chemistry*, 2014. **86**(13): p. 6285-6290.
185. Brownson, D.A. and C.E. Banks, *Graphene electrochemistry: an overview of potential applications*. *Analyst*, 2010. **135**(11): p. 2768-2778.
186. Avouris, P. and C. Dimitrakopoulos, *Graphene: synthesis and applications*. *Materials today*, 2012. **15**(3): p. 86-97.
187. Cao, X., et al., *Preparation of novel 3D graphene networks for supercapacitor applications*. *small*, 2011. **7**(22): p. 3163-3168.
188. Lambin, P., *Elastic properties and stability of physisorbed graphene*. *Applied Sciences*, 2014. **4**(2): p. 282-304.

189. Georgakilas, V., et al., *Functionalization of graphene: covalent and non-covalent approaches, derivatives and applications*. Chem. Rev, 2012. **112**(11): p. 6156-6214.
190. Zhao, X., et al., *Recent advances in the fabrication and structure-specific applications of graphene-based inorganic hybrid membranes*. Nanoscale, 2015. **7**(12): p. 5080-5093.
191. Geim, A.K. and K.S. Novoselov, *The rise of graphene*. Nature materials, 2007. **6**(3): p. 183-191.
192. Bai, H., et al., *On the Gelation of Graphene Oxide*. The Journal of Physical Chemistry C, 2011. **115**(13): p. 5545-5551.
193. Zhao, Y., et al., *3D nanostructured conductive polymer hydrogels for high-performance electrochemical devices*. Energy & Environmental Science, 2013. **6**(10): p. 2856-2870.
194. Zhang, L. and G. Shi, *Preparation of Highly Conductive Graphene Hydrogels for Fabricating Supercapacitors with High Rate Capability*. The Journal of Physical Chemistry C, 2011. **115**(34): p. 17206-17212.
195. Guiseppi-Elie, A., *Electroconductive hydrogels: Synthesis, characterization and biomedical applications*. Biomaterials, 2010. **31**(10): p. 2701-2716.
196. Wang, W., et al., *Preparation of reduced graphene oxide/gelatin composite films with reinforced mechanical strength*. Materials Research Bulletin, 2012. **47**(9): p. 2245-2251.
197. Bongo, M., et al., *PEDOT:gelatin composites mediate brain endothelial cell adhesion*. Journal of Materials Chemistry B, 2013. **1**(31): p. 3860-3867.
198. Pan, Y., et al., *Green fabrication of chitosan films reinforced with parallel aligned graphene oxide*. Carbohydrate Polymers, 2011. **83**(4): p. 1908-1915.

199. Liu, S., et al., *High performance dielectric elastomers by partially reduced graphene oxide and disruption of hydrogen bonding of polyurethanes*. *Polymer*, 2015. **56**: p. 375-384.
200. Huang, X., et al., *Graphene-Based Materials: Synthesis, Characterization, Properties, and Applications*. *Small*, 2011. **7**(14): p. 1876-1902.
201. Stankovich, S., et al., *Graphene-based composite materials*. *Nature*, 2006. **442**(7100): p. 282-286.
202. Takashima, Y., et al., *Expansion-contraction of photoresponsive artificial muscle regulated by host-guest interactions*. *Nature Communications*, 2012. **3**: p. 1270.
203. Nardes, A.M., et al., *Conductivity, work function, and environmental stability of PEDOT:PSS thin films treated with sorbitol*. *Organic Electronics*, 2008. **9**(5): p. 727-734.
204. Chen, Z., et al., *Three-dimensional flexible and conductive interconnected graphene networks grown by chemical vapour deposition*. *Nat Mater*, 2011. **10**(6): p. 424-428.
205. Naficy, S., G.M. Spinks, and G.G. Wallace, *Thin, Tough, pH-Sensitive Hydrogel Films with Rapid Load Recovery*. *ACS Applied Materials & Interfaces*, 2014. **6**(6): p. 4109-4114.
206. Lin, J., et al., *The synthesis and electrical conductivity of a polyacrylate/graphite hydrogel*. *Reactive and Functional Polymers*, 2007. **67**(4): p. 275-281.
207. Hu, Z., *Synthesis and Application of Modulated Polymer Gels*. *Science (New York, N.Y.)*, 1995. **269**(5223): p. 525-527.
208. Xu, Y., et al., *Strong and ductile poly(vinyl alcohol)/graphene oxide composite films with a layered structure*. *Carbon*, 2009. **47**(15): p. 3538-3543.

209. Xu, Y., et al., *Self-assembled graphene hydrogel via a one-step hydrothermal process*. ACS nano, 2010. **4**(7): p. 4324-4330.
210. Suzuki, A. and T. Tanaka, *Phase transition in polymer gels induced by visible light*. Nature, 1990. **346**(6282): p. 345-347.
211. Balint, R., N.J. Cassidy, and S.H. Cartmell, *Conductive polymers: Towards a smart biomaterial for tissue engineering*. Acta Biomaterialia, 2014. **10**(6): p. 2341-2353.
212. Bukhari, S.M.H., et al., *Synthesis and Characterization of Chemically Cross-Linked Acrylic Acid/Gelatin Hydrogels: Effect of pH and Composition on Swelling and Drug Release*. International Journal of Polymer Science, 2015. **2015**: p. 15.
213. Lira, L.M. and S.I. Córdoba de Torresi, *Conducting polymer–hydrogel composites for electrochemical release devices: Synthesis and characterization of semi-interpenetrating polyaniline–polyacrylamide networks*. Electrochemistry Communications, 2005. **7**(7): p. 717-723.
214. Guiseppi-Elie, A., A.M. Wilson, and K.E. Brown, *Electroconductive hydrogels: Novel materials for the controlled electrorelease of bioactive peptides*. American Chemical Society, Polymer Preprints, Division of Polymer Chemistry, 1997. **38**(2): p. 608-609.
215. Dispenza, C., et al., *Electrically conductive hydrogel composites made of polyaniline nanoparticles and poly (N-vinyl-2-pyrrolidone)*. Polymer, 2006. **47**(4): p. 961-971.
216. Byrne, P.O., *Medical devices having an electrically conductive hydrogel coating*. 1995, Patent No. 5,403,295.



217. Shi, Y., et al., *Conductive “smart” hybrid hydrogels with PNIPAM and nanostructured conductive polymers*. *Advanced Functional Materials*, 2015. **25**(8): p. 1219-1225.
218. Small, C.J., C.O. Too, and G.G. Wallace, *Responsive conducting polymer-hydrogel composites*. *Polymer Gels and Networks*, 1997. **5**(3): p. 251-265.
219. Kim, D.H., M. Abidian, and D.C. Martin, *Conducting polymers grown in hydrogel scaffolds coated on neural prosthetic devices*. *Journal of Biomedical Materials Research - Part A*, 2004. **71**(4): p. 577-585.
220. Chattopadhyay, D.K. and K. Raju, *Structural engineering of polyurethane coatings for high performance applications*. *Progress in polymer science*, 2007. **32**(3): p. 352-418.
221. Kim, H., Y. Miura, and C.W. Macosko, *Graphene/polyurethane nanocomposites for improved gas barrier and electrical conductivity*. *Chemistry of Materials*, 2010. **22**(11): p. 3441-3450.
222. Kuilla, T., et al., *Recent advances in graphene based polymer composites*. *Progress in Polymer Science*, 2010. **35**(11): p. 1350-1375.
223. Puri, P., R. Mehta, and S. Rattan, *Synthesis of Conductive Polyurethane/Graphite Composites for Electromagnetic Interference Shielding*. *Journal of Electronic Materials*, 2015. **44**(11): p. 4255-4268.
224. Seyedin, S., et al., *Compositional Effects of Large Graphene Oxide Sheets on the Spinnability and Properties of Polyurethane Composite Fibers*. *Advanced Materials Interfaces*, 2016. **3**(5): p. 1500672.
225. Wang, X., et al., *In situ polymerization of graphene nanosheets and polyurethane with enhanced mechanical and thermal properties*. *Journal of Materials Chemistry*, 2011. **21**(12): p. 4222-4227.

226. Cai, D., et al., *High performance polyurethane/functionalized graphene nanocomposites with improved mechanical and thermal properties*. Composites Science and Technology, 2012. **72**(6): p. 702-707.
227. Panda, S. and H.A. Ahmed, *Flexible temperature sensor and sensor array*. 2014, Patent Application No. 14/334,979.
228. Strümpfer, R., *Polymer composite thermistors for temperature and current sensors*. Journal of Applied Physics, 1996. **80**(11): p. 6091-6096.
229. Voutilainen, J.V., et al., *All Silk-Screen Printed Polymer-Based Remotely Readable Temperature Sensor*. IEEE Sensors Journal, 2015. **15**(2): p. 723-733.
230. Ehrhart, W.A., et al., *Conductive polyurethane-urea/polyethylene oxide polymer*. 1993, Patent No. 5,198,521.
231. Wei, H., et al., *Anticorrosive conductive polyurethane multiwalled carbon nanotube nanocomposites*. Journal of Materials Chemistry A, 2013. **1**(36): p. 10805-10813.
232. Li, M., et al., *Stretchable conductive polypyrrole/polyurethane (PPy/PU) strain sensor with netlike microcracks for human breath detection*. ACS applied materials & interfaces, 2014. **6**(2): p. 1313-1319.
233. Zhang, G.P. and X.T. Bi, *Electrically conductive blocked copolymer of polyaniline and poly(p-phenylene-terephthalamide)*. Synthetic Metals, 1991. **41**(1): p. 251-254.
234. Tzou, K.T. and R.V. Gregory, *Improved solution stability and spinnability of concentrated polyaniline solutions using N,N'-dimethyl propylene urea as the spin bath solvent*. Synthetic Metals, 1995. **69**(1): p. 109-112.

235. Rodrigues, P.C. and L. Akcelrud, *Networks and blends of polyaniline and polyurethane: correlations between composition and thermal, dynamic mechanical and electrical properties*. *Polymer*, 2003. **44**(22): p. 6891-6899.
236. Xu, J., et al., *Preparation of highly uniform and crosslinked polyurea microspheres through precipitation copolymerization and their property and structure characterization*. *Rsc Advances*, 2014. **4**(61): p. 32134-32141.
237. Dufour, B., et al., *Effect of plasticizing dopants on spectroscopic properties, supramolecular structure, and electrical transport in metallic polyaniline*. *Chemistry of materials*, 2001. **13**(11): p. 4032-4040.
238. Drelinkiewicz, A., M. Hasik, and M. Choczyński, *Preparation and properties of polyaniline containing palladium*. *Materials research bulletin*, 1998. **33**(5): p. 739-762.
239. Sahoo, N.G., et al., *Conducting Shape Memory Polyurethane-Polypyrrole Composites for an Electroactive Actuator*. *Macromolecular Materials and Engineering*, 2005. **290**(11): p. 1049-1055.
240. Spitalsky, Z., et al., *Carbon nanotube-polymer composites: Chemistry, processing, mechanical and electrical properties*. *Progress in Polymer Science*, 2010. **35**(3): p. 357-401.
241. Celzard, A., et al., *Critical concentration in percolating systems containing a high-aspect-ratio filler*. *Physical Review B*, 1996. **53**(10): p. 6209-6214.
242. Li, J., et al., *Correlations between Percolation Threshold, Dispersion State, and Aspect Ratio of Carbon Nanotubes*. *Advanced Functional Materials*, 2007. **17**(16): p. 3207-3215.

243. Du, F., J.E. Fischer, and K.I. Winey, *Effect of nanotube alignment on percolation conductivity in carbon nanotube/polymer composites*. Physical Review B, 2005. **72**(12): p. 121404.
244. Gojny, F.H., et al., *Evaluation and identification of electrical and thermal conduction mechanisms in carbon nanotube/epoxy composites*. Polymer, 2006. **47**(6): p. 2036-2045.
245. Haggenueller, R., et al., *Aligned single-wall carbon nanotubes in composites by melt processing methods*. Chemical Physics Letters, 2000. **330**(3): p. 219-225.
246. Tang, W., M.H. Santare, and S.G. Advani, *Melt processing and mechanical property characterization of multi-walled carbon nanotube/high density polyethylene (MWNT/HDPE) composite films*. Carbon, 2003. **41**(14): p. 2779-2785.
247. Zhu, J., et al., *Reinforcing Epoxy Polymer Composites Through Covalent Integration of Functionalized Nanotubes*. Advanced Functional Materials, 2004. **14**(7): p. 643-648.
248. Coleman, J.N., et al., *Small but strong: A review of the mechanical properties of carbon nanotube-polymer composites*. Carbon, 2006. **44**(9): p. 1624-1652.
249. Gojny, F.H., et al., *Surface modified multi-walled carbon nanotubes in CNT/epoxy-composites*. Chemical Physics Letters, 2003. **370**(5): p. 820-824.
250. Lee, S.-D., et al., *Effects of mechanical strain on the electric conductivity of multiwalled carbon nanotube (MWCNT)/polyurethane (PU) composites*. Fibers and Polymers, 2009. **10**(1): p. 71-76.
251. Salvetat, J.-P., et al., *Mechanical properties of carbon nanotubes*. Applied Physics A, 1999. **69**(3): p. 255-260.

252. Baublits, R.T., et al., *Enhancement with varying phosphate types, concentrations, and pump rates, without sodium chloride on beef biceps femoris quality and sensory characteristics*. Meat Science, 2006. **72**(3): p. 404-414.
253. Rao, G.P., C. Lu, and F. Su, *Sorption of divalent metal ions from aqueous solution by carbon nanotubes: A review*. Separation and Purification Technology, 2007. **58**(1): p. 224-231.
254. Yang, S., et al., *Adsorption of Ni(II) on oxidized multi-walled carbon nanotubes: Effect of contact time, pH, foreign ions and PAA*. Journal of Hazardous Materials, 2009. **166**(1): p. 109-116.
255. Baughman, R.H., et al., *Carbon Nanotube Actuators*. Science, 1999. **284**(5418): p. 1340-1344.
256. Liu, Z., et al., *Microwave Absorption of Single-Walled Carbon Nanotubes/Soluble Cross-Linked Polyurethane Composites*. The Journal of Physical Chemistry C, 2007. **111**(37): p. 13696-13700.
257. Ameli, A., et al., *Polypropylene/carbon nanotube nano/microcellular structures with high dielectric permittivity, low dielectric loss, and low percolation threshold*. Carbon, 2014. **71**: p. 206-217.
258. Buffa, F., et al., *Effect of nanotube functionalization on the properties of single-walled carbon nanotube/polyurethane composites*. Journal of Polymer Science Part B: Polymer Physics, 2007. **45**(4): p. 490-501.
259. Jung, Y.C., N.G. Sahoo, and J.W. Cho, *Polymeric Nanocomposites of Polyurethane Block Copolymers and Functionalized Multi-Walled Carbon Nanotubes as Crosslinkers*. Macromolecular Rapid Communications, 2006. **27**(2): p. 126-131.

260. Erik, T.T. and C. Tsu-Wei, *Aligned multi-walled carbon nanotube-reinforced composites: processing and mechanical characterization*. Journal of Physics D: Applied Physics, 2002. **35**(16): p. L77.
261. Sen, R., et al., *Preparation of Single-Walled Carbon Nanotube Reinforced Polystyrene and Polyurethane Nanofibers and Membranes by Electrospinning*. Nano Letters, 2004. **4**(3): p. 459-464.
262. Jung, Y.C., et al., *Electroactive shape memory performance of polyurethane composite having homogeneously dispersed and covalently crosslinked carbon nanotubes*. Carbon, 2010. **48**(5): p. 1598-1603.
263. Qu, B., et al., *Facile preparation of conductive composite hydrogels based on sodium alginate and graphite*. Materials Letters, 2014. **137**: p. 106-109.
264. Wang, D., et al., *Self-Assembled TiO<sub>2</sub>-Graphene Hybrid Nanostructures for Enhanced Li-Ion Insertion*. ACS Nano, 2009. **3**(4): p. 907-914.
265. Dreyer, D.R., et al., *The chemistry of graphene oxide*. Chemical Society Reviews, 2010. **39**(1): p. 228-240.
266. Dikin, D.A., et al., *Preparation and characterization of graphene oxide paper*. Nature, 2007. **448**(7152): p. 457-460.
267. Eda, G., G. Fanchini, and M. Chhowalla, *Large-area ultrathin films of reduced graphene oxide as a transparent and flexible electronic material*. Nat Nano, 2008. **3**(5): p. 270-274.
268. Huang, K.-J., et al., *Direct electrochemistry of catalase at amine-functionalized graphene/gold nanoparticles composite film for hydrogen peroxide sensor*. Electrochimica Acta, 2011. **56**(7): p. 2947-2953.
269. Wu, Q., et al., *Supercapacitors Based on Flexible Graphene/Polyaniline Nanofiber Composite Films*. ACS Nano, 2010. **4**(4): p. 1963-1970.

270. Dimiev, A.M., L.B. Alemany, and J.M. Tour, *Graphene Oxide. Origin of Acidity, Its Instability in Water, and a New Dynamic Structural Model*. ACS Nano, 2012. **7**(1): p. 576-588.
271. Novoselov, K.S., et al., *Electric Field Effect in Atomically Thin Carbon Films*. Science (Washington), 2004. **306**(5696): p. 666-669.
272. Yung, K.C., et al., *Laser direct patterning of a reduced-graphene oxide transparent circuit on a graphene oxide thin film*. Journal of Applied Physics, 2013. **113**(24): p. 244903.
273. Worsley, M.A., et al., *Synthesis of Graphene Aerogel with High Electrical Conductivity*. Journal of the American Chemical Society, 2010. **132**(40): p. 14067-14069.
274. Tiwari, J.N., et al., *Reduced graphene oxide-based hydrogels for the efficient capture of dye pollutants from aqueous solutions*. Carbon, 2013. **56**: p. 173-182.
275. George, P.M., et al., *Electrically controlled drug delivery from biotin-doped conductive polypyrrole*. Advanced Materials, 2006. **18**(5): p. 577-581.
276. Lee, W., et al., *Simultaneous enhancement of mechanical, electrical and thermal properties of graphene oxide paper by embedding dopamine*. Carbon, 2013. **65**: p. 296-304.
277. Du, J., et al., *Comparison of electrical properties between multi-walled carbon nanotube and graphene nanosheet/high density polyethylene composites with a segregated network structure*. Carbon, 2011. **49**(4): p. 1094-1100.
278. Wang, J., et al., *Preparation and mechanical and electrical properties of graphene nanosheets–poly (methyl methacrylate) nanocomposites via in situ suspension polymerization*. Journal of Applied Polymer Science, 2011. **122**(3): p. 1866-1871.

279. Sayyar, S., et al., *Processable conducting graphene/chitosan hydrogels for tissue engineering*. Journal of Materials Chemistry B, 2015. **3**(3): p. 481-490.
280. Brahim, S., D. Narinesingh, and A. Guiseppi-Elie, *Bio-smart hydrogels: Co-joined molecular recognition and signal transduction in biosensor fabrication and drug delivery*. Biosensors and Bioelectronics, 2002. **17**(11-12): p. 973-981.
281. Jalili, R., J.M. Razal, and G.G. Wallace, *Wet-spinning of PEDOT:PSS/Functionalized-SWNTs Composite: a Facile Route Toward Production of Strong and Highly Conducting Multifunctional Fibers*. Scientific Reports, 2013. **3**: p. 3438.
282. Gross, B.C., et al., *Evaluation of 3D printing and its potential impact on biotechnology and the chemical sciences*. 2014, ACS Publications.
283. Chia, H.N. and B.M. Wu, *Recent advances in 3D printing of biomaterials*. Journal of biological engineering, 2015. **9**(1): p. 4.
284. Hoque, M.E., Y.L. Chuan, and I. Pashby, *Extrusion based rapid prototyping technique: an advanced platform for tissue engineering scaffold fabrication*. Biopolymers, 2012. **97**(2): p. 83-93.
285. Rao, C.e.N.e.R., et al., *Graphene: the new two-dimensional nanomaterial*. Angewandte Chemie International Edition, 2009. **48**(42): p. 7752-7777.
286. Becerril, H.A., et al., *Evaluation of solution-processed reduced graphene oxide films as transparent conductors*. ACS nano, 2008. **2**(3): p. 463-470.
287. Kim, J., L.J. Cote, and J. Huang, *Two dimensional soft material: new faces of graphene oxide*. Accounts of chemical research, 2012. **45**(8): p. 1356-1364.
288. Allen, M.J., V.C. Tung, and R.B. Kaner, *Honeycomb Carbon: A Review of Graphene*. Chemical Reviews, 2010. **110**(1): p. 132-145.



289. Choi, W., et al., *Synthesis of Graphene and Its Applications: A Review*. Critical Reviews in Solid State and Materials Sciences, 2010. **35**(1): p. 52-71.
290. Ferrari, A.C., et al., *Raman Spectrum of Graphene and Graphene Layers*. Physical Review Letters, 2006. **97**(18): p. 187401.
291. Li, X., et al., *Carbon and Graphene Quantum Dots for Optoelectronic and Energy Devices: A Review*. Advanced Functional Materials, 2015. **25**(31): p. 4929-4947.
292. Oh, Y.J., et al., *Oxygen functional groups and electrochemical capacitive behavior of incompletely reduced graphene oxides as a thin-film electrode of supercapacitor*. Electrochimica Acta, 2014. **116**: p. 118-128.
293. Stankovich, S., et al., *Synthesis of graphene-based nanosheets via chemical reduction of exfoliated graphite oxide*. carbon, 2007. **45**(7): p. 1558-1565.
294. Park, S., et al., *Colloidal suspensions of highly reduced graphene oxide in a wide variety of organic solvents*. Nano letters, 2009. **9**(4): p. 1593-1597.
295. Chua, C.K. and M. Pumera, *The reduction of graphene oxide with hydrazine: elucidating its reductive capability based on a reaction-model approach*. Chemical Communications, 2016. **52**(1): p. 72-75.
296. Zhang, L., et al., *Size-controlled synthesis of graphene oxide sheets on a large scale using chemical exfoliation*. Carbon, 2009. **47**(14): p. 3365-3368.
297. Balandin, A.A., et al., *Superior thermal conductivity of single-layer graphene*. Nano letters, 2008. **8**(3): p. 902-907.
298. Saito, K., J. Nakamura, and A. Natori, *Ballistic thermal conductance of a graphene sheet*. Physical Review B, 2007. **76**(11): p. 115409.
299. Peres, N., J.L. Dos Santos, and T. Stauber, *Phenomenological study of the electronic transport coefficients of graphene*. Physical Review B, 2007. **76**(7): p. 073412.

300. Mingo, N. and D. Broido, *Carbon nanotube ballistic thermal conductance and its limits*. Physical review letters, 2005. **95**(9): p. 096105.
301. Kim, J.E., et al., *Graphene oxide liquid crystals*. Angewandte Chemie International Edition, 2011. **50**(13): p. 3043-3047.
302. Yu, C., et al., *Thermal Conductance and Thermopower of an Individual Single-Wall Carbon Nanotube*. Nano Letters, 2005. **5**(9): p. 1842-1846.
303. Jalili, R., et al., *Formation and processability of liquid crystalline dispersions of graphene oxide*. Materials Horizons, 2014. **1**(1): p. 87-91.
304. Jalili, R., et al., *Organic solvent-based graphene oxide liquid crystals: a facile route toward the next generation of self-assembled layer-by-layer multifunctional 3D architectures*. Acs Nano, 2013. **7**(5): p. 3981-3990.
305. Seyedin, M.Z., et al., *Achieving outstanding mechanical performance in reinforced elastomeric composite fibers using large sheets of graphene oxide*. Advanced Functional Materials, 2015. **25**(1): p. 94-104.
306. Aboutalebi, S.H., et al., *High-performance multifunctional graphene yarns: toward wearable all-carbon energy storage textiles*. ACS nano, 2014. **8**(3): p. 2456-2466.
307. Kim, B., et al., *Capacitive behaviour of thermally reduced graphene oxide in a novel ionic liquid containing di-cationic charge*. Synthetic Metals, 2014. **193**: p. 110-116.
308. Zhou, S., et al., *Chemical bonding of partially fluorinated graphene*. The Journal of Physical Chemistry C, 2014. **118**(45): p. 26402-26408.
309. Gao, Y., et al., *Reduced graphene oxide as a catalyst for hydrogenation of nitrobenzene at room temperature*. Chemical Communications, 2011. **47**(8): p. 2432-2434.

310. Wu, Z.-S., et al., *Synthesis of graphene sheets with high electrical conductivity and good thermal stability by hydrogen arc discharge exfoliation*. ACS nano, 2009. **3**(2): p. 411-417.
311. Javadi, M., et al., *Ionic interactions to tune mechanical and electrical properties of hydrated liquid crystal graphene oxide films*. Materials Chemistry and Physics, 2017. **186**: p. 90-97.
312. Zhang, M., et al., *Simple approach for large-scale production of reduced graphene oxide films*. Chemical Engineering Journal, 2014. **243**: p. 340-346.
313. He, Q., et al., *Transparent, flexible, all-reduced graphene oxide thin film transistors*. ACS nano, 2011. **5**(6): p. 5038-5044.
314. Yang, X., et al., *Ordered gelation of chemically converted graphene for next-generation electroconductive hydrogel films*. Angewandte Chemie International Edition, 2011. **50**(32): p. 7325-7328.
315. Pei, S., et al., *Direct reduction of graphene oxide films into highly conductive and flexible graphene films by hydrohalic acids*. Carbon, 2010. **48**(15): p. 4466-4474.
316. Park, K., J.-S. Kim, and A.L. Miller, *A study on effects of size and structure on hygroscopicity of nanoparticles using a tandem differential mobility analyzer and TEM*. Journal of Nanoparticle Research, 2009. **11**(1): p. 175-183.
317. Zhu, J., et al., *Pseudonegative thermal expansion and the state of water in graphene oxide layered assemblies*. ACS nano, 2012. **6**(9): p. 8357-8365.
318. Lerf, A., et al., *Hydration behavior and dynamics of water molecules in graphite oxide*. Journal of Physics and Chemistry of Solids, 2006. **67**(5): p. 1106-1110.
319. Jung, I., et al., *Tunable electrical conductivity of individual graphene oxide sheets reduced at "low" temperatures*. Nano Letters, 2008. **8**(12): p. 4283-4287.

320. Aboutalebi, S.H., et al., *Spontaneous formation of liquid crystals in ultralarge graphene oxide dispersions*. *Advanced Functional Materials*, 2011. **21**(15): p. 2978-2988.
321. Tuinstra, F. and J.L. Koenig, *Raman spectrum of graphite*. *The Journal of Chemical Physics*, 1970. **53**(3): p. 1126-1130.
322. Vallés, C., et al., *The rheological behaviour of concentrated dispersions of graphene oxide*. *Journal of Materials Science*, 2014. **49**(18): p. 6311-6320.
323. Verdejo, R., et al., *Graphene filled polymer nanocomposites*. *Journal of Materials Chemistry*, 2011. **21**(10): p. 3301-3310.
324. Bazant, M.Z. and T.M. Squires, *Induced-charge electrokinetic phenomena*. *Current Opinion in Colloid & Interface Science*, 2010. **15**(3): p. 203-213.
325. Li, D., et al., *Processable aqueous dispersions of graphene nanosheets*. *Nature nanotechnology*, 2008. **3**(2): p. 101-105.
326. Kusalik, P.G. and G. Patey, *On the molecular theory of aqueous electrolyte solutions. I. The solution of the RHNC approximation for models at finite concentration*. *The Journal of chemical physics*, 1988. **88**(12): p. 7715-7738.
327. Ennis, J., R. Kjellander, and D.J. Mitchell, *Dressed ion theory for bulk symmetric electrolytes in the restricted primitive model*. *The Journal of chemical physics*, 1995. **102**(2): p. 975-991.
328. Pelrine, R., R. Kornbluh, and G. Kofod, *High-Strain Actuator Materials Based on Dielectric Elastomers*. *Advanced Materials*, 2000. **12**(16): p. 1223-1225.
329. Chen, W., L. Yan, and P.R. Bangal, *Preparation of graphene by the rapid and mild thermal reduction of graphene oxide induced by microwaves*. *Carbon*, 2010. **48**(4): p. 1146-1152.

330. Dresselhaus, M., A. Jorio, and R. Saito, *Characterizing graphene, graphite, and carbon nanotubes by Raman spectroscopy*. *Annu. Rev. Condens. Matter Phys.*, 2010. **1**(1): p. 89-108.
331. Paredes, J., et al., *Atomic force and scanning tunneling microscopy imaging of graphene nanosheets derived from graphite oxide*. *Langmuir*, 2009. **25**(10): p. 5957-5968.
332. Graf, D., et al., *Spatially resolved Raman spectroscopy of single-and few-layer graphene*. *Nano letters*, 2007. **7**(2): p. 238-242.
333. Medhekar, N.V., et al., *Hydrogen bond networks in graphene oxide composite paper: structure and mechanical properties*. *Acs Nano*, 2010. **4**(4): p. 2300-2306.
334. Dikin, D.A., et al., *Preparation and characterization of graphene oxide paper*. *Nature*, 2007. **448**(7152): p. 457.
335. Gong, T., et al., *Thickness Dependence of the Mechanical Properties of Free-Standing Graphene Oxide Papers*. *Advanced Functional Materials*, 2015. **25**(24): p. 3756-3763.
336. Xu, Z. and C. Gao, *Graphene chiral liquid crystals and macroscopic assembled fibres*. *Nature Communications*, 2011. **2**: p. 571.
337. Chen, H., et al., *Mechanically strong, electrically conductive, and biocompatible graphene paper*. *Advanced Materials*, 2008. **20**(18): p. 3557-3561.
338. Li, Z., et al., *Superstructured assembly of nanocarbons: fullerenes, nanotubes, and graphene*. *Chemical reviews*, 2015. **115**(15): p. 7046-7117.
339. Cao, X., Z. Yin, and H. Zhang, *Three-dimensional graphene materials: preparation, structures and application in supercapacitors*. *Energy & Environmental Science*, 2014. **7**(6): p. 1850-1865.

340. Compton, O.C., et al., *Tuning the mechanical properties of graphene oxide paper and its associated polymer nanocomposites by controlling cooperative intersheet hydrogen bonding*. ACS nano, 2012. **6**(3): p. 2008-2019.
341. Haynes, W.M., *CRC handbook of chemistry and physics*. 2014: CRC press.
342. Li, A., C. Zhang, and Y.-F. Zhang, *Thermal Conductivity of Graphene-Polymer Composites: Mechanisms, Properties, and Applications*. Polymers, 2017. **9**(9): p. 437.
343. Ahmed, E.M., *Hydrogel: Preparation, characterization, and applications: A review*. Journal of advanced research, 2015. **6**(2): p. 105-121.
344. Nakamura, T., et al. *Development of flexible and wide-range polymer-based temperature sensor for human bodies*. in *Biomedical and Health Informatics (BHI), 2016 IEEE-EMBS International Conference on*. 2016. IEEE.
345. Ge, J., et al., *Drug release from electric-field-responsive nanoparticles*. ACS nano, 2011. **6**(1): p. 227-233.
346. Pan, L., et al., *Hierarchical nanostructured conducting polymer hydrogel with high electrochemical activity*. Proceedings of the National Academy of Sciences, 2012. **109**(24): p. 9287-9292.
347. Lu, Y., et al., *Elastic, conductive, polymeric hydrogels and sponges*. Scientific reports, 2014. **4**.
348. Pissis, P. and A. Kyritsis, *Electrical conductivity studies in hydrogels*. Solid State Ionics, 1997. **97**(1): p. 105-113.
349. Mawad, D., A. Lauto, and G.G. Wallace, *Conductive polymer hydrogels*, in *Polymeric hydrogels as smart biomaterials*. 2016, Springer. p. 19-44.

350. Psarras, G., *Hopping conductivity in polymer matrix–metal particles composites*. Composites Part A: applied science and manufacturing, 2006. **37**(10): p. 1545-1553.
351. Swarnakar, S., et al., *Matrix metalloproteinases in health and disease: regulation by melatonin*. Journal of Pineal Research, 2011. **50**(1): p. 8-20.
352. Yoo, D., J. Kim, and J.H. Kim, *Direct synthesis of highly conductive poly (3, 4-ethylenedioxythiophene): poly (4-styrenesulfonate)(PEDOT: PSS)/graphene composites and their applications in energy harvesting systems*. Nano Research, 2014. **7**(5): p. 717.
353. Baughman, R.H., A.A. Zakhidov, and W.A. De Heer, *Carbon nanotubes--the route toward applications*. science, 2002. **297**(5582): p. 787-792.
354. Borazan, I., et al. *The effect of acid treatment of PEDOT:PSS anode for organic solar cells*. in *Photovoltaic Specialist Conference (PVSC), 2015 IEEE 42nd*. 2015.
355. Dong, H. and S. Qi, *Realising the potential of graphene-based materials for biosurfaces—A future perspective*. Biosurface and Biotribology, 2015. **1**(4): p. 229-248.
356. Chung, C., et al., *Biomedical applications of graphene and graphene oxide*. Accounts of chemical research, 2013. **46**(10): p. 2211-2224.
357. Wang, Y., et al., *Graphene and graphene oxide: biofunctionalization and applications in biotechnology*. Trends in biotechnology, 2011. **29**(5): p. 205-212.
358. Seyedin, S., et al., *Compositional effects of large graphene oxide sheets on the spinnability and properties of polyurethane composite fibers*. Advanced Materials Interfaces, 2016. **3**(5).
359. Zhao, M. *Electrical fields in wound healing—an overriding signal that directs cell migration*. in *Seminars in cell & developmental biology*. 2009. Elsevier.

360. Park, S.Y., et al., *Enhanced differentiation of human neural stem cells into neurons on graphene*. *Advanced Materials*, 2011. **23**(36).
361. Schmidt, C.E., et al., *Stimulation of neurite outgrowth using an electrically conducting polymer*. *Proceedings of the National Academy of Sciences*, 1997. **94**(17): p. 8948-8953.
362. Jin, L., et al., *Stimulated osteogenic differentiation of human mesenchymal stem cells by reduced graphene oxide*. *Journal of nanoscience and nanotechnology*, 2015. **15**(10): p. 7966-7970.
363. Koerbitzer, B., et al., *Graphene electrodes for stimulation of neuronal cells*. *2D Materials*, 2016. **3**(2): p. 024004.
364. Javadi, M., et al., *Conductive Tough Hydrogel for Bioapplications*. *Macromolecular bioscience*, 2018. **18**(2).
365. Kwon, J.-Y., E.-Y. Kim, and H.-D. Kim, *Preparation and properties of waterborne-polyurethane coating materials containing conductive polyaniline*. *Macromolecular research*, 2004. **12**(3): p. 303-310.
366. Chen, D. and G. Chen, *The conductive property of polyurethane/expanded graphite powder composite foams*. *Journal of Reinforced Plastics and Composites*, 2011. **30**(9): p. 757-761.
367. Kotal, M., S.K. Srivastava, and B. Paramanik, *Enhancements in conductivity and thermal stabilities of polypyrrole/polyurethane nanoblends*. *The Journal of Physical Chemistry C*, 2011. **115**(5): p. 1496-1505.
368. Cho, J.W., et al., *Electroactive shape-memory polyurethane composites incorporating carbon nanotubes*. *Macromolecular Rapid Communications*, 2005. **26**(5): p. 412-416.



369. Lee, H.-F. and H.H. Yu, *Study of electroactive shape memory polyurethane-carbon nanotube hybrids*. *Soft Matter*, 2011. **7**(8): p. 3801-3807.
370. Carotenuto, G., et al. *Graphene-polymer composites*. in *IOP Conference Series: Materials Science and Engineering*. 2012. IOP Publishing.
371. Shang, S., W. Zeng, and X.-m. Tao, *High stretchable MWNTs/polyurethane conductive nanocomposites*. *Journal of Materials Chemistry*, 2011. **21**(20): p. 7274-7280.
372. Puri, P., R. Mehta, and S. Rattan, *Synthesis of conductive polyurethane/graphite composites for electromagnetic interference shielding*. *Journal of Electronic Materials*, 2015. **44**(11): p. 4255.
373. Seyedin, M.Z., et al., *Strain-Responsive Polyurethane/PEDOT: PSS Elastomeric Composite Fibers with High Electrical Conductivity*. *Advanced Functional Materials*, 2014. **24**(20): p. 2957-2966.
374. Narayan, R., et al., *Graphene oxide liquid crystals: discovery, evolution and applications*. *Advanced Materials*, 2016. **28**(16): p. 3045-3068.
375. Hu, N., et al., *Tunneling effect in a polymer/carbon nanotube nanocomposite strain sensor*. *Acta Materialia*, 2008. **56**(13): p. 2929-2936.
376. Lawrence, S.S., J. Willett, and C. Carriere, *Effect of moisture on the tensile properties of poly (hydroxy ester ether)*. *Polymer*, 2001. **42**(13): p. 5643-5650.
377. Shao, J.J., W. Lv, and Q.H. Yang, *Self-assembly of graphene oxide at interfaces*. *Advanced Materials*, 2014. **26**(32): p. 5586-5612.
378. Sato, S., *Liquid-crystal lens-cells with variable focal length*. *Japanese Journal of Applied Physics*, 1979. **18**(9): p. 1679.

379. Chen, X., et al., *Synthesis of “clean” and well-dispersive Pd nanoparticles with excellent electrocatalytic property on graphene oxide*. Journal of the American Chemical Society, 2011. **133**(11): p. 3693-3695.
380. Xu, Y., et al., *Strong and ductile poly (vinyl alcohol)/graphene oxide composite films with a layered structure*. Carbon, 2009. **47**(15): p. 3538-3543.
381. Ramesha, G., et al., *Graphene and graphene oxide as effective adsorbents toward anionic and cationic dyes*. Journal of colloid and interface science, 2011. **361**(1): p. 270-277.
382. Lu, G., L.E. Ocola, and J. Chen, *Gas detection using low-temperature reduced graphene oxide sheets*. Applied Physics Letters, 2009. **94**(8): p. 083111.
383. Zhu, J., et al., *Facile synthesis of metal oxide/reduced graphene oxide hybrids with high lithium storage capacity and stable cyclability*. Nanoscale, 2011. **3**(3): p. 1084-1089.
384. Gurunathan, S., et al., *Microbial reduction of graphene oxide by Escherichia coli: a green chemistry approach*. Colloids and Surfaces B: Biointerfaces, 2013. **102**: p. 772-777.
385. Liu, S., et al., *A method for the production of reduced graphene oxide using benzylamine as a reducing and stabilizing agent and its subsequent decoration with Ag nanoparticles for enzymeless hydrogen peroxide detection*. Carbon, 2011. **49**(10): p. 3158-3164.
386. Lu, G., L.E. Ocola, and J. Chen, *Reduced graphene oxide for room-temperature gas sensors*. Nanotechnology, 2009. **20**(44): p. 445502.
387. Dutta, T., et al., *ROS generation by reduced graphene oxide (rGO) induced by visible light showing antibacterial activity: comparison with graphene oxide (GO)*. Rsc Advances, 2015. **5**(98): p. 80192-80195.

388. Khodakarimi, S., et al., *Effects of process and post-process treatments on the electrical conductivity of the PEDOT: PSS films*. Journal of Materials Science: Materials in Electronics, 2016. **27**(2): p. 1278-1285.
389. Liu, Z., et al., *Transparent conductive electrodes from graphene/PEDOT: PSS hybrid inks for ultrathin organic photodetectors*. Advanced Materials, 2015. **27**(4): p. 669-675.
390. Chen, T., et al., *Ultra high permittivity and significantly enhanced electric field induced strain in PEDOT: PSS–RGO-PU intelligent shape-changing electro-active polymers*. RSC Advances, 2014. **4**(109): p. 64061-64067.
391. Yang, D., et al., *Chemical analysis of graphene oxide films after heat and chemical treatments by X-ray photoelectron and Micro-Raman spectroscopy*. Carbon, 2009. **47**(1): p. 145-152.
392. Hardy, J.G., J.Y. Lee, and C.E. Schmidt, *Biomimetic conducting polymer-based tissue scaffolds*. Current opinion in biotechnology, 2013. **24**(5): p. 847-854.
393. McCaig, C.D., et al., *Controlling cell behavior electrically: current views and future potential*. Physiological reviews, 2005. **85**(3): p. 943-978.
394. Stewart, E., et al., *Electrical stimulation using conductive polymer polypyrrole promotes differentiation of human neural stem cells: a biocompatible platform for translational neural tissue engineering*. Tissue Engineering Part C: Methods, 2014. **21**(4): p. 385-393.
395. Aguilar, M.R. and J. San Román, *Smart polymers and their applications*. 2014: Elsevier.
396. Jeong, B. and A. Gutowska, *Lessons from nature: stimuli-responsive polymers and their biomedical applications*. Trends in biotechnology, 2002. **20**(7): p. 305-311.

397. Huang, Z.-M., et al., *A review on polymer nanofibers by electrospinning and their applications in nanocomposites*. Composites science and technology, 2003. **63**(15): p. 2223-2253.
398. Smith, R.C., *Smart material systems: model development*. 2005: SIAM.
399. Evans, J.S., *Negative thermal expansion materials*. Journal of the Chemical Society, Dalton Transactions, 1999(19): p. 3317-3326.
400. Dove, M.T. and H. Fang, *Negative thermal expansion and associated anomalous physical properties: review of the lattice dynamics theoretical foundation*. Reports on Progress in Physics, 2016. **79**(6): p. 066503.
401. Beebe, D.J., et al., *Functional hydrogel structures for autonomous flow control inside microfluidic channels*. Nature, 2000. **404**(6778): p. 588-590.
402. Kirchmayer, D.M., R. Gorkin Iii, and M. in het Panhuis, *An overview of the suitability of hydrogel-forming polymers for extrusion-based 3D-printing*. Journal of Materials Chemistry B, 2015. **3**(20): p. 4105-4117.
403. Saleh, E., et al., *3D inkjet-printed UV-curable inks for multi-functional electromagnetic applications*. Additive Manufacturing, 2017. **13**: p. 143-148.
404. Dizon, J.R.C., et al., *Mechanical characterization of 3D-printed polymers*. Additive Manufacturing, 2018. **20**: p. 44-67.
405. Klemens, P., *Thermal Conductivity 14*. 2013: Springer.
406. Aziz, S., et al., *Controlled and scalable torsional actuation of twisted nylon 6 fiber*. Journal of Polymer Science Part B: Polymer Physics, 2016. **54**(13): p. 1278-1286.
407. Jones, L.S., Kaufmann, A. and Middaugh, C.R., *Silicone oil induced aggregation of proteins*. Journal of pharmaceutical sciences, 2005. 94(4): p.918-927.

408. Takenaka, K., Negative thermal expansion materials: technological key for control of thermal expansion. *Science and technology of advanced materials*, 2012. 13(1): p. 013001.
409. Gustafsson, S.E., *Transient plane source techniques for thermal conductivity and thermal diffusivity measurements of solid materials*. *Review of scientific instruments*, 1991. **62**(3): p. 797-804.
410. Bohac, V., et al., *Parameter estimations for measurements of thermal transport properties with the hot disk thermal constants analyzer*. *Review of Scientific Instruments*, 2000. **71**(6): p. 2452-2455.
411. Mihiretie, B., et al., *Thermal depth profiling of materials for defect detection using hot disk technique*. *AIP Advances*, 2016. **6**(8): p. 085217.
412. Jiang, Y. and Y. Li, *Novel 3D-Printed Hybrid Auxetic Mechanical Metamaterial with Chirality-Induced Sequential Cell Opening Mechanisms*. *Advanced Engineering Materials*, 2018. **20**(2): p. 1700744.
413. Svedman, P., *Irrigation treatment of leg ulcers*. *The Lancet*, 1983. **322**(8349): p. 532-534.
414. Kokubo, T. and H. Takadama, *How useful is SBF in predicting in vivo bone bioactivity*” *Biomaterials*, 2006. **27**(15): p. 2907-2915.
415. Pan, Y.X., et al., *A new process of fabricating electrically conducting nylon 6/graphite nanocomposites via intercalation polymerization*. *Journal of Polymer Science Part B: Polymer Physics*, 2000. **38**(12): p. 1626-1633.
416. Gojny, F.H., et al., *Influence of nano-modification on the mechanical and electrical properties of conventional fibre-reinforced composites*. *Composites Part A: Applied Science and Manufacturing*, 2005. **36**(11): p. 1525-1535.

417. Hu, G., et al., *Low percolation thresholds of electrical conductivity and rheology in poly (ethylene terephthalate) through the networks of multi-walled carbon nanotubes*. *Polymer*, 2006. **47**(1): p. 480-488.
418. Mattevi, C., et al., *Evolution of electrical, chemical, and structural properties of transparent and conducting chemically derived graphene thin films*. *Advanced Functional Materials*, 2009. **19**(16): p. 2577-2583.
419. Arora, S., T. Ghosh, and J. Muth, *Dielectric elastomer based prototype fiber actuators*. *Sensors and Actuators A: Physical*, 2007. **136**(1): p. 321-328.
420. Bruck, H.A., C.L. Moore, and T.L. Valentine, *Repeatable bending actuation in polyurethanes using opposing embedded one-way shape memory alloy wires exhibiting large deformation recovery*. *Smart materials and structures*, 2002. **11**(4): p. 509.
421. Hernandez, R., et al., *Microstructural organization of three-phase polydimethylsiloxane-based segmented polyurethanes*. *Macromolecules*, 2007. **40**(15): p. 5441-5449.
422. Tobushi, H., et al., *The influence of shape-holding conditions on shape recovery of polyurethane-shape memory polymer foams*. *Smart Materials and Structures*, 2004. **13**(4): p. 881.
423. Tsai, M.-C., et al., *Evaluation of biodegradable elastic scaffolds made of anionic polyurethane for cartilage tissue engineering*. *Colloids and Surfaces B: Biointerfaces*, 2015. **125**: p. 34-44.
424. Estes, G., R. Seymour, and S.L. Cooper, *Infrared studies of segmented polyurethane elastomers. II. Infrared dichroism*. *Macromolecules*, 1971. **4**(4): p. 452-457.
425. Kaviany, M., *Heat transfer physics*. 2014: Cambridge University Press.

426. Takenaka, K., *Negative thermal expansion materials: technological key for control of thermal expansion*. Science and technology of advanced materials, 2012. **13**(1): p. 013001.
427. Yoon, D., Y.-W. Son, and H. Cheong, *Negative thermal expansion coefficient of graphene measured by Raman spectroscopy*. Nano letters, 2011. **11**(8): p. 3227-3231.
428. Ramanathan, T., et al., *Functionalized graphene sheets for polymer nanocomposites*. Nature nanotechnology, 2008. **3**(6): p. 327.
429. Lessing, J.A., et al., *Flexible and stretchable electronic strain-limited layer for soft actuators*. 2018, Patent No. 9,993,921.
430. Bedell, S.W., et al., *Flexible and stretchable sensors formed by patterned spalling*. 2018, Patent No. 9,874,534.
431. Maiti, R., et al., *In vivo measurement of skin surface strain and sub-surface layer deformation induced by natural tissue stretching*. Journal of the Mechanical Behavior of Biomedical Materials, 2016. **62**: p. 556-569.
432. Fan, J.A., et al., *Fractal design concepts for stretchable electronics*. Nature Communications, 2014. **5**: p. 3266.
433. Huang, Y., et al., *Self-similar design for stretchable wireless LC strain sensors*. Sensors and Actuators A: Physical, 2015. **224**: p. 36-42.
434. Zalameda, J.N. and F.R. Parker. *Thermal inspection of composite honeycomb structures*. 2014.
435. Köse, M.E., B.F. Carroll, and K.S. Schanze, *Preparation and spectroscopic properties of multiluminophore luminescent oxygen and temperature sensor films*. Langmuir, 2005. **21**(20): p. 9121-9129.

436. Suehle, J.S., et al., *Tin oxide gas sensor fabricated using CMOS micro-hotplates and in-situ processing*. IEEE Electron Device Letters, 1993. **14**(3): p. 118-120.
437. Dargaville, T.R., et al., *Sensors and imaging for wound healing: A review*. Biosensors and Bioelectronics, 2013. **41**: p. 30-42.
438. Shi, L., et al., *PH in the bacteria-contaminated wound and its impact on clostridium histolyticum collagenase activity: Implications for the use of collagenase wound debridement agents*. Journal of Wound, Ostomy and Continence Nursing, 2011. **38**(5): p. 514-521.
439. Silver, J.H., J.W. Marchant, and S.L. Cooper, *Effect of polyol type on the physical properties and thrombogenicity of sulfonate-containing polyurethanes*. Journal of Biomedical Materials Research, 1993. **27**(11): p. 1443-1457.
440. Zhang, C., et al., *Synthesis and characterization of biodegradable elastomeric polyurethane scaffolds fabricated by the inkjet technique*. Biomaterials, 2008. **29**(28): p. 3781-3791.